First Principles Calculations for the Semiconductor Material Kesterite Cu_2ZnSnS_4 and Se-containing Derivatives

INAUGURAL DISSERTATION

TO OBTAIN THE ACADEMIC DEGREE
DOCTOR RERUM NATURALIUM (DR. RER. NAT.)

SUBMITTED TO
THE DEPARTMENT OF BIOLOGY, CHEMISTRY AND PHARMACY
OF FREIE UNIVERSITÄT BERLIN

by

Marcel Quennet

from Freiburg

2016

This work was prepared under the supervision of
Prof. Dr. Beate Paulus
(Freie Universität Berlin)
from October 2013 to September 2016

1. Gutachter: Prof. Dr. Beate Paulus

2. Gutachter: Prof. Dr. Martin Lerch

Disputation am: 29.11.2016

This page is intentionally left blank.

Acknowledgements

Foremost I would like to express my most sincere gratitude to my supervisor Prof. Dr. Beate Paulus for her help and support during my thesis and master studies in the last years. I am especially grateful for the opportunities provided by her since my first research internship in her group which gave me the possibility to specialize my expertise in theoretical chemistry and broaden my scientific horizon. She allowed me to follow my research ideas and gave me enough freedom to try new approaches, while she steadily guided my independent work when necessary.

I would also like to express my gratitude to Prof. Dr. Martin Lerch, who kindly accepted the task of being the second referee. Our discussion about disordered kesterites helped me to efficiently address the theoretical modeling of disordered kesterite systems.

I'm very grateful for the financial and scientific support by the Helmholtz-Zentrum Berlin and the MatSEC (Materials for Solar Energy Conversion) graduate school. To be a member of the MatSEC graduate school helped me to develop my scientific expertise further, whereby the helpful research colloquia were inspiring for my work and for new collaborations between theory and experiment. Hereby I want to thank Prof. Dr. Susan Schorr, Dr. Gabriele Lampert and Dr. Thomas Unold to name few for the great coordination and helpful scientific discussions about kesterites.

Moreover, I would like to thank all members of the AG Paulus and the group of Dr. Jean Christoph Tremblay for the pleasant working atmosphere during the last years. There are many colleagues to whom I am grateful for collaborations and helpful discussions related to my field of research. My special thanks goes to Dr. Lukas Hammerschmidt for the collaborations on skutterudite surfaces and helpful discussions about kesterites.

I am very grateful to Tobias Serwatka, whom I had the pleasure to supervise during his research internship on kesterite clusters. With his efforts and independence I could quickly proceed in the theoretical modeling of kesterite clusters. I'm especially thankful for the time and (scientific) discussions with Lukas Eugen Marsoner Steinkasserer, Gunter Hermann, Vincent Pohl and Johannes Horst Budau during the last years.

I want to thank the technical support of the Zentraleinrichtung für Datenverarbeitung (ZEDAT) for providing fast and uncomplicated technical support as well as the high performance computing resources. I'm grateful for the computing power and time provided by the North German Supercomputing Alliance (Norddeutscher Verbund zur Förderung des Hoch- und Höchstleistungsrechnens) without which this work would not have been possible at all.

Finally, I would like to thank my whole family for their support and their understanding during the last years.

Zusammenfassung

In den letzten Jahren stieg die weltweite Nachfrage nach elektrischer Energie aufgrund der steigenden Weltwirtschaft stark an, welche in der Zukunft nur mit nachhaltigen und erneuerbaren Energiequellen umweltfreundlich bedient werden kann. Ein besonders hohes Potential hierfür weisen Photovoltaik-Solarzellen durch die hohe Sonneneinstrahlung auf der Erde auf. Leider besitzen heutige Solarzellenmaterialien oft Nachteile wie hohe Kosten oder die Verwendung von seltenen oder umweltschädlichen Materialien. Ein vielversprechender Ersatz hierfür sind Kësterite ($Cu_2ZnSnS_xSe_{4-x}$), die aus nicht-giftigen Elementen bestehen, welche auf der Erde reichhaltig vorhanden sind und so eine zukünftige Verfügbarkeit garantieren.

Kësterite werden in dieser Arbeit daher mit quantenchemischen *first-principles* Methoden als Solarzellenabsorber geprüft, wobei Schlüsselfaktoren für die bisher niedrigen Effizienzen untersucht werden und ein Einblick in mögliche leistungssteigernde Materialmodifikationen gewährt wird. Erhöhte Energieausbeuten werden durch $Cu_2ZnSnS_xSe_{4-x}$ Legierungen erzielt, die allerdings durch Legierungsmuster eine schwankende Materialqualität aufweisen, die wiederum Schwankungen der Bandlücke verursachen. Weitere Qualitätsschwankungen treten durch Unordnungen auf den 2c und 2d Wyckoff Positionen in Cu_2ZnSnS_4 auf, deren Einfluss durch die Analyse der elektronischen Struktur mit Bezug zu unterschiedlichen Unordnungsmustern und Unordnungsanteilen untersucht wird. Dabei zeigt sich, dass die 2c/2d Unordnungen einer der Hauptverursacher für Bandlückenschwankungen und folglich niedrige Effizienzen sind, wobei die S/Se Legierungen nur einen kleinen Teil dazu beitragen.

Um den Kësterit Solarzellen zu einer stärkeren Verbreitung zu verhelfen, ist es notwendig durch Nanostrukturierungen die Effizienz über das Shockley–Queisser Limit anzuheben sowie die Materialkosten weiter zu reduzieren. Einen Schritt in Richtung der Nanostrukturierung ist durch die theoretische Untersuchung von Cu_2ZnSnS_4-Oberflächen und -Clustern gegeben, die beide unterschiedliche Grenzen der Nanostrukturierung darstellen. Durch die Stabilitätsuntersuchungen der niedrig indizierten Oberflächen durch Oberflächenenergien wird ein Einblick in strukturelle Stabilitätsmuster gegeben. Zusätzlich werden erfolgreich Oberflächenenergien für symmetrische nicht-stoichiometrische Oberflächen durch ein Extrapolationsschema bestimmt. Cluster dienen in dieser Arbeit als strukturelles Modell für realistische Nanokristalle mit einem festen bulk-ähnlichen Kern und einer relaxierten Oberfläche. In beiden Modellen zeigt sich eine Magnetisierung der Oberfläche innerhalb des Computermodells sowie in Clustern größenabhängige fundamentale Lücken sowie Oberflächenzustände in den Oberflächen, die zu einer größeren Energieausbeute verwendet werden können.

Die theoretischen Untersuchungen zeigen einen der Hauptgründe für die Bandlückenschwankungen und eine Möglichkeit die Leistung der Kësterit-Solarzellen durch Nanostrukturierung zu erhöhen. Durch eine Kombination der theoretischen Ergebnisse mit Experimenten wird ein möglicher Pfad für effektivere Kësterit-Solarzellen aufgezeigt.

Summary

In the last years the demand for electrical energy has been increasing continuously due to an expanding world economy, which has to be satisfied by sustainable and renewable energy sources to preserve the environment. Especially photovoltaic solar cells feature a high potential due to the immense energy reaching earth by solar radiation. Unfortunately, today's solar cell absorber materials often show certain disadvantages like high costs or the utilization of rare or environmentally harmful materials. A promising solar cell absorber are kesterites ($Cu_2ZnSnS_xSe_{4-x}$), which only consist of earth abundant, non-toxic, and highly available elements, assuring availability in the future.

This work reviews kesterites as a solar cell absorber by quantum chemical *first-principles* calculations to understand key factors for the still low efficiencies, and give insight on possible performance enhancing material modifications. Hereby $Cu_2ZnSnS_xSe_{4-x}$ alloys are utilized for band gap engineering to increase the efficiency, whereby varying material qualities due to different structural alloy patterns introduce small band gap fluctuations. Further varying material qualities are shown by disorders on the 2c and 2d Wyckoff positions in Cu_2ZnSnS_4, whose influence is shown by an analysis of the electronic structure with respect to different structural disorder patterns and proportions. The 2c/2d disorders are revealed to be one of the main reasons for the band gap fluctuations, which induce lower efficiencies, whereby the $Cu_2ZnSnS_xSe_{4-x}$ alloys only slightly contribute.

For a large-scale energy production via kesterite solar cells, further improvements are required, like efficiencies beyond the Shockley–Queisser limit and a reduction of material costs, which can be introduced by nanostructuring. A step towards nanostructuring is taken by theoretically investigating Cu_2ZnSnS_4 surfaces and clusters, which simulate different forms of nanostructuring. By studying the stability of different low-index surfaces via surface energies, an insight on structural stabilizing patterns is given, whereby the challenge of calculating surface energies for off-stoichiometric symmetric slabs is successfully addressed via an extrapolation scheme. Decreasing the nanostructure size further to finite clusters, a structural model is designed to simulate a realistic nanocrystal with a fixed bulk-like core and a relaxed surface. Both modeling schemes show a magnetization of the surface within the computational model. The Cu_2ZnSnS_4 clusters show a size-dependent fundamental gap and the Cu_2ZnSnS_4 surfaces feature surface states within the bulk band gap, which can be utilized for an increased energy harvest.

The quantum chemical *first-principles* investigations show a main reason for the band gap fluctuations and an opportunity for an enhancement of the solar cell performance by nanostructuring. By combining these theoretical findings with experiments, a possible route for more efficient kesterite solar cells is indicated.

This page is intentionally left blank.

Contents

List of Figures

List of Tables

List of Abbreviations

HF	Hartree-Fock
SCF	Self consistent field
SD	Slater determinant
SE	Schrödinger equation
BO	Born-Oppenheimer
MO-LCAO	Molecular orbital as linear combination of atomic orbitals
DFT	Density functional theory
KS	Kohn Sham
RKS	Restricted Kohn Sham
UKS	Unrestricted Kohn Sham
EX	Exchange and correlation
STO	Slater-type orbitals
GTO	Gaussian-type orbital
DFTB	Density Functional based Tight Binding
TDDFT	Time dependent Density Functional theory
GW	Single particle Green's function G and the screened Coulomb interaction W
BSE	Bethe–Salpeter equation
LDA	Local density approximation
GGA	Generalized gradient approximation
PP	Pseudo potential
PAW	Projector augmented wave method
BSSE	Basis set superposition error
BZ	Brillouin zone
DOS	Density of states
NPA	Natural Population Analysis
NAO	Natural atomic orbital
NO	Natural orbital
HOMO	Highest occupied molecular orbital
LUMO	Lowest unoccupied molecular orbital
SQ	Shockley–Queisser
CZTS	Cu_2ZnSnS_4
CZTSe	$Cu_2ZnSnSe_4$
CZTSSe	$Cu_2ZnSnS_xSe_{4-x}$
GaAs	Gallium Arsenide
CdTe	Cadmium Telluride
CIGS	Copper Indium Gallium Selenide
Cu	Copper
Zn	Zinc
Sn	Tin
S	Sulfur
Se	Selenium
Cu_{2a}	Copper on Wyckoff position 2a
Cu_{Zn}	Copper antisite on Zinc position
V_{Cu}	Vacancy at a Copper position
VASP	Vienna Ab initio Simulation Package

This page is intentionally left blank.

Chapter 1

Introduction

Over the last twenty years the demand for energy has been continuously increasing due to an expanding world economy, growing world population and increasing living standards especially in emerging countries. From 1990 to 2013, the world primary energy consumption increased from 370 Exajoule ($37x10^{19}$ Joule) to 575 Exajoule ($57.5x10^{19}$ Joule) [1], whereby the primary energy consumption is expected to keep further increasing. This energy today is mainly produced by fossil fuels, although its limited resources and climate-damaging combustion. Another main contributor to the total (electric) energy is nuclear energy with about 10.6 % [2], despite two large incidents in nuclear power plants in the last 30 years and the long remaining nuclear waste. With the knowledge about these disadvantages for the current and future population of the earth, many countries started a transition away from non-renewable and environmentally harmful energy sources to sustainable and renewable energy sources. The usage of renewable energy sources varies from country to country, whereby Germany is an early pioneer in this field. In 2015 the estimated primary energy consumption in Germany of 13.31 Exajoule is composed of energy produced by 33.9 % mineral oil, 21.1 % natural gas, 12.7 % hard coal, 11.8 % lignite, 12.5 % renewable sources and 7.5 % nuclear energy [1].

The renewable energy is produced from a wide variety of sources, for example wind, bio fuels, biomass, geo- and solarthermy, hydro-power and photovoltaics to name a few. This diversity is an advantage for a long-term transition to an environment-friendly and renewable energy production. Especially the photovoltaic energy production is a key factor, since the potential annual solar energy reaching earth is about 1575 to 49837 Exajoule [3]. Thus, to keep pace with the increasing demand for electrical and total primary energy, new materials have to be found for a more efficient electrical power generation by photovoltaic solar cells. The focus hereby lies on sustainable and environment-friendly materials, which are available at a reasonable cost and available in the future for an extensive application.

1.1 Electrical Energy Production via Solar Radiation

In general, solar radiation is converted into electrical energy by photovoltaic solar cells, which absorb the solar radiation of a certain wavelength region [4]. In principle, a solar cell consists of an *n-type* and *p-type* semiconductor, which form a *p-n-semiconductor junction* (see fig. 1.1). The n-type semiconductor features an excess of electrons, whereby the Fermi level lies closer to the conduction band than to the valence band. In contrast, in p-type semiconductors the Fermi level lies closer to the valence band than to the conduction band, whereby a hole excess is shown. The two different types are obtained by doping, for example, the widely used solar cell material silicon with phosphorus to obtain an n-type semiconductor or with boron to obtain a p-type semiconductor. The p-n junction describes the boundary interface between the n-type and p-type semiconductor in the solar cell. Each of the semiconductors is furthermore bound to a different electrode, to which a consumer can be connected.

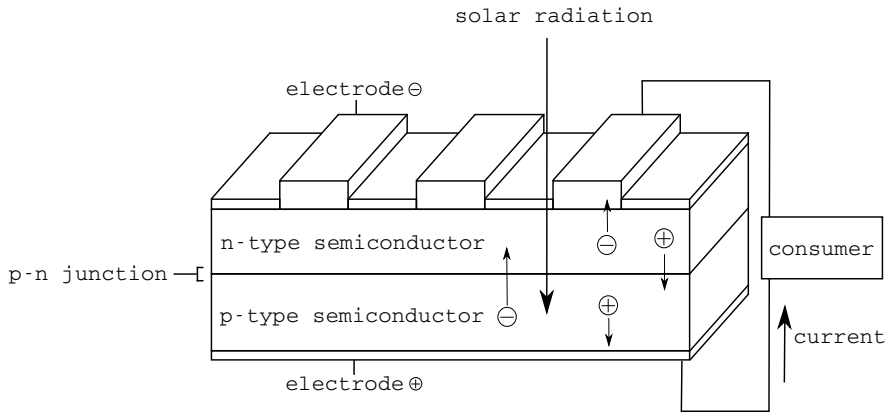

Figure 1.1: Schematic illustration of a model solar cell module. By absorbing the solar radiation, an electron-hole pair is generated in the semiconductors. Holes move to the positive electrode and electrons move to the negative electrode, generating an electric current.

There are various possibilities how the solar radiation can interact with the solar cell. For example the photons of the solar radiation can be reflected at the surface of the solar cell or pass through the material, if the photons exhibit too little energy. However, if the photons in the solar radiation feature a minimal energy larger than the band gap of the utilized semiconductors, the photons are absorbed in the solar cell module, leading to an excitation of an electron from the valence band to the conduction band, whereby charge carriers in form of electron-hole pairs are generated (see fig. 1.2). Subsequently, the electron-hole pairs move through the solar cell, whereby the holes move in directions of the positive electrode through the p-type semiconductor and the electrons move through the n-type semiconductor to the negative electrode [4]. The p-n junction forms a depletion region, which is an insulating region where the mobile charge carriers have diffused away [5]. Since on n-doped side cations and on the p-

doped side anions remain due to the electron diffusion, an electric field is generated pointing from the n- to the p-doped semiconductor (see fig. 1.2). The electron-hole pairs are separated by the drift generated by this electric field and additionally by carrier diffusion from zones higher concentration to lower concentration following the gradient of the electrochemical potential in the solar cell. As a result, a current is produced, which can be used by a consumer.

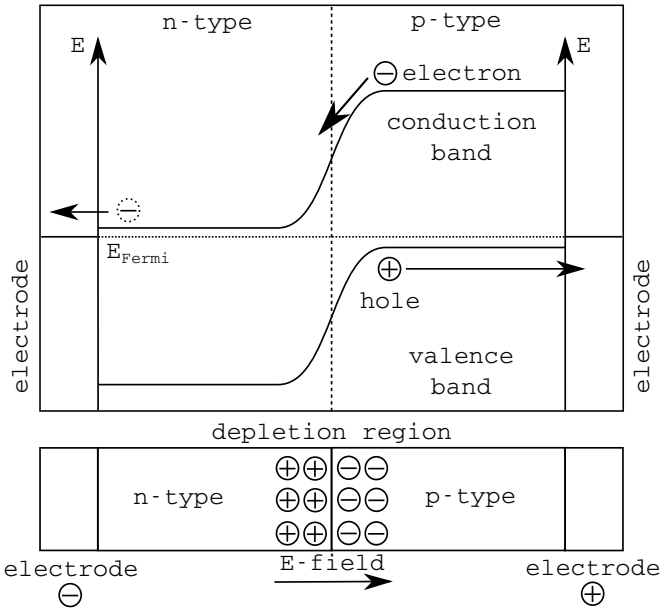

Figure 1.2: Schematic illustration of the p-n junction, depletion region and corresponding band diagram. After absorbing the solar radiation an electron-hole pair is generated. The hole moves to the positive electrode through the p-type semiconductor and the electron moves through the n-type semiconductor to the negative electrode [4, 5]. This results in an electric current, which can be utilized by consumers.

To characterize the potential efficiency of a solar cell, in 1961 W. Shockley and H. J. Queisser developed a scheme to estimate the solar cell efficiency. In general, the efficiency of a solar cell is defined as the portion of energy absorbed from light that can be converted into electricity. The Shockley–Queisser (SQ) limit gives the maximum theoretical efficiency η of a solar cell with a single p-n junction [6] (see fig. 1.3). This approximation is one of the most fundamental and most important approaches in solar cell research [7]. For example, a solar cell with a single p-n junction and a band gap of 1.34 eV shows a maximum solar conversion efficiency around 34 % under the constraints of solar radiation falling on an ideal solar cell with about 1000 W/m^2 [7]. Solar cells with multiple p-n junctions can even outperform this limit in theory, reaching a theoretical limit of 87 %, using concentrated sunlight with an infinite number of cells [8].

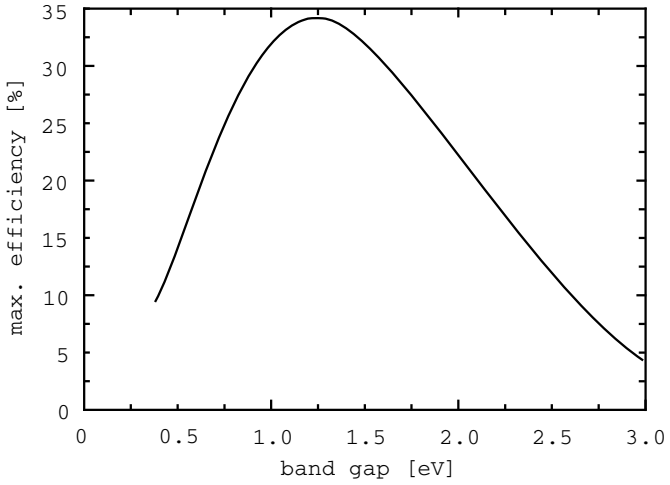

Figure 1.3: Simulated Shockley–Queisser limit for the efficiency of a solar cell, whereby the light source is approximated by a 6000 K blackbody spectrum, adapted from [6].

The relatively simple model after SQ only accounts for few possible loss mechanisms like the recombination of an electron-hole pair under radiation of a photon, which is the reverse process of the photon absorption. Furthermore only a small portion of the solar radiation spectrum can be used in a solar cell, which depends on the size of the band gap. Photons with energy lower than the band gap are not absorbed, while photons exhibiting a larger energy than the band gap are absorbed, whereby the additional energy is transformed into heat. However, the SQ model neglects loss mechanisms like optical losses, for example the quantum efficiency of a solar cell is smaller than one, meaning that not every suitable photon generates an electron-hole pair leading to an electric current. These optical losses contain for example reflection losses at the window layer or absorption of the photon at buffer or window layers [9]. In practice, there are various possibilities which are responsible for an efficiency deterioration of the solar cell. One of these limits is connected to the open-circuit voltage V_{OC}, which is the difference in electrical potential between two electrodes of a device under light radiation when disconnected from any circuit. The open-circuit voltage is hereby proportional to the efficiency η [6], which reflects its importance. Many factors like material fluctuations influence V_{OC}, for example secondary phases or changes of the material stoichiometry within the absorber material, which lead to additional recombination centers in the absorber material, effectively reducing V_{OC} [10]. This often occurs in disordered lattices or semiconductor alloys because of composition variations. All these imperfections lead to local variations of the band gap within the solar cell module, which deteriorate the performance of the solar cell [10], since the band gap $\mathrm{E_g}$ is proportional to the open-circuit voltage V_{OC} [6, 11]. The upper limit for the open circuit voltage of a solar cell is therefore the band gap.

Despite the various possibilities for an efficiency deterioration of a solar cell, the current conventional Si-based modules show suitable efficiencies of up to 20 % for commercial

products [12]. However, these solar cells show drawbacks like high costs of monocrystalline silicon due to the homogeneous crystalline framework with no grain boundaries and due to the utilized wafers thicknesses up to 240 micrometers (μm). To reduce the costs of the solar cell, silicon solar cells were further modified resulting in different silicon solar cell categories like polycrystalline and amorphous silicon solar cells. Polycrystalline silicon solar cells feature larger bulk-like particles, which show grain boundaries. An amorphous silicon solar cell is made of non-crystalline silicon, which features a higher band gap of 1.77 eV [13]. Hereby the electronic effects of nanostructuring are used, in which the band gap increases with decreasing nanostructure sizes, which can be utilized for band gap engineering. This size-dependency of the band gap is also known as the quantum confinement effect. The main aim behind amorphous silicon solar cells is to lower production costs while concurrently accepting lower efficiencies of about 10 % [14, 15].
A further famous material for multi-junction and thin film solar cells is gallium arsenide (GaAs), which is used in high-efficiency but high cost solar cells. In thin film solar cells, the solar cell is produced by depositing one or more thin layers (thin film) on a substrate, whereby the film thickness varies from a few nm (nanometers) to several μm. The thin film technology allows for flexible solar cells and lower costs, since the absorber material is only used in small amounts. The multi-junction solar cells feature multiple p-n junctions, which are often made of different semiconductor materials to efficiently absorb different wavelengths of light. GaAs-based devices hold the world record for the highest-efficiency single-junction solar cell at 29 % [16] with a band gap of 1.43 eV [17]. Due to its high efficiency, GaAs is commonly used for photovoltaic arrays for satellite applications.
Cadmium telluride (CdTe) is another prominent thin film photovoltaic material with a band gap of 1.5 eV [18], which has the smallest carbon footprint and lowest water usage during production with regard to later generated electricity and shortest energy payback time of all solar cell technologies [19–21]. Unfortunately, the toxicity of cadmium is an environmental concern which can be alleviated by the recycling of the solar cell modules [22]. Furthermore, the price of Te is a limiting factor for these photovoltaics [23].
One of the most prominent material classes for the thin film solar cells are the chalcopyrites $CuIn_xGa_{1-x}Se_2$ (CIGS) with a composition dependent band gap of 1.0 eV to 1.7 eV [24], already featuring a maximum lab efficiency of 20 % [25] and minimal lower efficiencies in commercial products. However, there are doubts about the availability and costs of indium and gallium in the future, which reduce the potential for an extensive application.
Overall, these solar cell absorber materials already achieve good efficiencies, but all show different disadvantages like high costs, utilization of rare or environmentally harmful materials, fragility of the monocrystalline layers, or low lifetimes. However, a promising material for thin film solar cells similar to chalcopyrites are kesterites

($Cu_2ZnSnS_xSe_{4-x}$), which feature similar electronic properties, lack the dependency on indium or gallium, and only contain non-toxic elements. Todays kesterite lab solar cells show an efficiency of 12.6 % [26], whereby they exhibit the same potential as CIGS solar cells with efficiencies over 20 %. In contrast to CIGS solar cells, the research on kesterite solar cells is still in the beginning, whereby the CIGS solar cell research started in the 1970s, showing similar low efficiencies at that time (see fig. 1.4). Due to this high potential and promising material properties for an application in thin film solar cells, kesterites are reviewed in this work by quantum chemical *first-principles* calculations to understand key factors for the low efficiencies and give insight on possible performance enhancing material modifications.

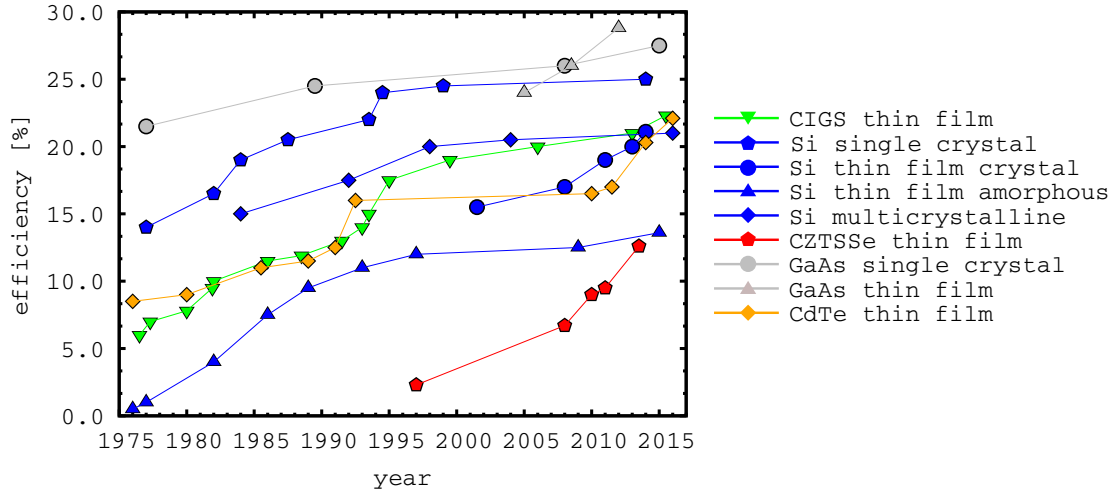

Figure 1.4: Development of research solar cell efficiencies from 1975 to 2016, adapted from the *Best Research Solar Cell Efficiencies* summarized by the National Renewable Energy Laboratory (Golden, Colorado) [27].

1.2 Kesterites as Solar Cell Absorber

Over the last years the material class of kesterites ($Cu_2ZnSnS_xSe_{4-x}$) has started to attract the interest of scientists for a utilization as an absorber layer in thin film solar cells due to its isolectronicity to the current thin film high performer chalcopyrites [28–30]. While featuring similar suitable electronic and optical properties as chalcopyrites, kesterites consist of earth abundant non-toxic elements which are available in a high concentration in the earth's crust, assuring availability in the future [31]. The photovoltaic effect in kesterites was first observed in 1988 [32], which lead in 1997 to the first kesterite solar cell with an efficiency of 2.3 % [33]. Consecutively researchers started to increase this efficiency in 2008 to 6.7 % [34, 35], in 2010 to 9.6 % [36] and in the following years to over 10 % [30, 37, 38]. The current kesterite thin film high performer features an efficiency of 12.6 % [26] in 2013, which is still far off from the theoretical limit of 31-32 % [39, 40].

The quaternary semiconductors Cu_2ZnSnS_4 (CZTS), $Cu_2ZnSnS_xSe_{4-x}$ (CZTSSe) and $Cu_2ZnSnSe_4$ (CZTSe) are I_2-II-IV-VI_4 compounds [41], which crystallize in a tetragonal crystal system with the space group $I\bar{4}$ for the kesterite structure and with the space group $I\bar{4}2m$ for the stannite structure [28, 42], whereby the kesterite structure is slightly more stable [43]. In the kesterite structure Cu, Zn, Sn and S/Se occupy the 2a and 2c, 2d, 2b and 8g Wyckoff positions respectively (see fig. 1.5), which is identical in CZTS, CZTSSe and CZTSe [28, 42]. CZTS features lattice constants of $a = 5.427$ Å and $c = 10.871$ Å [44], which are slightly enlarged in CZTSe with $a = 5.689$ Å and $c = 11.347$ Å [45] due to larger Se atoms.

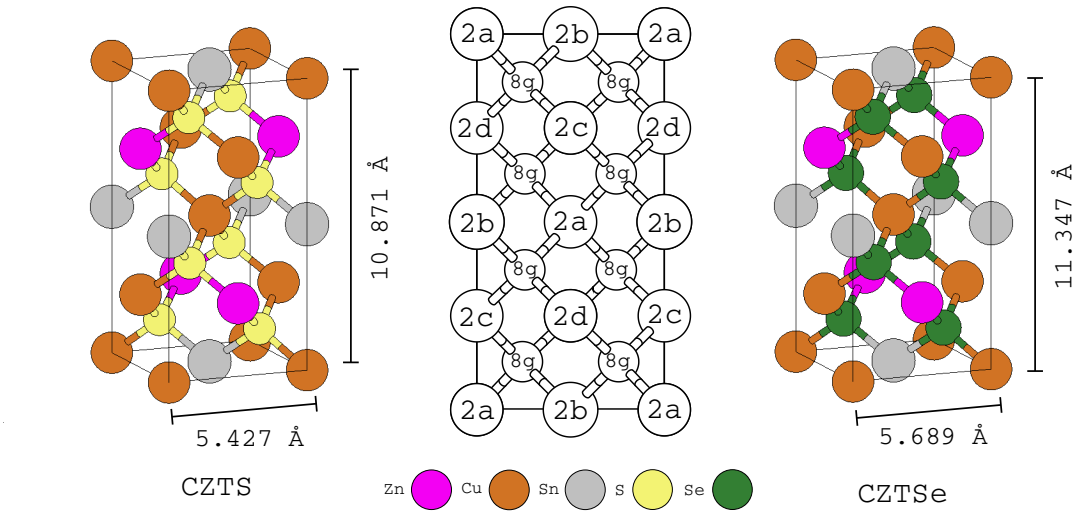

Figure 1.5: Bulk structures and lattice constants of CZTS [44] and CZTSe [45]. The ionic structure of both compounds is identical, whereas the lattice constants are slightly larger for CZTSe due to larger Se atoms. In the kesterite structure Cu, Zn, Sn and S/Se occupy the 2a and 2c, 2d, 2b and 8g Wyckoff positions respectively.

The lattice constants of CZTSSe alloys lie in between CZTS and CZTSe. Due to the similar electronic structure of Cu^+ and Zn^{2+}, both cations are indistinguishable by conventional X-ray diffraction, therefore neutron diffraction is applied for a structural analysis [28].
Kesterites were first prepared in 1967 from the vapor phase by chemical transport with iodine [46], whereby today there are various preparation methods like a solid state reaction of the pure elements in sealed and evacuated ampoules with resulting large single-phase crystals [47, 48] or the nanocrystal synthesis in different solution-based processes [49–63], whereby the nanocrystals feature sizes of up to 50 nm [53, 58, 62, 63]. Later, these nanocrystals are coated by different techniques on a substrate to form a polycrystalline thin film. The complexity of the structure often leads to defects [64, 65], featuring off-stoichiometry and varying material properties. Off-stoichiometric samples are also prepared on purpose to test composition boundaries [66], whereby in the high performing kesterites solar cells the off-stoichiometry is utilized in form of Cu-poor and Zn-rich samples [67, 68].
However, there are also stoichiometric defects like the most prominent 2c/2d disorders, in which Cu_{Zn} and Zn_{Cu} antisite are formed, which have been investigated experimentally [48, 69–74]. The complex structure of course features also the advantage of adjusting material properties by alloying different kesterite derived materials for example like Cu_2ZnSnS_4 and Cu_2FeSnS_4 [75] or Cu_2ZnSnS_4 and $Cu_2ZnSnSe_4$ [76–78].
Due to the similarity to chalcopyrites, the electronic properties are promising for the usage as a solar cell absorber like direct band gaps of 1.5 eV [32, 65, 79] and 1.0 eV [80] at the Γ-point for CZTS and CZTSe respectively, which can be adjusted in between by CZTSSe alloys [81]. Besides the ideal band gap, CZTS exhibit a high optical absorption of 10^4 cm^{-1} and p-type conductivity [79]. Overall, CZTS, CZTSe and CZTSSe are a promising material class for future thin film solar cells. Unfortunately, the efficiencies are still to low for a mainstream application in thin film solar cells, since the material suffers from different limiting factors. A deeper understanding of these limiting factors and additionally new routes for an efficiency enhancement can be given by quantum chemical simulation of the absorber material $Cu_2ZnSnS_xSe_{4-x}$. An advantage of these calculations is that they are faster and cheaper than experimental studies and therefore can help preselect experimental settings.

1.2.1 A Quantum Chemical Route to a Tailored Solar Cell Absorber

The theoretical and technological development in the last years lead to todays situation in which material properties can be predicted precisely by quantum chemical electron structure calculations [82], which can be used for an understanding of material properties as well as for predictions of a route to more efficient and cheaper solar cells. In recent years, many theoretical investigations have therefore been performed on kesterites. The theoretical studies especially focused on bulk properties like lattice parameters, electronic and optical properties of CZTS, CZTSSe and CZTSe, showing good agreement with experimental data while applying the widely used and low cost density functional theory (DFT) with various functionals [43, 83–91]. The quaternary semiconductor provides many possibilities for structural modifications like atom substitutions or alloying, which have been investigated theoretically [81, 90–108]. Several possible alloys have been theoretically investigated like the Cu_2ZnSnS_4 and Cu_2FeSnS_4 alloy [100], whereby the most prominent is the CZTSSe alloy [81, 93, 95, 98, 99, 105], which is used in the current high performing kesterite solar cell [26]. The experimental kesterite material often exhibits off-stoichiometry and defects like vacancies V_X and antisites X_Y, in which X and Y denote different atom types. Theoretical investigations by Chen et al. have shown that the Cu_{Zn} antisite is the dominant point defect in stoichiometric CZTS and CZTSe, whereby the off-stoichiometry often results from self compensating defect clusters, such as [V_{Cu}+Zn_{Cu}], [2 Cu_{Zn}+Sn_{Zn}] and [Zn_{Sn}+2 Zn_{Cu}] [109].
Unfortunately, despite these intense theoretical investigations, the kesterite solar cell modules are still at 13 % efficiency, whereby the reasons for these low efficiencies are still not fully understood until today. Concluding from the previous experimental and theoretical results, theory can help in two ways to increase the performance of kesterite thin film solar cells. The first step is to understand the limiting factors for the low efficiency from a theoretical point of view to support experimentalists during the synthesis and solar cell preparation. In a second step, further material modifications have to be theoretically investigated to estimate their impact on the performance of the CZTS solar cell for a possible enhancement of the efficiency beyond the prediction by the Shockley–Queisser limit.
First of all, kesterite solar cells suffer from a low open-circuit voltage, which contributes too low efficiencies [110]. Since the low-open circuit voltage is proportional to the band gap of the material, band gap fluctuations, namely varying band gaps within the absorber material due to varying material qualities, may be a reason for these low efficiencies. The low open-circuit voltages are often blamed on self-compensating defect clusters like the 2c/2d disorder antisites Cu_{Zn} and Zn_{Cu}, in which Cu_{2c} and Zn_{2d} are interchanged, which researchers started recently to investigate [111–114]. But these disorders are not the only source for a varying material quality. Especially the high performer material $Cu_2ZnSnS_xSe_{4-x}$ may give rise to an efficiency loss due to different structural patterns in the alloy, which may also cause band gap fluctuations. From a

theoretical point of view, the reasons for the band gap fluctuations have to be investigated and understood to support the experimentalists.
Furthermore, to increase the limiting efficiency beyond the prediction by the Shockley–Queisser limit, material modifications like nanostructuring are introduced, which provide opportunities like reduced material costs due to the utilization of less material and an increased efficiency [115]. Nanostructuring can be performed in different ways, which all feature the same increase of surface to volume ratio of the utilized material, whereby large bulk material is substituted by smaller nanoscale materials [116]. There are various examples for nanostructures like nanowires, nanomeshes, nanograined bulk materials or quantum dots [116, 117]. In nanoscale objects, quantum size effects are exploited, often enhancing the material properties [117, 118]. Another example for nanostructuring are nanostructured surfaces, which can reduce reflection losses if the size of the nanostructures is adjusted to the incoming wavelength of the light [115]. Additionally, patterned nanostructures can be designed for an increased light capture rate, in which the light is trapped in the absorber [115, 119, 120]. Other general features of nanoscale objects are the size-dependency of band gaps, known as the quantum confinement effect, and modifications of the relaxation dynamics of photoexcited charge carriers [4, 115]. Nanomaterials can also be utilized as part of multi-junction solar cells inheriting different band gaps, which increase the energy harvest from the solar radiation [121, 122]. In CZTS solar cells, nanostructuring can be introduced by increasing the surface to volume ratio by using larger thin films with a smaller bulk volume. But the surface to volume ratio can be further increased by utilizing a CZTS thin film composed of CZTS nanocrystals, which contain a small bulk-like core part and a relaxed surface. Unfortunately up until now the theoretical knowledge about CZTS nanostructures is still limited despite the possibility of nanoscale effects on the material properties [123–125]. The nanostructuring features therefore great possibilities for strongly enhanced CZTS thin film solar cells.
The last two paragraphs sum up the scope of this thesis, which is split in two ways, namely the theoretical understanding of the limiting factors for the efficiency and furthermore provide theoretical insight on material enhancing techniques like nanostructuring. The focus is set on the link between the lattice and electronic structure by quantum chemical electronic structure calculations, utilizing a periodic and finite DFT ansatz. In the beginning of chap. 3, the properties of the pure bulk materials CZTS and CZTSe are examined for structural and electronic reference properties for subsequent investigations of modified CZTS and CZTSe materials. The focus is then set on band gap engineering by CZTSSe alloys, in which the influence of different structural patterns on the band gap is investigated, since band gap fluctuations lead to deteriorated efficiencies [10]. Another possible factor for the low efficiency are experimentally observed 2c/2d disorders, whereby the focus is set on the structural influences of disorders as well as a subsequent analysis of the electronic structure as a function of the disorders. Combining the theoretical results of the CZTSSe alloys and 2c/2d disorder

with experimental studies, a path for a more efficient kesterite solar cells may be provided by a prediction of disruptive factors for the efficiency. A further enhancement is achievable with kesterite nanostructuring, which is performed in a first step in chap. 4, in which CZTS surfaces are investigated. Hereby the focus is first set on the stabilities in means of surface energies of CZTS surfaces, which are modeled in the periodic slab approach (see sec. 4.1.4), whereby the challenge of calculating surface energies for off-stoichiometric symmetric slabs is addressed via an extrapolation scheme. On top of the structural results, the focus then is shifted to the influence of nanostructuring on the electronic structure of surfaces. Afterwards a further step towards CZTS nanostructuring is performed in chap. 5, in which the size of the nanostructures is further reduced to CZTS nanocrystals, which are theoretically modeled in form of finite clusters with diameters of $\sim$ 1nm. The aim is to develop a realistic finite model to simulate the CZTS nanocrystals with sizes up to 50 nm from experiment [53, 58, 62, 63], whereby the model should exhibit the same structural features like a realistic nanocrystal, namely a fixed bulk-like core and a relaxed surface part surrounding this core after the full structure relaxation of the finite cluster. Subsequently a first insight on the electronic structure is given for further investigations of the electronic properties. With the help of these theoretical insights on the reasons for the low efficiency as well as influence of theoretically performance enhancing structural modifications, experimentalists can be supported in the construction of more efficient kesterite solar cells.

Chapter 2

Theoretical Background and Methods

Since the first steps of quantum mechanics in the 1920s, scientists from different fields have been fascinated by the at the time ground breaking ideas, leading to various new theoretical approaches over the last nearly 100 years. Especially the technological developments in the last 30 years lead to today's situation, in which a variety of complex systems can be described quantum mechanically. But not only technology developed rapidly, also theory evolved to adjust the theoretical models for an effective calculation of material properties on computers. Starting from the point where even atoms and small molecules were a great challenge to calculate, with todays technology even extended quantum systems like the quaternary semiconductor Cu_2ZnSnS_4 can be described within a moderate amount of computer time. On the basis of this immense progress, the underlying fundamental methods and ideas applied in this thesis are briefly presented in the following sections.

2.1 Hartree-Fock Theory

The first steps into the direction of describing systems by quantum mechanics was postulated in 1926 by E. Schrödinger, who introduced the existence of a wave function Ψ, which describes the quantum state of a system [126]. The time evolution of this quantum state is given by

$$i\frac{\partial}{\partial t}\Psi = \hat{H}\Psi, \tag{2.1}$$

where the system is characterized by the Hamiltonian $\hat{H}$ and the state by the wave function Ψ. This equation is also known as the time-dependent *Schrödinger equation* (SE), which is even for small systems difficult to solve. For larger systems however, this complexity can be reduced by different approximations, which depend on the investigated properties. A first complexity reduction is introduced by describing the investigated systems as stationary time-independent systems, in which the time-independent SE is sufficient for a good description of the investigated properties. Many material properties like band gaps are not time-dependent, therefore the assumption is a reasonable ansatz. A further approximation can be introduced by the neglect of relativistic effects (see ref. [127] and references therein). This method is often a reasonable approach for

atoms with only few electrons, whereby the neglect of relativistic effects in heavy atoms can lead to errors. An ansatz in between the full neglection and the fully relativistic description are relativistic pseudo potentials, which contain relativistic effects within their potential for the core electrons of the described atoms. The first general form of pseudo potentials hereby was introduced in 1935 by H. Hellmann [128]. The resulting non-relativistic time-independent Hamiltonian in atomic units, which are consistently utilized in the following sections, is given by

$$\hat{H} = -\sum_{i=1}^{N} \frac{1}{2}\Delta_i - \sum_{A=1}^{M} \frac{1}{2M_A}\Delta_A - \sum_{i=1}^{N}\sum_{A=1}^{M} \frac{Z_A}{r_{iA}} + \sum_{i=1}^{N}\sum_{j>i}^{N} \frac{1}{r_{ij}} + \sum_{A=1}^{M}\sum_{B>A}^{M} \frac{Z_A Z_B}{R_{AB}} \ , \quad (2.2)$$

with N as the number of electrons, M the number of nuclei and Z_A is the atomic number of nucleus A. M_A denotes the mass ratio of nucleus A to the mass of an electron, r_{ij} is the distance between electron i and j and R_{AB} is the distance between nucleus A and B. The distance between electron i and nucleus A is denoted by r_{iA} [129]. The first two terms describe the kinetic energy of the electrons and nuclei within the quantum system respectively. The following three terms describe the electrostatic potential between the electrons and nuclei, between electrons and between nuclei respectively. A further approximation was shortly published after the initial work of Schrödinger in 1927 by Born and Oppenheimer, who introduced the ansatz of decoupled electronic and nuclear degrees of freedom, referred to as the *Born-Oppenheimer approximation* (BO) [130]. The movement of electrons and nuclei can be treated separately within the BO-approximation, since the electrons move distinctly faster than the nuclei and therefore the movement of the nuclei is negligible for the electronic part. The resulting electronic Hamiltonian is given by

$$\hat{H}^{el} = -\frac{1}{2}\sum_{i=1}^{N} \Delta_i - \sum_{i=1}^{N}\sum_{A=1}^{M} \frac{Z_A}{r_{iA}} + \frac{1}{2}\sum_{i,j=1}^{N} \frac{1}{r_{ij}}. \quad (2.3)$$

Since the systems investigated in this thesis are always described by the electronic Hamiltonian, the notation "el" will be dropped in the further discussion. The electron-electron interaction in the last term is a crucial point when describing the quantum state of a system, whereby a direct solution is not possible even with the introduced approximations.

There are several approaches for an approximation of the initial wave function. One first approach for the wave function is the *Hartree-product*, which describes the N-particle wave function as a product of N one-particle wave functions, which is an exact solution for non-interacting electrons. However, the Hartree-product offends the Pauli-principle. A further ansatz is applied in the Hartree-Fock (HF) theory [129], in which the electronic wave function Ψ is constructed by a single Slater determinant (SD) of one-particle wave functions [131, 132]. In contrast to the Hartree-product, the SD is an

anti-symmetric product ansatz for the wave function, which obeys the Pauli Principle and is given by

$$\Psi(\mathbf{x}_1, \mathbf{x}_2, \ldots, \mathbf{x}_N) = \frac{1}{\sqrt{N!}} \begin{vmatrix} \chi_1(\mathbf{x}_1) & \chi_2(\mathbf{x}_1) & \ldots & \chi_N(\mathbf{x}_1) \\ \chi_1(\mathbf{x}_2) & \chi_2(\mathbf{x}_2) & \ldots & \chi_N(\mathbf{x}_2) \\ \vdots & \vdots & \ddots & \vdots \\ \chi_1(\mathbf{x}_N) & \chi_2(\mathbf{x}_N) & \ldots & \chi_N(\mathbf{x}_N) \end{vmatrix} = |\chi_1 \chi_2 \ldots \chi_N\rangle \quad (2.4)$$

with $\chi_i(\mathbf{x})$ as the one-particle wave function describing spin and spatial part of an electron and N as the number of spin orbitals and electrons. The spin orbital $\chi_i(\mathbf{x})$ hereby is a combined function of a spin function $\delta(s)$ with $\delta = \alpha, \beta$ and a spatial orbital $\psi(\mathbf{r})$.
To find the SD best describing the quantum system, the variational principle is applied. In the variational principle an initial guess for the SD is utilized, whereby the orbital coefficients of the spin orbitals $\chi_i(\mathbf{x})$ are varied until the energy reaches a minimum. The resulting SD is the wave function best describing the system [129]:

$$E_0 \leq \min_{\Psi} \langle \Psi | \hat{H} | \Psi \rangle \,. \quad (2.5)$$

The ground state energy is given by E_0 and Ψ is described by a SD. Following the Hartree-Fock equations, the N one-particle problem can be derived as

$$\hat{f}(\mathbf{x}_i)\chi(\mathbf{x}_i) = \epsilon_i \chi(\mathbf{x}_i), \quad (2.6)$$

where $\hat{f}(\mathbf{x}_i)$ is the Fock operator and ϵ_i are the eigenvalues of the one-particle wave function, also referred to as *orbital energies*. The Fock operator is defined as

$$\hat{f}(\mathbf{x}_i) = -\frac{1}{2}\Delta_i - \sum_{A=1}^{M} \frac{Z_A}{r_{iA}} + v^{HF}(\mathbf{x}_i). \quad (2.7)$$

The electrons in their spin orbital $\chi(\mathbf{x}_i)$ hereby only experience an average potential denoted by the effective one-electron operator $v^{\mathrm{HF}}(\mathbf{x}_i)$. Since the electrons only interact with all other electrons in the system by an effective potential, this is also called a *mean field approach*. The potential is generated by all other electrons in their spin orbitals $\chi_b(\mathbf{x})$ and is given by

$$v^{\mathrm{HF}}(\mathbf{x}_i) = \sum_b \hat{J}_b(\mathbf{x}_i) - \hat{K}_b(\mathbf{x}_i). \quad (2.8)$$

This potential is also referred to as *HF potential* [133], which is dependent on the spin orbitals of all other electrons.

Acting on a spin orbital $\chi_a(\mathbf{x}_1)$, the Coulomb operator $\hat{J}_b$ and exchange operator $\hat{K}_b$ can be defined as

$$\hat{J}_b(\mathbf{x}_1)\chi_a(\mathbf{x}_1) = \int \mathrm{d}\mathbf{x}_2 \chi_b^*(\mathbf{x}_2)\frac{1}{r_{12}}\chi_b(\mathbf{x}_2)\chi_a(\mathbf{x}_1), \tag{2.9}$$

and

$$\hat{K}_b(\mathbf{x}_1)\chi_a(\mathbf{x}_1) = \int \mathrm{d}\mathbf{x}_2 \chi_b^*(\mathbf{x}_2)\frac{1}{r_{12}}\chi_a(\mathbf{x}_2)\chi_b(\mathbf{x}_1)\ . \tag{2.10}$$

The Coulomb operator expresses the classical Coulomb repulsion between two electrons. For the exchange operator there is no classical equivalent. From eq. 2.10 it is clear that for anti-parallel spin of the two electrons, the exchange operator vanishes. The self interaction, defined as the interaction of an electron with itself, is dealt within HF explicitly, since the Coulomb and exchange integrals cancel each other out for identical spin orbitals.

The HF equations are iteratively solved within the self consistent field (SCF) approach [133]. The main idea behind the SCF method is to solve the HF eigenvalue equation (eq. 2.6) for an initial spin orbital and potential $v^{\mathrm{HF}}(\mathbf{x}_i)$ guess, and then subsequently calculate a new potential $v^{\mathrm{HF}}(\mathbf{x}_i)$ while incorporating the solution of the previous calculation. The self-consistency is achieved, when certain convergence criteria are reached after several iterations of this procedure. As a result of this procedure, a set of orthonormal spin orbitals χ_i with corresponding orbital energies are obtained after the solution of the HF equation (eq. 2.6). The resulting SD is the HF ground state wave function, which is the best variational single determinant solution for the ground state.

An approach for an effective solution of the HF equations was introduced by Roothan [134] and Hall [135] independently in 1951. Both proposed an ansatz for the spatial part of the HF orbitals $\psi_i(\mathbf{r})$ as a linear combination of atomic orbitals (MO-LCAO):

$$\psi_i = \sum_{\mu=1}^{K} C_{\mu i}\phi_\mu, \quad \text{with} \quad i = 1, 2, \ldots, K. \tag{2.11}$$

With K as the number of atomic orbitals, the expansion coefficients $C_{\mu i}$ and the atomic orbitals ϕ_μ as variants of solutions to hydrogen-like atoms. The application of these basis functions yields a matrix eigenvalue equation for the expansion coefficients

$$\mathbf{FC} = \epsilon\mathbf{SC}, \tag{2.12}$$

with the Fock matrix $\mathbf{F}$ and overlap matrix $\mathbf{S}$. $\mathbf{C}$ is a matrix of dimensionality $K * K$, which contains the expansion coefficients. This equation is also known as the *Roothan-Hall equation*. The diagonal matrix ϵ contains the corresponding orbital energies ϵ_i.

The Fock matrix **F** is hereby defined by

$$F_{\mu\nu} = \int \phi_\mu^*(\mathbf{r}_1)\hat{f}(\mathbf{r}_1)\phi_\nu(\mathbf{r}_1)\mathrm{d}\mathbf{r}_1, \tag{2.13}$$

and the overlap matrix **S** by

$$S_{\mu\nu} = \int \phi_\mu^*(\mathbf{r}_1)\phi_\nu(\mathbf{r}_1)\mathrm{d}\mathbf{r}_1. \tag{2.14}$$

The combination of Hartree-Fock and Roothan-Hall theory leads to one of the first possibilities for quantum mechanically calculated systems in an *ab initio* manner.

2.2 Density Functional Theory

As Hartree-Fock, Density functional theory (DFT) is a quantum chemical method, which is widely used for investigating the electronic structure of a many-body system. The popularity is based on the relatively good accuracy compared to experiment while concurrently featuring low computational costs. On the contrary to the wave function-based HF, the key quantity in DFT is the electron density ρ. In 1927 and 1928, a first idea of DFT was introduced by Thomas and Fermi [136, 137]. The breakthrough for DFT however was established nearly 40 years later by Hohenberg and Kohn, who stated two famous theorems, which build the basis for todays DFT [138]. The first theorem states that the exact ground state energy E_0 of a system can be solely described by the electron density $\rho(\mathbf{r})$. In the second theorem, Hohenberg and Kohn show that for every electron density function $\rho(\mathbf{r})$, which is normalized to the number N of electrons, the variational principle is fulfilled as

$$E_0 \leq E\left[\rho(\mathbf{r})\right] \ . \tag{2.15}$$

The total electron density of a system with N electrons is given by

$$\rho(\mathbf{r}) = N \int \ldots \int |\Psi(\mathbf{x}_1, \mathbf{x}_2, \mathbf{x}_3, \ldots, \mathbf{x}_N)|^2 \mathrm{d}\mathbf{s}_1 \mathrm{d}\mathbf{x}_2 \mathrm{d}\mathbf{x}_3 \ldots \mathrm{d}\mathbf{x}_N \ , \tag{2.16}$$

where $\mathbf{x}$ is the 4-dimensional vector of the position $\mathbf{r}$ and the spin s of an electron.
The integral and therefore the density represent the probability of finding one electron within a volume element $\mathrm{d}\mathbf{r}_1$ with an arbitrary spin.
Hereby the challenge to determine the kinetic energy T[ρ] as a functional of the electron density still remains like in the Thomas–Fermi model. Nearly one year later in 1965 a solution to this problem was proposed by Kohn and Sham (KS) [139] by applying an orbital-based approach. Kohn and Sham conducted using a reference system of N non-interacting electrons, which experience an external potential $V_\mathrm{S}(\mathbf{r}_i)$, in that way the electron density of the non-interacting system $\rho_\mathrm{S}(\mathbf{r})$ is equal to the electron density $\rho(\mathbf{r})$ of the interacting system.

The Hamiltonian for the system of non-interacting electrons is defined as

$$\hat{H}_{\mathrm{S}} = \sum_{i=1}^{N} -\frac{1}{2}\Delta_i + V_{\mathrm{S}}(\mathbf{r}_i) = \sum_{i=1}^{N} \hat{h}_i^{\mathrm{KS}} \ . \tag{2.17}$$

This Hamiltonian can be solved easily, because it consists of N non-interacting one-particle Hamiltonian $\hat{h}_i^{\mathrm{KS}}$. Their solutions are the non-interacting Kohn-Sham orbitals Φ_i^{KS}, where the KS eigenvalues (orbital energies) ϵ_i^{KS} are obtained by

$$\hat{h}_i^{\mathrm{KS}} |\Phi_i^{\mathrm{KS}}\rangle = \epsilon_i^{\mathrm{KS}} |\Phi_i^{\mathrm{KS}}\rangle \ . \tag{2.18}$$

Following this ansatz the first theorem of Hohenberg-Kohn can be fulfilled. The total energy as a function of the electron density is further defined by

$$E[\rho] = T_{\mathrm{S}}[\rho] + J[\rho] + E_{\mathrm{XC}}[\rho] + \int \rho(\mathbf{r}) V_{\mathrm{ext}}(\mathbf{r}) \mathrm{d}\mathbf{r} \ , \tag{2.19}$$

with $T_{\mathrm{S}}[\rho]$ as the kinetic energy of the non-interacting system, $V_{\mathrm{ext}}(\mathbf{r})$ is an external potential and $J[\rho]$ as the Hartree-term, which describes the classical Coulomb interaction of the electrons

$$J[\rho] = \frac{1}{2} \int\int \frac{\rho(\mathbf{r_1})\rho(\mathbf{r_2})}{r_{12}} \mathrm{d}\mathbf{r_1} \mathrm{d}\mathbf{r_2} \ . \tag{2.20}$$

The last term $E_{\mathrm{XC}}[\rho]$ is the *exchange-correlation energy*, which is obtained by

$$E_{\mathrm{XC}}[\rho] = (T[\rho] - T_{\mathrm{S}}[\rho]) + (V_{\mathrm{ee}}[\rho] - J[\rho]) \ . \tag{2.21}$$

where $T[\rho]$ is the kinetic energy of the real system and $T_{\mathrm{S}}[\rho]$ of the non-interacting system. At last, $V_{\mathrm{ee}}[\rho]$ defines the interaction energy between electrons of the full quantum chemical system. Applying the variational principle as in the HF approximation before under the constraints of orthonormal KS orbitals yields an expression for the external potential $V_{\mathrm{S}}(\mathbf{r}_i)$ introduced in eq. 2.17 [140, 141]:

$$V_{\mathrm{S}}(\mathbf{r}_i) = \int \frac{\rho(\mathbf{r}_j)}{\mathbf{r}_{ij}} \mathrm{d}\mathbf{r}_j + \frac{\partial E_{\mathrm{XC}}[\rho(\mathbf{r}_i)]}{\partial \rho(\mathbf{r}_i)} - \sum_{A}^{\mathrm{M}} \frac{Z_{\mathrm{A}}}{\mathbf{r}_{\mathrm{iA}}} \ . \tag{2.22}$$

The second term of the equation, the partial derivative of the exchange-correlation energy E_{XC} is often denoted as the exchange-correlation potential V_{XC} [141].
The exact exchange-correlation functional from eq. 2.21 yields the exact ground state energy $E_0[\rho]$, however since $E_{\mathrm{XC}}[\rho]$ is in general unknown, several approximations have been proposed since the original publication by Kohn and Sham in 1965. The quality of DFT calculations strongly depends on the applied exchange-correlation functional E_{XC}. One of the first and simplest approximation for the exchange-correlation functional is the local density approximation (LDA) [132, 142–144].

LDA assumes that the exchange-correlation functional of the inhomogeneous electron density can be locally described by the exchange-correlation functional of the homogeneous electron gas

$$E_{\mathrm{XC}}^{\mathrm{LDA}}[\rho] = \int \rho(\mathbf{r}) \epsilon_{\mathrm{XC}}^{\mathrm{LDA}}[\rho] \mathrm{d}\mathbf{r} \ , \tag{2.23}$$

where $\epsilon_{\mathrm{XC}}^{\mathrm{LDA}}$ is the exchange-correlation energy of the homogeneous electron gas. The exchange-correlation energy can be divided into a sum of the exchange and correlation parts

$$E_{\mathrm{XC}} = E_{\mathrm{X}} + E_{\mathrm{C}}. \tag{2.24}$$

The exchange part of the exchange-correlation energy can be solved analytically for the homogeneous electron gas and the correlation part is only solvable for high- and low-density limits and is often calculated via accurate quantum Monte Carlo methods [140, 145]. Two famous correlation parts were developed by Vosko, Wilk and Nusair, which were fitted to exact numerical data [143]. Unfortunately, the mapping of the exchange-correlation functional of the homogeneous electron gas to the inhomogeneous electron gas often leads to errors. An improvement to LDA is done in the generalized gradient approximation (GGA), which takes additionally to the electron density $\rho(\mathbf{r})$ at a point $\mathbf{r}$ the gradient of the density $\nabla\rho(\mathbf{r})$ at a point $\mathbf{r}$ into account. The exchange and correlation energies can be written as

$$E_{\mathrm{XC}}^{\mathrm{GGA}}[\rho] = \int \rho(\mathbf{r}) \epsilon_{\mathrm{XC}}[\rho, \nabla\rho] \mathrm{d}\mathbf{r} \ . \tag{2.25}$$

Incorporated as a separate function, the gradient in ϵ_{XC} is either added or multiplied to $\epsilon_{\mathrm{C}}^{\mathrm{LDA}}$ and $\epsilon_{\mathrm{X}}^{\mathrm{LDA}}$ in each case. Today there exist many different GGA functionals e.g. the Perdew-Burke-Ernzerhof (PBE) [146] or the Perdew-Wang (PW91) [147] functional. PW91 is the first reasonable GGA functional, which can be reliably used for a wide range of systems [147, 148]. A few years later Perdew et al. developed the PBE functional, which is based on PW91, but modified in several details (for further information see ref. [146] and [149]). A disadvantage is that with increasing gradient dependence the atomization and total energies will improve, however the bond lengths worsen compared to experiment. Th PBE functional was later revised for solid state systems, known as the PBEsol functional [150].
Due to the mentioned shortcomings of LDA- and GGA-functionals new approaches were developed. One approach are meta-GGA functionals, which include additionally higher order derivatives of $\nabla\rho$. Another path was followed in the hybrid-functionals, which include non-local Hartree-Fock exchange determined with Kohn-Sham orbitals into the GGA functional where often contrary trends by DFT and Hartree-Fock theory lead to excellent agreements with experimental reference data.

The exchange energy is defined by

$$E_{\mathrm{X}}^{\mathrm{hybrid}} = \alpha E_{\mathrm{X}}^{\mathrm{exact}} + (1-\alpha) E_{\mathrm{X}}^{\mathrm{DFT}} \ , \tag{2.26}$$

where α is a parameter, which differs for the different type of hybrid-functionals. One of the most commonly employed functionals is B3LYP with the form

$$E_{\mathrm{XC}}^{\mathrm{B3LYP}} = E_{\mathrm{XC}}^{\mathrm{LDA}} + a_0(E_{\mathrm{X}}^{\mathrm{exact}} - E_{\mathrm{X}}^{\mathrm{LDA}}) + a_{\mathrm{x}}(E_{\mathrm{X}}^{\mathrm{B88}} - E_{\mathrm{X}}^{\mathrm{LDA}}) + a_{\mathrm{c}}(E_{\mathrm{C}}^{\mathrm{LYP}} - E_{\mathrm{C}}^{\mathrm{LDA}}) \ , \tag{2.27}$$

with the parameters $\alpha_0 = 0.20$, $\alpha_x = 0.72$ and $\alpha_c = 0.81$, which are determined by a fit to properties of a standard set of molecules. The name is derived from the developers Becke [151], Lee, Yang and Parr [152], where the number three corresponds to the three parameters used. The GGA functional B88 is also derived by Becke [153].
A further development in hybrid-functionals is shown by the introduction of efficient screening techniques to take advantage of the fast spatial decay of the short range HF exchange, as employed in the Heyd–Scuseria–Ernzerhof (HSE) screened Coulomb hybrid density functional. In the hybrid-functionals HSE03 [154–156] and HSE06 [157] the slowly decaying long-range part of the Fock exchange interaction is replaced by the corresponding part of the PBE functional. The exchange-correlation energy is given by

$$E_{\mathrm{XC}}^{\mathrm{HSE}} = \frac{1}{4} E_{\mathrm{X}}^{\mathrm{exact,SR}}(\mu) + \frac{3}{4} E_{\mathrm{X}}^{\mathrm{PBE,SR}}(\mu) + E_{\mathrm{X}}^{\mathrm{PBE,LR}} + E_{\mathrm{C}}^{\mathrm{PBE}} \ , \tag{2.28}$$

whereby SR and LR represent the separation of the electron-electron interaction into a short- and long-ranged part respectively, only applied in the exchange interactions. μ denotes the HF screening parameter, which is usually set to 0.3 $\mathrm{Å}^{-1}$ for HSE03 and 0.2 $\mathrm{Å}^{-1}$ for HSE06.

2.3 Time-Dependent Density Functional Theory

Since DFT only describes the ground states properties of a system, time-dependent density functional theory (TDDFT) was developed to study properties of many-body systems in the presence of time-dependent potentials like electric or magnetic fields. Hereby features like excitation energies or photo absorption spectra can be calculated. As an extension to DFT with analogous foundations, the main obstacle in TDDFT is to show that the time-dependent wave function is equal to the time-dependent density. The derivation of an effective potential of a non-interacting system returning the same density as an interacting system is of importance, whose foundation was formulated in the Runge-Gross Theorems.

2.3.1 Runge-Gross Theorems

In 1984, E. Runge and E. K. U. Gross derived the Runge-Gross Theorems for arbitrary time-dependent systems as an analog to the time-independent Hohenberg-Kohn theorems [158]. The time-dependent electron density $\rho(\mathbf{r},t)$ can be constructed out of the time-dependent wave function $\Psi(\mathbf{x},t)$ from eq. 2.1 by

$$\rho(\mathbf{r},t) = N \int \dots \int |\Psi(\mathbf{x}_1,\mathbf{x}_2,\mathbf{x}_3,\dots,\mathbf{x}_N,t)|^2 \mathrm{d}\mathbf{s}_1 \mathrm{d}\mathbf{x}_2 \mathrm{d}\mathbf{x}_3 \dots \mathrm{d}\mathbf{x}_N \ , \tag{2.29}$$

with the number of electrons N and $\mathbf{x}_i$ is the 4-dimensional vector of the position $\mathbf{r}$ and the spin s of electron i. Runge and Gross showed that for a many-body system evolving from an initial wave function ($\Psi(t_0) = \Psi_0$), a one-to-one mapping between the time-dependent potential of the system and the density of the system exists. Applying two external spatially independent potentials to a wave function $\Psi(\mathbf{x},t)$, which only differ by an additive time-dependent function $c(t)$, yields two wave functions only differing by a phase factor $e^{-ic(t)}$. Runge and Gross have shown in their publication that this mapping is reversible, in other words the density is a functional of the external potential and of the initial wave function. The detailed proof of this theorem can be found in ref. [158]. As in the Hohenberg-Kohn formalism, for an effective utilization of TDDFT in computations the time-dependent density framework has to be applied to the Kohn-Sham theorems. For reasons of simplicity, in the following derivation only the spatial part of the quantum system is considered. The challenge is to determine a non-interacting time-dependent potential $V_\mathrm{S}(\mathbf{r},t)$, which transforms the time-dependent non-interacting density $\rho_\mathrm{S}(\mathbf{r},t)$ to the time-dependent interacting density $\rho(\mathbf{r},t)$. The time-dependent Hamiltonian of the non-interacting system is given by

$$\hat{H}_\mathrm{S}(t) = \sum_{i=1}^{N} -\frac{1}{2}\Delta_i + V_\mathrm{S}(\mathbf{r}_i,t), \tag{2.30}$$

with the now time-dependent potential $V_\mathrm{S}(\mathbf{r}_i,t)$. Applying the Hamiltonian to the time-dependent wave function $\Psi(\mathbf{r},t)$ yields

$$\hat{H}_\mathrm{S}(t)\Psi(\mathbf{r},t) = i\frac{\partial}{\partial t}\Psi(\mathbf{r},t) \quad \text{with} \quad \Psi(\mathbf{r},0) = \Psi(\mathbf{r}) \ . \tag{2.31}$$

As before in HF (see sec. 2.1) and DFT (see sec. 2.2), the wave function $\Psi(\mathbf{r},t)$ is constructed by a set of N one-particle functions $\Phi_i(\mathbf{r},t)$, which obey the equation

$$\left(-\frac{1}{2}\Delta + V_\mathrm{S}(\mathbf{r},t)\right)\Phi_i(\mathbf{r},t) = i\frac{\partial}{\partial t}\Phi_i(\mathbf{r},t) \quad \text{with } \Phi_i(\mathbf{r},0) = \Phi_i(\mathbf{r}) \tag{2.32}$$

The sum over all N one-particle functions results in the time-dependent non-interacting density, analog to eq. 2.29:

$$\rho_{\mathrm{S}}(\mathbf{r},t) = \sum_{i=1}^{N/2} |\Psi_i(\mathbf{r},t)|^2 \ . \tag{2.33}$$

The non-interacting density is hereby equal to the interacting density at all time

$$\rho_{\mathrm{S}}(\mathbf{r},t) = \rho(\mathbf{r},t). \tag{2.34}$$

The crucial part of solving the time-dependent Kohn-Sham equations is to find a good approximation for the external potential $V_{\mathrm{S}}(\mathbf{r},t)$. Analog to KS DFT, the time-dependent KS potential is given by

$$V_{\mathrm{S}}(\mathbf{r},t) = V_{\mathrm{ext}}(\mathbf{r},t) + \int \mathrm{d}^3\mathbf{r}\ \rho(\mathbf{r},t) V_J(\mathbf{r}) + V_{\mathrm{XC}}(\mathbf{r},t) \tag{2.35}$$

with the external potential $V_{\mathrm{ext}}(\mathbf{r},t)$, the Coulomb interaction $V_J(\mathbf{r})$ and the well known exchange-correlation potential $V_{\mathrm{XC}}(\mathbf{r},t)$. The former proof of the Hohenberg-Kohn theorem is based on the Rayleigh-Ritz principle, which is not applicable to the time-dependent system. Therefore, Runge and Gross proofed the time-dependency by an action integral of the form

$$A[\Psi] = \int \mathrm{d}t\, \langle \Psi(t)|\hat{H} - i\frac{\partial}{\partial t}|\Psi(t)\rangle \,, \tag{2.36}$$

which was treated as a functional of the wave function [158]. It only provides a stationary point for variations of the time-dependent Schrödinger equation. By uniquely mapping the wave function and resulting density, Runge and Gross expressed the action integral as an integral of the density

$$A[\rho] = A[\Psi[\rho]] \ . \tag{2.37}$$

For the detailed derivation see ref. [158]. Unfortunately, this proof results in paradox conclusions with respect to functional derivatives of the density with regard to an external potential [159]. Since the initial publication, many scientists critically discussed the foundations of the TDDFT approach (see [160] and references therein). Nevertheless, TDDFT with various functionals is used for calculations of excitation energies.

2.4 Solid State Systems and Periodic Boundary Conditions

The calculation of finite systems like atoms and molecules is mostly straight forward with respect to the computational model applied. Solid state systems in contrast, regarded as infinitely extended systems, however show computational challenges regarding the arising computational effort due to the system size. Providentially, ideal solid state systems feature a translational symmetry, which allows a structural description by a very small part of the whole system, namely the *unit cell*. The lattice of the unit cell can be characterized by the three basis vectors $\mathbf{a}_1$, $\mathbf{a}_2$, $\mathbf{a}_3$ in real space, whereby a given position in real space can be expressed by a real-space vector $\mathbf{R}$ as a linear combination of the three basis vectors [161]:

$$\mathbf{R} = n_1\mathbf{a}_1 + n_2\mathbf{a}_2 + n_3\mathbf{a}_3 \ . \tag{2.38}$$

n_i are the weights of the different basis vectors in real space. Another way to describe the periodic solid is the utilization of the reciprocal space, which is convenient for analytic studies of periodic structures. In reciprocal space the periodic solid can be characterized by

$$\mathbf{K} = m_1\mathbf{b}_1 + m_2\mathbf{b}_2 + m_3\mathbf{b}_3 \ , \tag{2.39}$$

where $\mathbf{K}$ is a reciprocal vector, obtained by a linear combination of the reciprocal lattice vectors $\mathbf{b}_1$, $\mathbf{b}_2$, $\mathbf{b}_3$. The weights of the reciprocal basis vectors are m_1, m_2 and m_3. Each vector with integer m_1, m_2, m_3 is a surface normal to the surface $(m_1m_2m_3)$, which are also denoted as the Miller indices h, k, l [161].
As a result of the translational symmetry of the unit cell, a periodic potential exists within the periodic crystal system. For a quantum chemical treatment of these solid state systems, this periodic potential has to be taken into account in the theoretical framework, which was done in 1929 by F. Bloch, who introduced the *Bloch wave* as a wave function for a particle in a periodic potential [162]. The resulting wave function is required to obey *Bloch's theorem* by reflecting the translational symmetry

$$\phi(\mathbf{k}, \mathbf{r} + \mathbf{R}) = e^{i\mathbf{kR}}\phi(\mathbf{k}, \mathbf{r}) \ . \tag{2.40}$$

$\mathbf{k}$ is a reciprocal vector, $\mathbf{R}$ is a translational vector and $e^{i\mathbf{kR}}$ is a plane wave [163–165]. These wave functions, referred to as Bloch functions, are hereby defined as

$$\phi(\mathbf{k}, \mathbf{r}) = e^{i\mathbf{kr}}u(\mathbf{r}) \ , \tag{2.41}$$

with $u(\mathbf{r}+\mathbf{R}) = u(\mathbf{r})$. This periodicity of the lattice leads to convenient features of the systems. Two vectors $\mathbf{k_1}$ and $\mathbf{k_2}$ are equivalent when they only differ by a lattice vector $\mathbf{K}$. Therefore, only $\mathbf{k}$-vectors in a small reference cell in reciprocal space have to be

taken into account, which is known as the first *Brillouin zone* (BZ). The corresponding cell in real space is the *Wigner-Seitz* cell. As an example, the Brillouin zone for the Cu_2ZnSnS_4 bulk is shown in fig. 2.1.

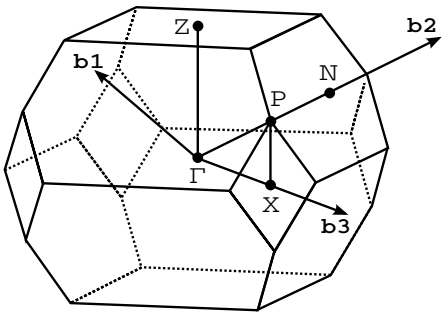

Figure 2.1: Brillouin zone of the space group $I\bar{4}$ for the unit cell of Cu_2ZnSnS_4 bulk with special high symmetry points.

For calculations of periodic systems, the periodic boundary conditions and the approaches discussed in HF (see sec. 2.1) and DFT (see sec. 2.2) have to be combined. The wave function of the solid state system, also referred to as *crystalline wave function* and denoted as $\psi_i(\mathbf{k}, \mathbf{r})$, can be defined by a linear combination of Bloch functions [166]:

$$\psi_i(\mathbf{k}, \mathbf{r}) = \sum_{\mu} c_{\mu i}(\mathbf{k}) \phi(\mathbf{k}, \mathbf{r}), \tag{2.42}$$

with the coefficients $c_{\mu i}(\mathbf{k})$, which are obtained by analogously solving the coupled set of matrix equations as previously shown in HF (see eq. 2.12):

$$\mathbf{F}(\mathbf{k})\mathbf{C}(\mathbf{k}) = \epsilon(\mathbf{k})\mathbf{S}(\mathbf{k})\mathbf{C}(\mathbf{k}) \ . \tag{2.43}$$

By solving this set of coupled matrix equations for each value of $\mathbf{k}$ separately, $\mathbf{k}$-dependent eigenvalues $\epsilon(\mathbf{k})$ are obtained, which is also referred to as *dispersion*. Hereby a small dispersion translates to a small dependency on the $\mathbf{k}$-vector. The eigenvalues $\epsilon(\mathbf{k})$ plotted as a function of $\mathbf{k}$ yields the electronic *band structure* of the solid state system, whereby only the first BZ has to be considered due to the translational symmetry. The electronic structure is characterized by a representative high symmetry path within the BZ (see fig. 2.1). Hereby the Fermi energy defines the highest occupied energy level, up to which the band structure is filled at 0K. One of the main features of the band structure is extracted by the band gap, which is the energy difference between the eigenvalues of valence and the conduction band. The size of this gap leads to a formal characterization of the solid state material, which can be classified as an insulator, a semiconductor or a metal (fig. 2.2).

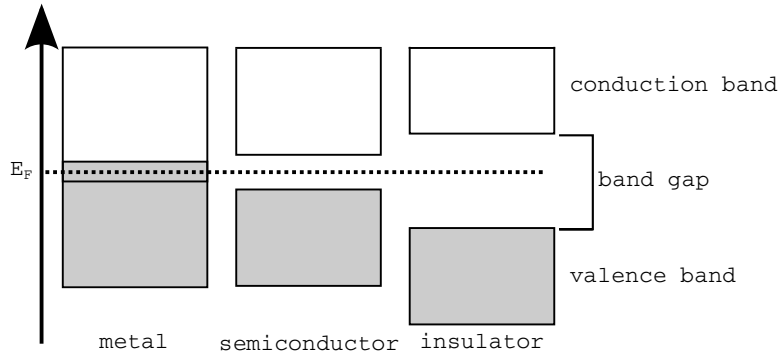

Figure 2.2: Schematic scheme of different band structure types. In metals the conduction and valence band typically overlap. Semiconductors show normally a small band gap, which band occupation changes with temperature. By strongly increasing the band gap an insulator is obtained. The Fermi energy is presented by the dashed line.

Band gaps can be separated into direct band gaps, in which the valence band maximum and the conduction band minimum are located at the same **k**-point, or indirect band gaps, in which the two extrema are located at different **k**-points (see fig. 2.3).

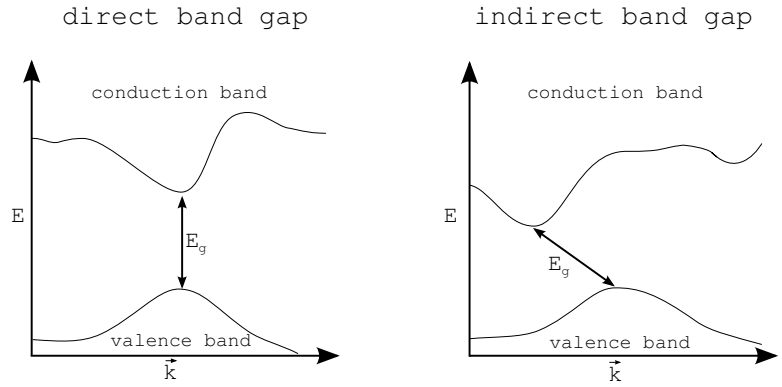

Figure 2.3: Two possibilities of band gaps. On the left side a direct band gap is shown, in which the gap is located at a specific **k**-point in the Brillouin zone. On the right side the indirect band gap is presented, in which the maximum of the valence band and the minimum of the conduction band are located at a different **k**-points in the BZ.

Closely related to the band structure is the DOS, which describes the number of states per interval of energy at each level that are available to be occupied by electrons. The DOS is given by

$$D_j(E) = \frac{2}{V_{\mathrm{BZ}}} \int_{BZ} \mathrm{d}\mathbf{k}\ \delta(E - E_j(\mathbf{k}))\ , \tag{2.44}$$

with the integral over the whole BZ, E_j as the j-th band energy and V_{BZ} is the volume of the BZ. The DOS is a useful tool when investigating the electronic properties of solid state materials.

These electronic properties are straightforward when utilizing perfect and periodic crys-

tals, which only works as a model system if the material features low amounts of defects and is prepared as large monocrystals. Part of this work sets focus on the modeling of CZTS nanostructures, whereby the material is modified to feature a high surface area in combination with a small bulk part. Surfaces are defined as a truncation of the ideal periodic crystal in one dimension in the computational model, also referred to as *slab model*. Hereby the termination of a crystal by a formation of a surface disrupts the usual boundary conditions in the direction perpendicular to the surface plane, thus changing the behavior of the electronic structure at the surface in contrast to the electronic structure in the bulk. Solving the electronic Schrödinger equation for this situation, two qualitatively different solutions are obtained (see fig. 2.4).
The bulk states decay exponentially into the vacuum and have Bloch character in the bulk, whereas the surface states found at the surface termination decay exponentially into the bulk and vacuum. With these qualitatively different solutions for the electronic Schrödinger equation the different behavior between surface and bulk atoms can be explained [167]. Surface states can have a crucial effect on the overall electronic behavior of the material [168].

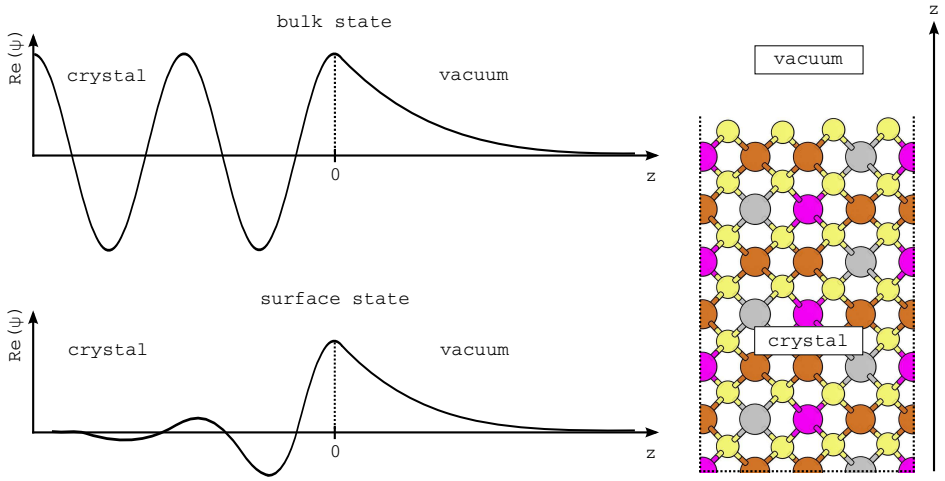

Figure 2.4: Solution to the one-dimensional Schrödinger equation for bulk states and surface states. Both states decay exponentially into the vacuum, whereby the bulk state features Bloch character in the bulk. The surface state also decays exponentially into the bulk. A model CZTS surface structure is shown in the right illustration.

2.5 Basis Set and Pseudo Potentials

For the mentioned Bloch functions two different approaches for an expansion in a basis set are here briefly introduced. The first type of a natural basis function for a translationally invariant system is given by Bloch's Theorem itself, namely a plane wave. This plane wave is a symmetry-adapted wave function, which fits the crystal's boundary conditions. Hence, the crystal wave function can be expressed as a linear combination of plane wave basis functions

$$\phi_n(\mathbf{k},\mathbf{r}) = \sum_{\mathbf{K}} c_n(\mathbf{k},\mathbf{K}) e^{i(\mathbf{k}+\mathbf{K})\mathbf{r}} \ , \tag{2.45}$$

with the mixing coefficients c_n and a reciprocal lattice vector $\mathbf{K}$ defined in eq 2.39. Due to their simplicity, plane waves have computational advantages over other types of basis sets. They are orthogonal and not localized on atoms, additionally they are not suffering from basis set superposition errors (BSSE) like atom centered basis sets. The size of the plane wave basis set, determined by the number of plane waves, is controlled by an energy cutoff E_{cut} [164]. The set of plane waves has to possess enough variational freedom to exhibit the typical plane wave behavior between atoms but also has to reproduce core-like behavior close to the atoms (see fig. 2.5).
To comply with both constraints, a high energy cutoff for the plane waves is required for an accurate description of the core region, which leads to problems with computational resources [164, 169]. Therefore pseudo potentials (PP) have been developed to approximate the electronic structure of the core region of the atoms up to a certain distance, whereby the description of the valence electrons remains as in the all electron calculation with respect to adjustments of the basis set to the utilized PP.

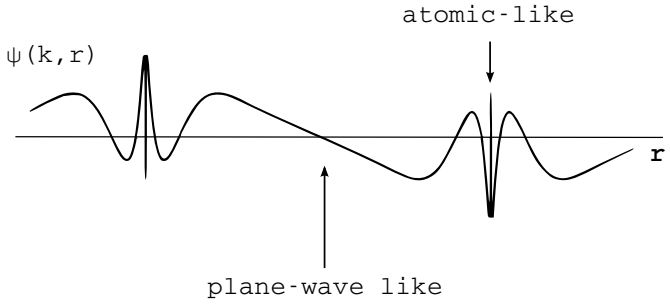

Figure 2.5: Schematic drawing of a Bloch function for a one dimensional crystal. Close to the nucleus the wave function oscillates rapidly, whereas in the region between two nuclei, the wave function is slowly varying [164].

Today there are several types of PPs, which can be divided into two types: norm-conserving pseudo potentials and ultrasoft pseudo potentials. Norm-conserving pseudo potentials enforce, outside of a cutoff radius that the pseudo-wave function and its corresponding all-electron wave function to be identical [170–172]. Inside of this cut-off radius, the norm of the pseudo-wave function and the all-electron wave function

are identical. Ultrasoft PPs reduce the basis set size by relaxing the norm-conserving constraints while maintaining the same accuracy, but losing the orthonormality of the orbitals. An advantage of this method are slowly varying wave functions, whereby for the same precision of a computation a smaller number of plane waves is required [173]. A related method is the projector augmented wave method (PAW) (for further details see ref. [174]), which is used in this thesis exclusively in all periodic calculations. PAW is considered a PP, although it formally retains all core electrons [163]. Kresse et al. derived in 1999 a formal relationship between ultrasoft PPs and the PAW method [175]. The second possibility for the expansion of the Bloch functions in a basis set are localized atomic basis functions. The crystal wave function can be expressed as a linear combination of atomic orbitals (LCAO)

$$\phi_n(\mathbf{k},\mathbf{r}) = \sum_{\mathbf{R}} \varphi_\mu(\mathbf{r} - \mathbf{A}_\varphi - \mathbf{R}) e^{i\mathbf{kR}} \ , \tag{2.46}$$

with the coordinate of an electron $\mathbf{r}$, the direct lattice vector $\mathbf{R}$ and the reciprocal lattice vector $\mathbf{k}$. A_φ denotes the coordinate of an atom in the reference cell, on which the atomic orbital φ is centered [166]. Due to computational advantages, the atomic orbitals themselves are normally a linear combination of products of Gaussian functions. Atomic orbitals feature a consistent description of core and valence electrons, whereby all electron calculations are easily possible. Unfortunately, they often suffer from the BSSE. The atom centered basis set is often used in non-periodic calculations and is defined by

$$\phi_n(\mathbf{r}) = \sum_{\mu=1}^{K} C_{\mu n} \varphi_\mu(\mathbf{r}) \ , \tag{2.47}$$

with K as the number of atomic orbitals, the expansion coefficients $C_{\mu n}$ and the basis functions φ_μ, which are atomic orbitals as variants of solutions to hydrogen-like atoms. There are different ways to express the atomic orbitals, whereby the most common are Slater-type orbitals (STO) and Gaussian-type orbitals (GTO) [163]. STOs are modified hydrogen-like orbitals with an unchanged angular part and a node-free modified radial part. Unfortunately STOs are not analytically integrable. GOTs are expressed as a linear combination of Gaussian functions, which can be integrated analytically, favoring their usage. Since an explicit description of all electrons is computationally expensive for heavy atoms, the core electrons can be substituted by a pseudo potential, while simultaneously treating the valence electrons explicitly, analogously to the PP idea used in the plane wave basis set [163]. There exist various type of PPs, which differ in the description of the core region in terms of the number of electrons included in the potential as well as the incorporation or neglect of relativistic effects.

2.6 Wulff Construction

The ground state structure of a crystal in nature formed during the crystal growth is dependent on the surface energy of the different surfaces. An approximation for the natural shape is obtained by the Wulff constructions [176]. The form of the crystal is the one with minimal free energy of the surface with a constant volume. Gibbs stated that a crystal will arrange itself in a way, so that the Gibbs free energy is minimized by adopting a low surface energy configuration, defined by

$$\Delta G_i = \sum_k \gamma_k O_k \ , \tag{2.48}$$

where γ_k is the surface energy of the k$^{\text{th}}$ crystal face and O_k represents the area of this surface. The equilibrium shape of a crystal is the one with minimal ΔG_i [176]. Wulff stated in 1901 a theorem, which is known as the *Gibbs-Wulff theorem*. Wulff postulated that the length of a vector $\mathbf{r_k}$ normal to a crystal face will be proportional to its surface energy γ_k. Drawing the vector $\mathbf{r_k}$ from the center of the crystal to the corresponding face, the vector $\mathbf{r_k}$ can be seen as the height of the k$^{\text{th}}$ face [177]. Several scientist have given proof to Wulff's theorem since the original publication [178–180].
The Wulff construction is prepared by a polar plot of the surface energy as a function of the orientation, whereby lines from the origin to every point on the polar plot are drawn. By drawing planes perpendicular to the surface normal at each intersection point of the polar plot, the inner envelope of these planes represents the Wulff construction.

2.7 Atomic Charge Analysis

The information about atomic charge distributions in molecules and solid state systems is important in rendering a chemical interpretation of the electronic structure. The analysis of atomic charges can lead to a useful understanding and correlation of chemical phenomena. Today there exist various methods for the determination of atomic charges [141, 163], whereby two methods will be briefly discussed in the following since they are utilized in this work.

2.7.1 Bader Charge Analysis

In 1990 R. Bader developed a method to divide many-atom systems into atomic parts [181]. Bader's method is to analyze the electron density of a system and evaluate its stationary points. Then the electron density will be divided into fragments by *zero flux surfaces*, which are two-dimensional surfaces on which the charge density is a minimum perpendicular to the surface. Typically, for many-atom systems, the electron density reaches a minimum between atoms, which is a natural place to divide atoms from each other. The enclosed charge within this volume can be assigned to an atom to calculate its atomic charge. The volume is also referred to as *Bader volume*.

2.7.2 Natural Population Analysis

The second charge analysis method employed in this thesis is the Natural Population Analysis (NPA) [182]. The method is based on natural atomic orbitals (NAO), which are orthonormal *atomic* orbitals of maximal occupancy. Closely related are the conventional natural orbitals (NO) as introduced by Löwdin [183], which in contrast are defined as orthonormal *molecular* orbitals of maximum occupancy. NOs are delocalized over the whole molecule and transform as irreducible representations of the full symmetry point group of the molecule, which is not present in NAOs, since they are by definition localized on atoms upon formation of the molecule. The NPA via NAOs shows advantages like intrinsically nonnegative quantities, an excellent numerical stability with respect to basis set changes and a good description of charge distributions in ionic compounds [182].

Chapter 3

Modified $Cu_2ZnSnS_xSe_{4-x}$ Bulk Structures

Over the last years, the interest in Cu_2ZnSnS_4 (CZTS), $Cu_2ZnSnSe_4$ (CZTSe), and $Cu_2ZnSnS_xSe_{4-x}$ (CZTSSe) as absorbers in thin film solar cells has grown due to their promising electronic properties and low material costs. In recent years, many theoretical papers have been published on the properties of CZTS and systems derived from CZTS. Since the applied computational and theoretical methods and results vary, up to now no standard method for describing the electronic structure of CZTS and CZTSe has been established. Therefore, in a first step of the research on CZTS and Se-containing derivatives is to investigate the bulk systems with respect to computational parameters and applied theoretical methods for the subsequent research on modified kesterite derived systems. This chapter focuses on the pure and perfect bulk systems. After determining the optimal technical settings and getting insight on structural properties and electronic structure of the bulk, the research continues with modified CZTS and CZTSe bulk systems. The focus is then set on CZTSSe alloys and 2c/2d disorders in CZTS, since both modifications are important in realistic devices. CZTSSe alloys are currently used in the high performance thin film kesterite solar cell with efficiencies up to 13 % [26]. Since there are a wide variety of different alloy mixtures possible, the main focus lies on the investigation on the optimal S/Se ratio for a highly efficient solar cell with respect to the Shockley-Queisser limit and on the investigation on band gap fluctuations upon alloying. The second structural modification occurs in the experimental samples, which feature a varying amount of 2c/2d disorders throughout the crystals [114, 184]. These disordered systems are a possible limitating factor for a constant quality and performance of the solar cell module, since minimal structural changes in the lattice can result in fluctuating electronic properties. Therefore, the research on this defect type is essential to understand a possible key factor for band gap fluctuations and observed low open-circuit voltages in experimental samples [113].

3.1 Technical Details

The periodic electronic-structure calculations were carried out within the Kohn Sham DFT framework as implemented in VASP 5.3.5 and VASP 5.4.1 [185–188], whereby both versions yield the same results. For the visualization of all structures XCrySDen [189, 190] was used. The calculations were performed with a plane wave basis set with an energy cut off of 550 eV with the projector augmented (PAW) potentials [174, 175]. The employed PAW potentials acted on the 5s, 5p and 4d electrons of Sn, 3s, 3p electrons of S, 4s, 4p electrons of Se and 4s, 3d electrons of Cu and Zn. For the electronic convergence, the Blocked-Davidson algorithm was applied as implemented in VASP and an electronic convergence criteria was set at least to 10^{-5} eV. The structural relaxation was set to a force convergence of 10^{-2} eV/Å^2 and was performed with the conjugate-gradient algorithm implemented in VASP [191]. A Gaussian smearing approach with a smearing factor σ of 0.01 eV and an enabled freedom of spin polarization was used to account for a possible magnetization during the modifications of the bulk material. In contrast to the structure relaxation the single point calculations for the DOS and accurate energies were performed with the tetrahedron method with Blöchl corrections [192] to account for precise energies. All employed k-grids were automatically constructed via the Monkhorst-Pack scheme [193] and centered at the Γ-point. The Bader charge analysis was performed with the Bader Charge Analysis code of the Henkelman group of the University of Texas at Austin [194–196]. Since the three bulk related topics have specific requirements for their modeling, the specific technical details are listed in the following.

CZTS and CZTSe Bulk Systems

The bulk CZTS and CZTSe kesterite unit cell with 16 atoms was fully optimized with the PBE [146], PBEsol [150], HSE06 [154–157] and PBE0 [197] functional to account for a suitable functional with respect to the experimental data like lattice constants and electronic properties. The Hartree-Fock screening parameter of the HSE06 functional was set to the default value of 0.2 Å^{-1}. The k-grid during the structure optimization was set to 8x8x4 for PBE and PBEsol and to 4x4x2 for HSE06 and PBE0, which has proven to be sufficient for the structural parameters as well as band gap determination. To account for the influence of minor changes in the lattice parameters as well as internal coordinates, on top of the fully optimized PBE-structure, single point calculations with the HSE06 and PBE0 functional were performed, denoted as HSE06$_{\mathrm{PBE}}$ and PBE0$_{\mathrm{PBE}}$. DOS were calculated with a 8x8x4 k-grid to ensure full electronic convergence with the GGA functionals and 6x6x4 for the hybrid-functionals. For every functional the Bader charges were computed.

CZTSSe Alloys

The CZTSSe kesterite unit cells with 16 atoms were fully optimized with the PBE functional at a 8x8x4 k-grid to account for lattice changes upon the different alloy degrees. The DOS were obtained with a 8x8x4 k-grid for the PBE functional. On top of the PBE-optimized structures single point HSE06 calculations with a 4x4x2 k-grid were performed for an accurate band gap. The Bader charges were computed with the PBE functional and HSE06 functional with the PBE-optimized structures.

2c/2d Disordered CZTS

To simulate different disorder fractions and patterns a supercell with 64 atoms was employed, consisting of 2x2x1 unit cells in kesterite structure. The supercells were fully optimized with a 4x4x4 k-grid with the PBE functional. Due to the size of the supercell, the 4x4x4 k-grid corresponds to a 8x8x4 k-grid in the bulk system with 16 atoms, which has shown converged structural properties. To accurately describe the electronic structure of the supercell the HSE06-functional was applied in a single point calculation on top of selected PBE-optimized structures. Due to computational costs and convergence challenges a 2x2x2 k-grid was utilized, which corresponds to a 4x4x2 k-grid in the normal unit cell. This k-grid is sufficient for a converged band gap. The Bader charges are calculated with the PBE functional. For the symmetry analysis of the disorder degrees and fractions the solid solution module of the CRYSTAL14 is employed [198, 199].

3.2 Cu_2ZnSnS_4 and $Cu_2ZnSnSe_4$ Bulk Systems

Over the last few years CZTS and CZTSe bulk systems have been studied extensively in theory, whereas only few methods and computational schemes have proven to be accurate and economically feasible at the same time. Theoreticians and computational scientists especially focused on DFT functionals within plane wave and atom centered basis set program codes [43, 81, 83, 85–91, 109, 200–209]. Only few scientists applied more advanced methods like the GW approximation for a more accurate electronic structure [84, 210]. This accuracy comes of course at a high computational cost, which is only applicable to small CZTS unit cells. Therefore most of the scientists kept the focus on DFT methods, since the results are accurate enough with relatively low computational costs. In this work as a first step for the investigation on the CZTS and CZTSe kesterite systems, the bulk systems are benchmarked against different theoretical methods for suitable computational parameters for the following research on modified kesterite systems. As used in early theoretical work by Paier et al. [43], the PBE and HSE06 functional are employed and additionally the closely related PBEsol and PBE0 functionals. The calculations focus on structural properties like lattice constants and the electronic structure in form of the DOS and band structures to reproduce first of all the published data and obtain especially the necessary compu-

tational parameters for a proper description of the investigated systems. Furthermore, these calculations give an important understanding of the properties of CZTS, CZTSe, and derived systems at the same computational level.

3.2.1 Structural Properties of the CZTS and CZTSe Bulk System

In the beginning the structural parameters obtained by the theoretical calculations in comparison to the experimental data are of special importance, since a strong structural deviation of lattice parameters from the experimental data can lead to drastically different electronic properties in later calculations. For all calculations the 16 atom unit cells of CZTS and CZTSe are employed as shown in fig. 3.1. Both compounds are in the kesterite structure, which is the lowest energetic form [43]. The structures only differ in the anion type on the 8g Wyckoff position, while the 2a, 2b, 2c and 2d positions are in both cases occupied Cu, Sn, Cu and Zn respectively. The cations form planes normal to the lattice constant c, on which the 2c/2d plane is occupied by Cu/Zn and the 2a/2b plane is occupied by Cu/Sn. These cation planes are connected by chalcogen planes on the 8g position.

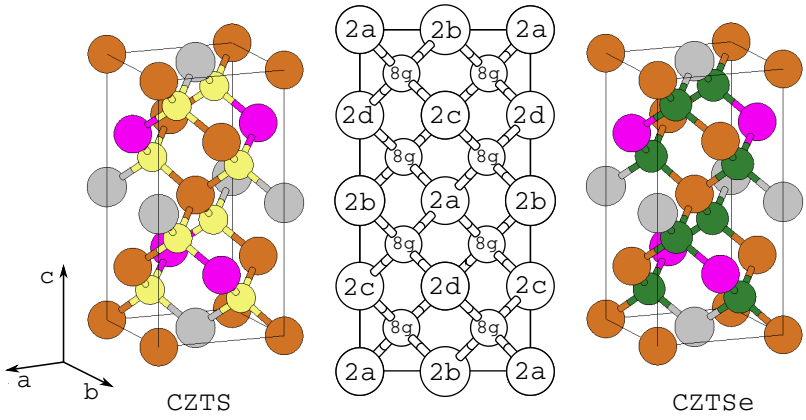

Figure 3.1: Bulk structures of CZTS and CZTSe. The ionic structure of both compounds is identical, whereas the lattice constants are slightly larger for CZTSe due to the larger atom radius of Se. Zn is shown in pink, Cu in brown, Sn in gray, S in yellow and Se in green.

The calculated lattice constants for CZTS and CZTSe are summarized in tab. 3.1. All utilized functionals yield reliable lattice parameters in comparison to experimental values, whereby the differences to experimental data varies. The PBE functional slightly overestimates both lattice constants a and c of the tetragonal Bravais lattice in both materials CZTS and CZTSe. PBEsol underestimates both lattice constants a and c in the CZTS system. In CZTSe however, the lattice constant a is overestimated and lattice constant c is underestimated. The hybrid-functionals HSE06 and PBE0 both slightly overestimate the lattice constant a for the CZTS system, whereas lattice constant c is slightly underestimated.

In the CZTSe system the HSE06 functional yields a slightly overestimated lattice constants a and c. PBE0 shows nearly identical results, while being closer to experimental lattice parameters than the HSE06 functional.

Table 3.1: Lattice parameters of CZTS and CZTSe as obtained by different DFT functionals in comparison to experimental values. Overall the different functional yield reasonable results and only minor deviations from the experimental data are shown.

material	functional	a [Å]	c [Å]	2a/c	volume [Å^3]
CZTS	PBE	5.464	10.920	1.001	325.96
	PBEsol	5.370	10.736	1.000	309.60
	HSE06	5.445	10.856	1.003	321.91
	PBE0	5.440	10.848	1.003	321.07
	EXP[44]	5.427	10.871	0.97	320.18
CZTSe	PBE	5.761	11.507	1.001	381.87
	PBEsol	5.761	11.298	1.001	361.42
	HSE06	5.738	11.369	1.009	374.25
	PBE0	5.731	11.356	1.009	372.96
	EXP[a][45]	5.689	11.347	1.003	367.24

[a] at room temperature

Since calculations with hybrid-functionals in VASP are in general more than a magnitude more expensive than GGA calculations, for structural optimizations a GGA functional is the functional of choice, especially with regard to larger unit cells in future research. In CZTS the PBE functional shows smaller deviations than the PBEsol functional from the experimental data, resulting in PBE being the functional of choice for structural related properties based of structures on the CZTS kesterite structure. In comparison of the two hybrid-functionals, the HSE06 functional shows a faster convergence with respect to the applied k-grid, while yielding nearly identical structural results as PBE0.

With this good agreement with experimental data of the lattice, the questions arises how these functionals perform with respect to the electronic structure, since the electronic properties are crucial when investigating solar cell absorber material. A link between the ionic and the electronic structure are atomic charges in form of Bader charges, since they are a result of the ionic structure, but also give a first insight on the electronic structure of the material. The Bader charge analysis with all DFT functionals shows an ionic character, which differs from the formal charges Cu^+, Zn^{2+}, Sn^{4+}, S^{2-} and Se^{2-}. Due to the charge definition in the Bader charge analysis, rational atomic charges are obtained rather than integer atomic charges. For all applied computational methods, the Bader charges show the same consistent behavior (see tab. 3.2).

Table 3.2: Bader charges for CZTS and CZTSe as obtained by different functionals. All DFT functionals indicate an ionic character of the system, which deviate from formal charges of Cu^+, Zn^{2+}, Sn^{4+}, S^{2-} and Se^{2-} ions.

material	atom	formal [e]	PBE [e]	PBEsol [e]	HSE06 [e]	PBE0 [e]
CZTS	Cu_{2a}	1	0.476	0.439	0.480	0.478
	Cu_{2c}	1	0.478	0.434	0.474	0.472
	Sn_{2b}	4	1.382	1.369	1.581	1.589
	Zn_{2d}	2	0.848	0.813	0.941	0.939
	S_{8g}	-2	-0.796	-0.764	-0.869	-0.869
CZTSe	Cu_{2a}	1	0.360	0.327	0.382	0.378
	Cu_{2c}	1	0.353	0.313	0.353	0.373
	Sn_{2b}	4	1.087	1.089	1.273	1.278
	Zn_{2d}	2	0.696	0.669	0.813	0.811
	Se_{8g}	-2	-0.624	-0.599	-0.711	-0.710

In CZTS, Cu_{2a} and Cu_{2c} exhibit a charge of 0.48 e with the PBE functional within the computational accuracy. Sn_{2b} shows an average of PBE and PBEsol charges of about 1.375 e and slightly higher charges with hybrid-functionals of 1.585 e. The PBE and PBEsol functionals yield a charge of 0.848 e and 0.813 e for Zn_{2d} respectively, whereas the hybrid-functionals predict slightly higher charges of 0.94 e. S_{8g} exhibits a charge of -0.796 e for PBE, -0.764 e for PBEsol, -0.869 e for HSE06 and -0.869 e for PBE0. In CZTSe S_{8g} is substituted with Se_{8g}, which shows Bader charges of about 0.2 e higher than S_{8g}. As a result of this substitution, the cation charges in CZTSe are in general about 0.1 e to 0.3 e lower than the CZTS counterpart. Overall the different DFT functionals yield similar Bader charges, whereby all functionals show the same tendencies with respect to the atom types. The hybrid-functionals show the same values for Cu as the GGA functionals, but also a stronger charge transfer from Zn and Sn to S. Concluding from the charge analysis, a formal charge assignment can be constructed as follows: $Cu^{0.5+}$, Zn^{1+}, $Sn^{1.5+}$ and $S^{0.9-}$ for CZTS and $Cu^{0.4+}$, $Zn^{0.8+}$, $Sn^{1.3+}$ and $Se^{0.7-}$ for CZTSe. In comparison to the formal charges of Cu^+, Zn^{2+}, Sn^{4+} and S^{2-} ions, the Bader charges show lower charges due to partially covalent bonds, but overall the same ratio between the ion charges as in the formal charge is obtained. The calculated Bader charges serve as a reference value for further research, since all structural changes result in changes of the atomic charges. Overall the structural properties as well as the first electronic properties in form of Bader charges reveal that GGA functionals yield results in good agreement with experimental data, while showing low computational costs. The additional non-local HF-exchange in the hybrid-functionals leads to an even better agreement with the experimental data, but overall to a remarkably higher computational costs. Therefore, for the structural parameters the GGA functionals show a sufficient accuracy. In comparison to other theoretical publications, the reported

structural values could be reproduced within the computational accuracy [43]. After this good agreement of the different functionals with experimental lattice parameters, the question arises if the applied functionals also show a good accordance with respect to the electronic structure of CZTS and CZTSe.

3.2.2 Electronic Structure of CZTS and CZTSe Bulk Systems

A precise analysis of the electronic properties of CZTS and CZTSe is of special importance for the solar cell absorber, since they are decisive for the efficiency and performance of the solar cell module. Since the Bader charges only show a rough picture of the electronic structure, a more sophisticated approach has to be chosen for a more detailed view on the electronic structure, which is performed in form of the analysis of the DOS and band structure. The DOS of CZTS and CZTSe are exemplarily shown for the PBE and the HSE06 functional in fig. 3.2, since the DOS obtained by GGA functionals and the DOS obtained by hybrid-functionals strongly resemble. No differences between the different spin components ($\uparrow$ / $\downarrow$) are observable, which reveals that CZTS and CZTSe show no magnetic properties within the computational framework applied. In CZTS the S-3s and S-3p states are visible between -13 eV and -16 eV and -6 eV to 0 eV respectively. The Zn-3d states form a narrow band at -7 eV to -8 eV, depending on the functional applied. The valence band consists of Cu-3d states from -2 eV to 0 eV, furthermore a combination of S-3p and Cu-3d states can be observed in the range of -6 eV to 0 eV. The first conduction bands are made up of Sn-5s and S-3p states, which are separated from the rest of the conduction bands by a larger gap. CZTSe shows a nearly identical electronic structure like CZTS. The main difference is the interchange of S states with Se states and energetically lower lying first conduction bands. The overall shape of the CZTSe and CZTS DOS resemble, as well as the identical behavior of the two spin components. A projection of the HSE06 DOS onto the different atoms and orbitals reveals the contribution to the valence and conduction band, illustrated in fig. 3.2. The main contribution on the valence band is made up by Cu-3d states and a minor contribution of S-3p states or Se-4p in CZTS and CZTSe respectively. The strong influence of the Sn-5s states and S-3p or Se-4p states for CZTS and CZTSe respectively is shown in the conduction band. The conduction band of CZTSe is shifted to lower energies in comparison to CZTS by 0.5 eV.
Overall the DOS for all functionals are qualitatively identical, with main changes in the band gap size and low lying Zn-3d states. The close resemblance of GGA and hybrid-functionals DOS lead to the concluding that the GGA functionals are sufficient for a qualitative discussion of the shape of the electronic structure, whereby more accurate DOS are only obtained by the addition of non-local HF-exchange in HSE06 and PBE0.

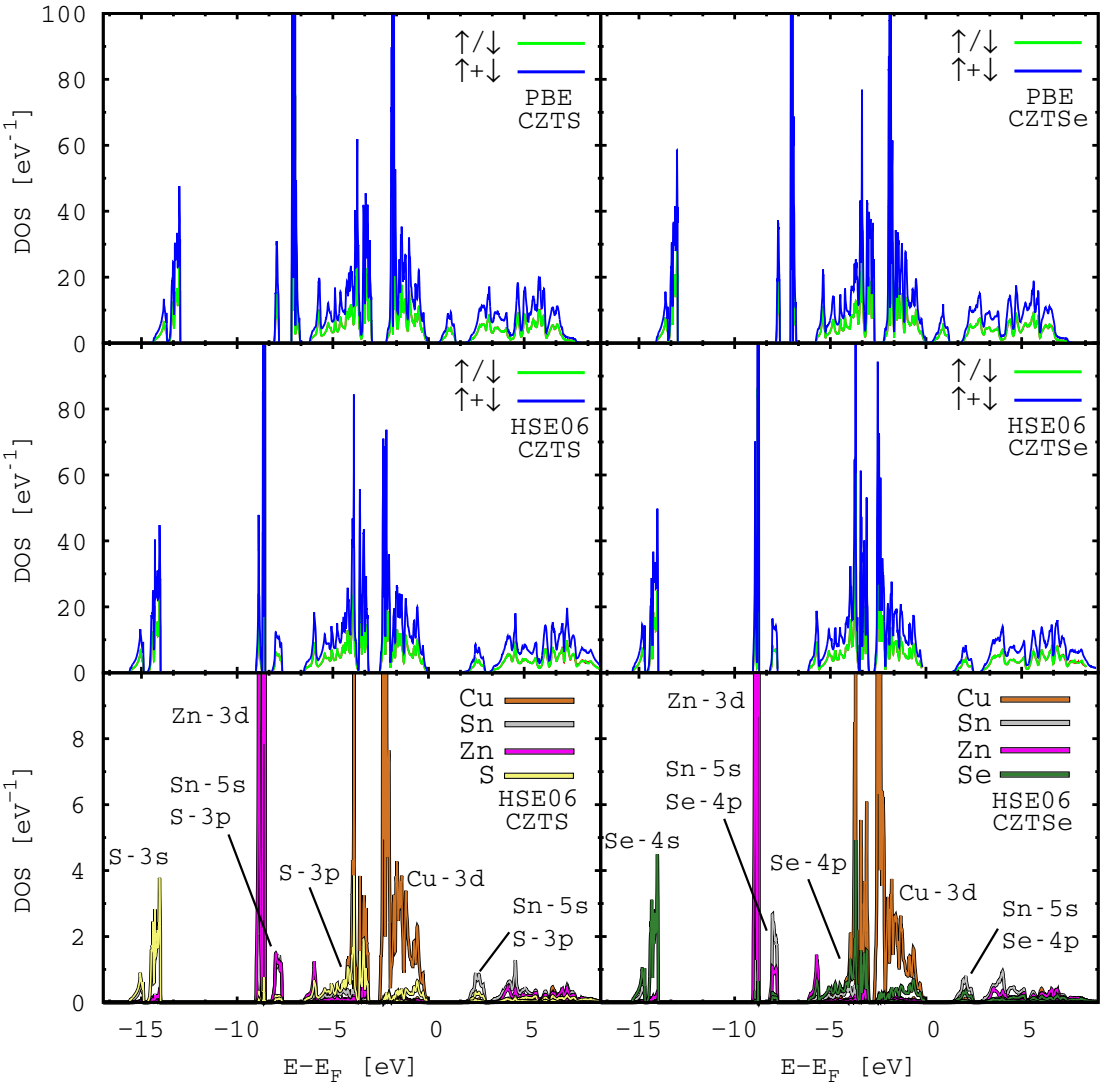

Figure 3.2: The total DOS of CZTS and CZTSe show a clear gap at the Fermi energy that size depends on the chosen DFT functional. The valence band consists of Cu-3d and S-3p states, whereas the conduction band is made up of Sn-5s and S-3p states. The overall electronic structures of CZTS and CZTSe strongly resemble. The different spin components ↑ / ↓ are identical.

The key feature for the benchmark of the functionals is given by the band gap E_g (see tab. 3.3). The experimental band gap of CZTS is in the range from 1.44 eV to 1.51 eV, classifying CZTS as a clear semiconductor [79, 211–213]. PBE and PBEsol clearly underestimate the band gap with 0.07 eV and 0.13 eV respectively. HSE06 shows a clear band gap of 1.47 eV with the HSE06-optimized structure, which is in excellent agreement with the experimental value. The PBE0 functional hereby overestimates the band gap about 0.6 eV, leading to a band gap of 2.11 eV in the optimized PBE0-structure. CZTSe shows a smaller band gap of about 0.8 eV to 1.0 eV in experiment [80]. The same tendency like in CZTS hold true for CZTSe regarding the performance of the functionals. PBE and PBEsol show small band gaps of 0.02 eV and 0.03 eV

respectively, whereas the HF-exchange of the hybrid-functionals expands the band gaps to 0.87 eV with HSE06 and 1.46 eV with PBE0. Overall the GGA functionals PBE and PBEsol crucially underestimate the band gap and the hybrid-functional HSE06 with screened HF-exchange shows an excellent agreement with experimental data, while PBE0 overestimates the band gaps of CZTS and CZTSe. The hybrid-functionals hereby essentially shift the valence and conduction band, leading to a larger band gap than the GGA functionals.

Table 3.3: Band gaps of CZTS and CZTSe as obtained by different functionals in comparison to experimental values.

	material	PBE	PBEsol	HSE06	$HSE06_{PBE}$	PBE0	$PBE0_{PBE}$	EXP [79, 80]
E_g [eV]	CZTS	0.07	0.13	1.47	1.17	2.11	1.79	1.44-1.51
	CZTSe	0.03	0.02	0.87	0.63	1.46	1.19	1.0

The influence of the ionic structure on the electronic structure is observed when using the PBE-structure with the hybrid-functionals, whereby a single point calculation with the hybrid-functional is performed on top of the PBE-optimized structure, denoted as $HSE06_{PBE}$ and $PBE0_{PBE}$. In the PBE-structure, HSE06 yields a band gap of 1.17 eV instead of 1.47 eV in the HSE06-structure. The PBE0 hybrid functional shows a band gap of 2.11 eV in the PBE0-structure and 1.79 eV in the PBE-structure. These smaller band gaps result out of the different lattice parameters between the GGA and hybrid-functionals. The hybrid-functional lattice constants are in general closer to the experimental values. The DOS in fig. 3.3 shows the DOS with different functionals (left) and the influence of the optimized PBE-structure on the band gaps obtained by hybrid-functionals (right).

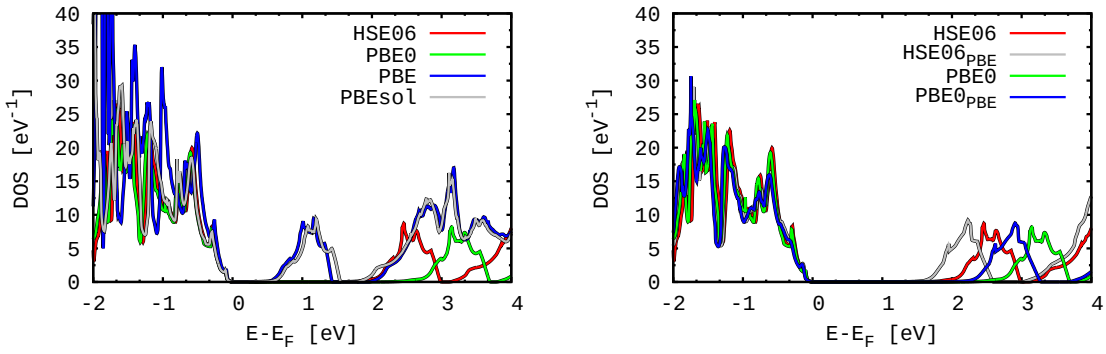

Figure 3.3: The left DOS shows the total DOS for the four different functionals within their optimized structures, whereby the right DOS shows the influence of the PBE-optimized structure on the electronic structure obtained by hybrid-functionals.

In the PBE and PBEsol DOS the maximum of the first conduction band is located at 1 eV, whereas in HSE06 and PBE0 the maximum is located at 2.5 eV and 3.25 eV respectively. The right DOS shows the hybrid-functionals benchmarked within the hybrid-functional optimized structure and the PBE-optimized structure, whereby the both hybrid structures lead to higher band gaps than the PBE-structures. The PBE-structure leads to a shift of the first conduction bands to lower energies, essentially decreasing the band gap. As shown in tab. 3.3, this results in a systematic error of -0.30 eV for HSE06 and -0.24 eV for PBE0, which has to be accounted for in further research when employing PBE-structures with hybrid-functional electronic structures. This systematic error reveals a strong influence of the lattice constants on the band gap, since the main difference between the PBE- and the hybrid-functional structure are the lattice constants. Therefore, a volume scan with optimization of internal parameters is performed for the CZTS and CZTSe structures in the boundaries of the CZTS and CZTSe PBE cell volume. The band gap serves as the key factor for the volume scan, displayed in fig. 3.4.

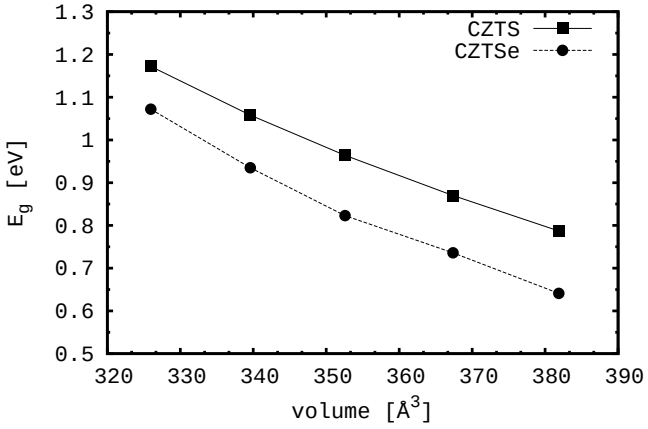

Figure 3.4: CZTS and CZTSe HSE06 band gaps as a function of the cell volume. The volume scan reveals a linear dependence of the band gap on the cell volume.

The volume scan reveals a nearly linear decrease of the band gap as a function of the cell volume, whereby the band gap decreases with increasing cell volume. Starting from 1.172 eV in the CZTS lattice parameters the band gap decreases to 0.787 eV for CZTS in the CZTSe lattice constants. CZTSe shows a band gap of 1.072 eV for the CZTS lattices constants and of 0.641 eV within the CZTSe lattice constants, which are over 0.1 eV lower than the CZTS counterparts. In conclusion the main difference in the band gaps between CZTS and CZTSe is induced by the different lattice parameters, whereby the effect of the different electronic structures of S and Se is small, but not negligible.

Since the DOS only yield an energetic resolution of the electronic structure, the resolution within the reciprocal space is given by the band structure in more details. The

band structures with the PBE, PBEsol and HSE06 functional and corresponding Brillouin zone with high symmetry path are shown in fig. 3.5. The band structures show a strong dispersive band at the Γ-point, which strongly decreases the band gap. As already analyzed in the DOS, the valence band are made up of Cu and S contributions, whereby the conduction band consists of S and Sn bands. The two conduction bands are well separated from the rest of the conduction bands by a larger gap, which depends on the applied DFT functional. All DFT functionals show a similar band topology, which mainly deviates in the size of the band gap as seen before.

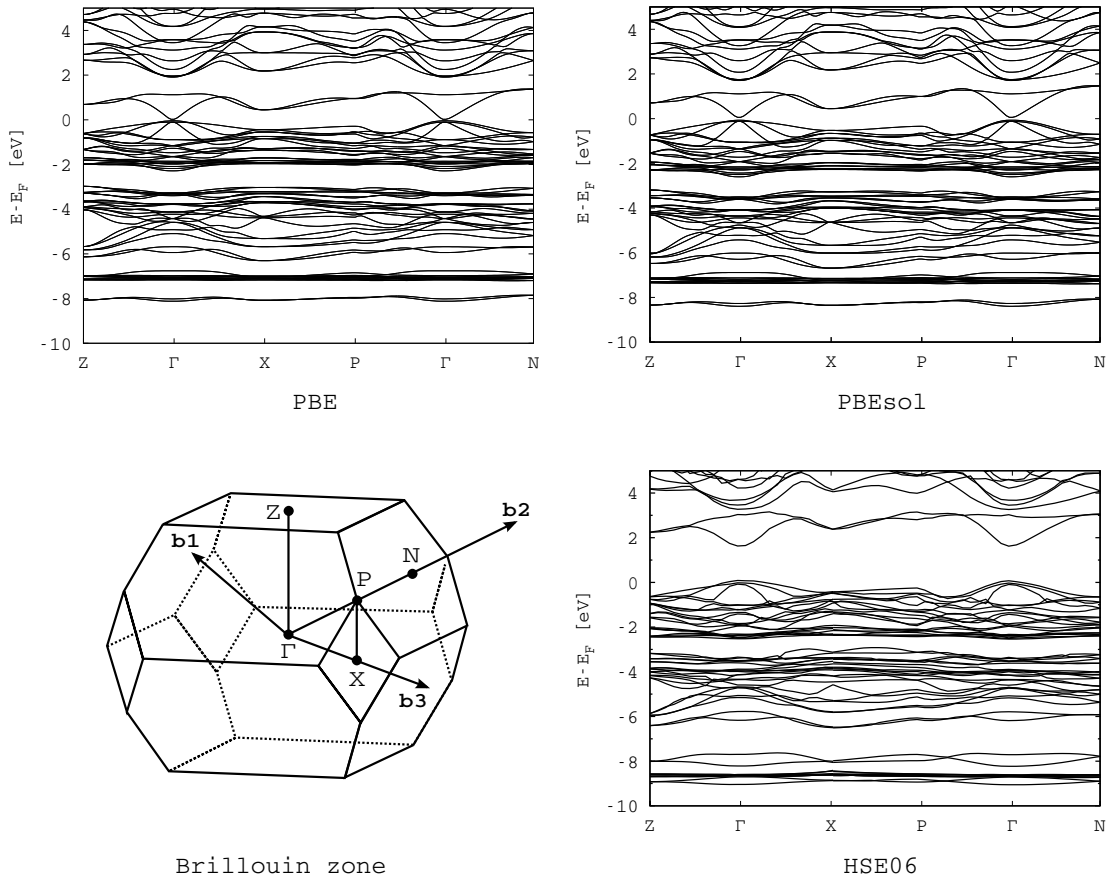

Figure 3.5: Band structure for CZTS with the PBE, PBEsol and HSE06 functional. All calculated band structures reveal a direct band gap at the Γ-point, which varies depending on the applied method.

The analysis of the electronic structure reveals several key factors for an accurate description of the solar cell absorber material. The theoretical investigations at the HSE06 level show that CZTS and CZTSe with band gaps of 1.47 eV and 0.87 eV are clear semiconductors. The direct band gap is located at the Γ-point and is a result of a strong dispersive band. Furthermore, Cu, S/Se and Sn are important for the electronic structure, since they are mainly responsible for the valence and conduction band. A distortion of any kind to these atom types may lead to large fluctuations in the electronic structure. Zn in contrast shows a minor importance, since the Zn-3d states

are located deep in the band structure and do not influence the band gap. Furthermore, from a theoretical perspective, the level of theory is critical for the investigation of the electronic structure. While yielding results in good agreement with experimental data with respect to structural properties, the GGA functionals PBE and PBEsol clearly fail to describe the electronic structure of CZTS and CZTSe precisely. By adding HF-exchange to the Kohn-Sham framework, screened in HSE06 and unscreened in PBE0, the size of the band gap is properly determined and with HSE06 in excellent agreement with the experimental band gap. Higher level of theory in form of sc-GW yields a slightly enlarged bang gap of 1.64 eV for CZTS [84, 210], but is in general not feasible for large unit cells and a large amount of structures. Solving the Bethe-Salpeter equations or applying the Random-Phase-Approximation on top of the sc-GW shows only minor changes of the band gap of up to 0.1 eV [210]. In conclusion the theoretical studies have shown optimal computational and theoretical methods for a further investigation on kesterite derived systems. The already published theoretical and experimental data could be reproduced. On the basis of this investigation, the focus is set to modified kesterite derived system in the following sections.

3.3 Band Gap Engineering by $Cu_2ZnSnS_xSe_{4-x}$ Alloys

A crucial point for the optimization of CZTS/CZTSe solar cells for a better absorption of the solar radiation and better efficiency is the knowledge about suitable material modifications. The quaternary semiconductor provides many possibilities for structural modifications. One ansatz is alloying of CZTS and CZTSe to engineer the band gap [81, 90–108]. The chemical formula $Cu_2ZnSnS_xSe_{4-x}$ reveals a wide variety of possible chemical compositions, for example $Cu_2ZnSnS_2Se_2$. Depending on the composition, due to the eight S atoms in the unit cell, there are also different structural patterns possible within each distinct chemical composition. Up until now, the knowledge about the influence of these different structural patterns on the structural and electronic properties is unknown, whereby scientist started in recent years to generally investigate the structural and electronic trends of the CZTS and CZTSe alloying process [81, 93, 95, 98, 99, 105]. Different structural alloy patterns may lead to band gap fluctuations due to a varying material composition, which is not optimal for realistic solar cells, since the performance of the solar cell module may not be predictable and reliable enough. Furthermore, possible band gap fluctuations in CZTSSe alloys may contribute to the low open-circuit voltage of kesterite solar cells [110]. Therefore, the theoretical investigation on the influence of these alloy patterns on the structural and electronic properties of CZTSSe alloys is essential for the understanding of a possible limiting factor in realistic kesterite solar cells.

3.3.1 $Cu_2ZnSnS_{4-x}Se_x$ Alloy Model

In the conventional CZTS unit cell, there are eight S atoms at the 8g Wyckoff position available for a substitution with Se. This leads overall to 2^8 different possibilities, which can be reduced by the crystal symmetry to a total of 42 structures. The alloy composition, referred to as *alloy fraction* in the following, therefore reaches from 0 % to 100 % in 12.5 % steps (e.g. see tab. 3.4). An alloy fraction of 12.5 % corresponds to one Se atom and seven S atoms, while an alloy fraction of 62.5 % shows five Se atoms and three S atoms. In every alloy fraction there are different S and Se distributions possible at the 8g position, which are referred to as *alloy pattern*. In the 12.5 % alloy fraction one S is substituted with Se, which leads to a total of eight alloy patterns. Since all 8g positions are symmetry equivalent, only one alloy pattern has to be considered. By considering the crystal symmetry, the distribution of the 42 structures into the different alloy fractions is shown in tab. 3.4.

Table 3.4: Number of structures obtained by a symmetry reduced structural analysis for different alloy fractions.

alloy fraction [%]	0.0	12.5	25.0	37.5	50.0	62.5	75.0	87.5	100.0
alloy patterns [#]	1	2	5	7	12	7	5	2	1

Since the structure optimization in section 3.2 has shown differences in the lattice parameters between CZTS and CZTSe due to the larger Se-atoms, all 42 structures are fully optimized at the PBE-level of theory. For the electronic structure PBE and HSE06 single point calculations are performed on top of the PBE-optimized structures, as described in sec. 3.1. The consideration of all different alloy patterns within an alloy fraction allows for a detailed analysis of the CZTSSe alloys. As a first step of this analysis, the change of the structural parameters is investigated in the next section.

3.3.2 Structural Properties of $Cu_2ZnSnS_xSe_{4-x}$ Alloys

All 42 structures were fully optimized, internal and external lattice parameters, whereby the low energy structures for every alloy fraction are exemplarily shown in fig. 3.6. The low energy structures of the alloy fractions 25.0 % and 75.0 % show an identical anion pattern, in which S in 25.0 % and Se in 75.0 % maximize their distance within the unit cell by occupying different horizontal planes with one horizontal 8g plane in between. Also the alloy fractions 37.5 % and 62.5 % show a similar topology regarding their minor alloy element, which try to avoid their close proximity in the same horizontal 8g plane. This leads to a vertical spreading of the minor alloy element within the unit cell. The 50 % alloy also exhibits this feature, in which in every 8g plane one S and Se atom can be found, leading to a maximum distance distribution of the anion types within the unit cell.

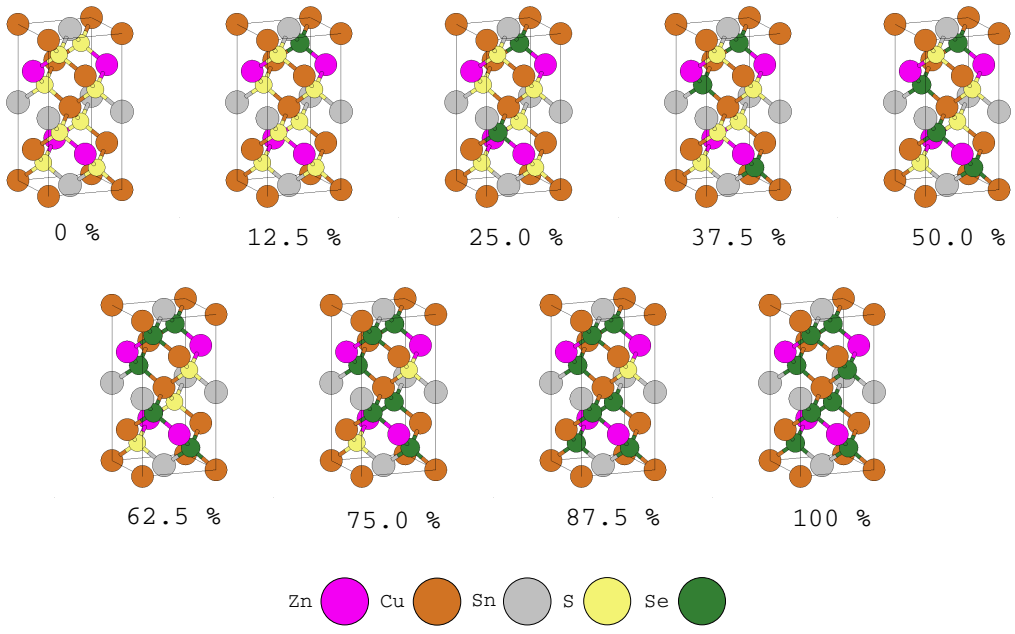

Figure 3.6: Low energy CZTSSe alloy structures for every investigated alloy fraction optimized at the PBE-level.

The substitution of S with the larger Se atoms leads to an expansion of the cell. The resulting optimized lattice constants are shown in tab. 3.5, whereby always the low energy structures of the different alloy fractions are shown, corresponding to the structures presented in fig. 3.6. The full details for all calculated structures can be found in app. A.

Table 3.5: Lattice parameters of CZTSSe alloys as obtained by PBE structure optimizations. Only the low energy structures are presented. The lattice parameters linearly increase with increasing Se amount.

fraction [%]	a [Å]	b [Å]	c [Å]	(a+b)/c	volume [Å^3]
0.0	5.464	5.464	10.921	1.001	326.04
12.5	5.499	5.497	10.995	1.000	332.35
25.0	5.538	5.531	11.073	1.000	339.18
37.5	5.570	5.577	11.142	1.000	346.14
50.0	5.607	5.615	11.207	1.001	352.79
62.5	5.646	5.648	11.283	1.001	359.75
75.0	5.685	5.687	11.363	1.000	366.89
87.5	5.723	5.718	11.437	1.000	374.17
100.0	5.761	5.761	11.507	1.001	381.91

The lattice parameter reveal that by partially substituting S with Se, the lattice constants increase linearly from the CZTS to the CTZSe lattice constants due to the larger atom radius of Se compared to S. This structural linearity is shown in fig. 3.7. In the minimum alloy fraction 0 % and the maximum alloy fraction of 100 % CZTS and CTZSe lattice parameters are obtained respectively. This behavior strictly follows Vegard's empirical heuristic law, which states that at the same temperature the lattice parameter of a solid solution of two materials with the same crystal structure can be approximated by an equation of the two constituents' lattice parameters [214, 215].

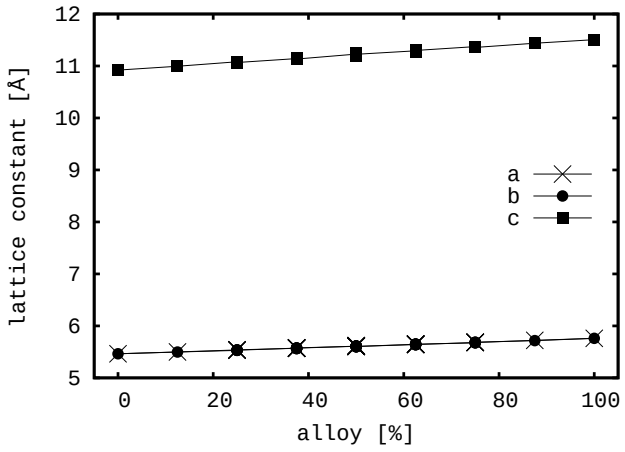

Figure 3.7: Lattice parameters a, b and c for the different CZTSSe alloys. The lattice parameter hereby follow strictly Vegard's law and linearly increase with increasing Se amount.

Closer analyzing the lattice constants a, b and c, the ratio (a+b)/c in all structures is close to one, which slightly varies throughout the different alloy fractions and patterns. This deviation of a and b is due to an anisotropic distribution of the anions within the 8g planes, whereby isotropic distributions lead to equal a and b parameters. Since the lattice parameters a and b start to deviate up on the substitution, the formerly tetragonal lattices changes to a orthorhombic lattice systems. Upon the full substitution to CZTSe, the lattice constants a and b are equal, whereby the initial tetragonal lattices of CZTSe is restored. Since not only the size but also the electronic structures of S and Se are different, the change of the lattice parameter probably also results in a changed electronic structure.

A closer look at the occurring Bader charges in the alloys reveal a decreasing mean Bader charge for the cations with increasing Se amount (see fig. 3.8). This behavior results out of the quantity that Se is about 0.2 e more positively charged than S. The different alloy patterns with their different binding motifs within an alloy fraction lead to not one uniform charge for an element as in the bulk, but rather lead to a range of different charges for one element, in the following referred to as *charge fluctuations*. With increasing alloy fraction an increasing charge fluctuation up to an alloy fraction of 50 % is observed, whereby afterwards the charge fluctuations decrease again. The mean cation charges linearly decrease with increasing alloy fraction, which is induced by the increasing amount of Se atoms and by the increase of the lattice constants. The anions show in all alloy fractions mean Bader charges of -0.799 e and -0.631 e for S and Se respectively with neglectable charge fluctuations. Overall these charge fluctuations and reduced charges of the cations with increasing Se amount may lead to fluctuations of electronic key factors like the band gap.

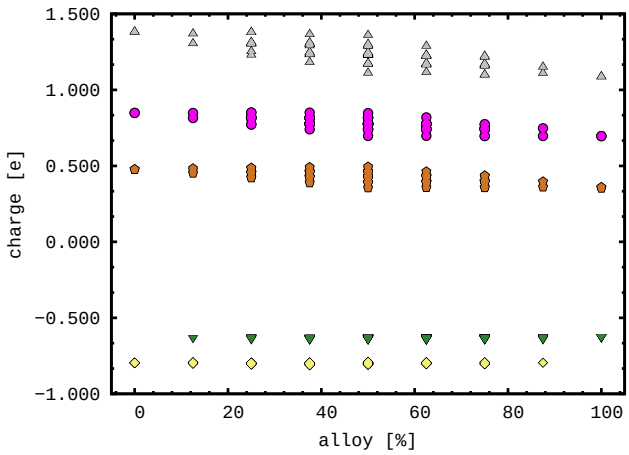

Figure 3.8: Bader charges for all CZTSSe alloys as a function of the alloy fraction at the PBE-level. Zn is shown in pink, Cu in brown, Sn in gray, S in yellow and Se in green.

Concluding from the research on the pure bulk systems CZTS and CZTSe, overall the CZTSSe alloys show an expected structural behavior. The lattice constants, and the cell volume as a result, increase linearly from the CZTS to the CZTSe lattice parameter, whereby for every fraction there are slight deviations since different alloy patterns and binding motifs are possible. Furthermore, upon alloying small charge fluctuations exist for the cations, whereby the anions feature only negligible charge fluctuations. The mean charges of the cations decrease with increasing alloy fraction, which is a result of the more positively charged and larger Se atoms. As seen in the investigation on the bulk properties, the electronic properties strongly depend on the lattice system, since the overlap of the electron densities changes. Therefore, in the next section a closer focus is set the influence of the alloying process on the electronic properties.

3.3.3 Electronic Structure of $Cu_2ZnSnS_xSe_{4-x}$ Alloys

The influence of the structural changes upon alloying on the electronic structure of CZTSSe is of special importance for the solar cell absorber, since the electronic structure determines the electronic properties of the solar cell module. In comparison to CZTS and CZTSe, the electronic structure of CZTSSe alloys strongly resembles the electronic structure of the two boundary materials. Hereby the contribution of the different atoms and orbitals to valence and conduction bands is identical to the ones in CZTS and CZTSe. In contrast to pure CZTS and CZTSe, the conduction band now consists of a mixture of Sn-5s, S-3p and Se-4p states. As a result of different alloy patterns within an alloy fraction, the DOS of an alloy fraction shows a DOS distribution rather than one distinct DOS. The different DOS reveal overall a similar shape of the states, whereby especially the conduction band reveals the influence of the structural changes on the electronic structure. The conduction band is shifted to lower energies with increasing Se amount, which effectively narrows the band gap.
The band structure gives further insight on the electronic structures of the alloys. The investigations of bulk CZTS and CZTSe have shown previously that the strongly dispersive band at Γ-point determines the size of the direct band gap. Therefore, the band structures at the high symmetry path within the first BZ from Z over Γ to X for selected alloy patterns are shown in fig. 3.10 for a more detailed analysis. Starting from the pure CZTS at 0 % the main changes can be observed in the conduction bands. With increasing alloy fraction the conduction band is shifted to lower energies and is therefore narrowing the band gap, whereby the band topology of all alloys resembles. The band gap linearly decreases with increasing Se amount, whereas at 100 % the CZTSe band structure is obtained. The valence band stays in place with respect to the computational accuracy and the employment of PBE-optimized structures.

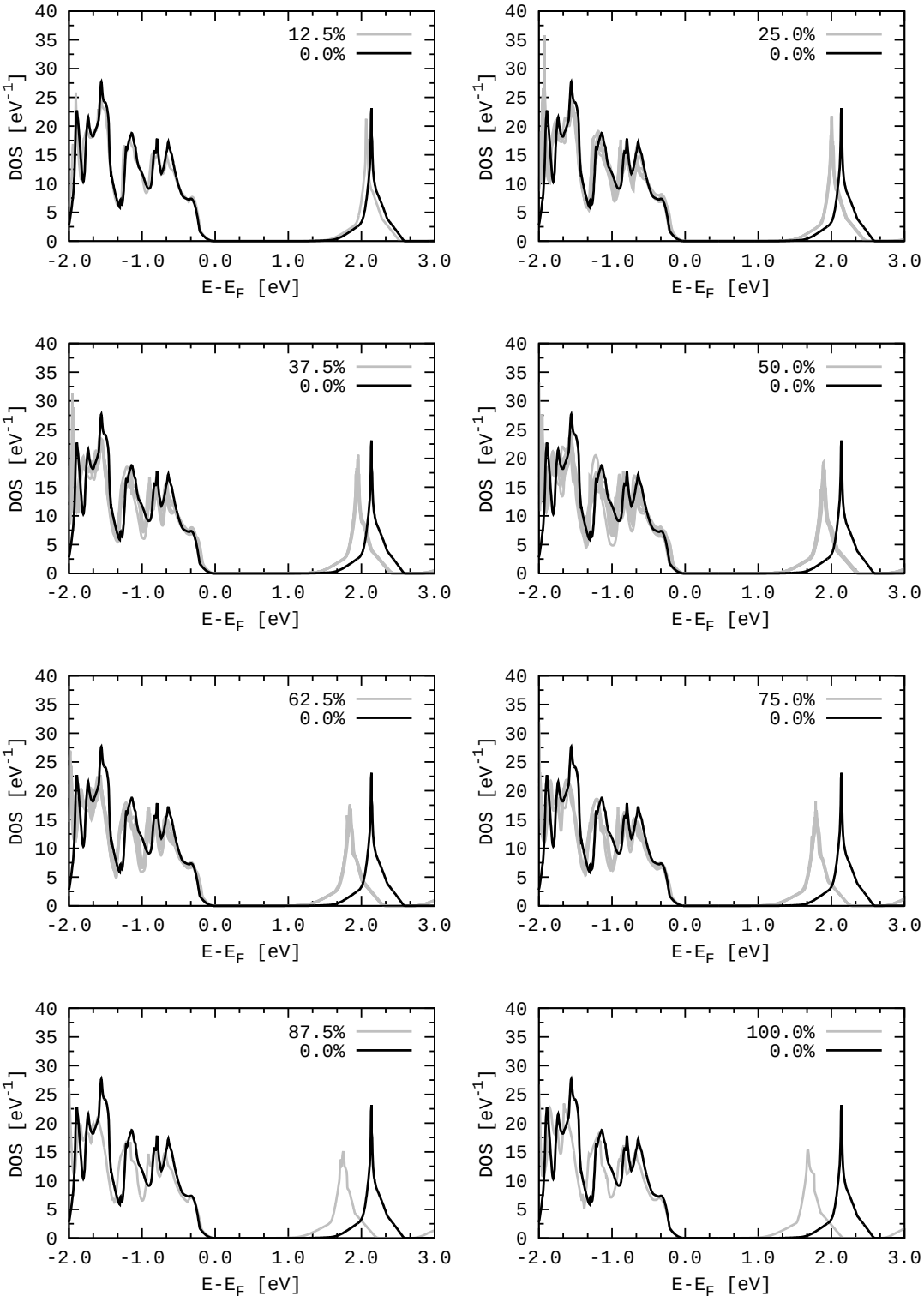

Figure 3.9: Total HSE06 DOS for all CZTSSe alloys fractions and patterns in the optimized PBE-structure. For every alloy fraction, there are different alloy patterns and therefore different DOS possible, which overlap in the corresponding alloy fraction.

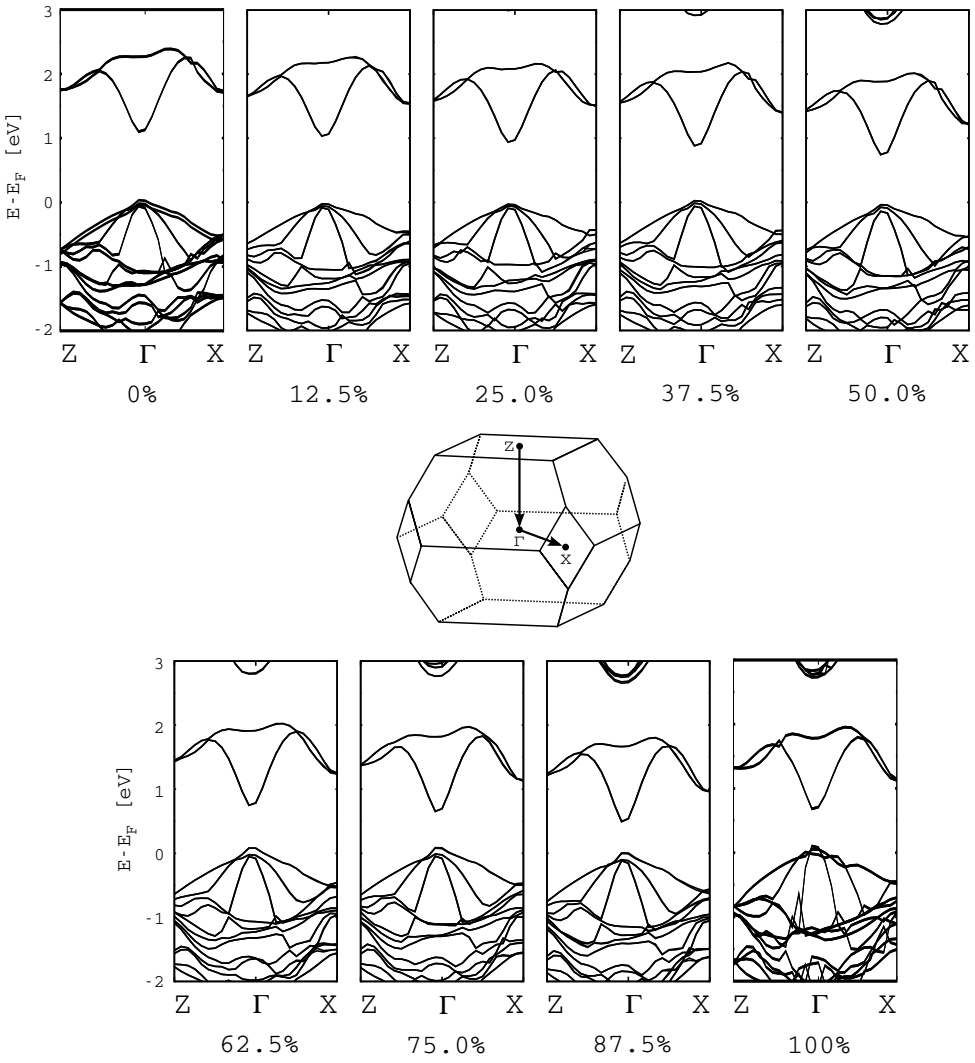

Figure 3.10: HSE06 band structures for selected CZTSSe alloys with the optimized PBE-structure, whereby always the low energy alloy pattern is shown.

A quantitative analysis of the band gap E_g is given in fig. 3.11. The PBE functional shows a random distribution of band gaps, whereby the pure compounds show a band gap of 0.064 eV and 0.033 eV. The alloy fractions in between tend to lower band gaps than the pure systems. Overall the PBE functional shows only the tendency to a lower band gap than CZTS, whereby the different alloy fractions show no consistent behavior. By introducing non-local screened HF-exchange via the HSE06 functional a clear trend can be observed, in which the band gap decreases linearly from 1.17 eV to 0.66 eV, which are the band gaps of CZTS and CZTSe respectively. As with the PBE functional, the HSE06 band gaps reveal a span of band gaps within an alloy fraction, referred to as *band gap fluctuations*, which are in the range from 0.015 eV to 0.030 eV over all alloy fractions. With respect to the systematic error of the PBE-structure of -0.3 eV, the values show an excellent agreement with the experimental band gaps of CZTS and CZTSe [79, 80].

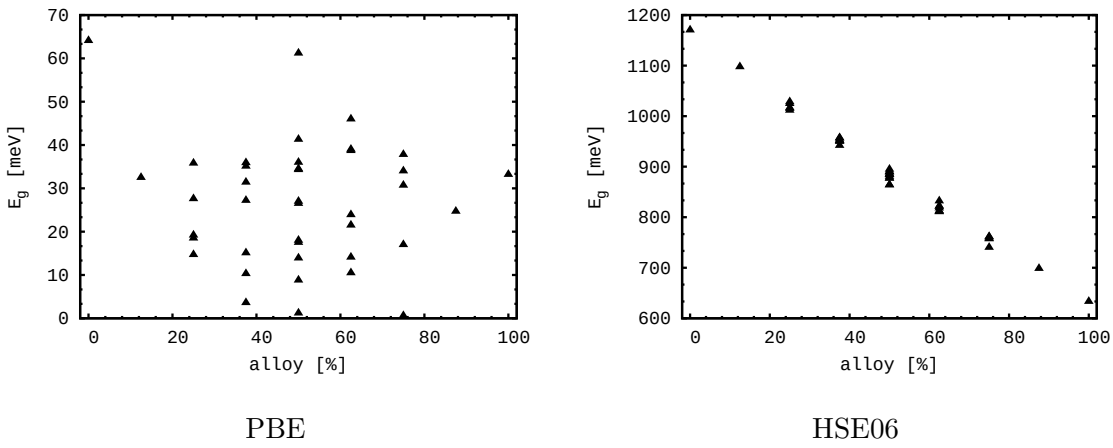

Figure 3.11: PBE and HSE06 band gap of the different alloy fractions. The HSE06 band gaps are given at the PBE-structure.

The decreasing band gap with increasing alloy fraction is an effect of the increasing cell volume upon alloying, as seen before in the bulk in sec. 3.2. However, within an alloy fraction, it is unclear if the varying band gaps are due to different cell volumes or due to different alloy patterns. The largest fluctuations in lattice parameters are observed in the 50 % alloy fraction, since it yields the highest amount of different structures. The structures with the lowest and highest band gap of alloy fraction 50 % show two distinct anion patterns (see fig. 3.12). The highest band gap structure (b) shows in every plane one S and one Se atom, whereas the lowest band gap structure (a) shows both the S and Se clustering two neighboring planes.

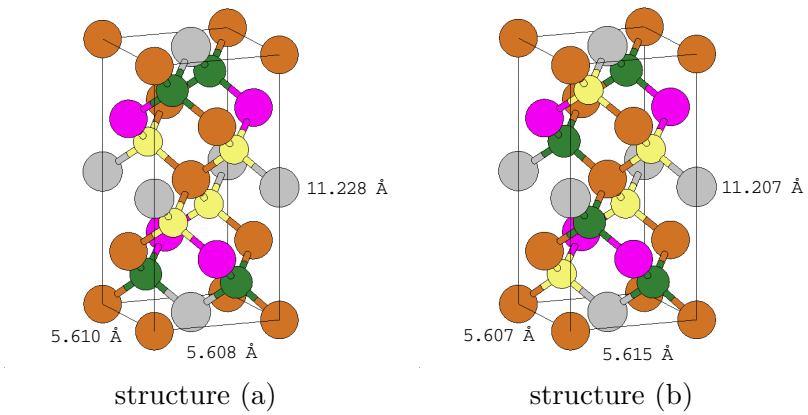

Figure 3.12: Two $CZTS_2Se_2$ alloy structures with the lowest band gap in structure (a) and the highest band gap in structure (b). Zn is shown in pink, Cu in brown, Sn in gray, S in yellow and Se in green.

A closer analysis of the HSE06 DOS for both structures in fig. 3.13 reveals the reason for the smaller band gap of structure (a) (0.864 eV) than structure (b) (0.895 eV). The conduction band of structure (a) is stronger shifted to lower energies, which results in a smaller band gap than structure (b). In contrast to the expectation that S and Se are solely responsible for this shift, the DOS reveals that the shift of the conduction band is due to minimal shifts of the Sn-5s and S-3p states to lower energies. It is further shown that in structure (a) due to the alloy pattern, the electronic structure of the different atom types are not identical anymore, which leads to atomic DOS fluctuations. This is especially seen in the Cu atoms, which deviate in the valence band in contrast to structure (b). Since the cell volumina of both structures are not equal, a clear contribution of the alloy pattern or cell volume can not be answered yet, while a strong indication on the influence of the alloy pattern is given.

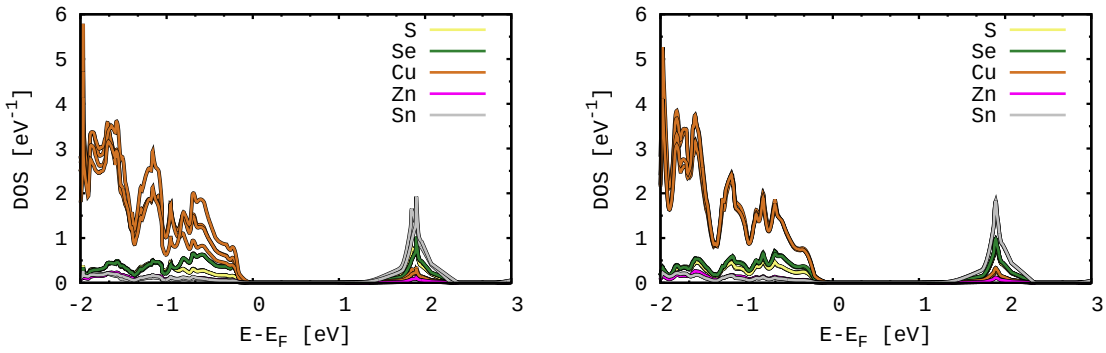

Figure 3.13: $CZTS_2Se_2$ HSE06 DOS for the highest and lowest band gap structures at the PBE-structures. Furthermore, in structure (a), the different Cu atoms are not equal anymore with respect to the DOS.

A clear correlation between the band gap of one alloy fraction and the cell volume within this fraction should reveal a linear behavior of the band gap as a function of the cell volume. The band gap as a function of the cell volume is shown in fig. 3.14 for all alloy fractions and for $CZTS_2Se_2$ in particular, since it shows the strongest band gap fluctuations of all fractions. The left graph shows the linear increase of the cell volume with linear decrease of the band gap, whereby for nearly every alloy fraction there is a distribution of band gaps with a distribution of cell volumes. In a first approximation the band gap correlates clearly linearly with the cell volume in the left graph for all alloy fractions. If the band gap is solely dependent on the cell volume, the same linear trend should be observed also for one selected alloy fraction. The alloy fraction 50 % shows no correlation between the cell volume and the band gap, which is also shown in all other alloy fractions (right graph, fig. 3.14). In conclusion two main trends influence the band gap. The strongest influence on the band gap is given by the increasing cell volume upon alloying, whereby the band gap decreases with increasing Se amount. However,

within an alloy fraction this clear correlation is not shown, whereas the fluctuations rather result out of different alloy patterns than different cell volumes. Furthermore, the cell volume change within an alloy fraction is small compared to the total change of cell volume for all alloy fractions.

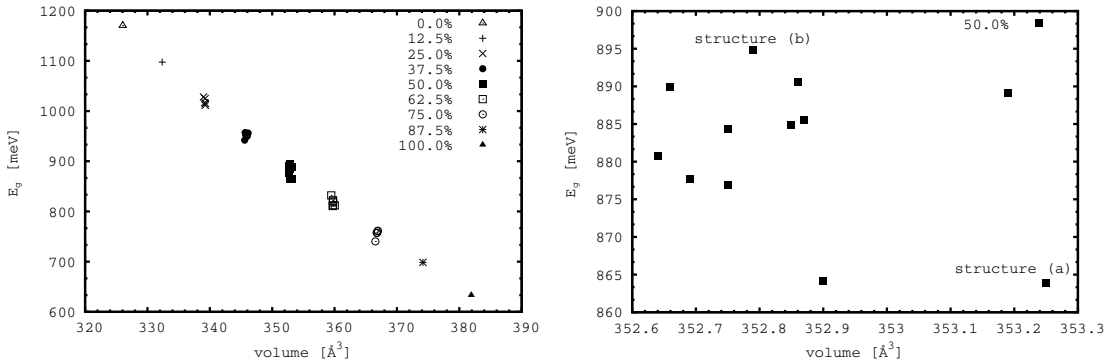

Figure 3.14: The HSE06 band gaps of CZTSSe alloys as a function of the cell volume are shown in the left graph. The right graph shows the band gap distribution in the $CZTS_2Se_2$ alloy with respect to the cell volume. The PBE-structures are always used.

In summary the theoretical studies have shown that by alloying CZTS and CZTSe the band gap can be linearly engineered to fit an optimal band gap for the application in thin film solar cell. With increasing Se amount the lattice expands due to larger Se atoms and the Bader charges of the cations start to decrease. Furthermore, since there are different binding motifs possible in CZTSSe alloys due to two different anion types, the cations show charge fluctuations within an alloy fraction. These different binding motifs and different lattice parameter within an alloy fraction result in a distribution of slightly different DOS rather than one distinct DOS for an alloy fraction. The electronic structures of the alloys reveal a linear decrease of the band gap with increasing Se amount, while this linearity is only seen with the HSE06 hybrid-functional. As in the CZTS and CZTSe bulk systems, this linear decrease of the band gap of an alloy fraction is strongly influenced by the enlargement of the lattice constants. The band gaps fluctuate up to 0.03 eV within alloy fraction 50 %, which is primarily introduced by different alloy patterns rather than the different cell volumes within the alloy fraction. In comparison to the total decrease of the band gap of 0.5 eV, this fluctuation is rather small and therefore only of minor importance. In addition to the DOS, the band structure reveals a similar band topology like bulk CZTS and CZTSe, whereby the main changes are seen in the shift of the conduction band to lower energies. The direct band gap hereby is still located at the Γ-point. The smaller band gaps are not solely a result of S-3p and Se-4p shifts but are also influenced by shifts of Sn-5s states to lower energies due to different binding motifs in the alloy patterns.
The theoretical investigations can help experimentalist to construct solar cells with higher efficiencies and a general better performance. From these results it can be

predicted that the maximal efficiency after the Shockley-Queisser limit can be reached with a band gap of 1.1 eV to 1.3 eV, which corresponds to an alloy fraction of 37.5 % to 62.5 % in which the systematic error of the PBE-structure is included. Furthermore, in experimental solar cells, slight band gap fluctuations are to be expected due to a varying material quality due to the different alloy patterns within an alloy fraction. Since an experimental sample consist of a variety of unit cells, depending on the arrangement of the alloy patterns the band gap fluctuations may average out in total or may also increase to values larger than the calculated 0.03 eV. These band gap fluctuations may contribute to the experimentally observed low open-circuit voltages [113], but due to their small dimension, most probably there is a further contributor. A first hint on a further possible influencing factor is given by the occurring disorders in experimental samples. The disorders often occurs on the 2c/2d Wyckoff positions, which are occupied by electronically similar Cu and Zn atoms. Therefore, in the following section the focus is set on 2c/2d disordered CZTS systems.

3.4 Band Gap Fluctuations in 2c/2d Disordered Cu_2ZnSnS_4

The promising material properties of CZTS and CZTSe are often tarnished by a varying quality of the samples and resulting in efficiencies below the theoretical maximum. A challenge while preparing the samples is the often occurring different defect types in the lattice system, which are a possible interference factor for efficiently performing CZTS and CZTSe solar cells. Especially a wide-spread industrial production is disrupted, since the properties of these defective structures can not be predicted accurately. The stoichiometric and off-stoichiometric CZTS and CZTSe samples hereby often suffer from several types of defects like self compensating defect clusters, such as [V_{Cu}+Zn_{Cu}], [2 Cu_{Zn}+Sn_{Zn}] and [Zn_{Sn}+2 Zn_{Cu}] [109]. V_{Cu} denotes a vacancy at a Cu position in the lattice and Zn_{Cu} are antisites, in which in this example a Cu is substituted with Zn. One of the most prominent defects are Cu_{Zn} and Zn_{Cu} antisite disorders, which occur at the 2c and 2d Wyckoff positions, normally occupied by Cu and Zn respectively. In recent times these disorders were closer investigated by researchers, since they are a possible candidate for the band gap fluctuations and resulting unexpected low open-circuit voltages of the solar cell samples [111–113]. However, the reason why these disorders may influence the electronic structure is not yet fully understood. For a deeper understanding, this problem has to be approached from the experimental as well as the theoretical side. An important first step for an experimental control of the disorders and a reliable base for an industry production was given by Ritscher et al. in 2016. They have shown that the 2c/2d disorders can be controlled by the annealing time and temperature [114]. On the basis of these experimental investigations the second crucial step is gaining a theoretical understanding for the changes of the electronic structure. In the following section the theoretical investigations will focus on the influence of different disorder degrees and patterns on the electronic structure of CZTS. With the combination of the experimentally controlled disorders and theoretical understanding of the influences, a path is partially cleared for an extensive application of CZTS thin film solar cells.

3.4.1 Disorder Model

In the CZTS bulk system, several disorder degrees and structural disorder patterns are possible at the 2c and 2d Wyckoff positions, in the following referred to as *disorder fraction* and *disorder pattern* respectively. To account for a fine grid of different disorder fractions and patterns, in the applied disorder model the normal tetragonal kesterite unit cell with 16 atoms is expanded to a 2x2x1 supercell with 64 atoms. Thus, the disorders can be introduced within two separated 2c/2d planes to account for horizontal and vertical disorders patterns (see fig. 3.15).

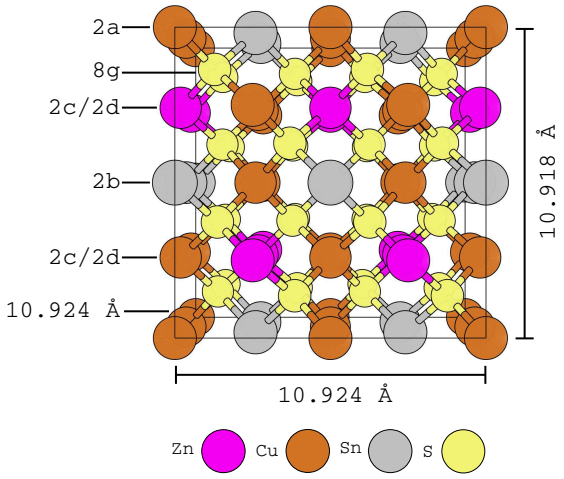

Figure 3.15: Applied disorder model with a 2x2x1 supercell. There are two possible 2c/2d planes, on which the disorders can be introduced. Within these two planes there are 16 possible atom positions, which have to be occupied by eight Zn and eight Cu atoms to retain the stoichiometry.

Within the two disorder planes, 16 positions are available for eight Zn and eight Cu atoms. Accounting for all possible disorder fractions and patterns, this leads in total to 12870 different possible structures via binomial coefficients. Since these calculations at DFT level are rather demanding, these structures are reduced to symmetry independent structures by applying the solid solution module of the CRYSTAL14 program package [198, 199]. By this symmetry analysis a total of 910 structures remain, which are categorized from 0 % to 100 % in 12.5 % steps. Upon disordering different disorder fractions and patterns are obtained. A disorder fraction of 50 % results in a change of eight out of 16 atom positions, in which eight positions are kept fixed and the other eight positions are disordered while remaining the stoichiometry. Upon creating the disordered system, all unit cells will contain the same stoichiometry for a valid comparison, since off-stoichiometric structures lead to a strong deviation in the electronic structure. For every disorder fraction, different structural disorder pattern are possible, which have to be accounted for due to a potential influence on structural and electronic properties. The distribution of the 910 disordered systems into the different disorder fractions is shown in tab. 3.6.

Table 3.6: Number of structures obtained by a symmetry reduced structural analysis for different disorder fractions.

disorder fraction [%]	0.0	12.5	25.0	37.5	50.0	62.5	75.0	87.5	100.0
disorder patterns [#]	1	6	62	214	344	214	62	6	1

The disorder fractions higher than 50 % should result in the same structures as the disorder fractions lower than 50 % due to the crystal symmetry. The disorder fractions higher than 50 % were initially investigated to research the computational accuracy of

the calculations, since small structural changes can lie within numerical fluctuations occurring in the computations. Without this test small lattice changes therefore may otherwise be interpreted as a physical phenomenon rather than solely existing due to numerical fluctuations. The electronic structures of Cu and Zn resemble with the assumption of Cu^+ and Zn^{2+} ions, but show differences in the binding lengths to S atoms. The calculations on the 1x1 unit cell reveal binding lengths of 2.365 Å and 2.315 Å for Zn_{2d}-S and Cu_{2c}-S respectively. Due to these minor differences in binding length, the disordered structures are structurally fully optimized, internal and external lattice parameters, to account for a computational equilibrium structure, leading to relaxed lattice constants and relaxed environments surrounding the disordered positions. All starting structures are tetragonal supercells, in which a distortion to an orthorhombic supercell during the structure optimization is allowed. With this applied disorder model structural and electronic changes upon disordering are investigated in the following sections.

3.4.2 The Influence of 2c/2d Disorders on the Cu_2ZnSnS_4 Structure

The studies on the bulk CZTS/CZTSe systems and the CZTSSe alloys have shown that the structural parameters crucially affect the electronic structure of the material. The minimal differences in binding lengths between Zn_{2d}-S and Cu_{2c}-S result in the structure optimization in changes in the lattice constants, since the system tries to minimize the stress introduced by the disorders. The lattice constants and the resulting cell volume as a function of the disorder fraction are shown in fig. 3.16 for all calculated disorder patterns, whereby the full tabularly data can be found in app. A.
Since every disorder fraction includes several disorder patterns, for every disorder fraction several lattice parameters are obtained. The lattice constants a, b and c reveal a similar trend, which shows an overall tendency to slightly larger lattice constants upon disordering. In general the mean lattice constants of every disorder fraction increases up to disorder fraction 50 %, whereby larger disorder fractions show decreasing mean lattice constants up to the fully ordered structure at 100 %. The maximum variation of lattice parameters is shown in disorder fraction 50 %, since the high amount of disorder patterns increases the possibility of a larger lattice parameter spread. The data further visualizes that the distribution of the lattice constant a and b is nearly identical with minor deviations. In the lattice constant c the disorder fractions smaller and higher than 50 % are not fully symmetric with respect to the disorder fraction 50 %, which is a result of the computational inaccuracy during the structure optimization. As a direct consequence of the change of the lattice parameters a, b and c, the mean cell volume of every fraction increases up to a disorder fraction of 50.0 %, whereas over 50.0 % disorder the mean cell volume decreases again. The fully ordered structures at 0 % and 100 % disorder fraction should yield from a chemical point of view the same lattice parameters. Their difference after the structure optimization can be regarded

as the computational accuracy for the structure optimization process. The difference of 1.75 Å^3 in cell volume between the two structures is in total about 30 % of the maximum volume increase of 6 Å^3. The mirrored structural behavior of disorder fractions lower and higher than 50 % show that the structures are identical and within the computational accuracy. Therefore, a detailed discussion of the disorder fractions higher than 50 % is not required in the following sections within the computational accuracy.

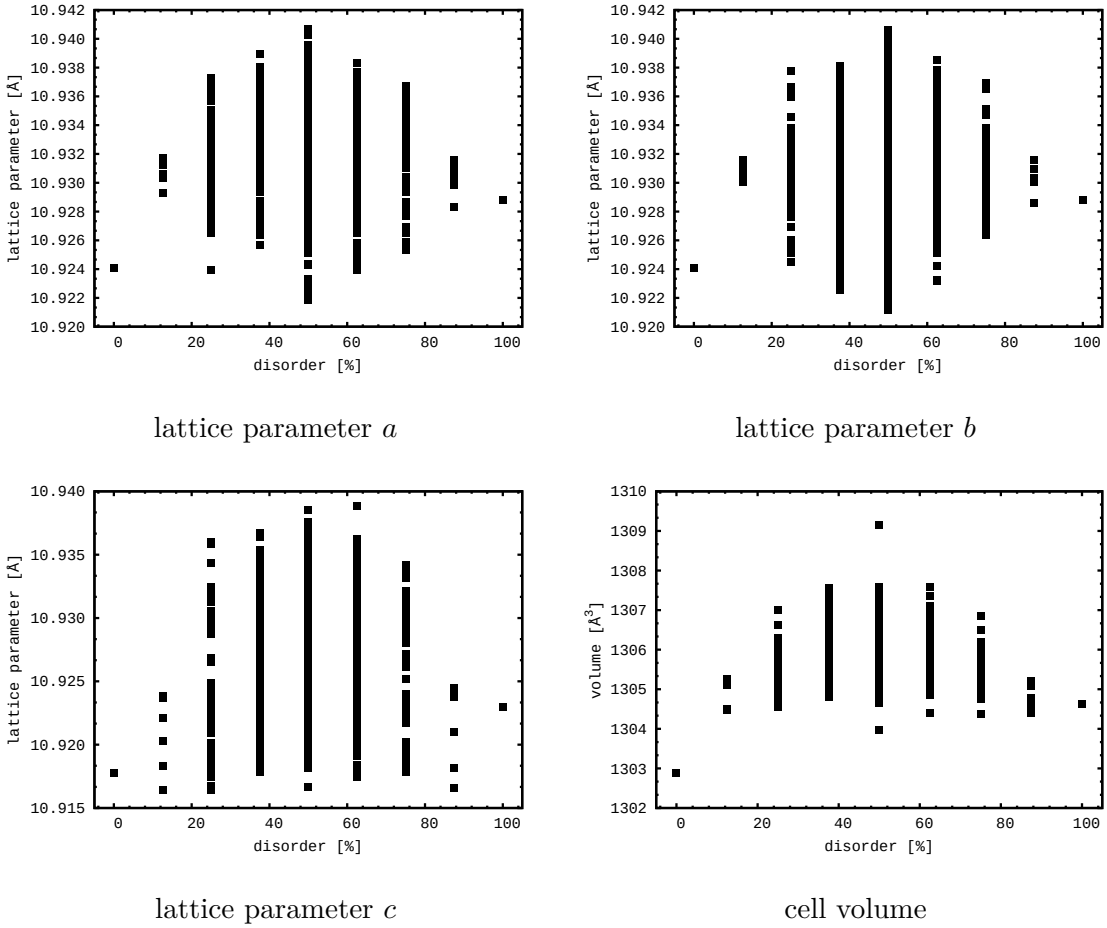

Figure 3.16: Lattice constants and cell volume as a function of the disorder fraction, as obtained by PBE structure optimizations.

A closer investigation of the 50 % disorders shows two exceptions within the cell volume distribution, which strongly stand out of the range of cell volumes (see fig. 3.17). The highest cell volume of 1309.14 Å^3 is shown by structure (b) where a full separation of Cu and Zn atoms in two different planes occurs. Structure (c) is similar to the fully ordered structure, whereby only the lower half of the structure is rotated by 90°. This rotation leads to the structure with the lowest cell volume of 1303.98 Å^3 for the disorder fraction of 50 %. Only the fully ordered structure (a) exhibits a smaller cell volume with 1302.88 Å^3. The last selected structure (d) shows a cell volume of 1305.53 Å^3, which

lies in between structure (b) and structure (c). Structure (d) is chosen as an example for a structure with a cell volume in between the extrema, whereby the investigated electronic structure in the next section shows correlations between ionic and electronic structure.

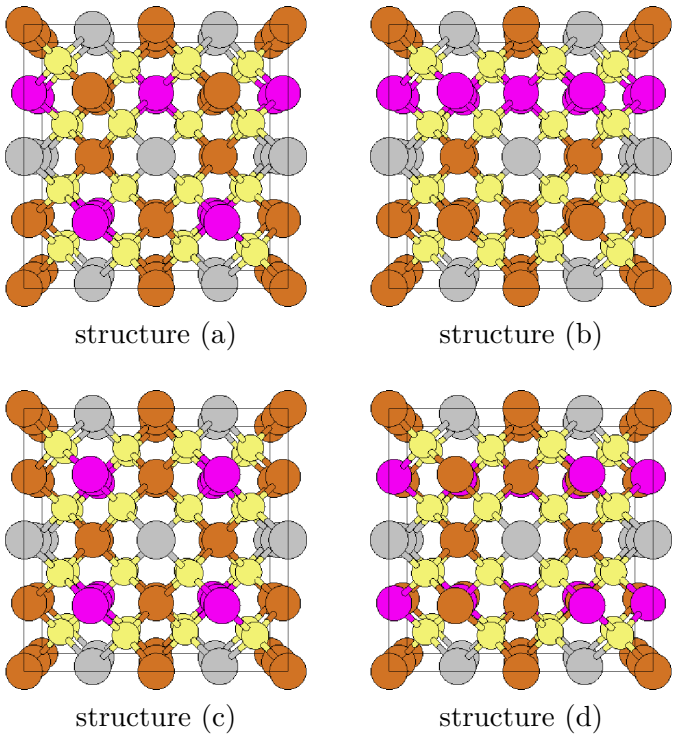

Figure 3.17: Different disordered structures with 50 % disorders are illustrated. Structure (a) shows the fully ordered structure, whereas structure (b)-(d) display structures with the same disorder fraction of 50 % but different disorder patterns. Zn is shown in pink, Cu in brown, Sn in gray and S in yellow.

The structural differences are a result of different binding lengths between Cu_{2a}, Sn_{2b}, Cu_{2c}, Zn_{2d} and S (see fig. 3.18). In structure (a) and (c) there is only one structural pattern in which S is bound to one Cu_{2a}, one Sn_{2b}, one Cu_{2c} and one Zn_{2d} (denoted as S-(Cu_{2a},Sn_{2b},Cu_{2c},Zn_{2d})), referred to as *binding motif* in the following. Upon a stronger disordering in structure (b) and structure (d) two new binding motifs are created:

- S-(Cu_{2a},Sn_{2b},Zn_{2c},Zn_{2d}),
- S-(Cu_{2a},Sn_{2b},Cu_{2c},Cu_{2d}).

The binding lengths in the binding motif of structure (a) are taken as a reference. In structure (b) the binding lengths between Cu_{2c}-S and Zn_{2d}-S remain, whereby the disordered binding lengths Zn_{2c}-S and Cu_{2d}-S relax to the same values as the ordered Cu_{2c}-S and Zn_{2d}-S. Remarkable are the changes of Cu_{2a}-S and Sn_{2b}-S, which increase when bound to S-(Zn_{2c},Zn_{2d}) and decrease when bound to S-(Cu_{2c},Cu_{2d}). The same

behavior is shown in structure (d) for the binding lengths of S-Sn_{2b} and S-Cu_{2a}. In contrast to structure (b), S-(Zn_{2c},Zn_{2d}) increases by 20 mÅ and S-(Cu_{2c},Cu_{2d}) decreases by 20 mÅ in structure (d).

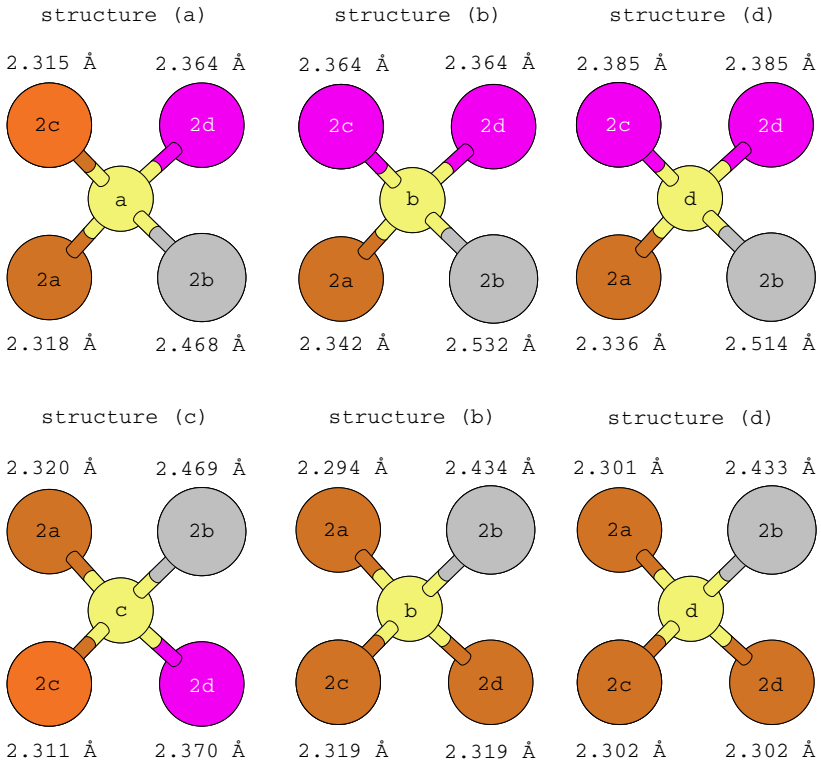

Figure 3.18: Different binding motifs and lengths of the four selected structures after the optimization at the PBE-level are shown. Zn is shown in pink, Cu in brown, Sn in gray and S in yellow.

The minimal changes in binding lengths in the different binding motifs summarize to noticeable changes in lattice parameter as seen before. The change of the structural parameters lead to different relative stabilities of the structures. The relative energies of the calculated structures are presented in fig. 3.19, whereby the total energy of the fully ordered structure is taken as reference energy. Overall the relative energies reveal that the introduction of disorders into the CZTS lattices costs energy. The required energy increases up to 1 eV at 50 % disorder fraction and then decreases to 100 %, which is as stable as the fully ordered structure. As in the cell volume, the relative stabilities of the disorder fraction lower and higher than 50 % are identical. The relative energies reveal the same ordering as observed in the cell volume for structure (a)-(d). Structure (c) shows the lowest relative energy, which is nearly as stable as the fully ordered structure, since a slight reordering of structure (c) to structure (a) needs less energy than a fully separated structure like structure (b). The highest cell volume in structure (b) also leads to the highest relative energy of over 1 eV in total. As in the cell volume, structure (d) is in between the selected extrema. The relative energies have to be compared with care, since this energetic ordering can be a result of different

basis set qualities.

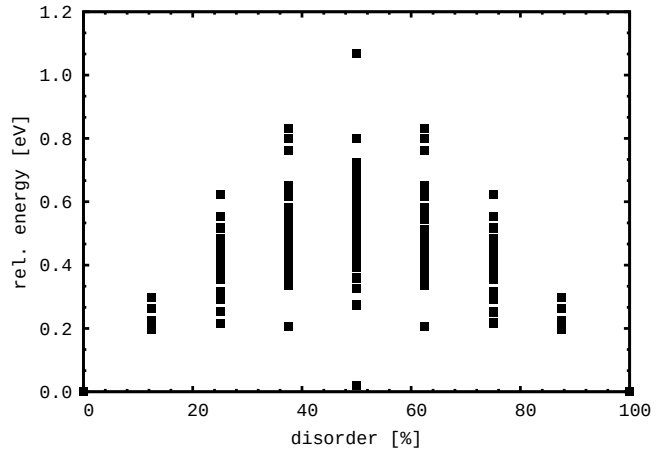

Figure 3.19: Relative energy of the disordered structures as a function of the disorder fraction with reference to the fully ordered structure. The relative energies are calculated at the PBE-level.

With constant energy cutoff of the plane waves, the basis set quality changes with changing cell volume, possibly resulting in energy differences which solely exist due to the computational parameters. Therefore, the energetic change with varying cell volume for structure (b) with the highest cell volume gives information about the influences of cell volume on the total energy, illustrated in fig. 3.20. The volume scan reveals that the unit cell energy varies about 0.021 eV within the boundaries of calculated cell volumes of structure (a) and structure (b). Hereby the lower cell volume leads to less stable structures, which is indicated by higher unit cell energies. Increasing the cell volume to values larger than the computational equilibrium value of 1309.14 $Å^3$ leads to slightly more stable structures, which is an effect of the changed basis set quality.

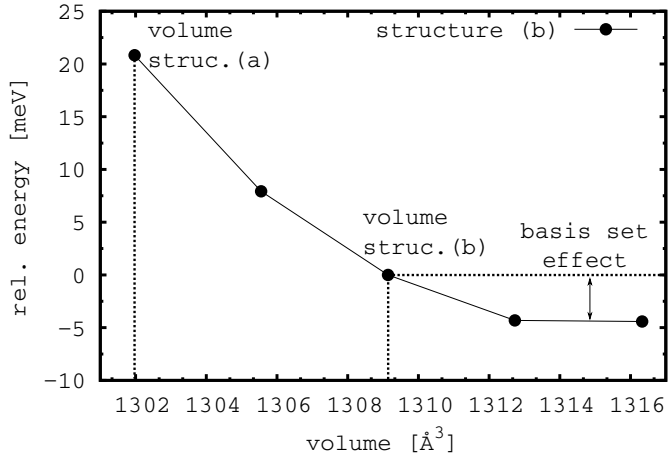

Figure 3.20: Total energy of structure (b) as a function of the cell volume at the PBE-level. The cell volume in the equilibrium is set to zero, whereby the cell volume is changed within the magnitude of the observed cell volume changes upon disordering.

These small changes are over a magnitude smaller than the calculated energy differences shown in fig. 3.19 and are therefore only of small importance. In comparison to experiment, small theoretical energy differences have to be considered with care, since the calculated structures are treated at 0 K in the vacuum. At normal conditions with 298 K and 100 kPa air pressure, the structural properties in experiment are influenced by thermodynamic effects like lattice vibrations and entropy. Small energy differences observed in the calculations may therefore not be present in experimental studies.
A link between ionic and electronic structure are the atomic charges, which are determined here by a Bader charge analysis (see fig. 3.21). All atom types show a set of different charges within a disorder fraction, which is due to different disorder patterns, referred to as *charge fluctuations* in the following. In the fully ordered structure Cu shows an atomic charge of 0.477 e, Sn of 1.382 e, Zn of 0.849 e and S of -0.796 e, referred to as *reference charges*.

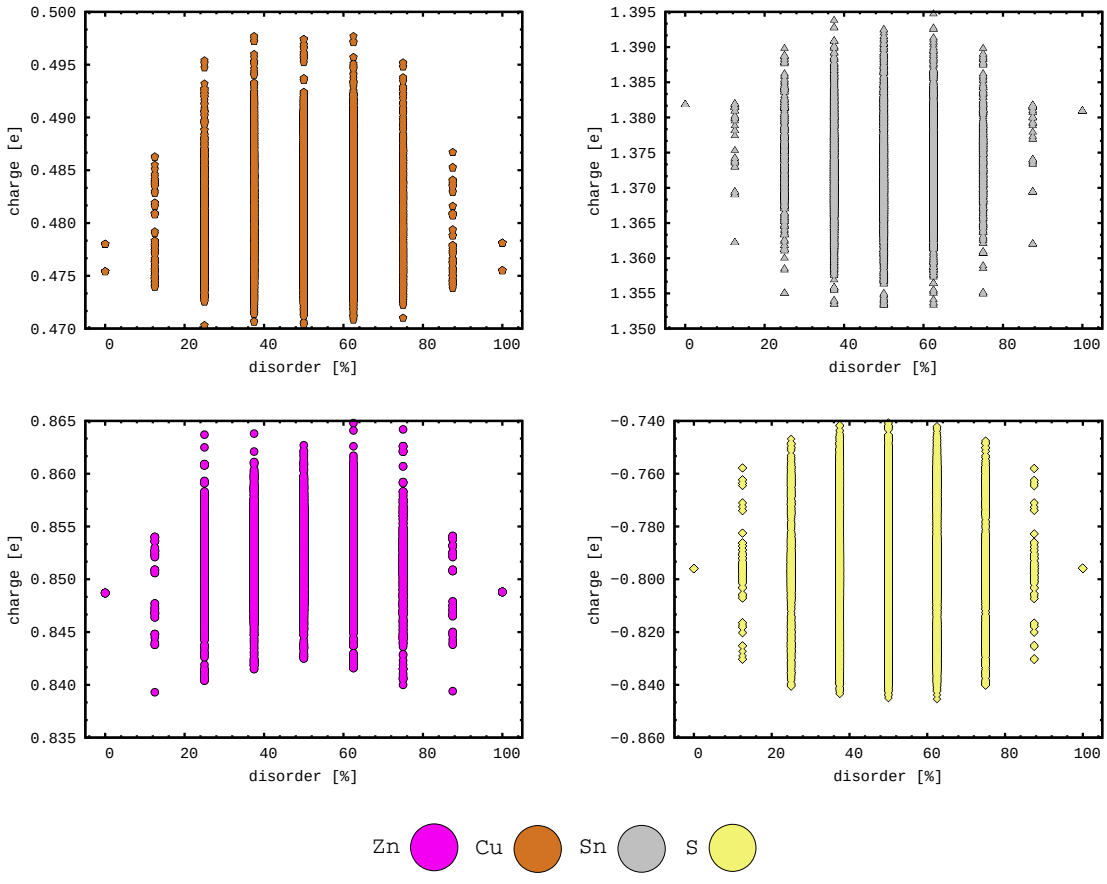

Figure 3.21: Bader charges for all calculated CZTS 2c/2d disordered systems as a function of the disorder fraction at the PBE-level. For every disorder fraction all charges of all disorder patterns are shown, resulting in a variety of charges for each atom type and disorder fraction.

Upon disordering, Cu exhibits charges including all disorder fractions from a minimum of 0.470 e to a maximum of 0.498 e. Zn shows over all disorder fractions atomic charges in a span from 0.839 e to 0.865 e and Sn from 1.353 e to 1.395 e. Therefore, the cationic charge fluctuations span only a range of 0.028 e for Cu, 0.026 e for Zn and 0.042 e for Sn. In contrast the charge fluctuations with S are 0.104 e from -0.741 e to -0.845 e, which is 2-4 times higher than the cations. Averaging over all disorder fractions, the mean Bader charges nearly stay identical (see full statistical analysis in app. A). Disorder fractions 25.0 % to 50 % show similar minimum and maximum charges, whereby the charge range is distinctly smaller in the disorder fraction 12.5 %. The disorder therefore introduces charge fluctuations within the unit cell, which vary depending on the disorder fraction.

The analysis of the previously selected 50 % structures give further insight on the charge fluctuations. The influence of the different binding motifs on the atomic charges is illustrated in fig. 3.22 for structure (a)-(d). Structure (a) and (c) show both for cations and anions identical charges, which is due to the similarity of the structures. Since there is only one binding motif, the atomic charges are consistent for every atom type. The high volume structure (b) shows a charge split from -0.757 e to -0.830 e with respect to the horizontal 2a/2b plane in the middle of the unit cell. S in the top half of the unit cell, bound to two $Zn_{2c,2d}$, Cu_{2a} and Sn_{2b}, shows more negative charges than S in the lower half, which are surrounded by three $Cu_{2a,2c,2d}$ and Sn_{2b}. Since Cu shows Bader charges only half as high as Zn, S bound to three Cu typically features lower Bader charges than S bound to two Zn and one Cu. By increasing the complexity of the structural pattern in structure (d), the analysis is aggravated, since a two dimensional cut covers details in depth. The atoms in the back are therefore minimally enlarged for an easier analysis. Structure (d) also shows similar strong charge fluctuations of S from -0.761 e to -0.835 e. The 2c/2d planes in structure (d) show consistent charges for the atom types Zn and Cu each, whereby the S atoms show a charge fluctuation due to different chemical environments. Remarkable are the two different 8g planes, one with uniformly charged S atoms and one with pairwise alternating charges, which is due to the different disorder patterns. Altogether the Bader charge analysis shows a correlation between the binding motifs and the charge fluctuations within the unit cell. With decreasing amount of binding motifs close to the ones in the ordered structure (a) (S-$Cu_{2a}Sn_{2b}Cu_{2c}Zn_{2d}$), the Bader charges start to fluctuate within the unit cell. The binding motifs S-$Cu_{2a}Sn_{2b}Zn_{2c}Zn_{2d}$ and S-$Cu_{2a}Sn_{2b}Cu_{2c}Cu_{2d}$ lead to strongly deviating charges from the ordered binding motif. The first binding motif leads to more negatively charged S and the second one to more positively charged S, whereby the charges are up to 0.1 e apart. Therefore these disorders lead to charge transfers within the unit cell depending on the binding motif.

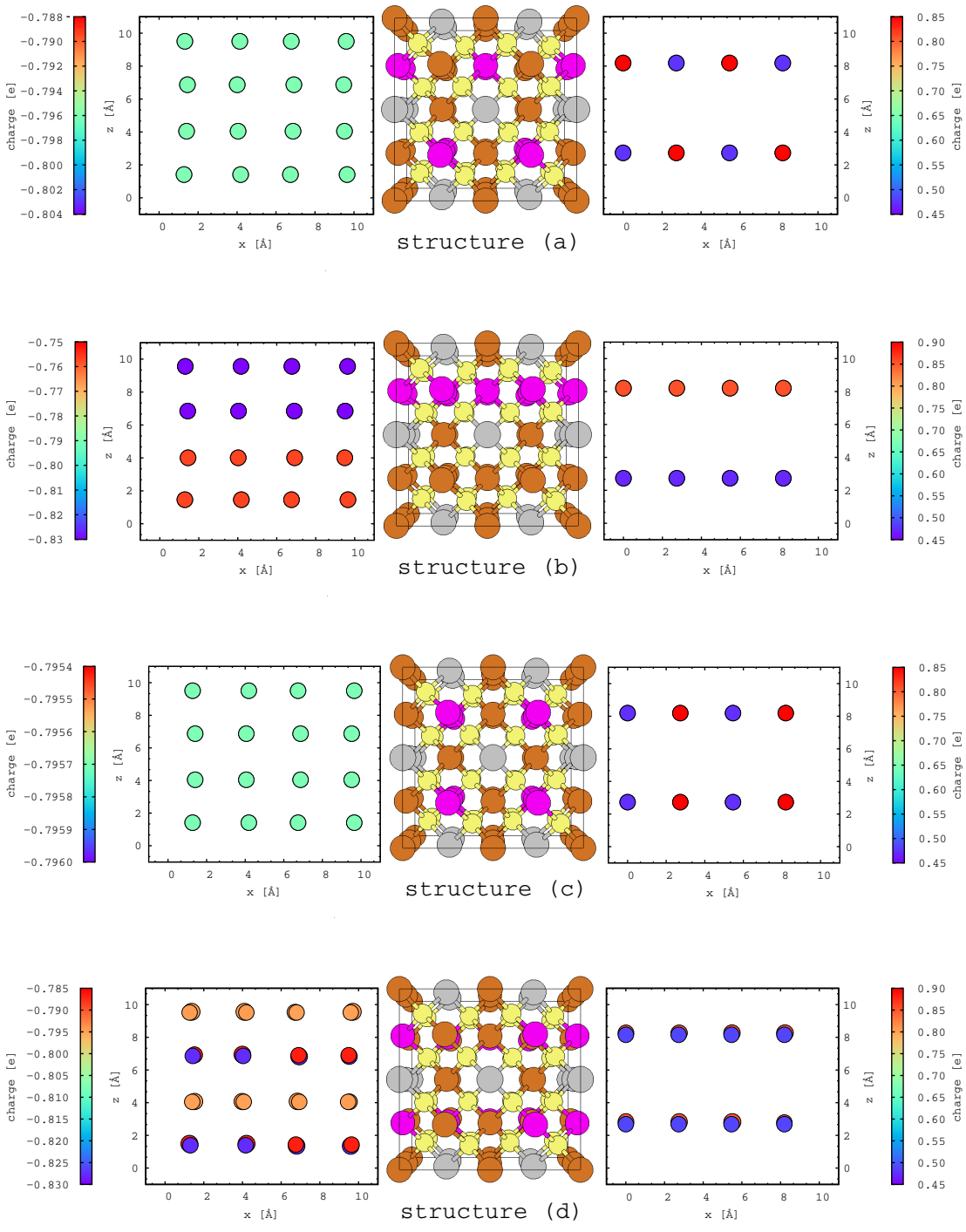

Figure 3.22: Structures and Bader charges for the selected CZTS 2c/2d disordered systems at the PBE-level. Zn is shown in pink, Cu in brown, Sn in gray and S in yellow.

Summarizing the structural trends in all disorder fractions and especially the three selected 50 % disorder structures, a correlation between the different structural parameters can be observed. Upon disordering, the lattice constants, and as a result the cell volume, slightly increase and vary within a disorder fraction due to the disorder patterns. Up to 50 % disorder fraction the mean lattice parameters increase, whereby after 50 % they start to decrease again, overall staying larger than the fully ordered structure. Corresponding disorder fractions (12.5 % and 87.5 %, 25.0 % and 75 %, 37.5 % and 62.5 %, 0 % and 100 %) show identical properties due to chemical equality, whereby minor differences are due to computational inaccuracies. The relative stabilities show that an introduction of disorders requires energy, which varies within each disorder fraction. The mean relative energy for every disorder fraction increases up to a disorder fraction of 50 %. As a result of the slightly distorted structures due to different Zn_{2d}-S and Cu_{2c}-S binding lengths, the Bader charges reveal charge fluctuations within the unit cell, which are due to newly formed binding motifs. The three selected disorder structure at 50 % show that a high cell volume leads to a high relative energy and high charge fluctuations, whereas the opposite holds true for the minimal cell volume structure. In comparison to experimental samples, the theoretical data has to be averaged for every disorder fraction, since in experimental samples only the disorder fraction is known. In a crystal sample there are several different disorder patterns present, which are not determinable experimentally. With this theoretical knowledge about the structural changes upon disordering, the focus is set on the change of the electronic structure in the next section.

3.4.3 Electronic Structure of 2c/2d Disordered Cu_2ZnSnS_4

An experimental limitation in the CZTSSe thin film solar cells are the low open-circuit voltages. Experimentalist and theoreticians conjecture about the origin of these low open-circuit voltages and have focused on the 2c/2d disorders as a possible key factor. With the observed minor changes in the lattice parameter and Bader charges in the previous section, the question arises how these deviations affect the electronic structure, which is analyzed in form of the DOS. Concluding from the structural analysis, the analysis of the electronic structure is performed for every disorder fraction as well as for the disorder patterns with different binding motifs. The DOS for every disorder fraction at the PBE-level is shown with the DOS of the fully ordered system as a reference system in fig. 3.23. For every disorder fraction a distribution of DOS is obtained rather than one unique DOS, which is a result of the high amount of different disorder pattern. In general the electronic structure of the disordered systems is similar to the ordered one in terms of atom and orbital contribution to the DOS (see sec. 3.2). The overall changes mainly occur in the valence and conduction band, which are slightly shifted with reference to the Fermi energy of every structure.

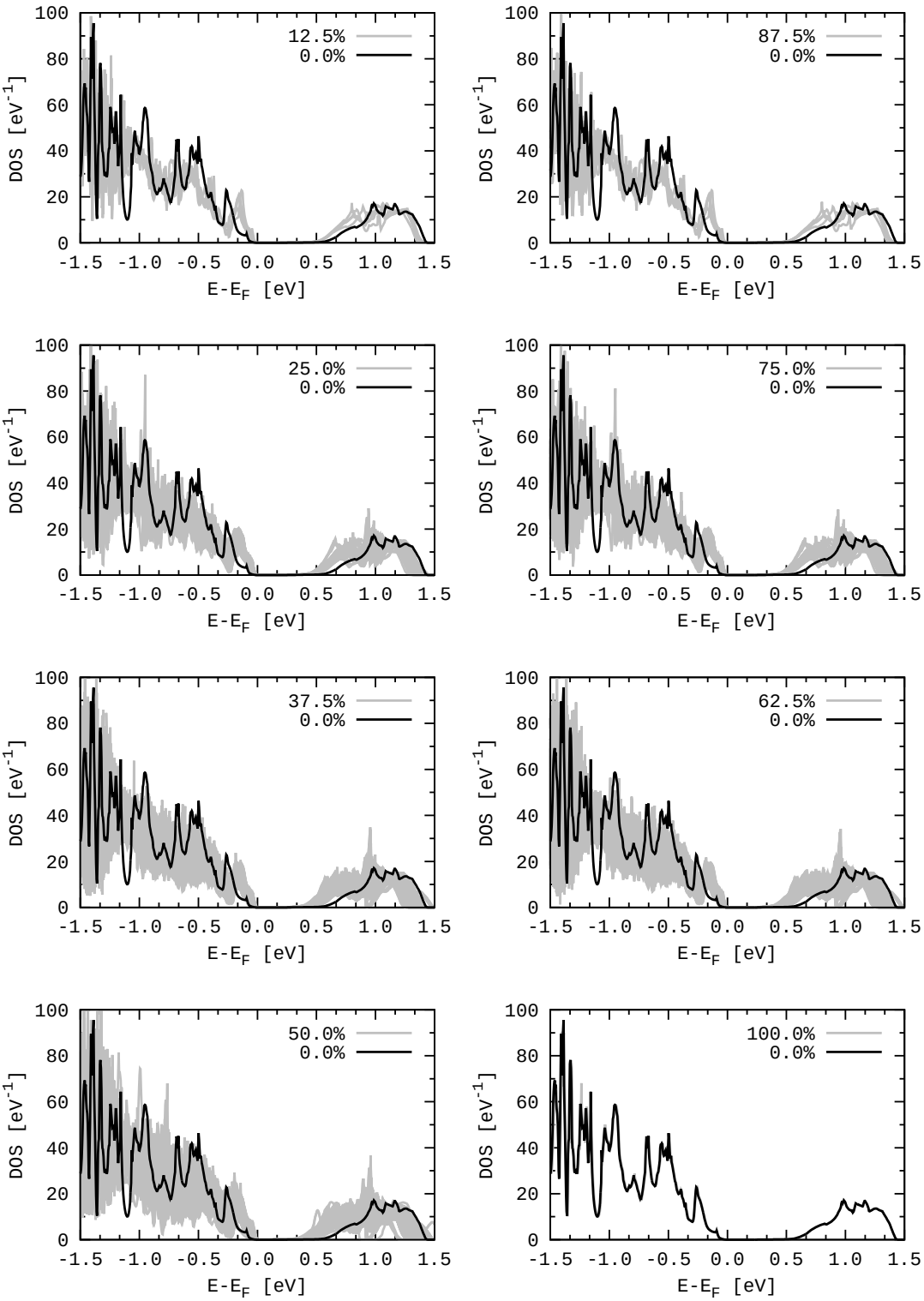

Figure 3.23: Total PBE DOS for all calculated disorder fractions. The fully ordered structure is taken as a reference system. For every disorder fraction all disorder patterns are shown.

The general trend shows in total a decrease of the band gap with increasing disorder fraction, whereby for every disorder fraction a variety of band gaps are obtained due to different disorder patterns. The shape of the valence and conduction band also slightly changes, hence few structures introduce a gap within the first conduction band (see fig. 3.24), which is not present in the ordered system. As in the structural analysis, disorder fractions lower and higher than 50 % yield identical results.

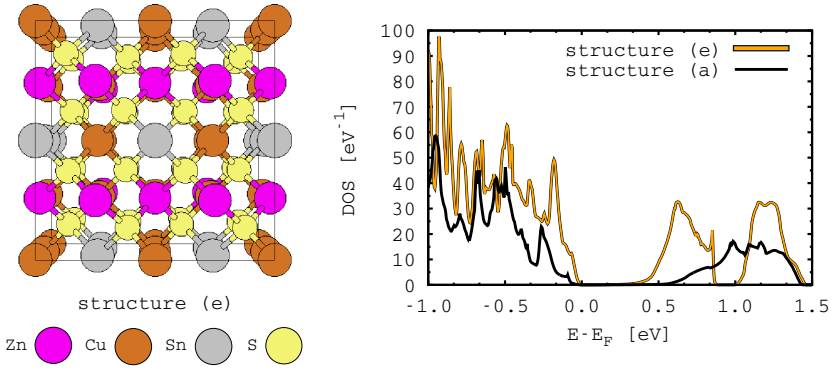

Figure 3.24: Total PBE DOS for a selected 50 % disorder structure, in which an additional gap is introduced within the first conduction bands. The fully ordered structure is taken as a reference system.

Focusing on the PBE band gaps as a function of the disorder fraction, the graph reveals overall a decrease of the band gap E_g upon disordering (see fig. 3.25). The absolute band gap of course strongly deviates from the experimental band gap of 1.5 eV, as previously shown in the research on the bulk system and CZTSSe alloys. Nevertheless, the PBE band gaps show a general trend to lower band gaps when the structure is disordered. Furthermore, several different band gaps within an disorder fraction are obtained due to different disorder patterns, in the following referred to as *band gap fluctuations*.

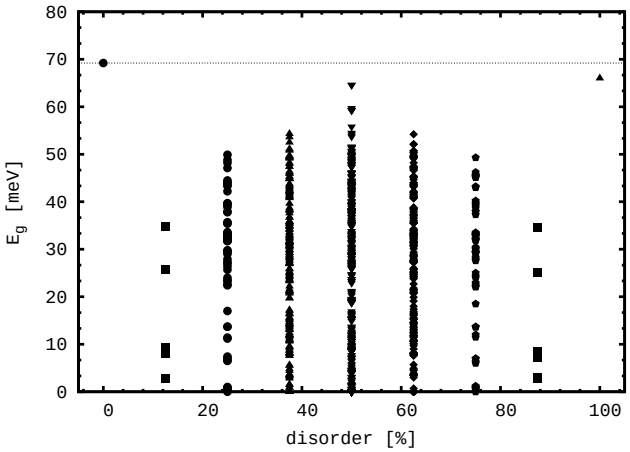

Figure 3.25: Band gap as a function of the disorder fraction at the PBE-level.

Since PBE strongly underestimates the band gap at the Γ-point, the question arises if the band gap fluctuations of 0.07 eV are also in the same magnitude when employing the hybrid-functional HSE06. Therefore, three single point calculations on top of the PBE-optimized structures were performed, whereby for every disorder fraction the structure with highest, lowest and medium band gap were chosen. These band gaps obtained by the HSE06 single point calculations as a function of the disorder fraction are presented in fig. 3.26.

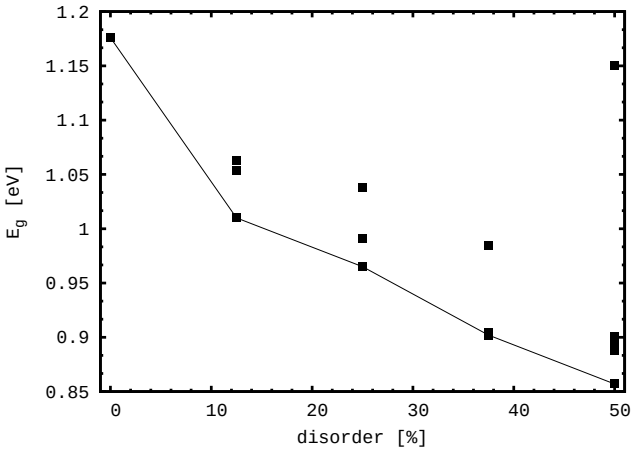

Figure 3.26: HSE06 band gaps obtained by single point HSE06 calculations on top of the PBE-optimized structures for the disorder fractions up to 50 %. Higher disorder fractions are not considered due to the crystal symmetry.

The non-local HF-exchange introduced into the Kohn-Sham approach leads overall to drastically higher band gaps. The ordered structure features a band gap of 1.176 eV, which is equivalent to the band gap in the normal 1x1 unit cell. As investigated previously, the difference between the $HSE06_{PBE}$ and experimental band gap of 1.5 eV lies in the underlying PBE-structure, which systematically lowers the HSE06 band gaps by 0.3 eV. Including this systematic error of the PBE-optimized structure, the corrected HSE06 band gap of 1.47 eV agrees perfectly with the experimental value. Unfortunately, a full HSE06 structure optimization of the 2x2x1 unit cell is not feasible. The selected single point calculations on top of the optimized PBE-structure show that disorder fraction 12.5 % yields a minimal band gap 1.01 eV, which is about 0.176 eV lower than the ordered system. The band gap further decreases in disorder fraction 25.0 % to 0.965 eV, which is a decrease of about 0.211 eV. In disorder fraction 37.5 % and 50.0 % the band gap is reduced to 0.902 eV and 0.857 eV respectively, corresponding to a diminished band gap by 0.274 eV and 0.319 eV respectively. The maximum band gap fluctuation is therefore as high as 0.320 eV for a disorder fraction of 50 %. Since there are disorder patterns within a disorder fraction, which are structurally close to the fully ordered structure like structure (c), the highest band gaps for disordered systems can be close to the fully ordered band gap, which is also seen in the PBE band gaps.

Therefore, the band gap fluctuation within each disorder fraction reach from 1.176 eV of the fully ordered structure to the minimum band gap for every disorder fraction. As a result the mean band gap decrease is estimated to be about 0.160 eV for the 50 % disorder fraction.
Until now the data only reveals a general trend to lower band gaps with increasing disorder degree, whereby the reason for different band gaps within a disorder fraction is not clear yet. Therefore, the previously three selected structures from the structural analysis are closer investigated by HSE06 DOS and HSE06 band gaps, to see if there is a correlation between the electronic structure and the binding motif or cell volume (see tab. 3.7). First of all the band gaps show that structure (a) and (c), which nearly share the same structure, have nearly the same band gap. The structural rotation of the lower half of structure (c) in contrast to structure (a) leads to a small band gap decrease of 0.026 eV. The stronger disorder patterns in structure (b) and structure (d) lead to decreased band gaps by over 0.320 eV to 0.855 eV and 0.857 eV respectively.

Table 3.7: HSE06 band gaps obtained by single point HSE06 calculations on top of the PBE-optimized structures for the selected structures (a)-(d).

structure	(a)	(b)	(c)	(d)
E_g [eV]	1.176	0.855	1.150	0.857

As seen in the research on CZTS/CZTSe bulk and CZTSSe alloys, the cell volume has shown a strong influence on the band gaps of the systems. Therefore, first an analysis of the band gap as a function of the cell volume is performed in fig. 3.27, in which the HSE06 band gap on top of the optimized PBE-structure as a function of the cell volume is shown. The investigated structures show cell volumes from 1302.88 Å^3 for structure (a) to 1309.14 Å^3 for structure (b), which is only a small difference of 6.26 Å^3.

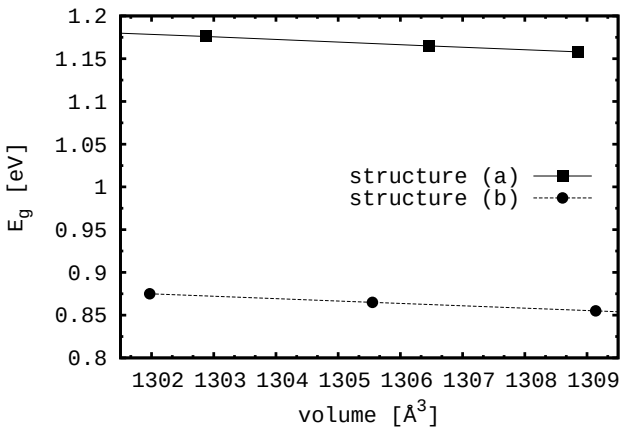

Figure 3.27: HSE06 band gap at the PBE-optimized structures as a function of the cell volume for the structures (a) and (b), within the calculated minimum and maximum cell volume.

Both structures show a decrease of the band gap with increasing cell volume within the range of the minimal and maximum cell volume of the disordered systems. For structure (a) and structure (b), the band gap decreases by 0.020 eV with increasing cell volume, which is small compared to the change in band gaps of 0.320 eV due to structural changes. This influence of the cell volume on the band gap is therefore nearly negligible regarding the overall band gap fluctuations.
A second influencing factor is given by the different binding motifs occurring upon disordering. The DOS are calculated at the HSE06-level with the PBE-optimized structure, whereby the Fermi energies of the structures are aligned for comparison. The electronic structure of structure (a) and (c) resembles with only slight deviations, which is also the case for the electronic structure of structure (b) and (d). Therefore, only the closer analysis of structure (a) and (d) is shown in fig. 3.28, whereby the comparison between structure (a) and (b) as well as structure (a) and (c) is illustrated in app. A. The main structural differences between structure (a) and (d) are the different binding motifs, whereby structure (a) features one and structure (d) features three different binding motifs. As seen before, the influence of the cell volume is neglectable. The projected DOS show that the conduction band of structure (d) is shifted by about 0.3 eV to lower energies. This leads to a decreased band gap of structure (d) in comparison to fully ordered structure (a). The projection on S and Sn elucidate the shift of the conduction band by 0.3 eV to lower energies. Hereby the different S states from the three different binding motifs in the conduction band show an identical behavior, which is also seen for the Sn states of the different binding motifs. In contrast, in the valence band the different binding motifs influence the S-3p states, leading to deviations between these states. Additionally the S-3p states of the three binding motif differ from the S-3p states of structure (a). The projected DOS on Sn in the valence band reveal identical states for the three binding motifs of structure (d), but an overall noticeable deviation from structure (a). The Cu-3d states in structure (a) at the valence band are nearly identical, whereas in structure (d) the Cu-3d states from Cu_{2a} and $Cu_{2c,2d}$ slightly differ due to the different binding motifs. Since the contribution of Zn to the valence and conduction band is small, no major differences are observed.
The beforehand mentioned nearly identical projected DOS of the three different binding motifs in structure (d) reveal that the change of the electronic structure within the unit cell is global and not localized at specific binding motifs. For a possible localization of the band gap fluctuation on different binding motifs within a unit cell, the unit cell has to be expanded by several supercells. The binding motifs within the 64 atom supercell are connected to each other, which results in a global and uniform electronic structure. Nevertheless, concluding from the projected DOS on different binding motifs and the cell volume scan, the new binding motifs remain a main reason for the smaller and fluctuating band gaps, since the influence of the cell volume on the band gap of about 0.020 eV is of minor importance in comparison to the overall band gap fluctuations of up to 0.320 eV.

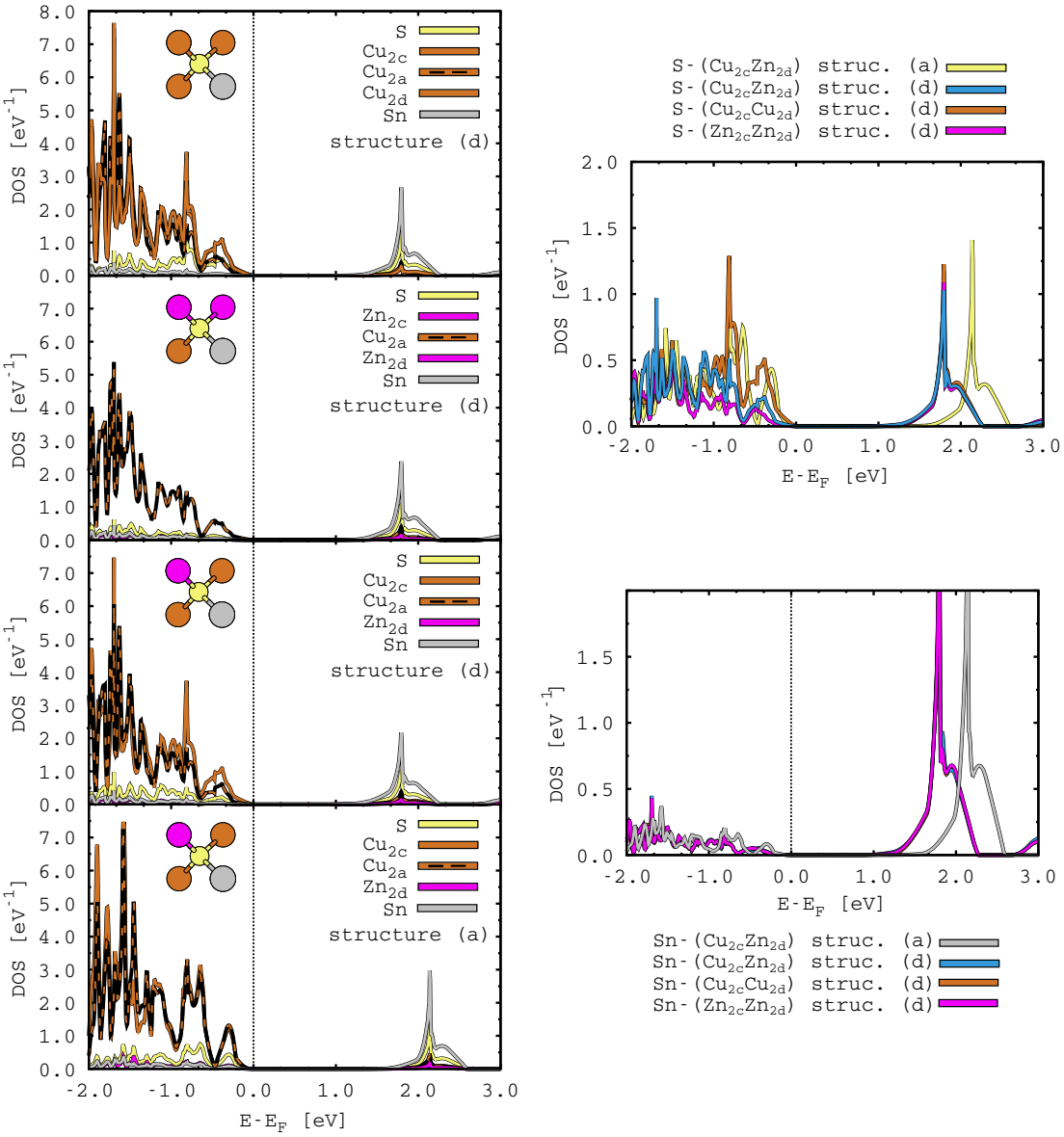

Figure 3.28: HSE06 DOS on top of the PBE-optimized structure for structure (d) and the reference structure (a) with their occurring binding motifs. The Fermi energies of the different structures are aligned for comparison. Zn is shown in pink, Cu in brown, Sn in gray and S in yellow.

In summary, the 2c/2d disorder investigations reveal a possible main reason for the band gap fluctuations in the solar cell absorber. The disordering of the 2c/2d Wyckoff positions leads to different degrees and patterns of disorders, which in a first step influence the lattice parameter. As an effect, the Bader charges start to locally fluctuate, since the binding motifs are changed. In structures in which there are only few changes in binding motifs from S-($Cu_{2c}Zn_{2d}$) to S-($Cu_{2c}Cu_{2d}$) and S-($Zn_{2c}Zn_{2d}$), there are only slight structural and charge deviations from the ordered structure. Upon an increasing amount of new binding motifs, the lattice constants start to further increase and the Bader charges show fluctuations within the unit cell, which are especially visible in S.

The cations also show charge fluctuations within the unit cell, but are in general much smaller than charge fluctuations in the anions. As a result of the different atom charges, the electronic structure is changed. The projected DOS reveal a shift mainly of the conduction band, which result in lower mean band gaps with band gap fluctuations within each disorder fraction. The band gap is decreased by up to 0.32 eV for the 50 % disorders, but even within the disorder fraction 50 %, there exist several structures with band gaps close to the fully ordered structure due to a similar amount of identical binding motifs as in the fully ordered structure. These band gap fluctuations exist within each disorder fraction due to the different disorder patterns. The influence of the different disorder patterns on the electronic structure is mainly observed in the S-3p states at the Fermi energy, which differ due to different chemical environments surrounding S. The theoretical influence of the different disorder fractions and patterns may result in crucial charge and band gap fluctuations in experimental samples. In the experiment, a CZTS crystal consists of several unit cells, therefore the possible experimental properties are an average over all values for different disorder patterns for each disorder fraction. These band gap fluctuations may lead in the solar cell module to erratic electronic properties like the experimentally observed low open-circuit voltages, which are a limiting factor for the efficiency and performance of the CZTS thin film solar cell. The control of these disorders during synthesis is a crucial point for solar cell modules with a constant quality. One route to CZTS samples with low disordering was given by Ritscher et al., who have shown a first step to overcome the disordering obstacle [114]. The theoretical investigations have shown that the 2c/2d are a strongly harming defect type for the absorber material. Combining both, theory and experiment, a solution for a more efficient kesterite solar cell is indicated.

Chapter 4

Nanostructuring by Cu_2ZnSnS_4 Surfaces

In material science there are many ways to alter the material properties in beneficial, or also unwillingly harmful ways. One of the prominent procedures is nanostructuring, in which large bulk materials like monocrystals are substituted by smaller nanostructures of the same material [116]. There are various examples for nanostructures like nanowires, nanomeshes, quantum dots or nanograined bulk materials to name few [116, 117]. Nanostructuring is often utilized, since the exploitation of quantum size effects often enhances the material properties [117, 118]. Therefore by nanostructuring the CZTS material, the electronic structure of CZTS may be altered to benefit the efficiency and performance of the CZTS thin film solar cells. In contrast to large bulk structures with nearly no surface area, nanostructures are also called high surface area materials. The structural distortion results in a reduced thermal conductivity and changed electronic structure. To investigate the influence of nanostructuring on the CZTS properties, two different models are employed to account for different surface to bulk ratios.

A first approximation is a closer investigation of structural and electronic properties of CZTS surfaces. Surface models show a surface to bulk ratio in which the bulk part dominates, which is reversed in CZTS clusters. CZTS clusters are the second approximation for CZTS nanostructures and are featured in chap. 5. In the research on CZTS surfaces, the first focus is set on the stability of the surface terminations via surface energies for an energetic ordering of the different surface planes. Selecting the most stable surface structure, a subsequent analysis of the electronic structure is of special importance, since it is an indicator for a beneficial or harmful effect of nanonstructuring on the properties of the absorber material. Unfortunately up until now the knowledge about CZTS surfaces is still limited despite the possibility of strong influences on the material properties [123–125]. Since the computational modeling of surfaces differs from the modeling of the bulk systems in earlier chapters, a first step is to set up a suitable modeling scheme for the investigation, which will be discussed in the next section.

4.1 Technical Details and Surface Model

4.1.1 Surface Model and Surface Stability

The research focuses on the low-index CZTS surfaces (001), (100), (110), (101), (111) and the experimentally occurring (112) with different surface terminations. The surface cuts are illustrated in fig. 4.1. A *termination* is defined as a cut parallel to the surface plane along the surface normal, leading to different terminations for a given surface plane, referred to in the following by the abbreviation *tx* with a consecutive numbering labeled by *x*. For every surface plane a scan through the bulk system along the surface normal was performed to account for all possible terminations of each surface plane whilst keeping the initial stoichiometry of the slab.

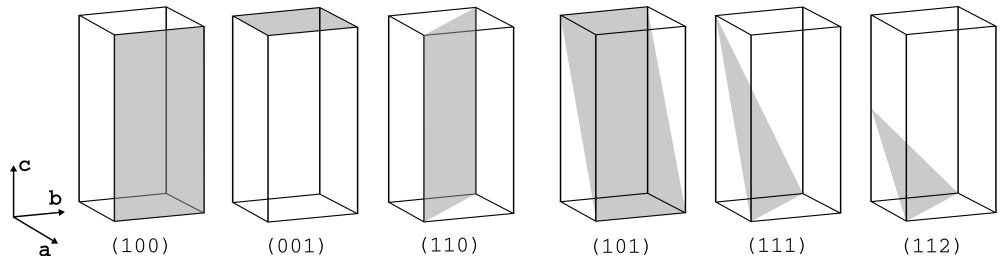

Figure 4.1: Investigated surfaces planes of CZTS. The gray planes mark the cuts through the bulk.

The investigated surfaces are modeled with the periodic *slab* approach, in which a thick vacuum layer is introduced into the unit cell on top of the surface terminations to prevent an interaction between the periodic image of the slabs normal to the surface plane. There are two ways to construct a slab. Asymmetric slabs (left slab in fig. 4.2), which feature two different terminations on top and bottom of the slab and symmetric slabs, which show two identical terminations (right slab in fig. 4.2).

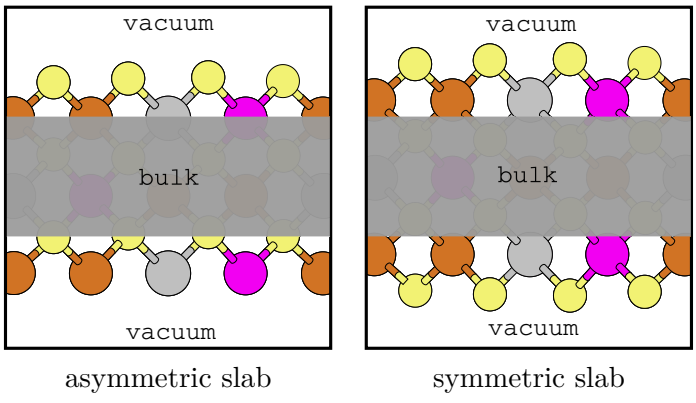

Figure 4.2: Visualization of asymmetric and symmetric slabs. Asymmetric slabs feature two different terminations, whereas both terminations are identical in symmetric slabs. CZTS asymmetric slabs are mostly stoichiometric, whereas symmetric slabs usually suffer from off-stoichiometry.

The symmetric slabs have the advantage of employing inversion symmetry as well as reflection symmetry. Asymmetric CZTS slabs hereby mostly exhibit integer multiples of the bulk stoichiometry, whereas symmetric CZTS slabs usually suffer from off-stoichiometry. The most stable surface cut and surface termination can be determined by the surface energy. The surface energy quantifies the disruption of intermolecular bonds upon creating a surface. Intrinsically the surfaces must be less energetically favorable than the bulk material, otherwise the bulk material would disintegrate. In general the surface energy can be calculated by

$$E_{\text{surf}} = \frac{1}{2A} \left(E_{\text{slab}} - n \cdot E_{\text{bulk}} \right). \tag{4.1}$$

Hereby E_{surf} is the surface energy of the newly formed surface, E_{slab} is the slab energy of the whole slab unit cell and E_{bulk} is the bulk energy per unit cell. At last n is the number of bulk units within the surface unit cell, which has to be an integer number. By definition, the lower the surface energy the more favorable the corresponding surface is. The different stoichiometries of asymmetric and symmetric slabs affect the investigation on the surface stability. Concluding from eq. 4.1 three points are critical for the calculation of the surface energy. The calculation of the bulk energy must be consistent with the calculation of the slab, otherwise the subtractions of the two energies lead to unreliable surface energies. Additionally, the number of bulk units n has to be an integer for meaningful results, because a division of the bulk in non-integer values is not possible. Unfortunately a non-integer value for n prevents an easy application of eq. 4.1 for the calculation of surface energies for several observed terminations. The third crucial part lies in the factor $\frac{1}{2}$ of the equation. For a real assignment of an absolute surface energy both surface terminations of the slab, top and bottom, have to be identical. Else only an average surface energy of two different surface terminations is calculated. Therefore, for two different terminations in asymmetric slabs the eq. 4.1 is modified to

$$E_{\text{surf2}} = \frac{1}{A} \left(E_{\text{slab}} - n \cdot E_{\text{bulk}} \right) \tag{4.2}$$

to calculate the sum of both surface energies by the two different terminations of the slab. To determine distinct surface energies for a given surface termination, symmetric slabs with respect to a mirror plane or inversion center in the middle of the slab have to be selected. These symmetric slabs however are mainly off-stoichiometric in CZTS systems, whereby an easy application of eq. 4.1 is not possible due to non-integer values for n. The challenge of calculating these surfaces energies is approached in sec. 4.1.3.

4.1.2 Surface Relaxation

Further information about the structural properties of a surface can be obtained by the evaluation of the relaxation energy, which is given by

$$E_{\text{relax}} = E_{\text{urlx}} - E_{\text{rlx}} \ , \tag{4.3}$$

where E_{urlx} is the surface energy of the unrelaxed slab in the ideal bulk structure before the structure optimization and E_{rlx} is the surface energy of the structurally optimized slab. The relaxation energy gives useful insights on the optimization process of the surface structure. The process of a surface structure optimization is often referred to as surface *relaxation* or surface *reconstruction*. A *relaxation* is hereby defined as a movement of the top surface atoms mainly in z-direction normal to the surface plane with only minor relaxations in x- and y-direction. A strong movement of the surface atoms in all three spatial directions is referred to as *reconstruction*.

4.1.3 Extrapolation Scheme for Surface Energies in Off-Stoichiometric Slabs

To solve the challenge of calculating the surface energies for symmetric off-stoichiometric slabs, a scheme by Gay et al. [216] is adopted, whereby the consistency of the obtained surface energies is validated with surface energies from stoichiometric asymmetric slabs after eq. 4.1. Gay et al. proposed a scheme, in which the surface energy does not rely on integer bulk units, but on an extrapolation with respect to the number of layers in the slab. Reformulation of eq. 4.1 yields

$$E_{\text{slab}}(N) = 2AE_{\text{surf}} + NE^{N}_{\text{bulk}}, \tag{4.4}$$

where N is the number of layers in the slab, rather than the number of bulk units. E^{N}_{bulk} represents the bulk energy per slab layer, which is averaged over the whole slab and is obtained by the slope of the linear regression. For thick enough slabs, the slab energy E_{slab} can be plotted as a function of the layers N. The surface energy is obtained by a linear regression through these data points and by extracting the y-intercept (see fig. 4.3). From the standard deviation of the y-intersect the error of the fit results, which is in the CZTS surfaces less than 2.5 % for all computed slabs.
For this scheme it is essential that the used slabs are thick enough to achieve a layer-independent surface energy. Furthermore, the allocation of layers has to be done with care. In the CZTS surfaces atoms with the same z-coordinate are assigned to one layer in the unrelaxed structure and this assignment is consistent also for the relaxed structures. A *multilayer* is defined as a combination of several layers with similar z-coordinates in the range of ± 0.05 Å.

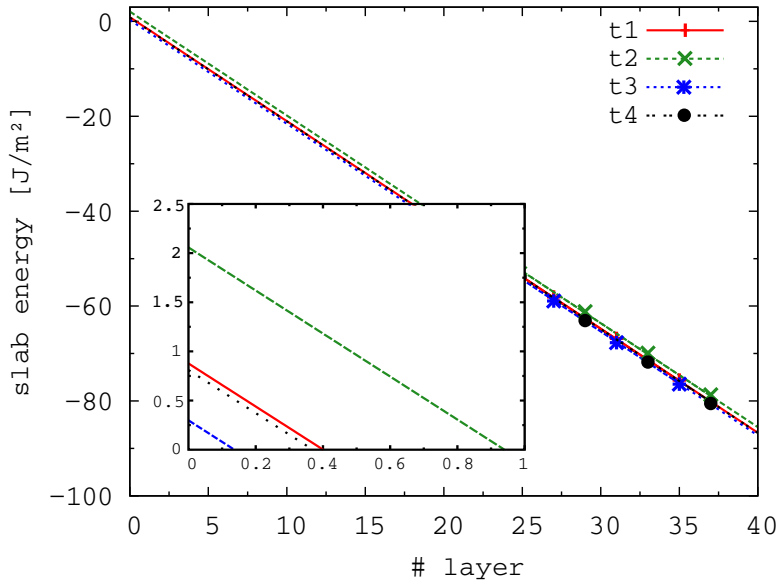

Figure 4.3: Applied extrapolation scheme for the symmetric (001) surface. The dots mark the computed slab energy at a chosen number of layers and the lines indicate the linear fit through these points. By extrapolation to zero layers, the surface energy is given by the y-intercept, corresponding to eq. 4.4. The different terminations of the (001) surface are denoted as t1-t4.

To check the reliability of this scheme, the surface energies of the symmetric slabs can be verified by the surface energies of the asymmetric slabs, which can be determined precisely with eq. 4.2. Comparing the relaxed surface structures of the extrapolation scheme and conventional scheme, the surfaces show nearly identical optimized structures, therefore the relaxation process is not noticeably influenced by the stoichiometry of the slab. As a result, the surface energies should principally yield the same results. Since the (101), (111) and (112) surface can not be constructed symmetrically due to the crystal symmetry, the validation is only performed for the (001), (100) and (110) surface. The surface energies obtained by the conventional scheme are regarded as the reference values. The surface energies at the PBE-level are presented in tab. 4.1, whereby values obtained by the extrapolation scheme are represented by †, all other values are obtained by eq. 4.2. The nomenclature *tx + ty* denotes the two terminations, which occur in the same slab and whose properties are derived from the same calculation. The abbreviation *urlx* stands for the surface energy of the unrelaxed slab, whereas *rlx* denotes the surface energy of the relaxed slab. The investigated terminations are illustrated in fig. 4.4, 4.5 and 4.6. In the following positive relative deviations in % denote a higher surface and relaxation energy by the extrapolation scheme than the conventional scheme. The *combined surface energies* of top and bottom termination are always used for a comparison of the schemes, since the stoichiometric slabs are mostly asymmetric. The two different calculation schemes show that both schemes yield (001) surface energies in excellent agreement for all relaxed and unrelaxed terminations with a minor deviation of a maximum of 1.9%. This deviation slightly increases in the

(100) surface up to 5.1 % for t5+t5, whereby unfortunately t2 shows a non converging electronic structure in off-stoichiometric slabs, but concluding from t1+t2-t1†, t2 is estimated to show a low surface energy. Also, the (110) surface only shows a maximum deviation of 4.0 % for t2a+t2b between the two calculation schemes, whereby the deviation for t1a+t1b is 1.5 % and for t3a+t3b 1.0 %. In comparison to experimental errors of 20-40% [217–220] this deviation is rather small and of minor importance.

Table 4.1: Comparison of surface energies in J/m^2 at the PBE-level obtained by the extrapolation scheme (denoted by †) and by the conventional formula after eq.4.2.

(001)			(100)			(110)		
term.	urlx	rlx	term.	urlx	rlx	term.	urlx	rlx
t1†	1.661	0.877	t1†	2.288	1.897	t1a†	2.004	1.753
t2†	2.471	2.057	t2*	0.481	-0.162	t1b†	0.670	0.165
t3†	0.395	0.299	t3†	1.878	1.335	t1a†+t1b†	2.674	1.917
t4†	1.217	0.810	t4†	0.901	0.390	t1a+t1b	2.652	1.889
t1†+t4†	2.877	1.687	t5†	1.310	0.948	t2a†	0.977	0.656
t2†+t3†	2.866	2.356	t1+t2	2.769	1.735	t2b†	0.430	0.248
t1+t4	2.832	1.656	t3†+t4†	2.779	1.725	t2a†+t2b†	1.408	0.905
t2+t3	2.823	2.338	t3+t4	2.766	1.700	t2a+t2b	1.416	0.870
			t5†+t5†	2.620	1.896	t3a†	1.379	0.488
			t5+t5	2.612	1.804	t3b†	1.508	0.908
						t3a†+t3b†	2.887	1.396
						t3a+t3b	2.818	1.382

† extrapolation scheme after eq. 4.4
tx+ty conventional scheme after eq. 4.2
* t1+t2-t1†

The relaxation energies, which are in a reasonable scale compared to other semiconductor surfaces [124, 221, 222], are presented in tab. 4.2. In contrast to the surface energies, the relaxation energy of each termination can be determined precisely, since both slab terminations can be relaxed independently, which can be utilized for more detailed validation of the extrapolation scheme. This leads to three relaxation energies, obtained by the extrapolation scheme after eq. 4.4 and by double-sided relaxations and by single-sided relaxations after eq. 4.2, whereby the conventional scheme is regarded as the reference value. The relaxation energies reveal that the (001) surface shows in t3 a maximal deviation of 12.9 %, whereby all other terminations show distinctly smaller deviations of 2.4 %, 3.8 %, and 2.0 % for t1, t2 and t4 respectively. A reason for the higher deviation in t3 is the overall small relaxation energy, which is prone to larger errors. Termination t1 and t5 in the (100) surface show a deviation between the schemes of -10.3 % and -10.5 % respectively, whereby the differences in t3 with -2.0 % and in t4 with 0.4 % are significantly lower. The maximum deviation in the (110) surface between the values obtained by the different relaxation schemes slightly

decreases to 9.1 % in t3b and -8.8 % in t2a. Termination t2b shows a smaller deviation of -6.2 %. The remaining terminations t1a, t1b and t3a exhibit considerably lower differences between the schemes of 1.6 %, -0.4 % and 0.5 % respectively.
Concluding from the calculated surface and relaxation energies, the extrapolation scheme has proven valid. The scheme offers a valuable possibility to calculate surface energies for otherwise incomputable surface systems, despite the small deviations of up to 5.1 % in the surface energy and up to 12.9 % in the relaxation energy in one rare case of the (100) surface. The stoichiometry of the slab shows only negligible influences on the structure of the surface termination. In further research on $CoSb_3$ skutterudite surfaces in my master thesis, I have further proven the validity of the extrapolation scheme [222]. A closer investigation on the surface topology in relation to the surface stability is performed in sec. 4.2.

Table 4.2: Relaxation energies in J/m^2 obtained by the extrapolation scheme (denoted by †) and the conventional formula after eq. 4.2 at the PBE-level.

(001)		(100)		(110)	
term.	E_{relax}	term.	E_{relax}	term.	E_{relax}
t1†	0.784	t1†	0.391	t1a†	0.252
t1*	0.766	t1*	0.436	t1a*	0.256
t2†	0.414	t2*	0.643	t1b†	0.505
t2*	0.399	t2*	0.685	t1b*	0.507
t3†	0.096	t3†	0.543	t1a†+t1b†	0.757
t3*	0.085	t3*	0.554	t1a*+t1b*	0.763
t4†	0.407	t4†	0.512	t1a+t1b	0.762
t4*	0.399	t4*	0.510	t2a†	0.321
t1†+t4†	1.190	t5†	0.362	t2a*	0.352
t1*+t4*	1.165	t5*	0.404	t2b†	0.182
t1+t4	1.176	t1+t2	1.034	t2b*	0.194
t2†+t3†	0.510	t1*+t2*	1.121	t2a†+t2b†	0.503
t2*+t3*	0.484	t3†+t4†	1.055	t2a*+t2b*	0.546
t2+t3	0.485	t3*+t4*	1.064	t2a+t2b	0.546
		t3+t4	1.066	t3a†	0.891
		t5†+t5†	0.724	t3a*	0.887
		t5*+t5*	0.808	t3b†	0.600
		t5+t5	0.808	t3b*	0.550
				t3a†+t3b†	1.491
				t3a*+t3b*	1.437
				t3a+t3b	1.436

† extrapolation scheme after eq. 4.4
* single-sided relaxation after eq. 4.2
tx+ty double-sided relaxation after eq. 4.2
* t1+t2-t1†

4.1.4 Computational Details

All calculations were performed within a periodic plane-wave DFT ansatz within the Kohn-Sham framework. To simulate the surfaces the periodic surface model was applied, in which the surface is modeled in a three-dimensional periodic unit cell with a bulk-like part and a surface part with vacuum region, referred to as *slab*. Hereby the vacuum gap was set to 15 Å to ensure non-interaction between the periodic images in the z-direction of the slabs. The slab model is presented in closer detail in sec. 4.1.1. For the visualization of all structures XCrySDen [189, 190] was utilized, whereas the Wulff construction was obtained with Wulffman [223]. As implemented in VASP 5.3.5 and VASP 5.4.1 [185–188] the PBE functional [146] and HSE06 functional [154–157] with the projector augmented wave method (PAW) [174, 175] were used for all computations. The applied PAW potentials acted on the 4s/3d electrons of Cu and Zn, the 5s, 5p and 4d electrons of Sn and 3s, 3p electrons of S. For the creation of the slabs PBE-optimized bulk lattice constants from the previous bulk calculations were utilized. The surface structure optimizations were performed with the PBE-functional, whereby a k-grid of 8x8x1 was applied for all surfaces except the (100) surface, in which a 8x4x1 k-grid was employed due to the lattice constants of the (100) unit cell. This quality level of k-grid ensures converged structures and surface energies. The k-grid was automatically constructed via the Monkhorst-Pack scheme [193], centered at the Γ-point. The relaxations were performed with the conjugate-gradient algorithm implemented in VASP [191] and a Gaussian smearing approach with a smearing factor σ of 0.01 eV was applied during the structure relaxation. The structures were relaxed until a force convergence of 10^{-2} eV/Å^2 and the freedom of spin polarization was enabled. The electronic wave functions were expanded to an energy cutoff of 550 eV. To reach electronic convergence, the Blocked-Davidson algorithm implemented in VASP was applied and the electronic convergence criteria was set to 10^{-5} eV. To ensure well converged surface energies, the slabs were created with 20 to 128 atoms, resulting in a slab thickness up to 64 Å. In the middle of each slab 5 Å was fixed to simulate a bulk-like behavior and the surface parts on top and bottom were simultaneously relaxed. In addition, single-sided relaxations were performed on the asymmetric slabs to identify the different contributions of the different terminations to the relaxation energy of the double-sided relaxation. Each slab was computed with at least four different slab thicknesses to ensure consistency in the surface energy and eliminate errors due to too small slabs. Since it is known that surfaces can reconstruct over several surface unit cells, test calculations for selected terminations of every surface plane up to a 2x2 surface super cell were performed. Since the structures between the normal 1x1 surface unit cell and 2x2 unit cells were identical, the 1x1 unit cell was chosen for all calculations to reduce computing time. The electronic properties in form of DOS were calculated for every structure with the PBE-functional applying the same k-grid as in the structure optimization. In calculations for the DOS and electronic energies, the tetrahedron method

with Blöch corrections was applied [192] with the PBE and HSE06 functional. The PBE band structures were calculated for the most stable slabs of every surface plane considered. To account for an accurate description of the electronic structure, for the most stable slab the DOS was determined with the HSE06-functional as a single point calculation on top of the PBE-optimized structure. There a 4x4x1 k-grid was applied, which is sufficiently accurate for the DOS. As a reference system the DOS for the bulk system was calculated with a 4x4x2 k-grid.

4.2 Stability of Cu_2ZnSnS_4 Surfaces

For each of the 4, 5, 6, 16, 12 and 10 different terminating layers of the (001), (100), (110), (101), (111) and (112) respectively (see fig. 4.4 to fig. 4.11) the surface stability and surface relaxation is analyzed. The surface stability is determined by the surface energy and the surface relaxation is quantified by the relaxation energy, which gives a first insight on the saturation degree of a termination of the unrelaxed structure, since strongly unsaturated surface terminations tend to relax or reconstruct stronger than initially saturated surface terminations. The full tabularly overview of all calculated surfaces and relaxation energies at the PBE-level is summarized in app. B.

(001) Surface

Starting with the (001) surface, there are four different terminations, which are separable into two cation terminating layers and two anion terminating layers. The cation terminations t2 and t4 feature Cu/Zn and Cu/Sn terminations respectively, while the anion termination are both S terminated (see fig. 4.4). The S terminations t1 and t3 hereby differ by the underlying layer directly below the S surface layer, whereby t1 shows an underlying Cu/Zn layer and t3 an underlying Cu/Sn layer.

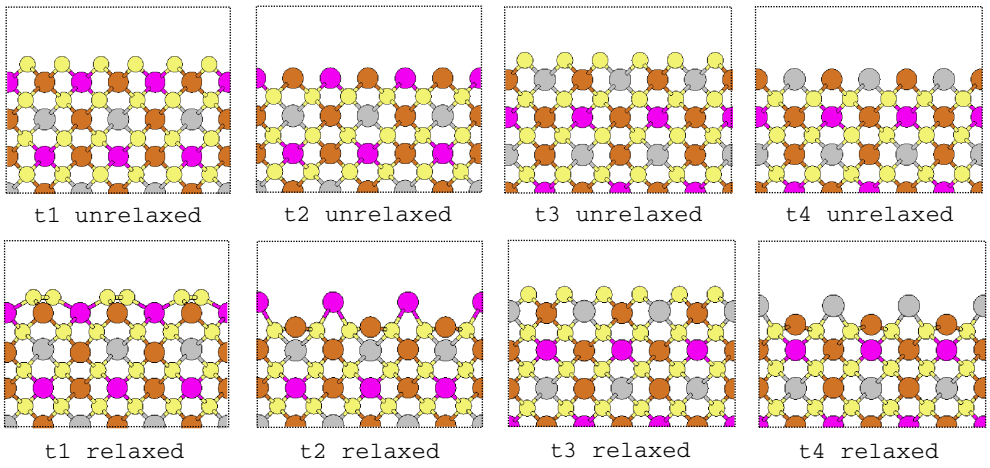

Figure 4.4: All unrelaxed and relaxed terminations of the (001) surface at the PBE-level are illustrated. Zn is shown in pink, Cu in brown, Sn in gray and S in yellow.

The (001) surface shows a wide range of surface energies from 0.299 J/m^2 to 2.057 J/m^2 (see tab. 4.3). The most stable termination is given by t3 with a surface energy of 0.299 J/m^2 and a relaxation energy of only 0.096 J/m^2. The surface S hereby only relax in z-direction towards the underlying Cu/Sn layer, whereby the binding lengths to Cu and Sn are shortened. In t1 with a similar termination topology, the S surface atoms in contrast reconstruct in x, y and z-direction and form S-S bridges to saturate the dangling terminating bonds, which leads to a relaxation energy of 0.784 J/m^2. A reason for the strong deviation between the relaxation energies of t1 and t3 are the underlying layers. The Cu/Sn layer in t3 stronger binds to the top S atoms in comparison to the underlying Zn/Cu layer, resulting in higher relaxation energies for t1 than t3. Furthermore, t1 also reveals a distinctly higher surface energy of 0.877 J/m^2.

Table 4.3: Surface and relaxation energies of the (001) surface as obtained by the conventional scheme after eq. 4.2 and extrapolation scheme after eq. 4.4 in J/m^2 at the PBE-level.

	E_{surf} [J/m^2]		E_{relax} [J/m^2]
term.	urlx	rlx	tx+tx
t1†	1.661	0.877	0.784
t2†	2.471	2.057	0.414
t3†	0.395	0.299	0.096
t4†	1.217	0.810	0.407
t1+t4	2.832	1.656	0.766 + 0.399
t2+t3	2.823	2.338	0.399 + 0.085

† extrapolation scheme after eq. 4.4
tx+ty conventional scheme after eq. 4.2

Switching to cationic terminations, t4 features a similar stability as the anionic termination t1 with a surface energy of 0.810 J/m^2, but a lower relaxation energy of 0.407 J/m^2. The cation top layer in t4 relaxes mainly in z-direction along the surface normal, whereby Sn moves out of the surface plane and Cu moves into the surface plane. A strongly resembling relaxed surface structure to t4 is shown in t2, whereby both feature nearly identical relaxation energy of 0.414 J/m^2 for t2. With 2.057 J/m^2 t2 features the highest surface energy of the (001) terminations, despite the structural similarity to t4. Overall in the (001) surface the key factor for stability are Zn and Sn in the top layers of the termination. Zn directly in the top layers leads to higher surface energies than the corresponding Sn terminations, which is also displayed in the relaxation energies.

(100) Surface

Structurally similar motifs as in the (001) surface occur in the (100) surface (see fig. 4.5). There exist one anionic termination (t1) and one purely cationic termination (t2), here now consisting of all three cations Cu/Zn/Sn. Furthermore, since S features different binding lengths to Cu, Sn and Zn, additional surface terminations are considered, in which the terminations consist of cations and anions simultaneously, featured in t3-t5. In contrast to the pure cation or anion terminating surfaces, these mixed anion-cation terminations feature a quite rough surface termination. While t1 features a full S surface termination, surface S is reduced subsequently in t3 to t5, whereby in t2 the full cation termination is obtained. Hereby t3 features three surface S, t4 one surface S and t5 two surface S.

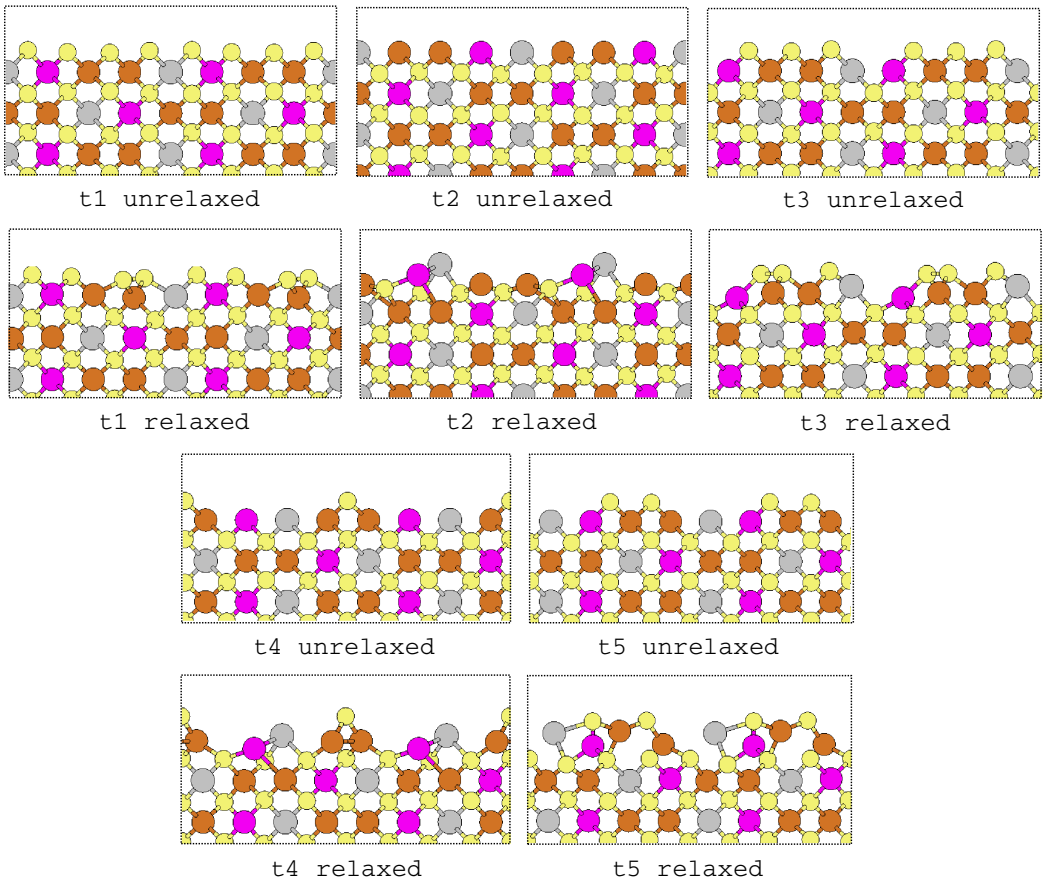

Figure 4.5: All unrelaxed and relaxed terminations of the (100) CZTS surface, calculated at the PBE-level. Zn is shown in pink, Cu in brown, Sn in gray and S in yellow.

Termination t1 with a full terminating S layer shows a high surface energy of 1.897 J/m^2 with a relaxation energy of 0.391 J/m^2 (see tab. 4.4). The termination reconstructs to form S-S dimers to saturate dangling bonds, which is similar to the relaxed structure (001) t1 structure, but shows strong deviations regarding the surface and relaxation energy in comparison to the (001) termination. Removing one S-atom from the top

layer leads to t3 with a surface energy of 1.335 J/m^2, whereby also S-S dimers are formed. Zn reconstructs into the surface plane, Sn slightly relaxes out of plane and Cu mainly saturates dangling bonds by a movement in the x-y plane, leading overall to a relaxation energy of 0.543 J/m^2. Removing two S-atoms from the top layer of t1, termination t5 is obtained with a surface energy of 0.948 J/m^2 and a low relaxation energy of 0.362 J/m^2. Remarkably, the two missing surface S on top of Sn and Zn result in a strong reconstruction of the surface termination, in which Cu and Sn strongly move out of the surface plane.

Table 4.4: Surface and relaxation energies of the (100) surface as obtained by the conventional scheme after eq. 4.2 and extrapolation scheme after eq. 4.4 in J/m^2 at the PBE-level.

	E_{surf} [J/m^2]		E_{relax} [J/m^2]
term.	urlx	rlx	tx+tx
t1†	2.288	1.897	0.391
t2*	0.481	-0.162	0.643
t3†	1.878	1.335	0.543
t4†	0.901	0.390	0.512
t5†	1.310	0.948	0.362
t1+t2	2.769	1.735	0.436 + 0.685
t3+t4	2.766	1.700	0.554 + 0.510
t5+t5	2.612	1.804	0.404 + 0.404

† extrapolation scheme after eq. 4.4
* single-sided relaxation after eq. 4.2
tx+ty conventional scheme after eq. 4.2
* t1+t2-t1†

In termination t4, obtained by a further removal of a surface S-atom in t5, the surface Zn and Sn form a bond since the surface S on top of both atoms is missing, also the Cu atoms approach each other and are bridged by a single S-atom. This reconstruction of the surface leads to the lowest surface energy of 0.390 J/m^2 for t4 in the (100) surface, since the termination is relatively charge balanced. The purely cationic termination t2 shows the highest relaxation energy of 0.685 J/m^2, obtained by the slab calculation of t1+t2. The surface energy is estimated by the difference of t1+t2-t1†, which yields a surface energy smaller than zero. In theory, while neglecting thermal and kinetic effects in the computational model, the bulk would instantly disintegrate in the (100) direction, which is not observed in experimental studies. In experimental studies the (200) surface occurs [60], underlining a higher stability of the (100) surface cut, which is however affected by Cu-poor surface terminations in experiment [224]. Overall the relaxation energies of the (100) surface are similar to the (001) surface, whereby the energy span is smaller in (100) due to more anion-cation balanced surface terminations, which is a key for an increased surface stability.

(110) Surface

Even more balanced surface terminations occur in the (110) surface, which features six different surface terminations (see fig. 4.6). The terminations hereby reveal two types of surface multilayer, Cu/S/Sn and Cu/S/Zn. An especially smooth surface cut is shown in t2+t2b, whereby t1a+t1b and t3a+t3b show singly bound surface S sticking out of the surface plane.

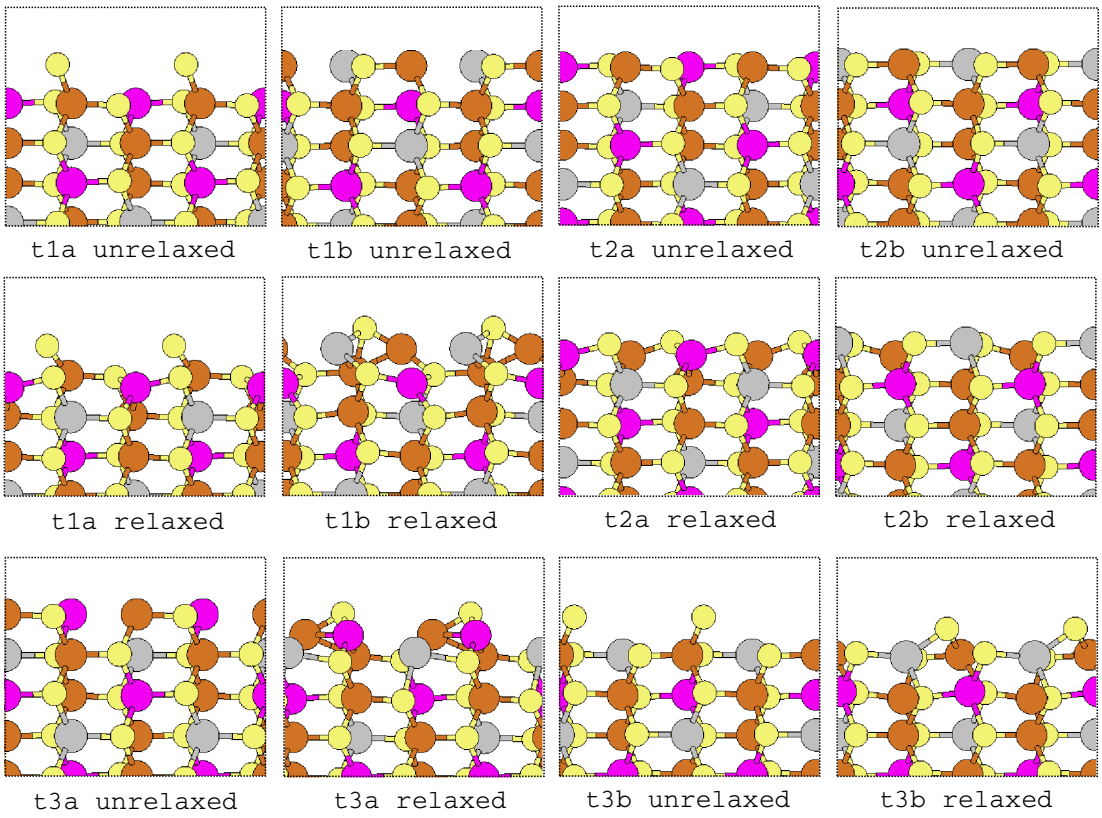

Figure 4.6: All unrelaxed and relaxed terminations of the (110) surface at the PBE-level. Zn is shown in pink, Cu in brown, Sn in gray and S in yellow.

The surface energies of the (110) surface are summarized in tab. 4.5. The terminations t1a and t1b show the two extrema in the (110) surface regarding the surface energy with 1.753 J/m^2 and 0.165 J/m^2 respectively. The relaxation energy of t1b is twice as high as the relaxation energy of t1a, which is a result of strong reconstructions of Sn and Cu at the surface termination. A similar situation is shown with t2b, which shows half the surface and relaxation energy of t2a. With 0.248 J/m^2 t2b shows the second most stable termination of the (110) surface, which is due to nearly saturated top layers at the termination. The strongest relaxation is shown in t3a with 0.891 J/m^2, whereas the surface energy is low with only 0.488 J/m^2. Termination t3b, which is similar to the least favorable termination t1a, shows the second highest surface energy of 0.980 J/m^2 and a medium relaxation energy of 0.600 J/m^2. Overall the occurrence of Sn or Zn in the top layer is crucial for the surface stability as seen before in the (001) and (100)

surfaces. Zn in the top layer leads to higher surface energies than Sn in the top layers as seen in t1a/t3b, t1b/t3a and t2a/t2b. This trend is similarly featured in the relaxation energies except for t1a/t3b.

Table 4.5: Surface and relaxation energies of the (110) surface as obtained by the conventional scheme after eq. 4.2 and extrapolation scheme after eq. 4.4 in J/m^2 at the PBE-level.

	E_{surf} $[J/m^2]$		E_{relax} $[J/m^2]$
term.	urlx	rlx	tx+tx
t1a†	2.004	1.753	0.252
t1b†	0.670	0.165	0.505
t1a+t1b	2.652	1.889	0.256 + 0.507
t2a†	0.977	0.656	0.321
t2b†	0.430	0.248	0.182
t2a+t2b	1.416	0.870	0.352 + 0.194
t3a†	1.379	0.488	0.891
t3b†	1.508	0.908	0.600
t3a+t3b	2.818	1.382	0.887 + 0.550

† extrapolation scheme after eq. 4.4
tx+ty conventional scheme after eq. 4.2

(101) Surface

The (101) shows 16 different terminations (see fig. 4.7), which surface energies can only be calculated as a combination of two terminations, since the crystal symmetry prevents the construction of symmetric slabs. The high amount of possible surface terminations is due to the structural complexity of the CZTS structure. In contrast to the (001), (100) and (110) surfaces, the (101) surface shows a step-like surface structure instead of a flat surface structure. The (101) surface cut leads overall to a balanced anion-cation ratio at the top layers. The surface terminations feature either a cation or anion exposed as the top layer of the termination. The combined surface energies from t1a+t1b to t8a+t8b range from 0.770 to 1.527 J/m^2 with relaxation energies in a broad span from 0.057 to 0.667 J/m^2 for the single terminations. The surface energies are hereby in a similar range like the (110) surface, whereby they are in general lower than the combined surface energies of the (001) and (100) surface. The small range of surface energies is due to similar step-like surface structures over all terminations.
A first approximation for the surface stability and saturation degree is shown by the relaxation energy of the slabs, which reveals two key factors (see tab. 4.6). The first structural feature shows that S as the top surface layer leads to an overall structural stabilization, resulting in lower relaxation energies compared to structures with a cationic top layer.

Figure 4.7: Unrelaxed and relaxed terminations of the (101) surface of CZTS at the PBE-level. Zn is shown in pink, Cu in brown, Sn in gray and S in yellow.

The second key factor is the position and type of the top surface cation, Zn in the top layer leads to higher relaxation energies than Sn, which is especially observed in t4a/t7b and t5b/t6a. The more saturated both atom types are at the surface termination in a similar structure, the closer the relaxation energies are, as seen in t1a and t2b with relaxation energies of 0.266 J/m^2 and 0.303 J/m^2 respectively. Termination t3a shows with 0.057 J/m^2 the lowest relaxation energy of the (101) surface, whereby t3b features the highest one with 0.667 J/m^2. The combined surface energies show t8a+t8b as the most stable slab with a surface energy of 0.770 J/m^2, whereas the most unfavorable slab is t4a+t4b with 1.527 J/m^2. The relaxation energies in both cases show a contrary trend, with a higher relaxation energy in total for t8a+t8b than t4a+t4b. All (101) slabs show the same structural similarity, whereby one surface is terminated by S and the second surface is terminated by a cation. These synergetic effects lead to the mentioned balanced surface energies as well as balanced relaxation energies of both terminations of the slab. The extraordinary stable t8a+t8b is followed by t2a+t2b with a 0.336 J/m^2 higher surface energy. Up till now, the (101) slab t8a+t8b shows the overall most stable slab in comparison to the combined surface energies of the (001), (100) and (110) surface.

Table 4.6: Surface and relaxation energies of the (101) surface as obtained by the conventional scheme after eq. 4.2 in J/m^2 at the PBE-level.

	E_{surf2} [J/m^2]		E_{relax} [J/m^2]
term.	urlx	rlx	txa + txb
t1a+t1b	1.912	1.150	0.266 + 0.494
t2a+t2b	1.965	1.106	0.557 + 0.303
t3a+t3b	1.842	1.114	0.057 + 0.667
t4a+t4b	2.191	1.527	0.312 + 0.351
t5a+t5b	2.090	1.504	0.302 + 0.283
t6a+t6b	2.193	1.386	0.663 + 0.144
t7a+t7b	2.316	1.396	0.309 + 0.611
t8a+t8b	1.608	0.770	0.596 + 0.243

(111) Surface

The 12 terminations of the (111) surface also show a step-like structure (see fig. 4.9) like the (101) surface. In contrast to the (101) surface, the (111) surface shows alternating cation planes of Cu/Zn and Cu/Sn along the lattice parameter a (see fig. 4.8), which is not present in the (101) surface. The initial surface cut leads to terminations with singly bound cations (see t1b or t4b) or singly bound anions (see t2a, t4a or t5a), which is in general an unfavorable starting structure due to a high amount of unsaturated bonds at the surface termination. As in the (101) surface, the crystal symmetry prevents the construction of symmetric slabs.

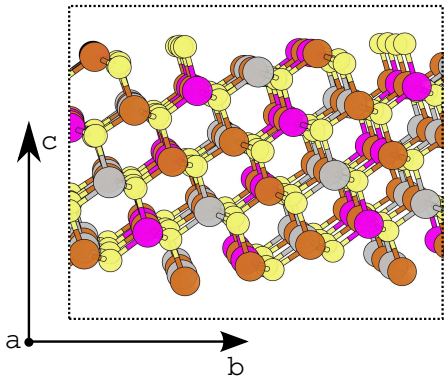

Figure 4.8: Unrelaxed model structure of the slab t1a+t1b of the (111) surface. The structure shows alternating Cu/Zn and Cu/Sn atoms in the direction of lattice parameter a. Zn is shown in pink, Cu in brown, Sn in gray and S in yellow.

Due to the structural similarity to the (101) surface, the (111) surface energies are in a similar range from 0.839 J/m^2 to 1.461 J/m^2 for the relaxed structures (see tab. 4.7). The relaxation energies shows slightly increased minimum and maximum values from 0.113 J/m^2 to 0.782 J/m^2 in comparison to the (101) surface. The (111) surface energies show characteristic features, which justify the energetic order of the slabs. The most stable (111) slab is obtained with t3a+t3b with a surface energy of 0.839 J/m^2, closely followed by t6a+t6b with 0.856 J/m^2. The extraordinary stabilities of both slabs are the smooth step-like surface planes with no singly bound surface atoms. This also results in similar relaxation energies of 0.471 J/m^2 for t3a, 0.113 J/m^2 for t3b, 0.409 J/m^2 for t6a and 0.183 J/m^2 for t6b. The terminations t2a+t2b and t5a+t5b form the second group of structures with similar surface energies, since both slabs feature one smooth termination with no singly bound surface atoms and one termination with singly bound S. Hereby also the relaxation energies resemble with 0.585 J/m^2 + 0.279 J/m^2 for t2a+t2b and 0.563 J/m^2 + 0.348 J/m^2 for t5a+t5b.

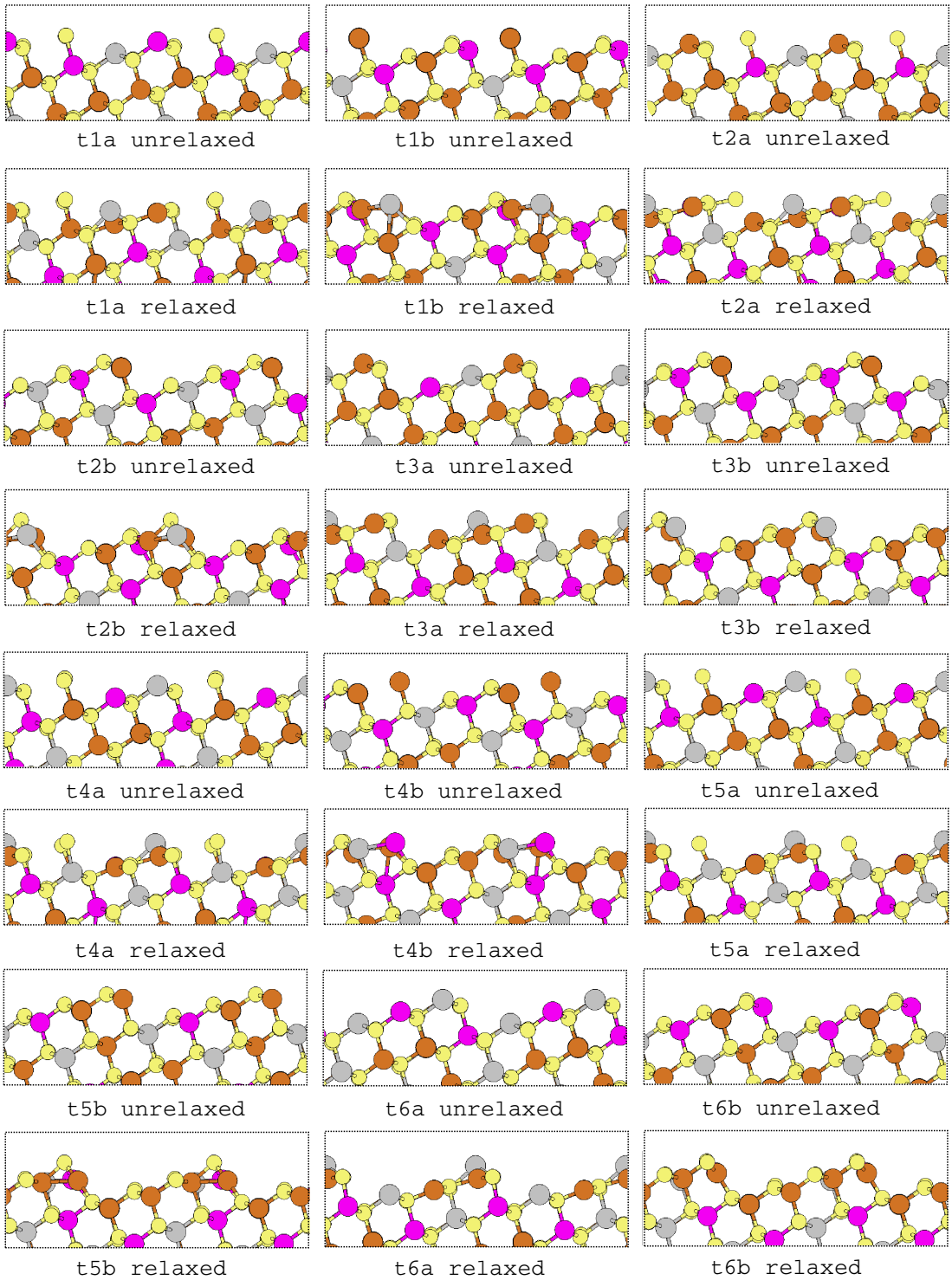

Figure 4.9: Unrelaxed and relaxed terminations of the (111) surface of CZTS. All structures are obtained at the PBE-level. Zn is shown in pink, Cu in brown, Sn in gray and S in yellow.

The last surface group is formed by t1a+t1b and t4a+t4b, in which one termination shows singly bound cations and the other termination shows singly bound anions. The surface energy of 1.107 J/m^2 for t1a+t1b is similar to the group before, whereby t4a+t4b shows the most unfavorable slab of the (111) surface with 1.461 J/m^2. The lower surface energy of t1a+t1b than t4a+t4b is a result of the strong relaxation of t1a with 0.782 J/m^2, whereby t1b shows a relaxation energy of 0.416 J/m^2, t4a of 0.595 J/m^2 and t4b of 0.402 J/m^2. The stability and relaxation process of the (111) surface are primarily determined by the amount and type of singly bound surface atoms. The most stable slabs are obtained by both terminations only showing smooth surface terminations with no singly bound surface atoms. Upon increasing the number of singly bound surface atoms, the stability decreases as well as the relaxation energy increases. As seen in all surface planes before, Zn and Sn in the top layers strongly influence the stability of the slab, which is especially observed in t1a+t1b and t4a+t4b, in which Sn and Zn are initially singly bound respectively. Unfortunately the magnitude of the stability resulting from Sn and Zn at the top layers can not be determined independently. One overall stabilizing factor is the widely balanced anion-cation ratio in the top layers of the (111) surface, which lead to overall low surface energies and reasonable relaxation energies.

Table 4.7: Surface and relaxation energies of the (111) surface as obtained by the conventional scheme after eq. 4.2 in J/m^2 at the PBE-level.

	E_{surf2} [J/m^2]		E_{relax} [J/m^2]
term.	urlx	rlx	txa + txb
t1a+t1b	2.482	1.107	0.782 + 0.416
t2a+t2b	1.915	1.047	0.585 + 0.279
t3a+t3b	1.428	0.839	0.471 + 0.113
t4a+t4b	2.458	1.461	0.595 + 0.402
t5a+t5b	2.073	1.163	0.563 + 0.348
t6a+t6b	1.442	0.856	0.409 + 0.183

(112) Surface

The (112) surface features ten different terminations (see fig. 4.11), which in contrast to the (101) and (111) surfaces show a flat surface structure like the (001), (100) and (110) surfaces. The slabs hereby can be divided in two different termination topologies, one anion terminating layer and one cation terminating layer, which is especially seen in t1a+t1b. As in the (111) surface, the (112) surface shows alternating cation planes of Cu/Zn and Cu/Sn along the lattice parameter b (see fig. 4.10), which leads to a more balanced anion-cation ratio at the surface termination. As in the (101) and (111) surfaces, the crystal symmetry prevents the construction of symmetric slabs.

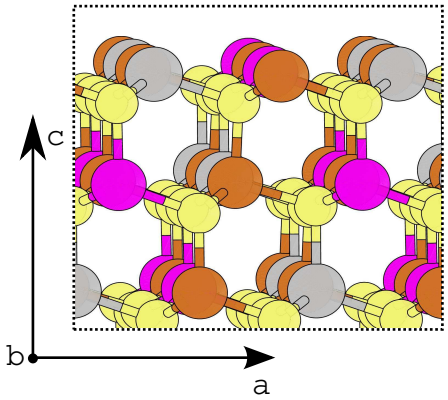

Figure 4.10: Unrelaxed model structure of the termination t5a of the (112) surface. The structure shows alternating Cu/Zn and Cu/Sn atoms in the direction of lattice parameter b. Zn is shown in pink, Cu in brown, Sn in gray and S in yellow.

The combined surface energies at the PBE-level range from 0.768 J/m^2 to 2.339 J/m^2 for the relaxed structures (see tab. 4.5). This broad energy range is due to terminations with a high amount of unsaturated surface atoms. This unfavorable situation is especially seen in t1a+t1b to t4a+t4b. The first slab t1a+t1b shows four singly bound S at t1a and four singly bound cations in t1b. By transferring one S from t1a to t1b, t2a+t2b is obtained. This process leads to an increasing saturation of the terminations up to the nearly saturated termination t5a+t5b, whereby only one binding partner of the surface atoms is missing and no singly bound surface atoms are present. As a energetic result, slab t1a+t1b shows the highest surface energy of 2.339 J/m^2, which decreases to 1.742 J/m^2 in t2a+t2b, 1.422 J/m^2 in t3a+t3b, 1.265 J/m^2 in t4a+t4b and 0.768 J/m^2 in t5a+t5b. The relaxed structures show that the singly bound surface atoms form multiple new bonds to saturate their dangling bonds, which results in high relaxation energies.

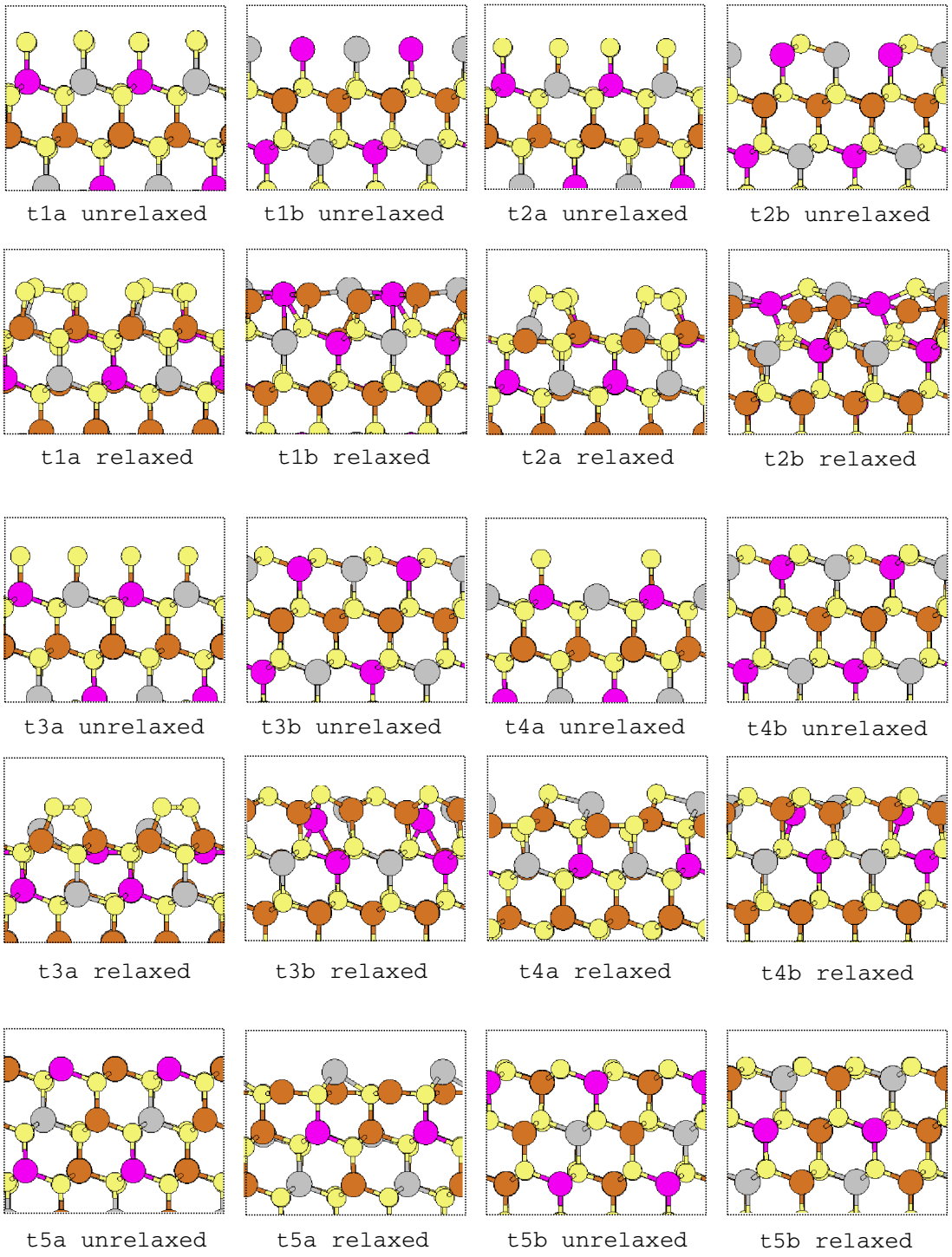

Figure 4.11: Unrelaxed and unrelaxed terminations of the (112) surface of CZTS at the PBE-level. Zn is shown in pink, Cu in brown, Sn in gray and S in yellow.

A similar energetic order as in the surface energies is seen in the relaxation energies, with a relaxation energy of 2.129 J/m^2 for t1a+t1b, 2.301 J/m^2 for t2a+t2b, 1.726 J/m^2 for t3a+t3b, 0.928 J/m^2 for t4a+t4b and 0.594 J/m^2 for t5a+t5b. The slab t1a+t1b hereby changes the position in the energetic ordering with t2a+t2b, since t2a shows the strongest relaxation energy and therefore strongly increases the total relaxation energy of t2a+t2b. The main contribution to the relaxation energy is hereby the top S layer, whereas the bottom cation layer shows a smaller influence on the total relaxation energy. As in the (111) surface before, the structural stability is mainly determined by the different amounts of singly bound surface atoms. With decreasing amount of singly bound surface atoms, the surface stability increases while concurrently the relaxation energy decreases. The lowest surface energy for t5a+t5b of all calculated slabs gives strong evidence for the main occurrence in experimental studies [225–234].

Table 4.8: Surface and relaxation energies of the (112) surface as obtained by the conventional scheme after eq. 4.2 in J/m^2 at the PBE-level.

	E_{surf2} [J/m^2]		E_{relax} [J/m^2]
term.	urlx	rlx	txa + txb
t1a+t1b	4.854	2.339	1.228 + 0.901
t2a+t2b	4.047	1.742	1.500 + 0.801
t3a+t3b	3.154	1.422	1.170 + 0.556
t4a+t4b	2.282	1.265	0.642 + 0.286
t5a+t5b	1.361	0.768	0.558 + 0.036

Atomic Surface Charges

Besides the calculated surface and relaxation energies, a further indication on the stability of the surfaces are given by atomic charges, determined here by a Bader charge analysis [194–196]. The atomic charges give a first insight on the electronic structure of the atoms within the slab. The Bader charges of 0.477 e, 1.382 e, 0.848 e and -0.796 e for Cu, Sn, Zn and S respectively of the bulk are taken as reference values. In the middle of all slabs the mean charges over all slabs of 0.48 e for Cu, 1.40 e for Sn, 0.85 e for Zn and -0.80 e for S are nearly identical to the bulk Bader charges, confirming converged slab thicknesses. Moving from the bulk-like part in the middle of the slab to the surface, the Bader charges start to deviate from the reference charges of the bulk, whereby the largest deviations are shown directly at the surface (see fig. 4.12 and 4.13). The Bader charges of all stoichiometric slabs are illustrated in app. B. The charges of the surfaces atoms are referred to as *surface charges* in the following, whereby the charges in the middle of the slab are referred to as *bulk-like charges*. In asymmetric slabs, deviations between top and bottom surface charges occur due to different terminating layers. The stability of a slab hereby can be approximated by the deviation of the Bader charges at the termination from the bulk-like Bader charges. Remarkable about all investigated slabs is that the surface atom charges nearly all show uniformly more neutral Bader charges than the bulk-like charges. The different surface stabilities are reflected in the Bader charges within a surface plane as well as in comparison of all surface planes. This is seen in the (001) and (100) surfaces with similar surface energies and similar strong deviations of the surface charges from the bulk-like charges. The highly stable (110) surface shows only minor deviation of the surface charges from the bulk-like charges, which is also present in the most stable slabs of the (101), (111) and (112) surfaces. In all surface planes, the most unstable slabs show stronger deviations of the surface charges from the bulk-like charges than the most stable slab of the corresponding surface plane.

In summary, a general trend is observed in the charge analysis. Stable slabs show mainly Bader charges close to the one in the bulk-like part of the slab, even at the surface terminations. With decreasing surface stability the Bader charges stronger deviate at the surface terminations, showing nearly neutral charged atoms, for example in the (112) surface with terminations t1a+t1b. The charge trends are an effect of the surface structure relaxation, whereby the atoms relax to saturate dangling bonds due to the initial surface cut. Deviations from the bulk-like charges indicate binding situations differing from the bulk structure, whereby identical charges on the surface as in the bulk reveal a bulk-like termination in terms of valency as well as a stable surface structure. In addition to the surface energies and relaxation energies, the Bader charges therefore can be utilized as an approximation for the surface stability.

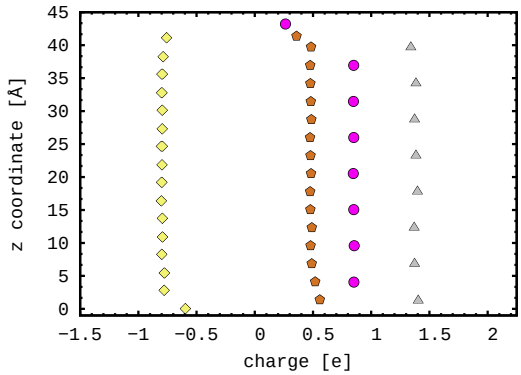

most unstable (001) slab t2+t3

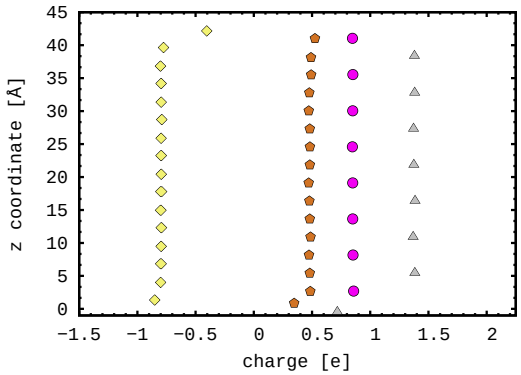

most stable (001) slab t1+t4

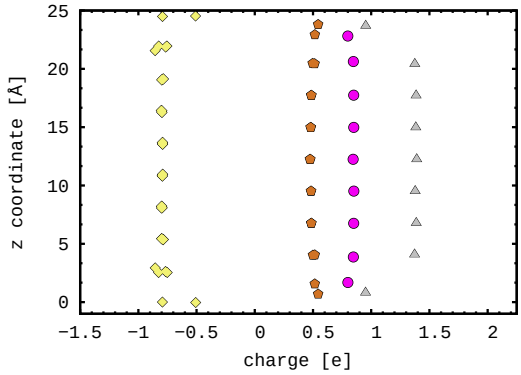

most unstable (100) slab t5+t5

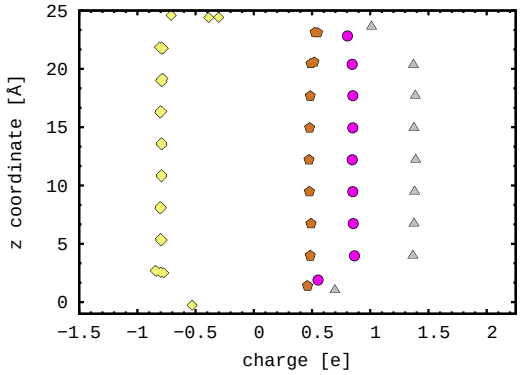

most stable (100) slab t3+t4

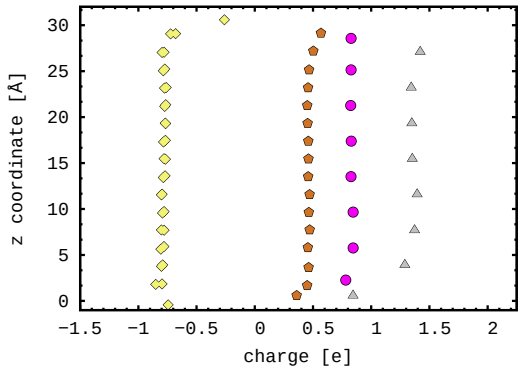

most unstable (110) slab t1a+t1b

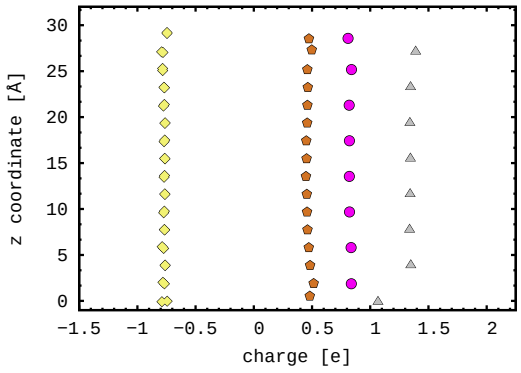

most stable (110) slab t2a+t2b

Figure 4.12: Bader charges at the PBE-level of the most stable and unstable (001),(100) and (110) slab plotted as a function of the z-coordinate of the surface. The first mentioned termination is located at z=max, whereby the second termination is located at z=min. Zn is shown in pink, Cu in brown, Sn in gray and S in yellow.

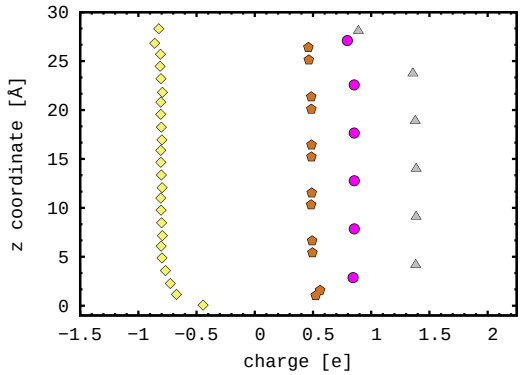

most unstable (101) slab t4a+t4b

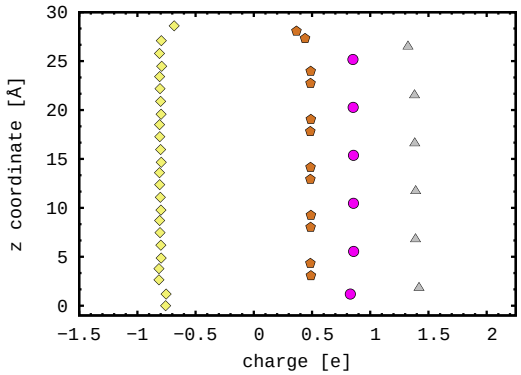

most stable (101) slab t8a+t8b

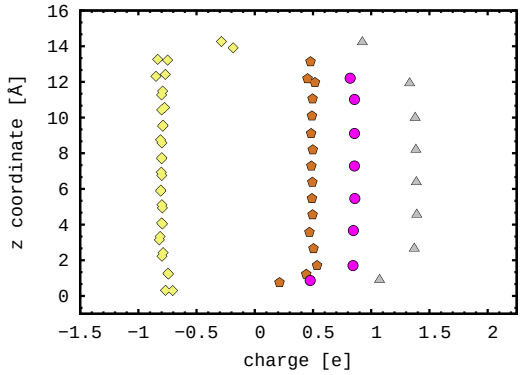

most unstable (111) slab t4a+t4b

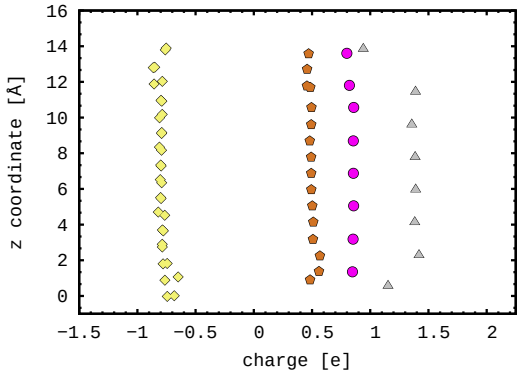

most stable (111) slab t3a+t3b

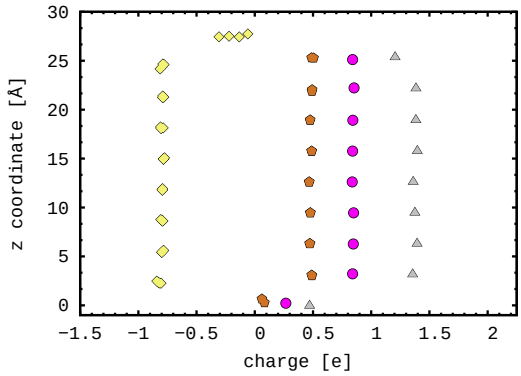

most unstable (112) slab t1a+t1b

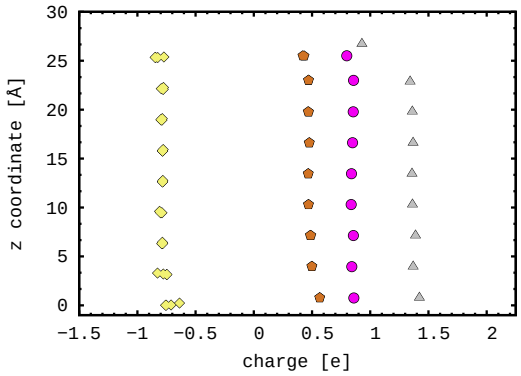

most stable (112) slab t5a+t5b

Figure 4.13: Bader charges at the PBE-level of the most stable and unstable (101), (111) and (112) slab plotted as a function of the z-coordinate of the surface. The first mentioned termination is located at z=max, whereby the second termination is located at z=min. Zn is shown in pink, Cu in brown, Sn in gray and S in yellow.

4.2.1 Summary of CZTS Surface Stabilities

Summarizing the investigation on the structural properties of CZTS surfaces, surface energies, relaxation energies and Bader charges are useful tools for a determination of the surface stability. The surface energies of all surfaces show reasonable values in comparison to other semiconductor surface energies [221, 222]. Also, the relaxation energies are in a reasonable scale in regard to the ionic binding situation in the bulk, leading to strong relaxations and reconstructions at the surface termination. These relaxation energies correspond to atom shifts directly at the terminating layer of up to 0.9 Å in z-direction for few single cations and about 0.6 Å in x- and y-direction, especially for S, which form surface dimers. The size of relaxation energies hereby strongly depends on the initial surface termination. The Bader charges show the same tendency, in so far as Bader charges at the surface terminations of the unrelaxed surfaces close to the bulk lead to low relaxation energies. Several key factors for stable CZTS surfaces are shown:

a) balanced anion-cation ratios at the surface terminations,

b) Sn at the surface termination leads to lower surface and relaxation energies than Zn in the same structures,

c) no or only few singly bound surface atoms,

d) Bader charges close to the bulk at the surface termination.

Considering all key factors above, as a result the (112) surface shows overall the most stable slab, followed by the (101), (111), (110), (001) and (100) surface, summarized in tab. 4.9.

Table 4.9: Summarized surface energies of the most stable slabs as obtained by eq. 4.2 at the PBE-level.

surface	terminations	E_{surf2} [J/m^2]	E_{relax} [J/m^2]
(001)	t1+t4	1.656	0.766 + 0.399
(100)	t3+t4	1.700	0.554 + 0.510
(110)	t2a+t2b	0.870	0.352 + 0.194
(101)	t8a+t8b	0.770	0.596 + 0.243
(111)	t3a+t3b	0.839	0.471 + 0.113
(112)	t5a+t5b	0.768	0.558 + 0.036

The stability of the (112) surface is hereby in good agreement with the high occurrence in experimental studies [225–234]. The different contributions to the surface energies of the (101), (111) and (112) can only be estimated based on the relaxation energies and Bader charges, whereby low relaxation energies and Bader charges close to the

bulk are set as a reference for a stable surface termination. The terminations txb of the (101), (111) and (112) surfaces therefore contribute a lower surface energy to the combined surface energy than their opposing terminations txa, meaning that the txb terminations are estimated to be more stable. Unfortunately there are no publications on experimental surfaces energies for CZTS so far, so a comparison to experiment is not possible yet.

Following the construction scheme after Wulff [177], out of the combined surface energies E_{surf2} for the surface planes a plot of a possible nanocrystal in the vacuum in thermodynamic equilibrium can be constructed (see fig. 4.14). The Wulff construction mainly consists of the (112) and (101) surface due to their low surface energies, which are followed by the (110) and (111) surface. The high surface energies of the (001) and (100) surface lead to an absence in the Wulff construction. In comparison to experiments [49, 50, 52–54, 56, 58–62], in which the nanocrystals mostly indicate spherical to ellipsoid shapes, but no identical structure over all studies, the theoretical Wulff construction resembles with respect to the shape and the occurrence of the (112) and (110) surface.

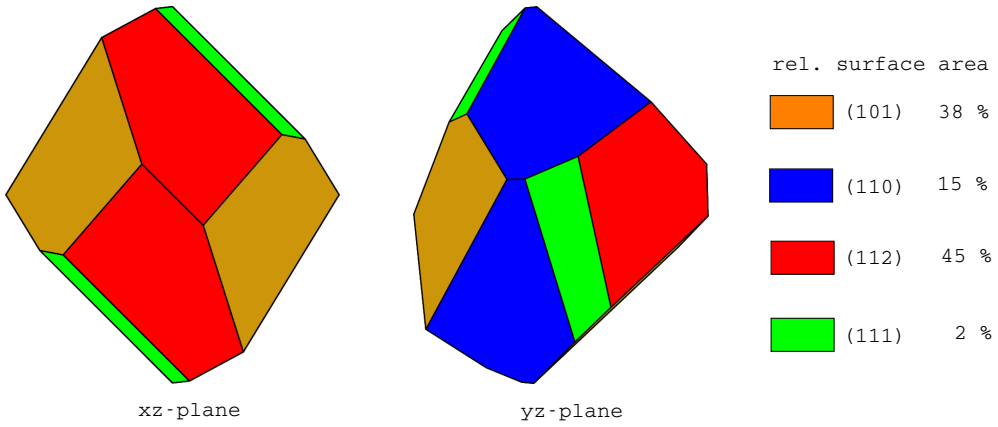

Figure 4.14: Wulff construction for the six calculated asymmetric surfaces of CZTS. Due to the high surface energy E_{surf2} of the (001) and (100) surface they are absent in the Wulff construction. The main relative surface areas are the (112) surface and (101) surface, followed by the (110) and (111) surface. All surface energies were calculated at the PBE-level.

4.3 Electronic Structure of Cu_2ZnSnS_4 Surfaces

Due to the importance of surfaces in the thin film solar cell, the influence of the surface termination on the electronic structure is investigated. In the following the characteristics of the most stable (112) slab are exemplarily illustrated and compared to the electronic structure of the bulk, all other investigated slabs show similar electronic properties. The PBE DOS of all relaxed stoichiometric slabs and the PBE band structures for the most stable slabs are illustrated in app. B. The (112) slab with termination t5a+t5b shows the lowest surface energy and therefore the highest tendency for an experimental occurrence. The focus of the analysis of the electronic structure is set on the HSE06 DOS with the PBE-optimized structure as basis for an insight on the electronic changes upon nanostructuring. The utilized slabs are at least 16 Å thick to guarantee a bulk-like part in the middle of the slab and a surface part at both terminations. In general the total DOS of the slab shows similar properties like the bulk DOS (see fig. 4.15) for the low lying states from -15 eV to -1 eV, whereby the Fermi energies of the bulk and the (112) surface are aligned for comparison. The main difference is shown at the Fermi energy, at which the slab DOS shows states located at the Fermi energy within the band gap. Furthermore, the α- and β-spin components ($\uparrow$ / $\downarrow$) of these states are not identical anymore, which results in a magnetization of the slab (see inset in fig. 4.15).

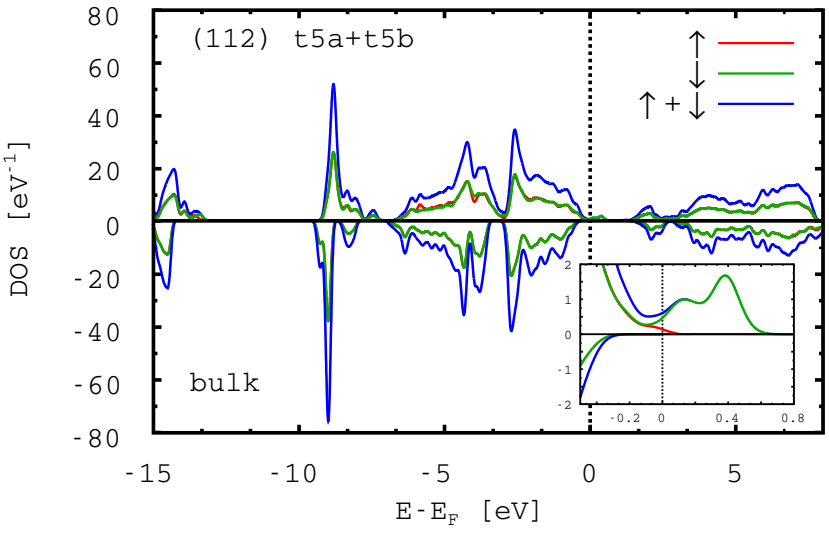

Figure 4.15: Total HSE06 DOS for the bulk (bottom) and the most stable (112) surface (top) are shown. The PBE-optimized structures are utilized. The inset shows a zoom on the surface states at the Fermi energy.

A further projection of the slab DOS on different parts in the (112) slab reveals two different types of DOS, i) a bulk-projected DOS and ii) two surface-projected DOS (see fig. 4.16). The *bulk-projected* DOS is defined as a projection of the DOS on the multilayer in the middle of the slab, which should yield a nearly identical electronic

structure as the real bulk system when the slab thickness is converged. The *surface-projected* DOS is a DOS projection on the terminating multilayer of the two surface terminations to account for changes of the electronic structure at the surface termination. The illustrated DOS are averaged for every atom type within the highlighted multilayer.

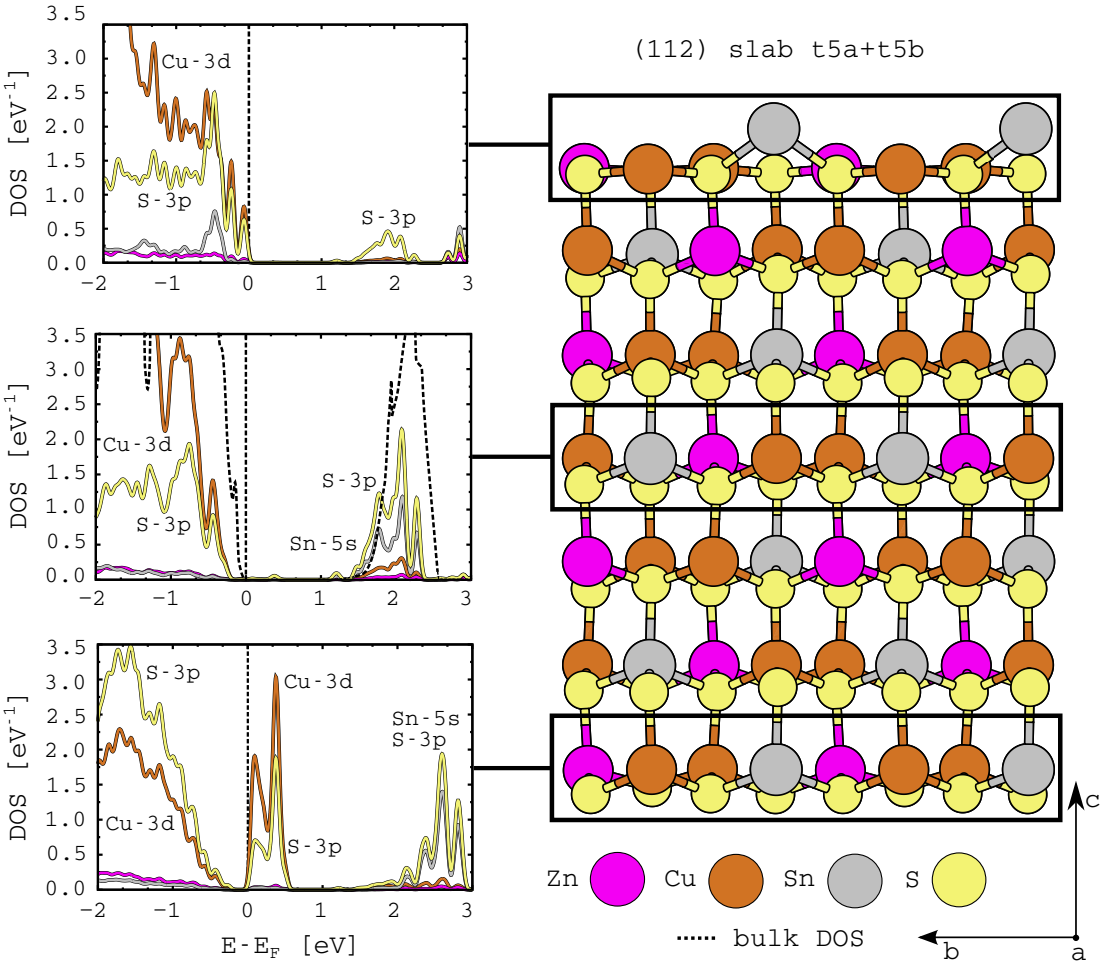

Figure 4.16: Projected HSE06 DOS for different parts of the most stable (112) surface. The DOS are projected on the surface areas (top and bottom) and on the multilayer in the middle of the slab, referred to as bulk-projected DOS. The DOS are averaged for every atom type within the highlighted multilayer.

The bulk-projected DOS in the middle of the slab still shows a clear band gap and no states within the bulk band gap. The DOS from the bulk calculation (dashed DOS) hereby strongly resembles the bulk-projected DOS in the slab. Upon further projecting the DOS on the surface terminations, the cause for the occurring states within the band gap is revealed. The top termination of the slab shows a nearly bulk-like band gap of over 1 eV, whereby the Cu-3d and S-3p states of the valence band are slightly shifted to the Fermi energy compared to the bulk-projected DOS. The conduction band reveals vanished Sn-5s states, which are normally present in the bulk conduction band.

The top surface termination features a first conduction band solely consisting of S-3p states. The disappearance of the Sn-5s states is due to the relaxation of the Sn-atoms, as a comparison of the unrelaxed and relaxed PBE DOS shows (see fig. 4.17). The conduction band is here shifted to lower energies in comparison to the HSE06 DOS due to the utilization of the PBE functional.

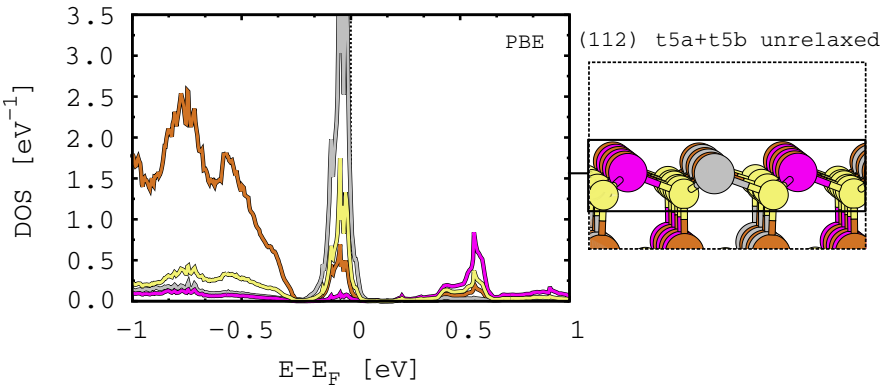

Figure 4.17: Projected PBE DOS for the top termination of the unrelaxed (112) t5a+t5b slab. The DOS is projected on the surface area. The DOS are averaged for every atom type within the highlighted multilayer. Zn is shown in pink, Cu in brown, Sn in gray and S in yellow.

The projection on the bottom surface of the slab discloses the origin of the states within the band gap. The termination on bottom of the slab features Cu-3d and S-3p surface states within the band gap, which arise from dangling bonds, both of Cu and S. Remarkable are the dominating S-3p states in the valence band below the Fermi energy, whereby the surface states are slightly dominated by Cu-3d states. In contrast to the top surface termination, the conduction band of the bottom termination still consists of S-3p and Sn-5s states. In comparison to experimental surfaces in general, these Cu surface states may not occur in experimental measurements due to Cu poor surface terminations [224]. Combing the DOS of fig. 4.15 and 4.16, the magnetization of the slab occurs directly at the bottom surface termination due to the dangling bonds of Cu and S, whereby both atoms contribute equally to the magnetization (see fig. 4.18). The bulk-like layers and top surface termination in contrast show no magnetization.
In summary the nanostructuring of the CZTS material leads to electronic surface structures, which feature surface states within the bulk band gap. These surface states show differing α- and β-spin components at the surface termination, which indicate a magnetic behavior of the termination within the computational model applied. Both new properties are present in all most stable slabs of every surface plane. The newly arising surface states from the dangling bonds at the surface termination decrease the band gap of the slab at the surface, whereas the bulk-like band gap in the middle of the slab is nearly identical to the bulk band gap. The surface states indicate a metallic behavior at the surface termination, which leads to an increased electric conductivity

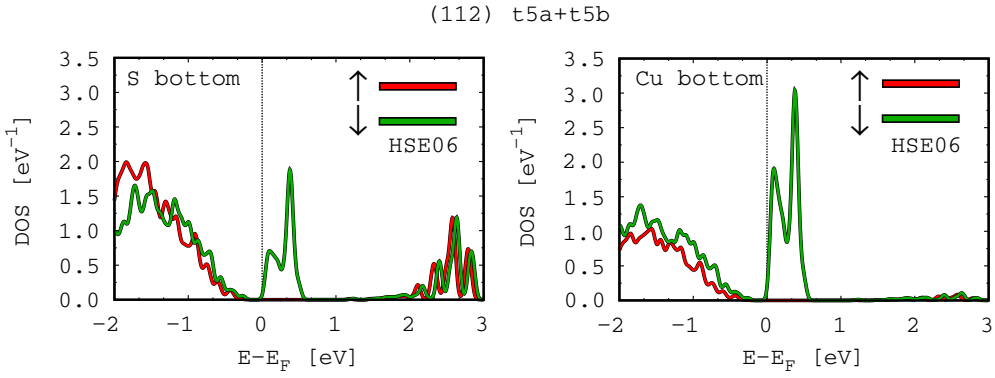

Figure 4.18: Projected HSE06 DOS on the different spin-components of Cu and S of the bottom termination of the relaxed (112) t5a+t5b slab. The DOS is projected on the surface area and is averaged for every atom type within the highlighted multilayer

at the termination of CZTS nanostructures. This increased electric conductivity may contribute to a compensation of conductivity losses at interfaces between CZTS grains or different materials within the thin film solar cell. Furthermore, these surface states may also form recombination centers for excitons at the surface termination, which has to be verified by exciton calculations via for example the Bethe–Salpeter equations [235, 236]. The surface states within the band gap can lead to an increasing energy harvest from the solar radiation due to exhibiting different band gaps and therefore increasing the absorption range of the solar radiation [122]. Therefore, the effects of nanostructuring in total may help to improve the performance and efficiency of the solar cell module due to the increased electric conductivity at the surface terminations and variations of the band gap.

Chapter 5

Nanostructuring by Cu_2ZnSnS_4 Clusters

The previous studies on the nanostructuring of CZTS by surfaces have shown a first effect on the electronic structure like magnetic and conducting surfaces. The next step in researching the influence of nanostructuring on the material properties is a further increase of the surface area in comparison to the bulk volume, namely the modeling of CZTS nanocrystals. CZTS nanocrystals are not only of importance for the theoretical considerations, they also play an important role for the preparation of CZTS thin film solar cells. Instead of preparing CZTS by a solid state reaction of the pure elements in sealed and evacuated ampoules with resulting large single-phase crystals [47, 48], CZTS can also be synthesized in form of nanocrystals in different solution-based processes [49–63]. These nanocrystals then serve as a precursor for the thin films in the solar cell, since they can be coated by different techniques on the glass substrate to form a large polycrystalline absorber film. Nanocrystals in general have attracted scientists over the last years due significant changes in their properties compared to the parent bulk material. The exploitation of quantum size effects can benefit the material properties [117, 118]. Consequently, nanocrystals provide an interesting possibility for an effective engineering for better performing CZTS solar cells. Unfortunately, the effect of CZTS nanostructuring in form of nanocrystals is hard to model from a theoretical point of view. In experiments, researchers have observed quantum confinement effects in the polycrystalline films with varying sizes of the nanocrystals [237]. From a theoretical point of view, the simulation of systems with diameters of up to 50 nm as in experiments [53, 58, 62, 63] and several hundred atoms are especially demanding at a reasonable computational level. A first step for a theoretical research on these nanocrystals is to set up a suitable model, which is structurally similar to realistic nanocrystals. In a first approximation, a realistic nanocrystal features a bulk-like core region and a distorted surface area. Therefore, a first focus is set in this work on a computational model, which features the same structural properties as a realistic CZTS nanocrystal. The nanocrystals are hereby modeled as finite *clusters*. Having found the structural properties in a first approach, a first insight on the electronic structure of CZTS clusters follows. Combining this theoretical model with experiments, a prediction about material modifications for more efficient CZTS solar cells may be provided.

5.1 Technical Framework

5.1.1 Cluster Model

The CZTS nanocrystals are modeled by CZTS clusters, which are obtained by a spherical-like cut out the PBE-optimized bulk structure from the previous investigation on the bulk system (see fig. 5.1). A spherical-like structure is chosen to equally distribute the occurring forces due to the truncation of the bulk over the whole surface area during the structure optimization.

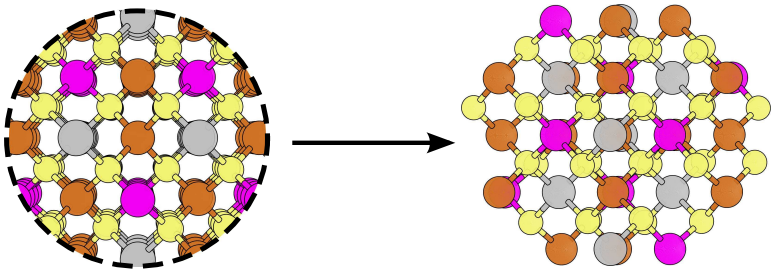

Figure 5.1: The initial nanocluster is cut out of the PBE-optimized bulk system, as optimized in the studies on the bulk systems in sec. 3.2. Then the clusters are adjusted for stoichiometry, which results in a reduction of symmetry to the point group C_1. Zn is shown in pink, Cu in brown, Sn in gray and S in yellow.

The focus is set on stoichiometric clusters for a valid comparison to the periodic bulk properties, since off-stoichiometric structures show strongly varying structural and electronic properties, in which the origin of the changes cannot be assigned precisely. Unfortunately as in the studies on CZTS surfaces, symmetric clusters are only obtained by utilizing off-stoichiometric structures. Therefore, the spherical-like initial clusters are adjusted by removing or adding atoms to obtain bulk stoichiometry, which results in a reduction of symmetry to the point group C_1. As a result of the combination of stoichiometry and the tetragonal unit cell of CZTS, the clusters show spherical-like or ellipsoid-like structures. The clusters are unsaturated at the surface termination to investigate the structural changes upon a distortion of the surface areas. Furthermore, initial calculations with a hydrogen passivation lead to non-converging electronic structures and a creation of H_2 molecules, indicating at least in vacuum that the pure material will form stable stoichiometric clusters. For the structural investigations six clusters are selected (see tab. 5.1). The clusters are named after their centering atom and number of atoms in the cluster. *Cu32* denotes a stoichiometric cluster with 32 atoms, which is centered at a Cu atom. The clusters show a diameter of 0.7 nm to 1.4 nm containing 32 and 96 atoms respectively.

Table 5.1: Stoichiometry of all selected CZTS clusters from 32 to 96 atoms. All investigated clusters feature multiples of the bulk stoichiometry Cu_2ZnSnS_4.

cluster	stoichiometry
Cu32	$Cu_8Zn_4Sn_4S_{16}$
Cu64	$Cu_{16}Zn_8Sn_8S_{32}$
Sn64	$Cu_{16}Zn_8Sn_8S_{32}$
Zn64	$Cu_{16}Zn_8Sn_8S_{32}$
S64	$Cu_{16}Zn_8Sn_8S_{32}$
Cu96	$Cu_{24}Zn_{12}Sn_{12}S_{48}$

A first approach for the theoretical modeling of the CZTS clusters is the investigation of structural influences. Hereby two key factors are of interest:

a) The development of a *core-shell system* with increasing cluster size.

b) Clusters with the same number of atoms, but different structure.

The second point b) is investigated with respect to the core-shell system, whereby clusters with the same number of atoms, but different structures are created. The first point a) gives insight on structural changes upon increasing the cluster size, which are quantified by the *critical size* of the cluster and the definition of the core-shell system. The *critical size* of the cluster is hereby defined as a diameter and atom number threshold at which the cluster can be divided in a core-shell system, which is achieved when a structural division in a bulk-like core part and a distorted shell part is possible. (see fig. 5.2).

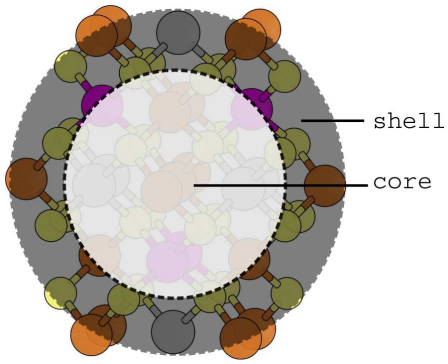

Figure 5.2: Core-shell system of the CZTS cluster. The core stays bulk-like after the structure optimization, whereas the shell strongly reconstructs due to the truncation of the material. Zn is shown in pink, Cu in brown, Sn in gray and S in yellow.

The *core* part of the cluster features after the structure optimization a nearly fixed bulk-like structure in the center of the cluster obeying the valency and nearly all bond lengths of the initial bulk structure. The *shell* part of the cluster describes the outer part, which is exposed to the vacuum in the applied computational model and strongly reconstructs to saturate the dangling bonds. The shell is the finite analog to the CZTS surface structures in chap. 4.
At a certain critical size of the cluster, the core-shell system is established after a structure optimization and can act as a model structure for a realistic nanocrystal. This model cluster should in general feature similar structural properties as a realistic nanocrystal and may also feature similar electronic properties. In the limit of increasing the cluster size, namely decreasing the surface to bulk ratio of the structure, the CZTS surface model from the previous investigations should be reached. Unfortunately, clusters with sizes of several 100 atoms are beyond the scope of computational resources at the DFT-level or approximated DFT methods like Density Functional based Tight Binding (DFTB) [238, 239]. For these tasks suitable classical force fields have to be fitted for CZTS, which can be based on this first approach by quantum chemical methods.
To quantify a core-shell system, the structural changes have to be analyzed analytically, since a rough approximation of the structural changes by eye is only possible for small (< 30 atoms) structures. This analysis is performed by the *distance* and *change matrix* of a cluster, whereby the center of the cluster is taken as a reference point. The distance matrix contains all distances between every atom within the cluster and is defined by

$$\mathbf{D}_{ij} = |\mathbf{r}_{ji}| \,. \tag{5.1}$$

The indices here represent the ith and jth atom of the cluster, whereby $\mathbf{r}_{ij}$ denotes the inner atomic distance between both atoms. The distance matrix $\mathbf{D}_{ij}$ has the dimension of NxN, where N is the total number of atoms within the cluster. The change matrix, also a NxN matrix, is defined as the difference between the distance matrices of the relaxed cluster ($\mathbf{D}_{\mathrm{rlx}}$) and the unrelaxed cluster ($\mathbf{D}_{\mathrm{urlx}}$), which corresponds to the bulk structure:

$$\mathbf{D}_{\mathrm{change}} = \mathbf{D}_{\mathrm{rlx}} - \mathbf{D}_{\mathrm{urlx}}. \tag{5.2}$$

The process of the structure optimization is then visualized by a heat map of the change and distance matrix, illustrated in fig. 5.3. Red and blue indicate large and small inner atomic distances r_{ij} in the distance matrix respectively. In the change matrix positive values indicate an expansion of the inner atomic distance between two atoms (red), whereas a contraction of the inner atomic distance between two atoms is shown by negative values (blue). The difference of inter atomic distances is hereby denoted as Δr_{ij}.

The heat maps are constructed as follows:

a) The center of the cluster is shown at x=0 and y=0 with the corresponding label for the centering atom.

b) The atom label indicates several atoms of the same type and with the same distance to the central atom.

c) By moving along the x- or y-axis, a radial scan towards the surface of the cluster is performed, i.e. at y=max and x=max the most outer atoms are reached.

d) In the distance matrix the inner atomic distance r_{ij} and in the change matrix the difference Δr_{ij} of the inner atomic distances of unrelaxed and relaxed structures are shown.

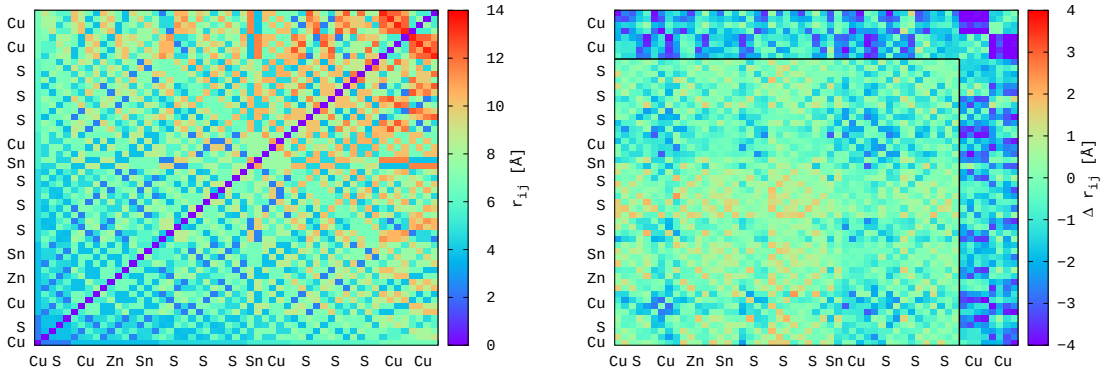

Figure 5.3: Distance and change matrix for an off-stoichiometric symmetric in S_4 CZTS cluster with 55 atoms centered at Cu (Cu55). The left heat map shows the distance matrix of an unrelaxed cluster. The right heat map represents the change matrix of the relaxation. The black line indicates the division in core and shell part, which occurs here at 45 atoms.

From the given example Cu55 can be concluded that the model cluster mainly relaxes in the outer shell, indicated by blue at y,x=max, whereby the core shows only minimal relaxations (green). The atom cutoff for the core-shell system is indicated by a black line. This model cluster Cu55 therefore features a core-shell system with 45 atoms in the core and 10 atoms in the shell. The distance matrix reveals the approximated maximum diameter of the cluster. The radial sequence of atoms of the unrelaxed structure is kept as a reference and is not adopted to the new radial sequence of the relaxed cluster. Additionally, the imperfect spherical structure leads to contractions, which are not exclusively located at x=max or y=max, referred to as *structural anisotropy*. The unrelaxed structure of the above illustrated matrices is exemplarily shown in fig. 5.4.

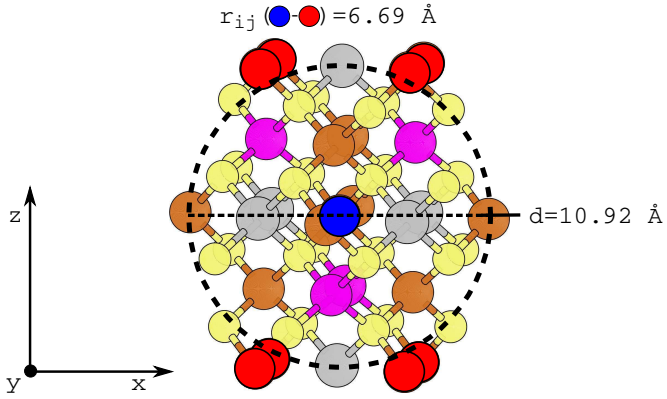

Figure 5.4: Structural features of Cu55. Due to the tetragonal unit cell of CZTS, the clusters are ellipsoid shaped rather than perfectly spherical. This leads to an anisotropic radial distribution of atoms within the nanocluster. r_{ij} denotes the distance between the red and blue Cu atoms, whereby d denotes the diameter of the cluster. Zn is shown in pink, Cu in brown, Sn in gray and S in yellow.

With these starting conditions, the structural behavior of a core-shell system can easily be detected.
An approximation for the different stabilities of the investigated clusters can be obtained by their binding energy, which can be defined as

$$E_{\text{bind}} = \text{Cu}_\alpha\text{Zn}_\beta\text{Sn}_\gamma\text{S}_\omega - [\alpha \cdot \text{Cu}_{(\text{g})} + \beta \cdot \text{Zn}_{(\text{g})} + \gamma \cdot \text{Sn}_{(\text{g})} + \omega \cdot \text{S}_{(\text{g})}], \tag{5.3}$$

where $\text{Cu}_\alpha\text{Zn}_\beta\text{Sn}_\gamma\text{S}_\omega$ is the energy of the relaxed cluster and $\alpha{\cdot}\text{Cu}_{(\text{g})}$, $\beta{\cdot}\text{Zn}_{(\text{g})}$, $\gamma{\cdot}\text{Sn}_{(\text{g})}$ and $\omega{\cdot}\text{S}_{(\text{g})}$ are the atomic energies times their stoichiometric factor in the nanocluster. The atoms assumed in their electronic ground state are hereby taken as a reference energy for an approximation of the binding energies, whereby the binding energy only acts as a comparison tool for the different clusters. The absolute binding energies are not comparable to other cluster systems. They further reveal, if there is a stabilizing effect with increasing cluster size or with different structure. Another indicator for the relaxation process and the stability of a CZTS cluster is the relaxation energy, which gives information about the energy gain during the structure optimization. The relaxation energy is given by

$$E_{\text{relax}} = E_{\text{rlx}} - E_{\text{urlx}}, \tag{5.4}$$

with E_{rlx} as the total energy of the relaxed cluster and E_{urlx} as the total energy of the unrelaxed cluster. With the help of these tools the influence of nanostructuring on the structural properties of CZTS is investigated.

5.1.2 Computational Details

The finite clusters were calculated within the Kohn Sham DFT framework as implemented in Turbomole 7.0.1 [240]. For the visualization of the structures XCrySDen [189, 190] and VMD [241] were used. In all calculations the hybrid-functional PBE0 [197] and the def2-TZVP basis set [242, 243] were employed. As proven in previous chapters, PBE0 yields good agreement with experimental data with respect to the structural description of CZTS. All atoms except Sn were treated by an all electron basis set, whereby Sn was treated with the ECP28MDF effective core potential (ECP) with 28 core electrons, which is a fully relativistic ECP obtained by a multi electron fit [244]. On top of this ECP also the def2-TZVP basis set was used for Sn. The clusters were fully optimized without constraints in the point-group C_1 in vacuum. The electronic structure was converged until an energy convergence threshold of 10^{-6} eV was reached. In every calculation an unrestricted Kohn Sham approach was utilized to include additional degrees of freedom for the electronic structure. Since bulk CZTS in experiment and in the previous investigations in sec. 3.2 shows no magnetism, a singlet state was assumed for the electronic structure. For a verification of these starting points, restricted DFT calculations are performed for two specific clusters to investigate the particular influence of the initial starting condition of an unrestricted singlet KS ansatz on the ionic structure in CZTS clusters (see fig. 5.5). In both structures the clear structural pattern of core and shell (separated by the black lines, also referred to as *cutoff radius*) remains, therefore the singlet unrestricted electronic starting structure is a valid ansatz for the investigations of the structural properties. On top of every optimized structure, single point calculations for the atomic charges via a Natural Population Analysis (see sec. 2.7.2) were performed [182]. For a closer analysis of the orbitals and spin difference densities, the electronic structure is visualized with Orbkit [245]. As reference system for the binding energy, atomic energies are calculated with the same settings as in the cluster calculations, whereby the atoms are assumed in the electronic ground state.
For selected examples, TDDFT single point calculations were performed on top of the PBE0-optimized structures and orbitals to obtain optical spectra and optical gaps for a comparison to experimental studies performed by experimental cooperation partners. The same settings as in the PBE0/def2-TZVP calculations were utilized. As a starting point for the TDDFT calculations, the electronic convergence threshold was set to 10^{-7} eV for well converged PBE0/def2-TZVP orbitals.

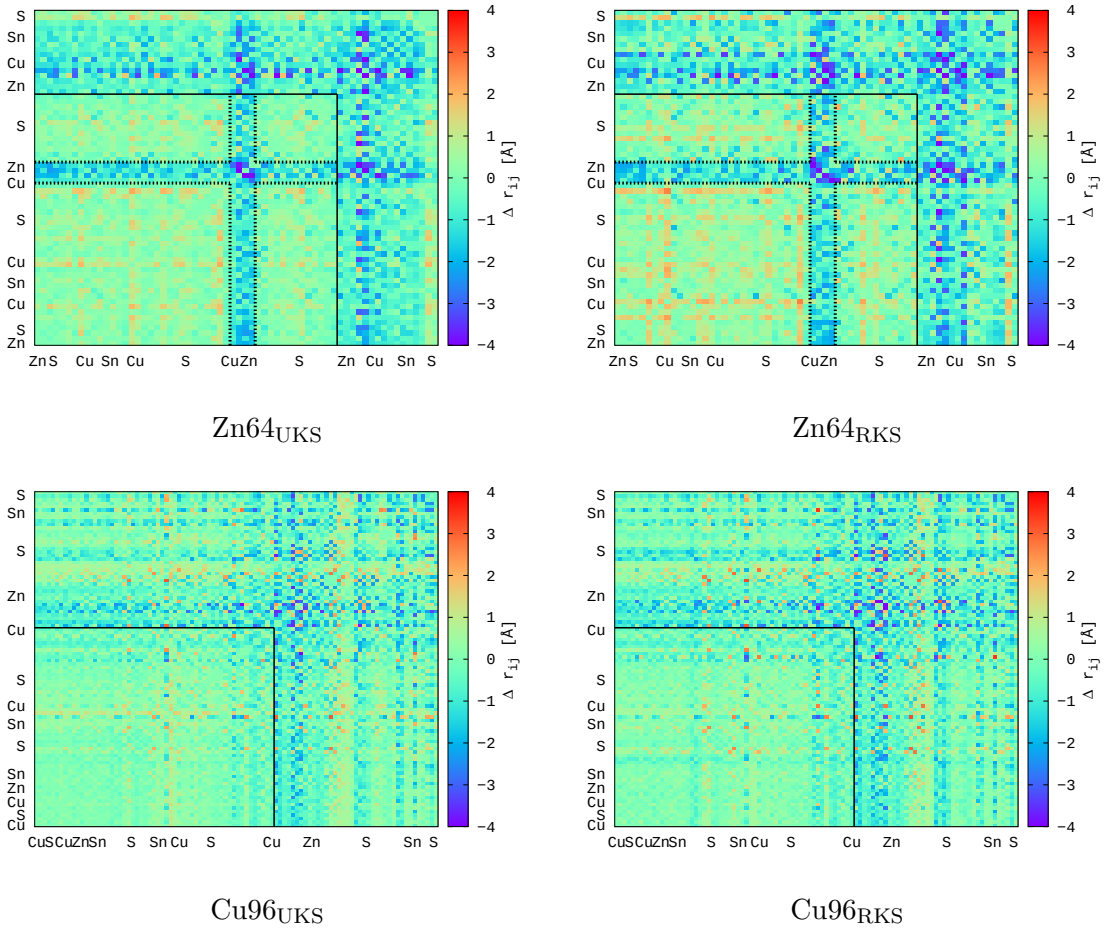

Figure 5.5: Change matrices of Zn64 and Cu96 with an unrestricted (UKS) singlet and a restricted (RKS) singlet Kohn Sham DFT ansatz. Cu96 shows an $\langle S^2 \rangle$ expectation value of 0.0 after the structure optimization, whereby Zn64 yields an expectation value of 2.82. A more detailed discussion of $\langle S^2 \rangle$ expectation values is shown in sec. 5.3. The black lines indicate an atom cutoff for the division in core and shell, whereas the atoms included by the dashed line are located in the most outer shell of the cluster due to the ellipsoid shape.

5.2 Structural Properties of Cu_2ZnSnS_4 Clusters

For the influence of the cluster sizes on the structural properties, the clusters Cu32, Cu64 and Cu96 are selected. The clusters Cu64, Zn64, Sn64 and S64 are chosen for the investigation of clusters with the same number of atoms, but different structures. Starting with the size effects, the unrelaxed (urlx) and relaxed (rlx) clusters Cu32, Cu64 and Cu96 are illustrated in fig. 5.6. An analysis by eye yields strong reconstructions of the clusters during the structure optimization to satisfy dangling bonds. Cu32 shows strong reconstructions, whereby S-S dimers at the surface area are formed. By doubling the size in Cu64, the surface also strongly reconstructs, whereby the core indicates only minimal relaxations. The same behavior is shown in Cu96, in which the core part of the cluster is hardly visible.

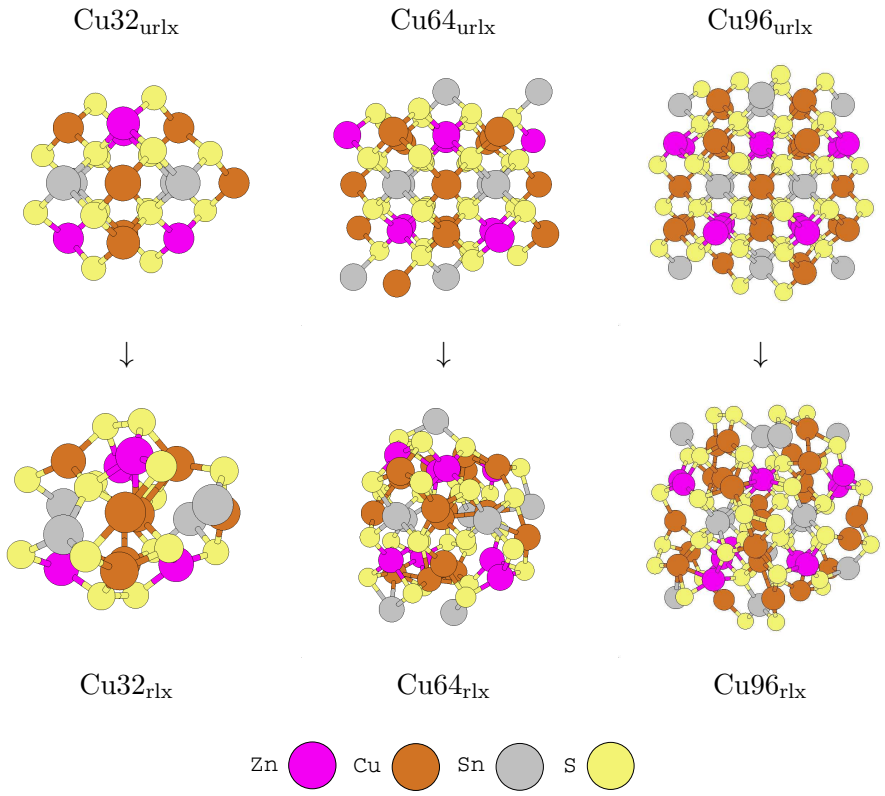

Figure 5.6: Unrelaxed (urlx) and relaxed (rlx) clusters Cu32, Cu64 and Cu96 at the PBE0/def2-TZVP level are shown.

The introduction of the change matrix facilitates the quantitative analysis of the structure relaxation, illustrated in fig. 5.7. Cu32 shows contractions over the whole structure, whereby especially the most outer Cu atoms contract. The core region also slightly contracts, whereas one Cu-S and one S-S bond within the core slightly expand. Doubling the cluster size, a clear structural pattern is obtained in Cu64. Cu64 features a core region of 46 atoms, indicated by the black lines, in which the main part of the core atoms show only minor relaxations.

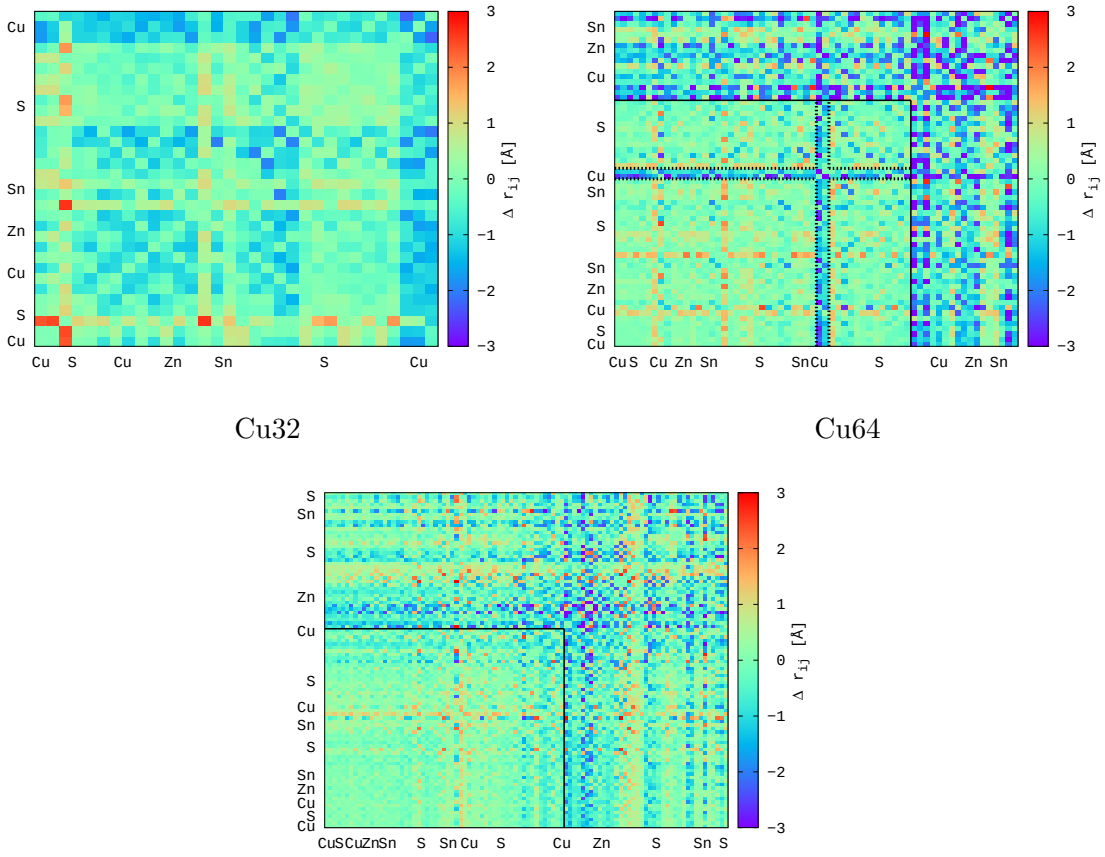

Figure 5.7: Change matrices of differently sized Cu-centered clusters at the PBE0/def2-TZVP level. The black lines indicate an atom cutoff for the division in core and shell, whereas the atoms included by the dashed lines are located in the most outer shell of the cluster due to the ellipsoid shape.

The contraction of Cu enclosed by dashed lines in the change matrix is due to the structural anisotropy, whereby the Cu at this radius are exposed at the shell to the vacuum, leading to missing binding partners and stronger reconstructions than other atoms with the same inner atomic distance to the central atom (see fig. 5.8). Cu64 shows first indications for the critical size for the establishment of a core-shell system. Further increasing the cluster size to 96 atoms in Cu96, this trend is underlined. Cu96 shows that only the outer shell (40 atoms) relaxes and the core (56 atoms) stays bulk like, whereby both parts are separated by a black line in the change matrix. As in Cu64, the structural anisotropy of Cu96 leads to contractions in the shell, which are not exclusively located at r_{ij}=max but also at the cutoff radius between core and shell. Cu96 features a clear core-shell system. Combining the structural patterns of Cu32 to Cu96, the core-shell system is established at a cluster size of 64 atoms or approximately a diameter over 1 nm.

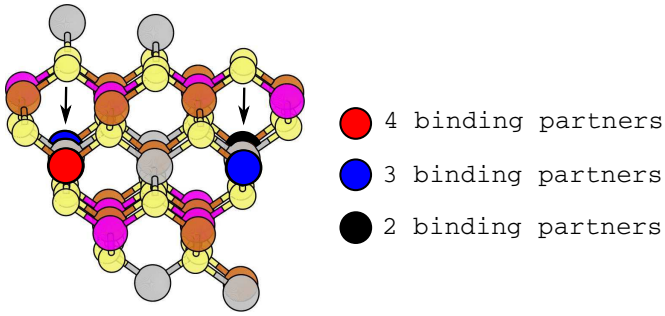

Figure 5.8: Visualization of the ellipsoid structure of Cu64. The red Cu shows four binding partners, blue shows three binding partners and black Cu shows two binding partners. Zn is shown in pink, Cu in brown, Sn in gray and S in yellow.

The four selected structures with the same number of atoms but different structures feature a similar structural behavior like Cu32, Cu64 and Cu96. Concluding from the size effects above, clusters with 64 atoms are chosen for an established core-shell system. Cu64, Zn64, Sn64 and S64 differ in their centering atom, which leads to different structures. The selected unrelaxed and relaxed clusters are illustrated in fig. 5.9. Sn64 and Zn64 show a similar structure, whereby the similarity is reduced after the structure relaxation. As in the structures before, all clusters show strong reconstructions of the shell, whereby first indications by eye are shown for a nearly unrelaxed core.

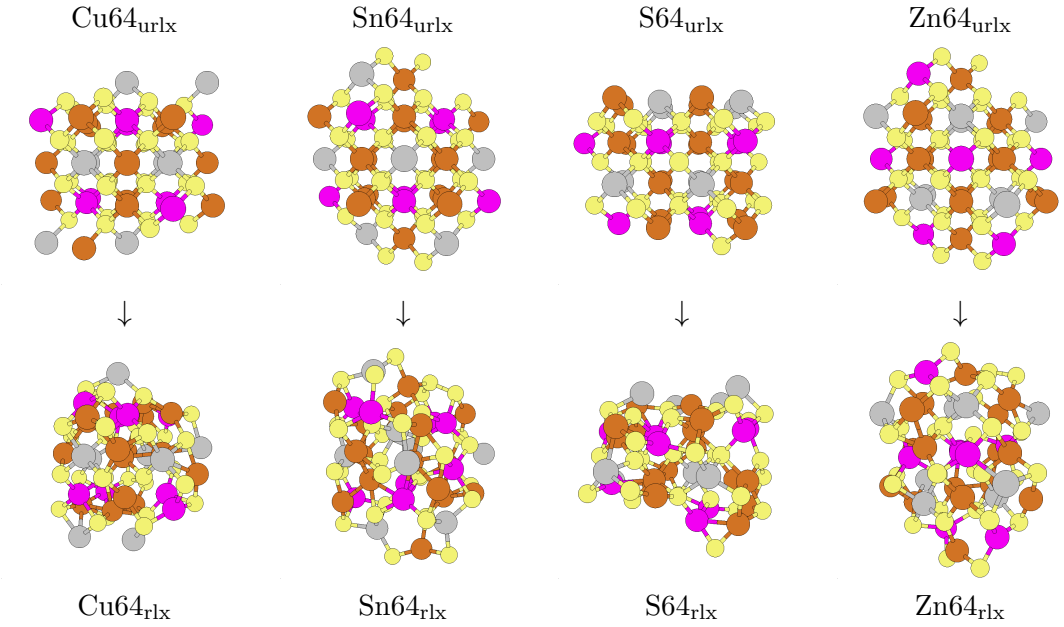

Figure 5.9: Unrelaxed and relaxed clusters with 64 atoms at the PBE0/def2-TZVP level. All clusters are centered at different atom types. Zn is shown in pink, Cu in brown, Sn in gray and S in yellow.

The more detailed analysis by change matrices reveals similar structural patterns for all clusters after the structure relaxation, illustrated in fig. 5.10. All four clusters feature a shell part, at which strong contractions occur due to the unsaturated termination of the clusters. In the core, the clusters show slight deviations. As observed before, Cu64 features a core, which hardly relaxes. Zn64 in total shows a similar relaxation as Cu64, whereby the reconstruction regions are broadened, which is due to Zn/Cu exposed at the surface in contrast to Sn/Cu in Cu64. This is a structural similarity to the previously observed trends in the relaxations of the surfaces in chap. 4. The core of Zn64 contains about 47 atoms, whereby as in Cu64, a shell part is included (indicated by dashed lines) due to the ellipsoid shape of the cluster.

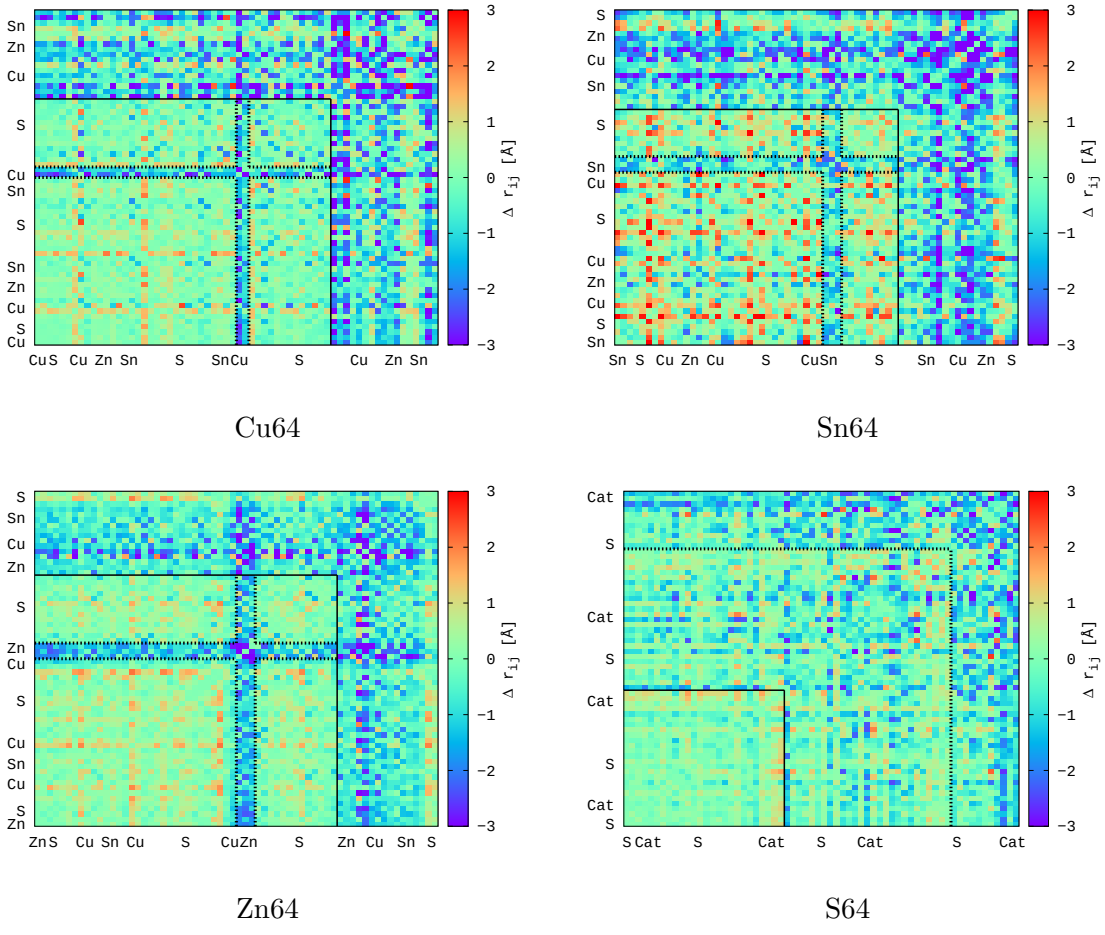

Figure 5.10: Change matrices of all clusters with 64 atoms at the PBE0/def2-TZVP level. All clusters are centered at different atom types. The label *Cat* in S64 denotes several cation types, which vary to frequently for a clear labeling. The black lines indicate an atom cutoff for the division in core and shell, whereas the atoms included by the dashed line are located in the most outer shell of the cluster due to the structural anisotropy.

S64 shows in the core region minor relaxations, whereby the pattern is not as distinct as in Cu64 and Zn64. The core can be described by 25 atoms, whereby a first inner shell spans from 25 to 52 atoms and the outer shell from 53 to 64 atoms. Depending on the initial conditions, the first shell up to 52 atoms may also be included in the core region. The last cluster, Sn64, features a relaxation of the central part. The Sn atom in the center moves out of the center towards the outer shell in z-direction (see fig. 5.11), showing that the Sn-centered cluster is structurally not as stable as the Cu- and Zn-centered clusters, which is influenced by different surface topologies in the different clusters. Though the central atom reconstructs heavily, the rest of the central part stays more or less on the bulk-like position, so that even for the Sn64 cluster one can talk of a core-shell system, because the outer shell relaxes more strongly. Excluding the central atom relaxations, Sn64 features a similar core-shell structure (44 atoms core, 20 atoms shell) as Cu64 and Zn64. In summary, a lower limit of 64 atoms is necessary for an established core-shell system, whereby the size of the core varies with different structures.

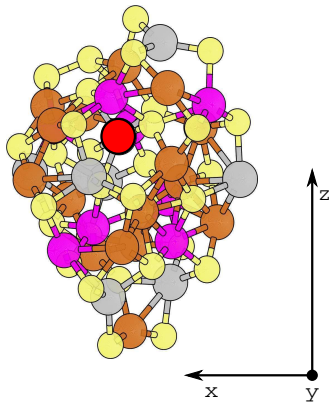

Figure 5.11: Structural features of Sn64 at the PBE0/def2-TZVP level. During the structure relaxation, the central Sn atom relaxes into z-direction, indicated by the red highlighted Sn atom. Zn is shown in pink, Cu in brown, Sn in gray and S in yellow.

Information about the stability of the different clusters can be derived from the binding energy after eq. 5.3 and the relaxation energy after eq. 5.4. The calculated binding and relaxation energies at the PBE0/def2-TZVP level per atom are summarized in tab. 5.2. The binding and relaxation energy of Cu96 are taken as a reference, since it shows the most stable cluster with respect to the employed reference energies of the atoms. Positive values therefore indicate less stable structures and fewer relaxations. Increasing the cluster size with the clusters Cu32, Cu64 and Cu96 yields a slight stabilization of the clusters. The differences in stability in Sn64, Cu64, Zn64 and S64 are distinctly larger. Cu64 and Sn64 feature the same stability, whereby Zn64 and S64 show less favorable stabilities. The relaxation energies for the differently sized clusters show overall no clear trend. In comparison to Cu96, Cu32 and Cu64 feature a stronger relaxation than

Cu96, whereby Cu64 relaxes unexpectedly even more than Cu32, which may be a result of unfavorable unrelaxed shell of Cu64. A stronger relaxation of Cu32 than Cu96 is reasonable, since the increasing structure relaxes less due to the larger bulk-part. The different structures in Cu64, Zn64, Sn64 and S64 show varying relaxation energies. The more stable structures Cu64 and Sn64 hereby exhibit a larger energy gain during the relaxation than the more unstable ones Sn64 and S64. A reason for this varying stabilities are the different shells as well as different central atoms. Since the surface areas all feature a similar amount of different atom types, no clear trend can be observed yet. By increasing the data set a statistical analysis may show a correlation between the stability and the surface topology.

Table 5.2: Binding energy and relaxation energy per atom for all calculated CZTS clusters at the PBE0/def2-TZVP level. The binding and relaxation energy of Cu96 serves as a reference, since it shows the most stable structure. Positive values indicate smaller binding and relaxation energies.

cluster	rel. E_{bind}/atom [meV]	rel. E_{relax}/atom [meV]
Cu32	0.06	-0.09
Cu64	0.04	-0.14
Sn64	0.04	-0.11
Zn64	0.08	0.01
S64	0.11	-0.07
Cu96	0.00	0.00

A first step to the analysis of the electronic structure of the relaxed clusters are atomic charges, determined here by a Natural Population Analysis [182]. The charges for the differently sized clusters are shown in fig. 5.12. At x=0, the central atom of a cluster is shown, whereby proceeding to x=max the most outer atom with respect to the central atom is reached. Since Cu96 features a clear core-shell system, the atomic charges in the most inner core are taken as reference charges. Hereby Cu features a mean charge in the core of 0.75 e, S of -1.18 e, Zn of 1.45 e and Sn of 1.41 e. The charges in the inner core of the cluster are referred to as *core charges* in the following, whereby charges in the outer reconstructed shell are referred to as *shell charges*. Cu32 shows charge deviations between the core and shell charges. In the core, all Cu atoms show similar charges, which is also shown for all S atoms and all Zn atoms in the core. Moving to the shell, especially the S charges start to deviate, showing partially lower charges than the core charges of S, which is due to a lack of binding partners at the surface. The Cu atoms exposed at the surface show charges nearly identical to the core charges, which is a result of the reconstruction. The Cu32 core charges are similar to the reference charges, which is a result of the bulk valency in the center of the cluster. Cu64 shows a similar behavior in the core with only small deviations from the reference charges. The second S group (shell) reveals charge fluctuations, which slightly normalize in the third S shell. The two low S charges in the second S shell are due to the anisotropic

structure, resulting in a lack of binding partners. However, Zn shows identical charges in the core and shell, indicating a full saturation of surface Zn. Cu slightly starts to deviate from the core to the shell atoms, but shows only minor fluctuations in the outer shell. The Sn charges decrease slightly while moving to the surface. Cu96 reveals negligible Cu and Zn charge deviations throughout the cluster, whereas the Sn charges decrease from the core to the shell part of the cluster. In the shell, Sn is only charged with a mean charge of 0.9 e, whereas in the core charges are 1.41 e. S shows strong charge fluctuations in the shell part of the cluster where the charges decrease to half the value of the core charges. As in Cu64 before, charge fluctuation exist within the core-shell region due to the anisotropy of the structure.

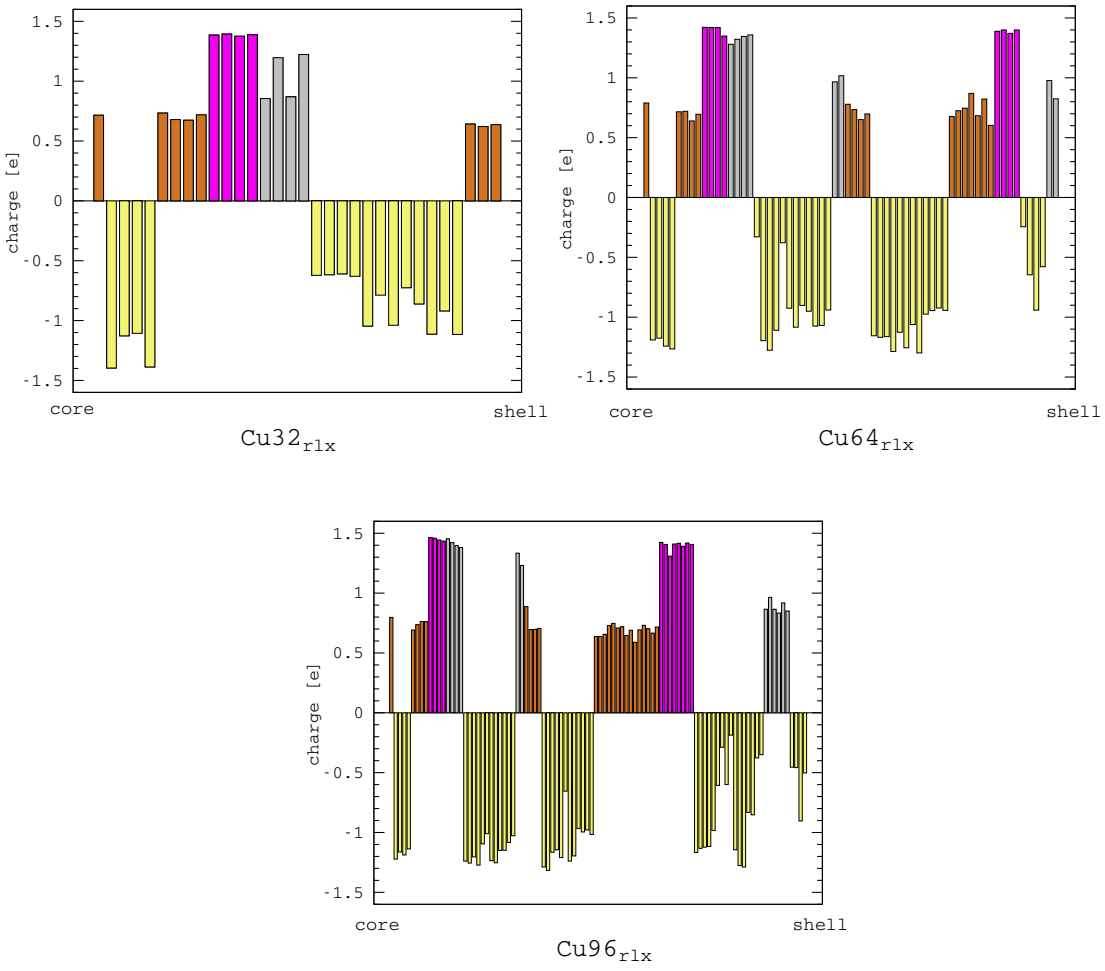

Figure 5.12: Natural population analysis for the clusters with increasing size at the PBE0/def2-TZVP level. The radial sequence of the atoms starts from the core at x=0 to the surface at x=max. Zn is shown in pink, Cu in brown, Sn in gray and S in yellow.

The charges for the differently structured 64 atom clusters are illustrated in fig. 5.13, whereby the clusters feature a similar behavior as seen before. Over all four structures, Zn in the core and shell shows neglectable charge fluctuations, which slightly increase in case of Cu. Sn in the core is more positively charged than in the shell, whereby S

is more negatively charged in the core than in the shell. The different S in the shell sometimes display especially low charges due to the structural anisotropy, where few S atoms are exposed at the surface and lacking binding partners. Concluding from the charge analysis, the same trends hold true for the differently structure clusters as well as differently sized clusters.

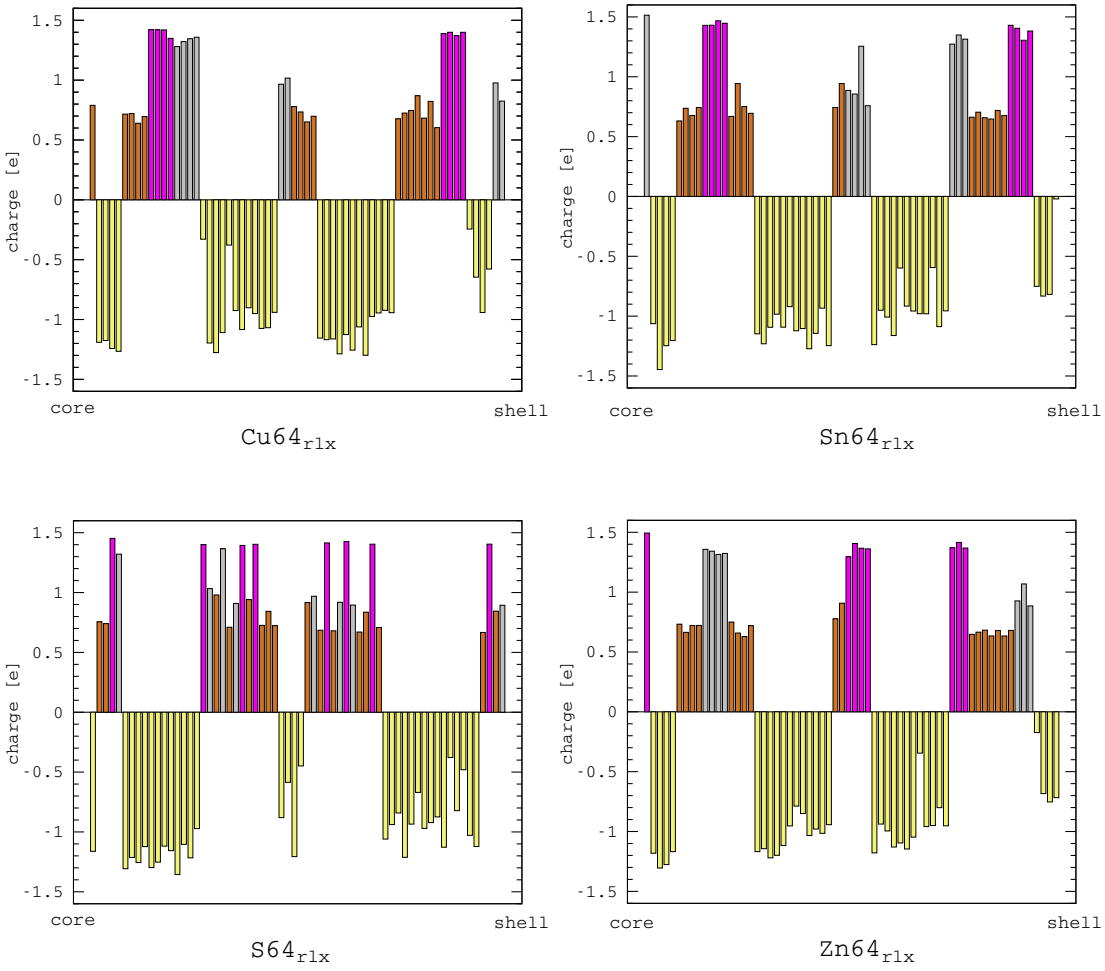

Figure 5.13: Natural population analysis for the clusters with the same number of atoms, but different starting structure at the PBE0/def2-TZVP level. The radial sequence of the atoms starts from the core at x=0 to the surface at x=max. Zn is shown in pink, Cu in brown, Sn in gray and S in yellow.

In summary, the structural properties reveal that the critical size for a structurally converged cluster in form of a core-shell system is approximately at 64 atoms or 1 nm in diameter. Increasing the size of the clusters to 96 atoms in Cu96, the core-shell system is further underlined. Furthermore, the different structures of the 64 atom clusters show that the centering atom is important for a bulk-like structure in the core. Cu, Zn and S feature a nearly bulk-like core in the center of the cluster, whereas the central atom in Sn64 strongly reconstructs. The clusters are slightly stabilized with increasing size, whereby stability fluctuations occur in clusters with 64 atoms due to

different structures. Cu- and Zn-centered 64 atom clusters are hereby more stable than Sn- and S-centered clusters. The charge analysis reveals that charge changes mainly occur between Sn/S in the core and Sn/S in the shell, whereby Cu and Zn show constant charges in core and shell. Core Cu/Zn and shell Cu/Zn hereby only minimally differ. The 64 atom cutoff lies within the computational limits of the DFT-framework, whereas the experimental sizes of usually up to 50 nm [53, 58, 62, 63] are only calculable with classical force fields, which can be based on the quantum chemical data obtained by this study. Furthermore, by utilizing DFTB (Density Functional based Tight Binding) [238, 239], the cluster sizes may be increased over 100 atoms. By introducing pseudo potentials for all atom types, the cluster size may also be further increased, whereby preliminary calculations have shown that the pseudo potentials influence the structure of the relaxed cluster. In comparison to the previous studies on CZTS surfaces, similar structural properties are observed. The reconstructions in the clusters are more prominent, since the stabilizing bulk-part is smaller than in the slabs, but overall similar patterns are observed like the formation of S-S dimers or bonds between cations due to a lack of binding partners at the surface termination. The charge analysis of both nanostructuring models features charge deviations between the bulk-like part of the structures and the surface part of the structures. Hereby the bulk-like part are the middle of the slab or the core of the cluster and the surface part refers to the surface termination in the slabs and shell in the cluster. In both models, the charges at the surface termination show distinctly lower charges than the bulk region, whereby the clusters show more stable shell Zn and Cu charges than the slabs, which is a result of the stronger reconstructions in the clusters to satisfy the dangling bonds.

5.3 Electronic Structure of Cu_2ZnSnS_4 Clusters

A first insight on the electronic structure of CZTS clusters is given by the analysis of the energy difference between the eigenvalues of the highest occupied (HOMO) and lowest unoccupied (LUMO) molecular orbitals obtained after the atomic charge analysis, which serve as an approximation for the fundamental gap [246]. The HOMO/LUMO gaps at the PBE0/def2-TZVP level with an unrestricted singlet KS ansatz are summarized in tab. 5.3.

Table 5.3: HOMO/LUMO gaps and $\langle S^2 \rangle$ expectation values for all calculated CZTS clusters at the PBE0/def2-TZVP level with an unrestricted singlet KS ansatz as obtained after the atomic charge analysis.

cluster	Δ E [eV]	$\langle S^2 \rangle$
Cu32	2.43	0.0
Cu64	1.29	1.88
Sn64	1.70	1.01
Zn64	1.48	2.82
S64	0.77	3.97
Cu96	0.98	0.0

The HOMO/LUMO gaps reveal deviations with respect to different cluster sizes and different structures with the same number of atoms. The PBE0 bulk band gap of 2.11 eV from sec. 3.2 is taken as a reference. Starting with Cu32, the cluster features a HOMO/LUMO gap of 2.43 eV. The gap then decreases with increasing cluster size from 1.29 eV to 0.98 eV for Cu64 and Cu96 respectively. The different structures for the 64 atom clusters yield a broad range of HOMO/LUMO gaps from 0.77 eV for S64 to 1.70 eV for Sn64, whereby Zn64 with 1.48 eV and Cu64 with 1.29 eV lie within the extrema. A possible reason for this variation lies in the changed $\langle S^2 \rangle$ eigenvalues from the initial $\langle S^2 \rangle = 0$, which is an effect of the unrestricted KS ansatz. This change indicates that the initial singlet guess yields an insufficient description of the electronic structure for these clusters. Sn64 shows an expectation value $\langle S^2 \rangle$ of 1.01, Cu64 of 1.88, Zn64 of 2.82 and S64 of 3.97, which strongly deviate from the initial guess. As a result, the clusters show a magnetized shell, indicated by the visualization of the spin difference density calculated as α - β spin density (see fig. 5.14). The spin difference density shows unevenly distributed α- and β-spins on the surface of the clusters, which is in good agreement with the same observation in the DOS of the CZTS surfaces in sec. 4.3. The different $\langle S^2 \rangle$ eigenvalues are a result of remaining dangling bonds at the shell, which are often localized at S, Cu and Sn, leading to different energies for α- and β-orbitals and therefore different HOMO/LUMO gaps. Therefore, the electronic results of the 64 atom clusters have to be considered with care and need further investigations for a correctly described spin state.

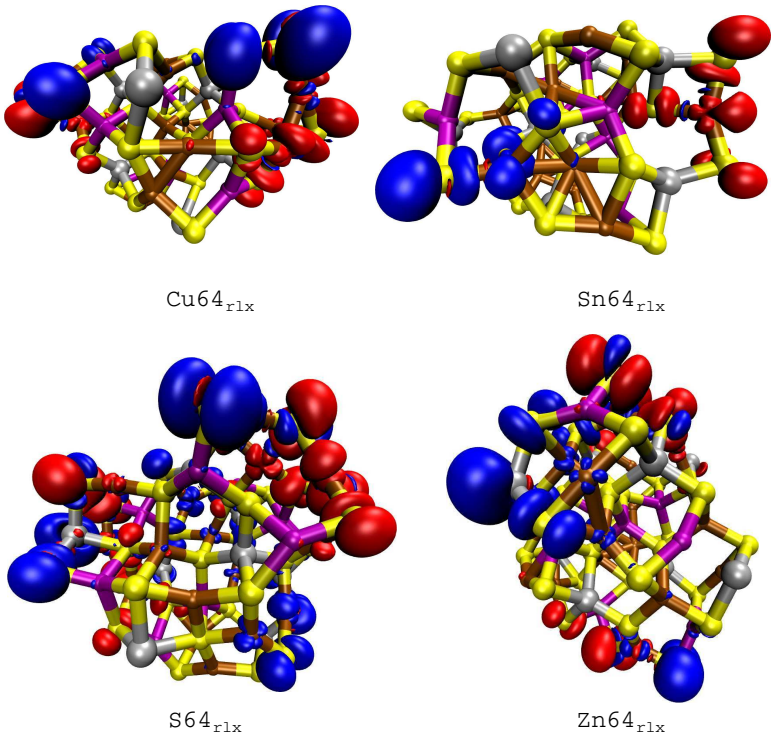

Figure 5.14: Spin difference densities for all 64 atom clusters at the PBE0/def2-TZVP level, obtained by the difference of α and β spin density. Red and blue indicate β- and α-densities respectively. Zn is shown in pink, Cu in brown, Sn in gray and S in yellow.

Since the band gaps in experiment are mostly determined optically, subsequent TDDFT single point calculations on top of the PBE0 structure optimizations were performed for optical spectra and optical gaps. Since the initial guess for the electronic structure of the 64 atom clusters is insufficient, the TDDFT optical absorption spectra and optical gaps are calculated for Cu32 and Cu96, since they show an unchanged expectation value $\langle S^2 \rangle$ after the atomic charge analysis, illustrated in fig. 5.15.
The TDDFT spectra show that Cu32 features a high density of possible excitation energies in the range from 1.8 eV to 2.6 eV. Cu96 in contrast, in which only the first ten excitations could be calculated due to computational limits, shows two excitation domains from 0.55 eV to 0.65 eV and from 1.05 eV to 1.4 eV, which are separated by a larger gap. The TDDFT calculations show that the optical gap is 1.816 eV in Cu32 and 0.543 eV in Cu96 (see tab. 5.4).

Table 5.4: TDDFT optical gaps for the CZTS clusters Cu32 and Cu96 on top of the PBE0/def2-TZVP atomic charge analysis.

cluster	Δ E_{TDDFT} [eV]
Cu32	1.816
Cu96	0.543

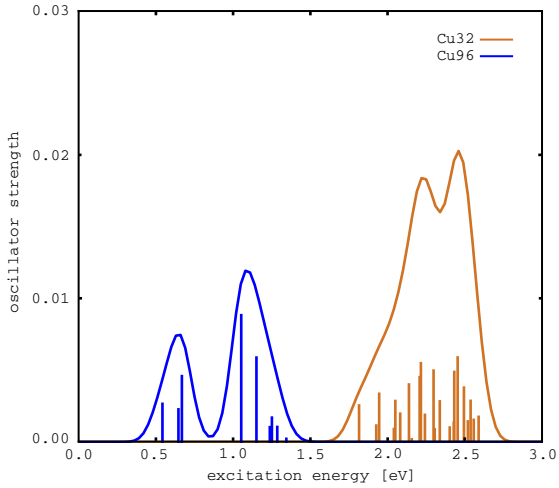

Figure 5.15: TDDFT spectra for Cu32 and Cu96 on top of the PBE0/def2-TZVP calculations. In Cu32 40 excitations were considered, whereby in Cu96 ten excitations were considered due to computational limits. The curves are obtained by a Gaussian distribution of the oscillator strengths with a σ of 0.1 eV.

The resulting electron-hole pair binding energy, as the difference between HOMO/LUMO gap and the optical gap, is 0.614 eV for Cu32 and 0.437 eV for Cu96. These values are noticeably higher than the exciton binding energy of 10 meV in the experimental bulk structure [65], which is caused by the small sizes of the clusters as well by influences of the surface terminations. Unfortunately there are no UV-VIS absorption spectra available yet for isolated CZTS nanocrystals, therefore a comparison to experiment is not possible at the moment.

In summary the first insight on the electronic structure of CZTS clusters reveals that the HOMO/LUMO gap decreases with increasing cluster size, which is similar to the reported quantum confinement effect in experiment. In contrast to a real quantum confinement effect, in which the gap decreases in the limit to the bulk band gap, the cluster gap decreases below the bulk band gap, which possibly is a result of the small size of the clusters in comparison to the large nanocrystals of up to 50 nm in experiment [53, 58, 62, 63, 237]. In this cluster model, the surface affects the electronic structure stronger than in experiment, since the surface to bulk ratio is noticeably higher. The influence of the cluster shell is especially shown in the 64 atom clusters, which feature a broad range of different HOMO/LUMO gaps despite featuring the same number of atoms. Due to the remaining dangling bonds at the surface, these clusters feature different $\langle S^2 \rangle$ eigenvalues, which differ from the initial ansatz and therefore require further investigations of the electronic structure. The electronic description can be improved by utilizing multi-reference methods. Furthermore, the G_0W_0-approximation may be applied to obtain more accurate HOMO/LUMO gaps as implemented in Turbomole [240], since the difference of HOMO and LUMO only yields an approximation for the fundamental gap, which strongly depends on the DFT functional applied [246]. The spin difference densities of the 64 atom clusters reveal a magnetization of the surface area,

which is in good agreement with the investigations on the CZTS surfaces. In contrast, the initial singlet ansatz is valid for Cu32 and Cu96, which show no spin contamination. Overall the applied cluster model yields a promising first ansatz for the simulation of the structural properties of a realistic CZTS nanocrystal. The structural model and data can serve as a basis for future research on adapted force fields for CZTS. For the electronic structure more advanced methods are required for a more accurate description of the electronic properties. From the first insight on the electronic structure, the varying HOMO/LUMO gaps due to quantum confinement like effects can be utilized in experiment for an increased energy harvest, since differently sized nanocrystals are able to absorb a broader range of wavelengths from the solar radiation. Therefore, the nanostructuring of CZTS yields a promising opportunity to increase the performance of the kesterite solar cell while reducing the material costs.

Chapter 6

Conclusion

The always increasing worldwide energy demand can only be satisfied in a long-term perspective by a sustainable and renewable energy production to circumvent permanent damage to earth's climate. Especially a renewable energy production via photovoltaic solar cells is an important key for the transfer from todays fossil fuels powered energy production to a climate-friendly energy production. Many solar cell materials utilized today are often too expensive, too environmentally harmful or too rare. A promising alternative are kesterites ($Cu_2ZnSnS_xSe_{4-x}$), which are a possible absorber for solar cells. They consist of earth abundant non-toxic elements, which are available in a high concentration in the earth's crust.

The presented work reviews kesterites as a solar cell absorber by quantum chemical *first-principles* calculations applying density functional theory to understand key factors for the low efficiency of maximum 13 % and possible performance enhancing material modifications. Hereby the first focus lay on the structural and electronic properties of the bulk material without modifications, which served as reference properties for further investigations. The bulk calculations revealed a strong dependence of the electronic structure on the lattice constants, which is the main reason for the smaller band gap of CZTSe in comparison to CZTS due to larger lattice constants as a result of larger Se atoms, whereby the different electronic structures of Se and S exhibit only a small influence. CZTS and CZTSe feature optimal electronic properties like a strong dispersive band at the Γ-point with band gaps of 1.47 eV and 0.89 eV respectively, which are optimal after the Shockley-Queisser limit.

There are various possible reasons for the low efficiencies, whereby many are connected to the low open-circuit voltage, which is caused by band gap fluctuations within the absorber due to varying material qualities. Since the efficiency is a function of the open circuit voltage and band gap, lower efficiencies are obtained than predicted by the Shockley-Queisser limit. Varying material qualities often occur in semiconductor alloys and disordered lattice structures. Therefore, the current high performer alloy CZTSSe and 2c/2d disordered CZTS systems were investigated for hints to the band gap fluctuations. CZTSSe exhibits the possibility of a linear band gap engineering between 1.0 eV and 1.5 eV by varying the CZTS and CZTSe compositions. The *first-principles* investigations revealed that there exist slight band gap variations of up to 30 meV

for different structural alloy patterns within the same alloy composition. These small variations surely contribute to the low efficiencies, but are due to their size not solely responsible. Further insight on the band gap fluctuations were shown in 2c/2d disordered CZTS systems, in which defect pairs of Cu_{Zn} and Zn_{Cu} antisites occur. These antisites are responsible for slight structural deviations from the fully ordered structure in terms of slightly enlarged lattice constants. Furthermore, due to different binding motifs upon disordering, increasing charge fluctuations occur within the unit cell, which lead as a result to varying electronic properties. In general, the band gap decreases by a maximum of 320 meV upon disordering, whereby for every disorder fraction different band gaps are obtained due to different structural disorder patterns. Based on these electronic structure calculations, the 2c/2d disorders are therefore the main factor for the occurring band gap fluctuations, low open-circuit voltage, and resulting low efficiencies of the kesterite solar cell, whereby the CZTSSe alloys contribute only slightly. Only increasing the efficiency by eliminating obstacles in form of material defects is certainly not enough for a long-term transition to a more sustainable energy production. To enhance the kesterite solar cells further, the material can be structurally modified by nanostructuring. In this work, the effects of nanostructuring on CZTS were investigated with two different computational models: the periodic slab approach for CZTS surfaces and a cluster model for CZTS nanocrystals. The first model focused on low-index CZTS surfaces. The low-index surfaces were energetically ordered by the calculation of surface energies, whereby the challenge of calculating surface energies for off-stoichiometric symmetric slabs was successfully addressed by an extrapolation scheme. The (112) surface is revealed as the most stable surface of the investigated surface planes, closely followed by the (101), (111), (110), (001) and (100) surface. The extraordinary stability of the (112) surface is in good agreement with the strong occurrence in experimental studies. The electronic structures revealed surface states within the bulk band gap, which are directly located at the surface termination. This leads to a metallic surface termination, whereby the projected DOS on the surface further shows a magnetic behavior. These additional electronic states can contribute to an increased energy harvest and furthermore may compensate conductivity losses at interfaces or grain boundaries. To account for a higher surface to bulk volume ratio, a computational model was set up for realistic CZTS nanocrystals. The structural model successfully featured the core-shell system of a fixed bulk-like structure in the nanocrystal's core and a relaxed surface area, which is also expected from an experimental CZTS nanocrystal. Varying the size and structure of the clusters, size and structure effects in the structure optimizations were observed, which result in a lower size limit of 64 atoms and a diameter of $\sim$ 1 nm for the structural simulation of an experimental CZTS nanocrystal. The first insight on the electronic structure showed that the fundamental gap exhibits a size dependency, which is similar to the quantum confinement effects observed in experimental studies, in which the band gap increases with decreasing nanocrystal size. This size dependency can be utilized for band gap

engineering to adjust the kesterite solar cell for a maximum efficiency. By varying the nanocrystal size, different HOMO/LUMO gaps were obtained, which can be used for the absorption of a broader range of wavelengths of the solar radiation, effectively increasing the energy harvest. The clusters feature like the CZTS surfaces a magnetic surface area. The optical gaps for two selected clusters revealed a large electron-hole pair binding energy, which is a result of the small size of the finite cluster.
Overall, the quantum chemical *first-principles* investigations have shown a main reason for the observed low efficiencies and an opportunity for an enhancement of the solar cell performance by nanostructuring. By combining these theoretical findings with experiments, a possible route for more efficient kesterite solar cells is given.

Bibliography

[1] Bundesministerium für Wirtschaft und Energie (Hrsg.), *Energiedaten: Gesamtausgabe (Stand: Mai 2016)*, **2016**, [Online; accessed 17.09.2016], URL: `http://www.bmwi.de/BMWi/Redaktion/PDF/E/energiestatistiken-grafiken`.

[2] International Energy Agency, *Key World Energy Statistics 2015*, **2015**, [Online; accessed 17.09.2016], URL: `https://www.iea.org/publications/freepublications/publication/KeyWorld_Statistics_2015.pdf`.

[3] United Nations Development Programme and World Energy Council, *Energy and the challenge of sustainability*, **2000**, [Online; accessed 18.09.2016], URL: `http://www.undp.org/content/dam/aplaws/publication/en/publications/environment-energy/www-ee-library/sustainable-energy/world-energy-assessment-energy-and-the-challenge-of-sustainability/World\%20Energy\%20Assessment-2000.pdf`.

[4] P. Würfel, *Physics of Solar Cells*, Wiley-VCH Verlag GmbH: Weinheim, 2005.

[5] S. M. Sze and K. K. Ng, *Physics of Semiconductor Devices*, 3rd ed., John Wiley & Sons Inc.: New Jersey, 2006.

[6] W. Shockley and H. J. Queisser, *J. Appl. Phys.*, **1961**, *32*, 510.

[7] S. Rühle, *Sol. Energy*, **2016**, *130*, 139–147.

[8] A. De Vos, *J. Phys. D: Appl. Phys.*, **1980**, *13*, 839–846.

[9] S. Siebentritt, *Thin Solid Films*, **2013**, *535*, 1–4.

[10] U. Rau and J. H. Werner, *Appl. Phys. Lett.*, **2004**, *84*, 3735.

[11] S. Bourdais et al., *Adv. Energy Mater.*, **2016**, *6*, 1502276.

[12] Fraunhofer Institute for Solar Energy Systems, *Photovoltaics Report*, **2016**, [Online; accessed 24.09.2016], URL: `https://www.ise.fraunhofer.de/de/downloads/pdf-files/aktuelles/photovoltaics-report-in-englischer-sprache.pdf`.

[13] B. Abeles and T. Tiedje, *Phys. Rev. Lett.*, **1983**, *51*, 2003–2006.

[14] J. Y. Huang et al., *Sol. Energ. Mat. Sol. Cells*, **2012**, *98*, 277–282.

[15] T. Matsui et al., *Appl. Phys. Lett.*, **2015**, *106*, 053901.

[16] E. Yablonovitch, O. D. Miller, and S. R. Kurtz, *38th IEEE Photovoltaic Specialists Conference*, **2012**, 001556–001559.

[17] A. Sasaki, M. Nishiuma, and Y. Takeda, *Jpn. J. Appl. Phys.*, **1980**, *19*, 1695–1702.

[18] G. Fonthal et al., *J. Phys. Chem. Solids*, **2000**, *61*, 579–583.

[19] V. Fthenakis and H. C. Kim, *Renew. Sustainable Energy Rev.*, **2010**, *14*, 2039–2048.

[20] J. Peng, L. Lu, and H. Yang, *Renew. Sustainable Energy Rev.*, **2013**, *19*, 255–274.

[21] M. J. M. de Wild-Scholten, *Sol. Energ. Mat. Sol. Cells*, **2013**, *119*, 296–305.

[22] V. M. Fthenakis, *Renew. Sustainable Energy Rev.*, **2004**, *8*, 303–334.

[23] M. Woodhouse et al., *Sol. Energ. Mat. Sol. Cells*, **2013**, *115*, 199–212.

[24] T. Tinoco et al., *Phys. Status Solidi A*, **1991**, *124*, 427–434.

[25] I. Repins et al., *Prog. Photovolt: Res. Appl.*, **2008**, *16*, 235–239.

[26] W. Wang et al., *Adv. Energy Mater.*, **2013**, *4*, 1301465.

[27] National Renewable Energy Laboratory (NREL), *Research Cell Efficiency Records*, **2016**, [Online; accessed 24.09.2016], URL: `http://www.nrel.gov/ncpv/images/efficiency_chart.jpg`.

[28] S. Schorr, *Thin Solid Films*, **2007**, *515*, 5985–5991.

[29] M. A. Green et al., *Prog. Photovolt: Res. Appl.*, **2013**, *21*, 827–837.

[30] T. K. Todorov et al., *Adv. Energy Mater.*, **2012**, *3*, 34–38.

[31] S. Siebentritt and S. Schorr, *Prog. Photovolt: Res. Appl.*, **2012**, *20*, 512–519.

[32] K. Ito and T. Nakazawa, *Jpn. J. Appl. Phys.*, **1988**, *27*, 2094–2097.

[33] T. M. Friedlmeier et al., *Proceedings of the 14th European Conference of Photovoltaic Science and Engineering and Exhibition*, Bedford, UK, **1997**, 1242.

[34] H. Katagiri et al., *Appl. Phys. Express*, **2008**, *1*, 041201.

[35] H. Katagiri et al., *Thin Solid Films*, **2009**, *517*, 2455–2460.

[36] T. K. Todorov, K. B. Reuter, and D. B. Mitzi, *Adv. Mater.*, **2010**, *22*, 156–159.

[37] D. A. R. Barkhouse et al., *Prog. Photovolt: Res. Appl.*, **2011**, *20*, 6–11.

[38] Y. Seog Lee et al., *Adv. Energy Mater.*, **2014**, *5*, 1401372.

[39] Q. Guo, H. W. Hillhouse, and R. Agrawal, *J. Am. Chem. Soc.*, **2009**, *131*, 11672–11673.

[40] W. Ki and H. W. Hillhouse, *Adv. Energy Mater.*, **2011**, *1*, 732–735.

[41] L. Guen and W.S. Glaunsinger, *J. Solid State Chem.*, **1980**, *35*, 10–21.

[42] S. Schorr, *Sol. Energ. Mat. Sol. Cells*, **2011**, *95*, 1482–1488.

[43] J. Paier et al., *Phys. Rev. B*, **2009**, *79*, 115126.

[44] R. S. Hall, J. T. Szymanski, and J. M. Stewart, *Can. Mineral.*, **1978**, *16*, 131–137.

[45] A. Nateprov et al., *Surf. Engin. Appl. Electrochem.*, **2013**, *49*, 423–426.

[46] R. Nitsche, D.F. Sargent, and P. Wild, *J. Cryst. Growth*, **1967**, *1*, 52–53.

[47] G. P. Bernardini et al., *Eur. J. Mineral.*, **1990**, *2*, 219–226.

[48] S. Schorr, H.-J. Hoebler, and M. Tovar, *Eur. J. Mineral.*, **2007**, *19*, 65–73.

[49] X. Lin et al., *RSC Adv.*, **2012**, *2*, 9894.

[50] O. Zaberca et al., *Nanotechnology*, **2012**, *23*, 185402.

[51] S. K. Saha, A. Guchhait, and A. J. Pal, *Phys. Chem. Chem. Phys.*, **2012**, *14*, 8090.

[52] S. M. Camara, L. Wang, and X. Zhang, *Nanotechnology*, **2013**, *24*, 495401.

[53] M. Zhou et al., *J. Alloys Compd.*, **2013**, *574*, 272–277.

[54] H. Zhou et al., *Energy Environ. Sci.*, **2013**, *6*, 2822.

[55] W. Li et al., *CrystEngComm*, **2013**, *15*, 8966.

[56] X. Yan, X. Hu, and S. Komarneni, *J. Korean Phys. Soc.*, **2015**, *66*, 1511–1515.

[57] J. Guo et al., *Nanoscale. Res. Lett.*, **2015**, *10*, 1–6.

[58] S. A. Vanalakar et al., *Phys. Status Solidi C*, **2015**, *12*, 500–503.

[59] I. Calvet et al., *Bol. Soc. Esp. Ceram. V.*, **2015**, *54*, 175–180.

[60] N. Kattan et al., *Applied Materials Today*, **2015**, *1*, 52–59.

[61] D. Kim et al., *J. Nanosci. Nanotechnol.*, **2016**, *16*, 5082–5086.

[62] A.G. Kannan, T.E. Manjulavalli, and J. Chandrasekaran, *Procedia Eng.*, **2016**, *141*, 15–22.

[63] N. Mirbagheri et al., *Nanotechnology*, **2016**, *27*, 185603.

[64] N. Nakayama and K. Ito, *Appl. Surf. Sci.*, **1996**, *92*, 171–175.

[65] K. Hönes et al., *Physica B: Condensed Matter*, **2009**, *404*, 4949–4952.

[66] L. E. V. Rios et al., *J. Alloys Compd.*, **2016**, *657*, 408–413.

[67] A. D. Collord, H. Xin, and H. W. Hillhouse, *IEEE J. Photovolt*, **2015**, *5*, 288–298.

[68] A. Fairbrother et al., *J. Mater. Chem. A*, **2015**, *3*, 9451–9455.

[69] L. Choubrac et al., *Phys. Chem. Chem. Phys.*, **2013**, *15*, 10722.

[70] G. Rey et al., *Appl. Phys. Lett.*, **2014**, *105*, 112106.

[71] A. Lafond et al., *Acta Crystallogr. Sect. B-Struct. Sci.*, **2014**, *70*, 390–394.

[72] M. Grossberg et al., *Curr. Appl. Phys.*, **2014**, *14*, 1424–1427.

[73] M. Y. Valakh et al., *Phys. Status Solidi RRL*, **2013**, *7*, 258–261.

[74] G. Rey et al., *Sol. Energ. Mat. Sol. Cells*, **2016**, *151*, 131–138.

[75] P. Kevin et al., *J. Am. Chem. Soc.*, **2015**, *137*, 15086–15089.

[76] Y. Zhao et al., *RSC Adv.*, **2013**, *3*, 26160.

[77] U. Ghorpade et al., *Chem. Commun.*, **2014**, *50*, 11258.

[78] G. Brammertz et al., *Appl. Phys. Lett.*, **2013**, *103*, 163904.

[79] J. Seol et al., *Sol. Energy Mater. Sol. Cells*, **2003**, *75*, 155–162.

[80] S. J. Ahn et al., *Appl. Phys. Lett.*, **2010**, *97*, 021905.

[81] S. Chen et al., *Phys. Rev. B*, **2011**, *83*, 125201.

[82] P. Pyykkö and John F. Stanton, *Chem. Rev.*, **2012**, *112*, 1–3.

[83] S. Nakamura, T. Maeda, and T. Wada, *Phys. Status Solidi C*, **2009**, *6*, 1261–1265.

[84] S. Botti, D. Kammerlander, and M. A. L. Marques, *Appl. Phys. Lett.*, **2011**, *98*, 241915.

[85] N. B. M. Amiri and A. Postnikov, *Phys. Rev. B*, **2010**, *82*, 205204.

[86] S. Chen et al., *Appl. Phys. Lett.*, **2009**, *94*, 041903.

[87] C. Persson, *J. Appl. Phys.*, **2010**, *107*, 053710.

[88] X. He and H. Shen, *Phys. Scr.*, **2012**, *85*, 035302.

[89] S. Chen et al., *Phys. Rev. B*, **2010**, *81*, 245204.

[90] S. Chen et al., *Phys. Rev. B*, **2010**, *82*, 195203.

[91] C.-R. Li et al., *Phys. Lett. A*, **2013**, *377*, 2398–2402.

[92] T. Fukushima, K. Yamauchi, and S. Picozzi, *Phys. Rev. B*, **2010**, *82*, 014102.

[93] I. Camps et al., *Semicond. Sci. Technol.*, **2012**, *27*, 115001.

[94] X. Wang et al., *J. Appl. Phys.*, **2012**, *112*, 023701.

[95] A. Khare et al., *J. Appl. Phys.*, **2012**, *111*, 123704.

[96] M. Kumar and C. Persson, *IJTAS*, **2013**, *5*, 1–8.

[97] Q. Shu et al., *Phys. Rev. B*, **2013**, *87*, 115208.

[98] P. P. Gunaicha et al., *So. Energy*, **2014**, *102*, 276–281.

[99] S. Bensalem et al., *J. Alloys Compd.*, **2014**, *589*, 137–142.

[100] T. Shibuya et al., *Appl. Phys. Lett.*, **2014**, *104*, 021912.

[101] Y. Dong et al., *Appl. Phys. Lett.*, **2014**, *104*, 252107.

[102] O. Y. Khyzhun et al., *Physica B*, **2015**, *461*, 75–84.

[103] O. Mebkhout et al., *J. Alloys Compd.*, **2015**, *653*, 140–147.

[104] S. G. Choi et al., *Phys. Rev. Applied*, **2015**, *4*, 054006.

[105] Z.-Y. Zhao, Q.-L. Liu, and X. Zhao, *J. Alloys Compd.*, **2015**, *618*, 248–253.

[106] M. Guc et al., *RSC Adv.*, **2016**, *6*, 13278–13285.

[107] N. Ullah et al., *Int. J. Mod. Phys. B*, **2016**, 1650137.

[108] M. Ya. Valakh et al., *RSC Adv.*, **2016**, *6*, 67756–67763.

[109] S. Chen et al., *Adv. Mater.*, **2013**, *25*, 1522–1539.

[110] D. B. Mitzi et al., *Phil. Trans. R. Soc. A*, **2013**, *371*, 20110432.

[111] M. Kumar, H. Zhao, and C. Persson, *Thin Solid Films*, **2013**, *535*, 318–321.

[112] S. Shang et al., *J. Phys. Chem. C*, **2014**, *118*, 24884–24889.

[113] J. J. S. Scragg et al., *Phys. Status Solidi B*, **2015**, *253*, 247–254.

[114] A. Ritscher, M. Hoelzel, and M. Lerch, *J. Solid State Chem.*, **2016**, *238*, 68–73.

[115] M. C. Beard, J. M. Luther, and A. J. Nozik, *Nature Nanotech.*, **2014**, *9*, 951–954.

[116] H. Gleiter, *Acta Mater.*, **2000**, *48*, 1–29.

[117] K. Nielsch et al., *Adv. Energy Mater.*, **2011**, *1*, 713–731.

[118] M. G. Kanatzidis, *Chem. Mater.*, **2010**, *22*, 648–659.

[119] M. D. Kelzenberg et al., *Nat. Mater.*, **2010**, *9*, 239–244.

[120] E. Garnett and P. Yang, *Nano Lett.*, **2010**, *10*, 1082–1087.

[121] J. J. Choi et al., *Adv. Mater.*, **2011**, *23*, 3144–3148.

[122] X. Wang et al., *Nat. Photon.*, **2011**, *5*, 480–484.

[123] P. Xu et al., *Phys. Rev. B*, **2013**, *88*, 045427.

[124] K. Yu and E. A. Carter, *Chem. Mater.*, **2015**, *27*, 2920–2927.

[125] Y. Zhang et al., *A novel strategy to control defects and secondary phases of CZTS by surfactant Potassium*, 2015. eprint: `arXiv:1509.00717`.

[126] E. Schrödinger. *E. Phys. Rev.*, **1926**, *37*, 863.

[127] P. Schwerdtfeger, *ChemPhysChem*, **2011**, *12*, 3143–3155.

[128] H. Hellmann, *J. Chem. Phys.*, **1935**, *3*, 61.

[129] A. Szabo and N. S. Ostlund, *Modern Quantum Chemistry*, 1st ed., Dover Publication, Inc Mineola: New York, 1996.

[130] M. Born and R. Oppenheimer, *Ann. Phys.*, **1927**, *389*, 457–484.

[131] V. Fock, *Z. Phys.*, **1930**, *61*, 126–148.

[132] J. C. Slater, *Phys. Rev.*, **1951**, *81*, 385–390.

[133] I. N. Levine, *Quantum Chemistry*, 5th ed., Prentice Hall: Upper Saddle River, 2000.

[134] C. C. J. Roothaan, *Rev. Mod. Phys.*, **1951**, *23*, 69–89.

[135] G. G. Hall, *Proc. R. Soc. A*, **1951**, *205*, 541–552.

[136] L. H. Thomas, *Math. Proc. Camb. Phil. Soc.*, **1927**, *23*, 542–548.

[137] E. Fermi, *Z. Phys.*, **1928**, *48*, 73–79.

[138] P. Hohenberg and W. Kohn, *Phys. Rev.*, **1964**, *136*, B864–B871.

[139] W. Kohn and L. J. Sham, *Phys. Rev.*, **1965**, *140*, A1133–A1138.

[140] R.G. Parr and Y. Weitao, *Density-Functional Theory of Atoms and Molecules*, Oxford University Press: Oxford, 1989.

[141] W. Koch and M. C. Holthausen, *A Chemist's Guide to Density Functional Theory*, Wiley-VCH Verlag GmbH: Weinheim, 2001.

[142] D. M. Ceperley and B. J. Alder, *Phys. Rev. Lett.*, **1980**, *45*, 566–569.

[143] S. H. Vosko, L. Wilk, and M. Nusair, *Can. J. Phys.*, **1980**, *58*, 1200–1211.

[144] P. A. M. Dirac, *Math. Proc. Camb. Phil. Soc.*, **1930**, *26*, 376–385.

[145] J.-L. Calais, *Int. J. Quantum Chem.*, **1993**, *47*, 101–101.

[146] J. P. Perdew, K. Burke, and M. Ernzerhof, *Phys. Rev. Lett.*, **1996**, *77*, 3865–3868.

[147] J. P. Perdew and Y. Wang, *Phys. Rev. B*, **1992**, *45*, 13244–13249.

[148] J. P. Perdew et al., *Phys. Rev. B*, **1993**, *48*, 4978–4978.

[149] J. P. Perdew, K. Burke, and M. Ernzerhof, *Phys. Rev. Lett.*, **1997**, *78*, 1396–1396.

[150] J. P. Perdew et al., *Phys. Rev. Lett.*, **2008**, *100*, 136406.

[151] A. D. Becke, *J. Chem. Phys*, **1993**, *98*, 5648.

[152] C. Lee, W. Yang, and R. G. Parr, *Phys. Rev. B*, **1988**, *37*, 785–789.

[153] A. D. Becke, *Phys. Rev. A*, **1988**, *38*, 3098–3100.

[154] J. Heyd, G. E. Scuseria, and M. Ernzerhof, *J. Chem. Phys.*, **2003**, *118*, 8207.

[155] J. Heyd and G. E. Scuseria, *J. Chem. Phys.*, **2004**, *121*, 1187.

[156] J. Heyd, Gustavo E. S., and M. Ernzerhof, *J. Chem. Phys.*, **2006**, *124*, 219906.

[157] A. V. Krukau et al., *J. Chem. Phys.*, **2006**, *125*, 224106.

[158] E. Runge and E. K. U. Gross, *Phys. Rev. Lett.*, **1984**, *52*, 997–1000.

[159] R. van Leeuwen, *Phys. Rev. Lett.*, **1998**, *80*, 1280–1283.

[160] J. Schirmer and A. Dreuw, *Phys. Rev. A*, **2007**, *75*, 022513.

[161] N.W. Ashcroft and N.D. Mermin, *Solid state physics*, Saunders College: Philadelphia, 1976.

[162] F. Bloch, *Z. Phys.*, **1929**, *52*, 555–600.

[163] F. Jensen, *Introduction to Computational Chemistry*, 2nd ed., John Wiley & Sons: West Sussex, 2007.

[164] R. Dronskowski, *Computational Chemistry of Solid State Materials*, Wiley-Blackwell: New Jersey, 2005.

[165] K. Kopitzki and P. Herzog, *Einführung in die Festkörperphysik*, Vieweg+Teubner Verlag: Wiesbaden, 2002.

[166] C. Pisani, *Quantum-Mechanical Ab-initio Calculation of the Properties of Crystalline Materials*, 1st ed., Springer Verlag: Heidelberg, 1996.

[167] D. Feng and G. Jin, *Introduction to Condensed Matter Physics*, World Scientific: Singapur, 2005.

[168] S.G. Davison and M. Stęślicka, *Basic theory of surface states*, Clarendon Press: Oxford, 1992.

[169] J. Hafner, *J. Comput. Chem.*, **2008**, *29*, 2044–2078.

[170] D. R. Hamann, M. Schlüter, and C. Chiang, *Phys. Rev. Lett.*, **1979**, *43*, 1494–1497.

[171] G. B. Bachelet, D. R. Hamann, and M. Schlüter, *Phys. Rev. B*, **1982**, *26*, 4199–4228.

[172] G. B. Bachelet, D. R. Hamann, and M. Schlüter, *Phys. Rev. B*, **1984**, *29*, 2309–2309.

[173] D. Vanderbilt, *Phys. Rev. B*, **1990**, *41*, 7892–7895.

[174] P. E. Blöchl, *Phys. Rev. B*, **1994**, *50*, 17953–17979.

[175] G. Kresse and D. Joubert, *Phys. Rev. B*, **1999**, *59*, 1758–1775.

[176] J. W. Gibbs et al., *The collected works of J. Willard Gibbs*, Longmans, Green and Co.: London, 1902.

[177] G. Wulff, *Z. Kristallogr.*, **1901**, *34*, 449–480.

[178] C. Herring, *Phys. Rev.*, **1951**, *82*, 87–93.

[179] M. v. Laue. *Z. Kristallogr.*, **1943**, *105*, 124–133.

[180] R. F. Strickland-Constable, *Kinetics and Mechanism of Crystallization*, Academic Press: London, 1968.

[181] R. Bader, *Atoms in Molecules: A Quantum Theory*, 1st ed., Oxford University Press: Oxford, 1990.

[182] A. E. Reed, R. B. Weinstock, and F. Weinhold, *J. Chem. Phys.*, **1985**, *83*, 735.

[183] P. O. Löwdin, *Phys. Rev.*, **1955**, *97*, 1474–1489.

[184] L. Yin et al., *RSC Adv.*, **2015**, *5*, 40369–40374.

[185] G. Kresse and J. Hafner, *Phys. Rev. B*, **1993**, *47*, 558–561.

[186] G. Kresse and J. Hafner, *Phys. Rev. B*, **1994**, *49*, 14251–14269.

[187] G. Kresse and J. Furthmüller, *Phys. Rev. B*, **1996**, *54*, 11169–11186.

[188] G. Kresse and J. Furthmüller, *Comput. Mater. Sci.*, **1996**, *6*, 15–50.

[189] A. Kokalj, *J. Mol. Graph. Model*, **1999**, *17*, 176–179.

[190] A. Kokalj, *Comp. Mater. Sci.*, **2003**, *28*, 155–168.

[191] W. H. Press et al., *Numerical Recipes: the art of scientific computing*, Cambridge Univ. Press: New York, 1986.

[192] E. Blöchl P, O. Jepsen, and O. K. Andersen, *Phys. Rev. B*, **1994**, *49*, 16223–16233.

[193] H. J. Monkhorst and J. D. Pack, *Phys. Rev. B*, **1976**, *13*, 5188–5192.

[194] G. Henkelman, A. Arnaldsson, and Jónsson H, *Comput. Mater. Sci.*, **2006**, *36*, 354–360.

[195] E. Sanville et al., *J. Comput. Chem.*, **2007**, *28*, 899–908.

[196] W. Tang, E. Sanville, and G. Henkelman, *J. Phys.: Condens. Matter*, **2009**, *21*, 084204.

[197] C. Adamo and V. Barone, *J. Chem. Phys.*, **1999**, *110*, 6158.

[198] R. Dovesi et al., *Int. J. Quantum Chem.*, **2014**, *114*, 1287–1317.

[199] R. Dovesi et al., *CRYSTAL14, User's Manual*, 2014.

[200] K. Biswas, S. Lany, and A. Zunger, *Appl. Phys. Lett.*, **2010**, *96*, 201902.

[201] S. Chen et al., *Appl. Phys. Lett.*, **2010**, *96*, 021902.

[202] S. G. Choi et al., *J. Appl. Phys.*, **2012**, *111*, 033506.

[203] A. Khare et al., *J. Appl. Phys.*, **2012**, *111*, 083707.

[204] X. He et al., *Acta Metall. Sin. Engl.*, **2013**, *26*, 285–292.

[205] A. J. Jackson and A. Walsh, *J. Mater. Chem. A*, **2014**, *2*, 7829–7836.

[206] A. H. Reshak et al., *Int. J. Electrochem. Sci.*, **2014**, *9*, 955–974.

[207] S. V. Baryshev and E. Thimsen, *Chem. Mater.*, **2015**, *27*, 2294–2298.

[208] P. Sarker, M. M. Al-Jassim, and M. N. Huda, *J. Appl. Phys.*, **2015**, *117*, 035702.

[209] Y. Hirate et al., *J. Appl. Phys.*, **2015**, *117*, 015702.

[210] S. Körbel et al., *Phys. Rev. B*, **2015**, *91*, 075134.

[211] H. Katagiri et al., *Sol. Energy Mater. Sol. Cells*, **2001**, *65*, 141–148.

[212] T. Tanaka et al., *J. Phys. Chem. Solids*, **2005**, *66*, 1978–1981.

[213] N. Kamoun, H. Bouzouita, and B. Rezig, *Thin Solid Films*, **2007**, *515*, 5949–5952.

[214] L. Vegard, *Z. Phys.*, **1921**, *5*, 17–26.

[215] A. R. Denton and N. W. Ashcroft, *Phys. Rev. A*, **1991**, *43*, 3161–3164.

[216] J. G. Gay, *J. Vac. Sci. Technol. A*, **1984**, *2*, 931.

[217] J. J. Gilman, *J. Appl. Phys.*, **1960**, *31*, 2208.

[218] P. L. Gutshall and G. E. Gross, *J. Appl. Phys.*, **1965**, *36*, 2459.

[219] P. Kraatz, *J. Appl. Phys.*, **1974**, *45*, 4741.

[220] S. J. Burns, *J. Appl. Phys.*, **1970**, *41*, 2086.

[221] A. A. Stekolnikov, J. Furthmüller, and F. Bechstedt, *Phys. Rev. B*, **2002**, *65*, 115318.

[222] L. Hammerschmidt et al., *Surf. Sci.*, **2015**, *637-638*, 124–131.

[223] A. R. Roosen, R. P. McCormack, and W. C. Carter, *Comp. Mater. Sci.*, **1998**, *11*, 16–26.

[224] M. Bär et al., *Appl. Phys. Lett.*, **2011**, *99*, 112103.

[225] L. Sun et al., *Sol. Energy Mater. Sol. Cells*, **2011**, *95*, 2907–2913.

[226] Y. Arba et al., *J. Optoelectron. Adv. Mater.*, **2013**, *15*, 1200–1203.

[227] J. Zhang et al., *Int. J. Photoenergy*, **2013**, *2013*, 1–6.

[228] M. R. Byeon et al., *Thin Solid Films*, **2013**, *546*, 387–392.

[229] U. Chalapathi, S. Uthanna, and V. Sundara Raja, *IRESR*, **2013**, *5*, 031610.

[230] V. Kheraj et al., *J. Cryst. Growth*, **2013**, *362*, 174–177.

[231] Z. Seboui, Y. Cuminal, and N. Kamoun-Turki, *IRESR*, **2013**, *5*, 023113.

[232] J. Wang et al., *J. Alloys Compd.*, **2013**, *552*, 418–422.

[233] M. Patel, I. Mukhopadhyay, and A. Ray, *Semicond. Sci. Technol.*, **2013**, *28*, 055001.

[234] X. Jiang et al., *Surf. Coat. Technol.*, **2013**, *228*, S408–S411.

[235] Y. Nambu, *Progr. Theoret. Phys.*, **1950**, *5*, 614–633.

[236] E. E. Salpeter and H. A. Bethe, *Phys. Rev.*, **1951**, *84*, 1232–1242.

[237] A. Safdar et al., *Mat. Sci. Semicon. Proc.*, **2016**, *41*, 420–427.

[238] D. Porezag et al., *Phys. Rev. B*, **1995**, *51*, 12947–12957.

[239] M. Elstner et al., *Phys. Rev. B*, **1998**, *58*, 7260–7268.

[240] *TURBOMOLE V7.0 2015, a development of University of Karlsruhe and Forschungszentrum Karlsruhe GmbH, 1989-2007, TURBOMOLE GmbH, since 2007; available from* `http://www.turbomole.com`.

[241] W. Humphrey, A. Dalke, and K. Schulten, *J. Mol. Graphics*, **1996**, *14*, 33–38.

[242] F. Weigend and R. Ahlrichs, *Phys. Chem. Chem. Phys.*, **2005**, *7*, 3297.

[243] F. Weigend, *Phys. Chem. Chem. Phys.*, **2006**, *8*, 1057.

[244] B. Metz, H. Stoll, and M. Dolg, *J. Chem. Phys.*, **2000**, *113*, 2563.

[245] G. Hermann et al., *J. Comput. Chem.*, **2016**, *37*, 1511–1520.

[246] J.-L. Bredas, *Mater. Horiz.*, **2014**, *1*, 17–19.

Appendix A

Modified $Cu_2ZnSnS_xSe_{4-x}$ Bulk Structures

Band Gap Engineering by $Cu_2ZnSnS_xSe_{4-x}$ Alloys

Table A.1: Lattice parameters for all calculated CZTSSe alloys at the PBE-level. The band gaps E_g are calculated by HSE06 single point calculations on top of the PBE-optimized structure. E_{rel} is calculated with respect to the low energy structure of the corresponding alloy fraction.

fraction [%]	pattern [#]	a [Å]	b [Å]	c [Å]	volume [Å^3]	E_{rel} [meV]	E_g [eV]
0.0	1	5.464	5.464	10.921	326.04	0	1.170
12.5	1	5.499	5.497	10.995	332.35	0	1.098
25.0	1	5.537	5.530	11.080	339.26	19	1.012
25.0	2	5.537	5.534	11.064	338.99	14	1.028
25.0	3	5.538	5.531	11.073	339.18	0	1.017
25.0	4	5.541	5.532	11.068	339.28	23	1.015
25.0	5	5.533	5.540	11.067	339.23	8	1.025
37.5	1	5.573	5.570	11.142	345.83	28	0.951
37.5	2	5.572	5.563	11.150	345.59	23	0.942
37.5	3	5.569	5.568	11.147	345.66	19	0.957
37.5	4	5.572	5.573	11.138	345.83	0	0.952
37.5	5	5.581	5.566	11.132	345.79	24	0.953
37.5	6	5.570	5.577	11.142	346.14	0	0.956
37.5	7	5.577	5.572	11.133	346.00	24	0.950
50.0	1	5.610	5.608	11.228	353.25	62	0.864
50.0	2	5.609	5.607	11.214	352.69	41	0.878
50.0	3	5.614	5.601	11.216	352.66	40	0.890
50.0	4	5.609	5.611	11.222	353.19	26	0.889
50.0	5	5.608	5.611	11.213	352.86	51	0.891
50.0	6	5.608	5.598	11.242	352.90	48	0.864

Continued on next page

fraction [%]	pattern [#]	a [Å]	b [Å]	c [Å]	volume [Å^3]	E_{rel} [meV]	E_g [eV]
50.0	7	5.613	5.602	11.218	352.75	36	0.877
50.0	8	5.610	5.607	11.219	352.85	36	0.885
50.0	9	5.605	5.605	11.224	352.64	47	0.881
50.0	10	5.607	5.615	11.207	352.79	0	0.895
50.0	11	5.612	5.612	11.204	352.87	24	0.886
50.0	12	5.623	5.602	11.198	352.75	48	0.884
62.5	1	5.647	5.642	11.291	359.73	34	0.811
62.5	2	5.647	5.637	11.302	359.70	26	0.812
62.5	3	5.646	5.648	11.283	359.75	0	0.822
62.5	4	5.644	5.652	11.278	359.76	24	0.818
62.5	5	5.648	5.643	11.280	359.47	0	0.832
62.5	6	5.654	5.641	11.278	359.74	24	0.821
62.5	7	5.642	5.648	11.298	360.03	27	0.812
75.0	1	5.682	5.673	11.372	366.54	35	0.740
75.0	2	5.686	5.682	11.358	366.95	17	0.762
75.0	3	5.685	5.680	11.363	366.89	0	0.760
75.0	4	5.686	5.678	11.361	366.74	25	0.757
75.0	5	5.680	5.687	11.357	366.84	14	0.758
87.5	1	5.722	5.718	11.437	374.17	0	0.699
100.0	1	5.761	5.761	11.507	381.91	0	0.633

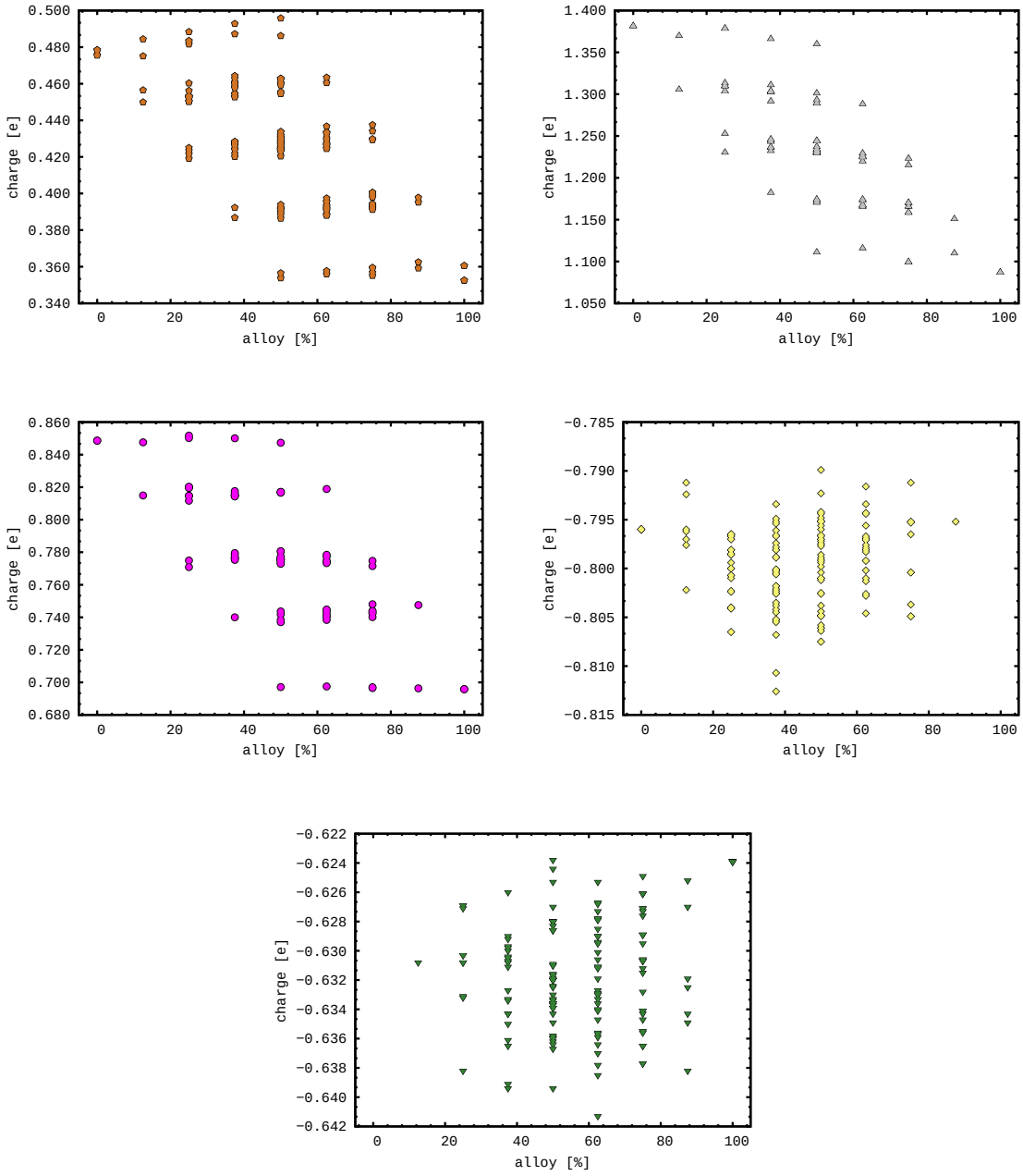

Figure A.1: Bader charges for the different CZTSSe alloys as a function of the alloy fraction at the PBE-level. Zn is shown in pink, Cu in brown, Sn in gray, S in yellow and Se in green.

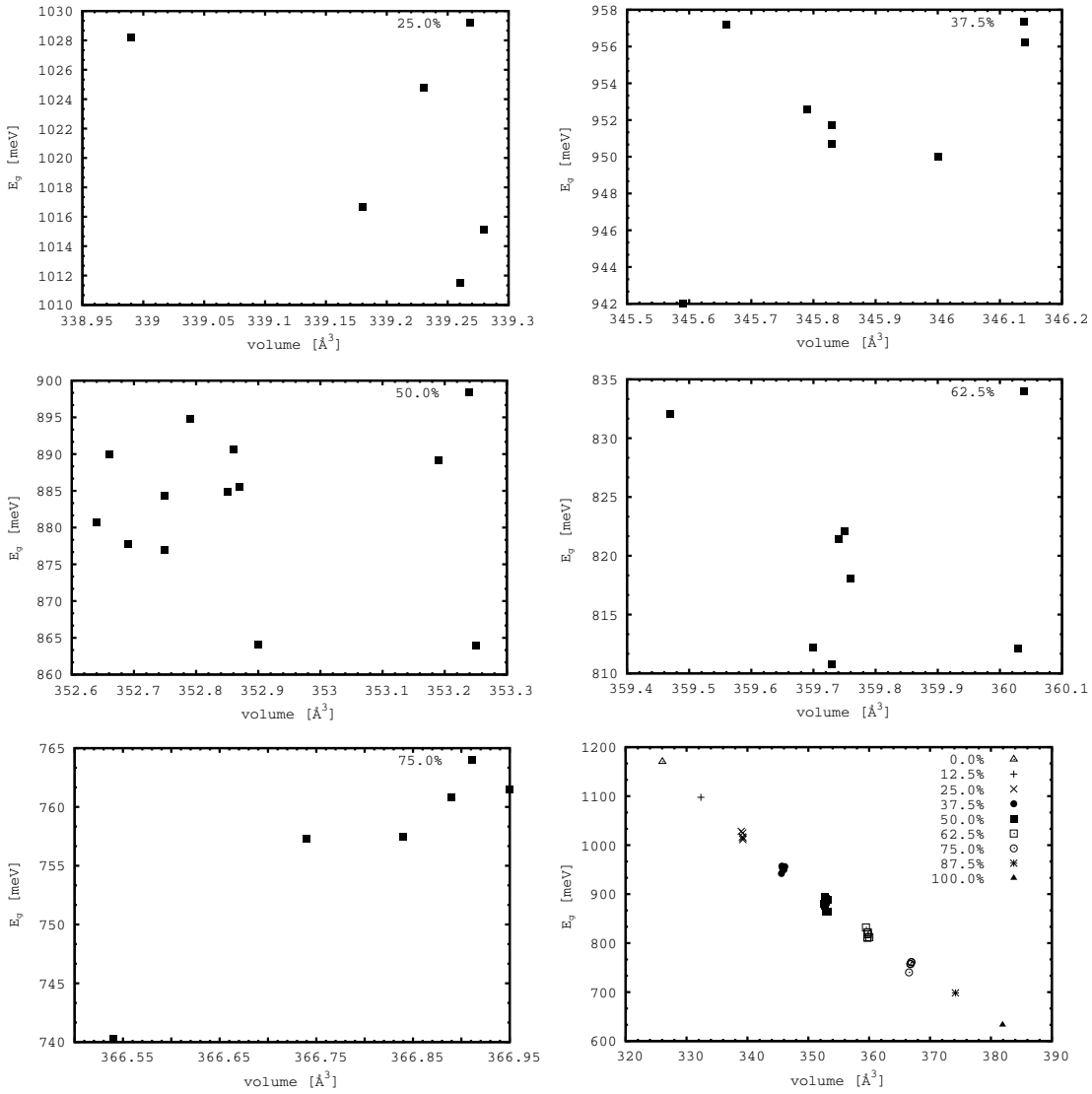

Figure A.2: CZTSSe band gaps as a function of the cell volume calculated at the HSE06-level on top of the PBE optimized structures.

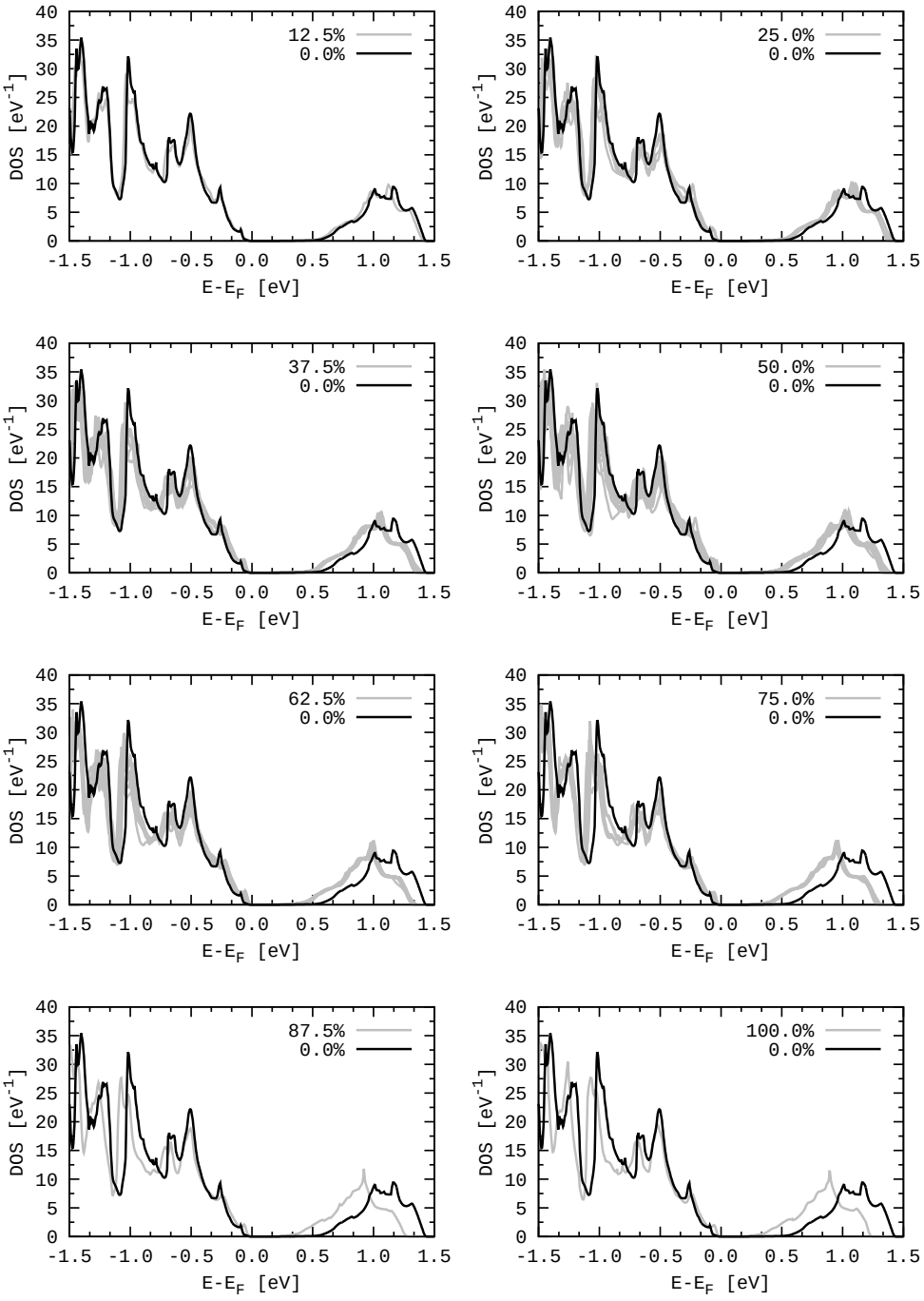

Figure A.3: Total PBE DOS for all CZTSSe alloys fractions and patterns in the PBE-structure. For every alloy fraction, there are different alloy patterns and therefore different DOS possible, which overlap in the corresponding alloy fraction.

Band Gap Fluctuations in 2c/2d Disordered Cu_2ZnSnS_4

Table A.2: Calculated lattice parameters and band gaps E_g of 2c/2d disordered CZTS systems at the PBE-level.

fraction [%]	pattern [#]	E_{rel} [meV]	E_g [meV]	a [Å]	b [Å]	c [Å]	volume [Å^3]
0.0	910	0	69	10.924	10.924	10.918	1302.88
12.5	904	195	9	10.932	10.931	10.922	1305.12
12.5	905	197	8	10.929	10.930	10.920	1304.51
12.5	906	298	34	10.931	10.931	10.916	1304.47
12.5	907	263	2	10.931	10.930	10.924	1305.15
12.5	908	262	2	10.930	10.932	10.924	1305.25
12.5	909	226	25	10.931	10.931	10.918	1304.50
25.0	630	290	27	10.934	10.935	10.921	1305.73
25.0	631	446	32	10.936	10.931	10.919	1305.22
25.0	632	442	29	10.932	10.931	10.929	1305.99
25.0	633	623	1	10.933	10.936	10.929	1306.63
25.0	634	373	35	10.930	10.936	10.918	1305.08
25.0	635	372	43	10.933	10.932	10.919	1305.09
25.0	636	553	7	10.933	10.938	10.924	1306.30
25.0	637	517	0	10.926	10.928	10.936	1305.77
25.0	638	483	0	10.933	10.929	10.927	1305.61
25.0	639	290	27	10.931	10.930	10.923	1305.04
25.0	640	253	31	10.932	10.932	10.916	1304.59
25.0	853	440	33	10.934	10.934	10.920	1305.46
25.0	854	425	35	10.930	10.929	10.931	1305.80
25.0	855	459	29	10.932	10.934	10.920	1305.28
25.0	856	391	26	10.930	10.929	10.930	1305.56
25.0	857	425	37	10.937	10.930	10.922	1305.54
25.0	858	438	33	10.935	10.931	10.919	1305.17
25.0	859	394	17	10.927	10.928	10.931	1305.34
25.0	860	426	38	10.935	10.932	10.919	1305.25
25.0	861	440	33	10.933	10.934	10.920	1305.43
25.0	862	365	47	10.930	10.928	10.930	1305.56
25.0	863	354	44	10.934	10.930	10.921	1305.15
25.0	864	388	37	10.931	10.932	10.923	1305.25
25.0	865	364	13	10.928	10.926	10.932	1305.22
25.0	866	367	32	10.934	10.930	10.922	1305.35
25.0	867	369	29	10.934	10.933	10.920	1305.41
25.0	868	369	27	10.932	10.931	10.923	1305.35
25.0	869	364	13	10.928	10.926	10.932	1305.20
25.0	870	388	39	10.932	10.933	10.919	1304.99
25.0	871	353	44	10.935	10.929	10.922	1305.26
25.0	872	354	44	10.934	10.930	10.921	1305.18

Continued on next page

fraction [%]	pattern [#]	E_{rel} [meV]	E_g [meV]	a [Å]	b [Å]	c [Å]	volume [Å^3]
25.0	873	317	39	10.931	10.931	10.922	1305.00
25.0	874	366	48	10.927	10.925	10.934	1305.38
25.0	875	437	33	10.936	10.933	10.920	1305.70
25.0	876	425	39	10.937	10.930	10.919	1305.28
25.0	877	387	11	10.928	10.928	10.931	1305.49
25.0	878	390	25	10.931	10.930	10.931	1305.93
25.0	879	353	43	10.935	10.928	10.923	1305.26
25.0	880	367	33	10.934	10.930	10.919	1305.02
25.0	881	290	29	10.933	10.932	10.920	1305.14
25.0	882	443	31	10.934	10.933	10.922	1305.70
25.0	883	445	32	10.931	10.936	10.919	1305.40
25.0	884	372	42	10.932	10.933	10.922	1305.34
25.0	885	373	35	10.936	10.931	10.918	1305.23
25.0	886	554	7	10.936	10.932	10.922	1305.74
25.0	887	623	0	10.937	10.933	10.930	1307.00
25.0	888	515	0	10.929	10.928	10.936	1306.05
25.0	889	483	0	10.929	10.933	10.927	1305.63
25.0	890	291	23	10.930	10.930	10.924	1305.16
25.0	891	253	31	10.932	10.931	10.917	1304.56
25.0	892	254	24	10.933	10.932	10.918	1304.86
25.0	893	371	33	10.933	10.931	10.918	1304.72
25.0	894	372	32	10.931	10.934	10.917	1304.75
25.0	895	373	22	10.927	10.928	10.932	1305.44
25.0	896	373	22	10.928	10.927	10.931	1305.34
25.0	897	517	6	10.937	10.933	10.924	1306.20
25.0	898	517	6	10.932	10.937	10.923	1305.98
25.0	899	483	0	10.928	10.928	10.932	1305.61
25.0	900	477	11	10.932	10.932	10.925	1305.68
25.0	901	254	23	10.932	10.932	10.918	1304.74
25.0	902	216	49	10.924	10.925	10.932	1304.63
25.0	903	216	48	10.927	10.926	10.930	1304.77
37.5	524	552	27	10.935	10.936	10.922	1306.13
37.5	525	548	35	10.935	10.934	10.936	1307.57
37.5	526	616	31	10.938	10.933	10.927	1306.61
37.5	527	650	35	10.939	10.935	10.922	1306.35
37.5	528	481	41	10.930	10.935	10.926	1305.84
37.5	529	550	30	10.935	10.938	10.922	1306.26
37.5	530	581	44	10.935	10.935	10.921	1305.88
37.5	531	511	28	10.927	10.930	10.935	1305.97
37.5	532	543	13	10.933	10.927	10.932	1306.07
37.5	533	639	28	10.930	10.931	10.935	1306.52
37.5	534	477	29	10.933	10.938	10.922	1306.04
37.5	535	508	35	10.931	10.927	10.934	1306.00
37.5	536	542	12	10.929	10.932	10.933	1306.39

Continued on next page

fraction [%]	pattern [#]	E_{rel} [meV]	E_g [meV]	a [Å]	b [Å]	c [Å]	volume [Å^3]
37.5	537	543	35	10.935	10.937	10.921	1306.11
37.5	538	579	48	10.935	10.934	10.924	1306.15
37.5	539	636	31	10.932	10.932	10.937	1307.10
37.5	540	476	8	10.932	10.934	10.924	1305.70
37.5	541	509	41	10.931	10.937	10.924	1305.87
37.5	542	569	25	10.931	10.935	10.929	1306.44
37.5	543	567	23	10.932	10.934	10.932	1306.76
37.5	544	406	35	10.932	10.934	10.919	1305.22
37.5	545	480	43	10.930	10.928	10.933	1305.88
37.5	546	475	34	10.931	10.934	10.924	1305.68
37.5	547	480	46	10.933	10.933	10.925	1305.90
37.5	548	476	33	10.932	10.924	10.934	1305.75
37.5	549	579	44	10.936	10.931	10.927	1306.24
37.5	550	411	33	10.930	10.936	10.920	1305.31
37.5	551	405	42	10.932	10.931	10.924	1305.28
37.5	552	509	53	10.934	10.934	10.923	1305.86
37.5	553	472	3	10.932	10.929	10.931	1305.97
37.5	554	407	42	10.930	10.934	10.924	1305.46
37.5	555	406	34	10.927	10.935	10.924	1305.30
37.5	556	473	16	10.927	10.931	10.932	1305.74
37.5	557	509	51	10.934	10.933	10.923	1305.84
37.5	558	438	35	10.926	10.931	10.934	1305.87
37.5	559	441	25	10.932	10.931	10.929	1305.94
37.5	560	482	12	10.934	10.930	10.927	1305.85
37.5	561	552	29	10.937	10.934	10.922	1306.07
37.5	562	477	16	10.930	10.935	10.926	1305.98
37.5	563	549	31	10.937	10.933	10.921	1305.89
37.5	564	617	8	10.934	10.934	10.927	1306.29
37.5	565	410	14	10.928	10.935	10.929	1305.98
37.5	566	479	50	10.934	10.933	10.925	1305.95
37.5	567	550	24	10.936	10.935	10.922	1306.04
37.5	568	507	26	10.927	10.930	10.935	1306.02
37.5	569	406	14	10.934	10.930	10.923	1305.27
37.5	570	479	49	10.933	10.934	10.922	1305.66
37.5	571	511	31	10.931	10.926	10.935	1305.97
37.5	572	543	31	10.935	10.934	10.925	1306.29
37.5	573	476	38	10.932	10.934	10.926	1305.92
37.5	574	371	29	10.930	10.930	10.929	1305.74
37.5	575	404	43	10.936	10.934	10.922	1306.09
37.5	576	483	27	10.935	10.931	10.925	1305.80
37.5	577	479	33	10.937	10.933	10.921	1305.85
37.5	578	409	46	10.929	10.929	10.931	1305.60
37.5	579	409	40	10.936	10.936	10.920	1305.96
37.5	596	450	21	10.934	10.933	10.921	1305.48

Continued on next page

fraction [%]	pattern [#]	E_{rel} [meV]	E_g [meV]	a [Å]	b [Å]	c [Å]	volume [Å^3]
37.5	597	411	43	10.934	10.931	10.922	1305.43
37.5	598	643	14	10.937	10.936	10.923	1306.42
37.5	599	645	4	10.935	10.935	10.925	1306.43
37.5	600	412	49	10.933	10.934	10.918	1305.14
37.5	601	644	4	10.933	10.937	10.930	1306.92
37.5	602	643	15	10.937	10.938	10.923	1306.54
37.5	603	571	3	10.929	10.935	10.928	1306.09
37.5	604	571	3	10.935	10.929	10.928	1306.01
37.5	605	830	0	10.934	10.934	10.934	1307.28
37.5	606	378	32	10.933	10.934	10.919	1305.19
37.5	607	574	14	10.931	10.928	10.934	1306.09
37.5	608	574	14	10.927	10.931	10.934	1306.04
37.5	609	573	8	10.934	10.936	10.924	1306.30
37.5	610	574	9	10.935	10.936	10.923	1306.23
37.5	611	798	10	10.932	10.938	10.935	1307.48
37.5	612	575	8	10.935	10.934	10.922	1305.89
37.5	613	574	7	10.935	10.933	10.924	1306.04
37.5	614	798	10	10.938	10.931	10.935	1307.46
37.5	615	763	0	10.933	10.933	10.937	1307.17
37.5	616	206	12	10.928	10.927	10.927	1304.84
37.5	617	450	20	10.933	10.933	10.922	1305.56
37.5	618	410	13	10.927	10.932	10.933	1305.93
37.5	619	411	49	10.934	10.933	10.918	1305.20
37.5	620	376	22	10.936	10.928	10.922	1305.19
37.5	621	412	44	10.932	10.934	10.919	1305.16
37.5	622	372	23	10.933	10.931	10.922	1305.25
37.5	623	377	32	10.934	10.933	10.919	1305.26
37.5	624	340	0	10.927	10.932	10.926	1305.15
37.5	625	205	15	10.933	10.932	10.922	1305.38
37.5	626	411	11	10.931	10.927	10.930	1305.55
37.5	627	372	25	10.933	10.935	10.919	1305.42
37.5	628	376	23	10.928	10.936	10.918	1304.81
37.5	629	340	1	10.932	10.927	10.927	1305.35
37.5	703	549	31	10.933	10.937	10.921	1305.95
37.5	704	479	49	10.934	10.933	10.922	1305.61
37.5	705	543	32	10.935	10.936	10.923	1306.16
37.5	706	579	49	10.936	10.937	10.922	1306.34
37.5	707	552	29	10.934	10.937	10.922	1306.11
37.5	708	617	8	10.933	10.934	10.927	1306.29
37.5	709	651	35	10.934	10.938	10.920	1305.98
37.5	710	511	31	10.926	10.930	10.935	1305.95
37.5	711	542	13	10.931	10.928	10.934	1306.17
37.5	712	636	30	10.931	10.931	10.935	1306.70
37.5	713	479	50	10.933	10.933	10.924	1305.82

Continued on next page

fraction [%]	pattern [#]	E_{rel} [meV]	E_g [meV]	a [Å]	b [Å]	c [Å]	volume [Å^3]
37.5	714	507	25	10.931	10.931	10.932	1306.23
37.5	715	542	13	10.927	10.933	10.932	1306.00
37.5	716	475	38	10.934	10.932	10.926	1305.96
37.5	717	510	42	10.938	10.931	10.920	1305.60
37.5	718	567	24	10.930	10.931	10.934	1306.37
37.5	719	550	24	10.935	10.936	10.922	1305.98
37.5	720	580	42	10.932	10.932	10.932	1306.46
37.5	721	638	25	10.932	10.936	10.932	1306.85
37.5	722	569	27	10.931	10.931	10.934	1306.55
37.5	723	405	42	10.932	10.934	10.921	1305.42
37.5	724	479	31	10.931	10.936	10.924	1305.87
37.5	725	477	38	10.930	10.938	10.920	1305.58
37.5	726	409	36	10.930	10.930	10.931	1305.74
37.5	727	406	36	10.937	10.929	10.920	1305.28
37.5	728	509	52	10.934	10.936	10.921	1305.86
37.5	729	483	27	10.930	10.935	10.925	1305.76
37.5	730	476	34	10.934	10.931	10.923	1305.60
37.5	731	579	45	10.932	10.937	10.926	1306.38
37.5	732	473	15	10.931	10.927	10.931	1305.65
37.5	733	408	47	10.931	10.931	10.929	1305.86
37.5	734	405	42	10.931	10.932	10.922	1305.16
37.5	735	473	3	10.928	10.931	10.930	1305.68
37.5	736	439	38	10.935	10.929	10.925	1305.71
37.5	737	510	54	10.935	10.935	10.920	1305.77
37.5	738	442	28	10.935	10.935	10.920	1305.73
37.5	739	476	16	10.935	10.930	10.927	1305.96
37.5	740	551	37	10.935	10.935	10.924	1306.12
37.5	741	406	14	10.930	10.934	10.923	1305.47
37.5	742	478	29	10.937	10.932	10.921	1305.79
37.5	743	542	32	10.935	10.932	10.930	1306.64
37.5	744	482	12	10.930	10.934	10.928	1305.99
37.5	745	552	27	10.936	10.936	10.922	1306.22
37.5	746	617	32	10.933	10.938	10.923	1306.32
37.5	747	508	35	10.927	10.931	10.935	1306.03
37.5	748	412	15	10.932	10.929	10.923	1305.10
37.5	749	481	41	10.935	10.931	10.924	1305.84
37.5	750	511	28	10.931	10.926	10.935	1306.02
37.5	751	477	8	10.934	10.931	10.923	1305.41
37.5	752	550	30	10.937	10.934	10.922	1306.09
37.5	753	372	31	10.932	10.933	10.924	1305.51
37.5	754	406	34	10.934	10.932	10.922	1305.50
37.5	755	479	45	10.932	10.933	10.926	1305.89
37.5	756	407	42	10.934	10.930	10.924	1305.52
37.5	757	481	46	10.933	10.933	10.922	1305.59

Continued on next page

fraction [%]	pattern [#]	E_{rel} [meV]	E_g [meV]	a [Å]	b [Å]	c [Å]	volume [Å^3]
37.5	758	411	33	10.937	10.930	10.920	1305.31
37.5	785	478	41	10.933	10.932	10.923	1305.51
37.5	786	483	9	10.932	10.928	10.930	1305.79
37.5	787	512	5	10.933	10.928	10.930	1305.87
37.5	788	543	23	10.937	10.933	10.921	1305.94
37.5	789	511	10	10.933	10.931	10.928	1305.98
37.5	790	544	21	10.935	10.931	10.925	1305.89
37.5	791	478	0	10.927	10.930	10.935	1305.95
37.5	792	510	31	10.932	10.926	10.935	1306.08
37.5	793	568	41	10.933	10.928	10.934	1306.36
37.5	794	471	19	10.937	10.926	10.924	1305.37
37.5	795	503	2	10.928	10.928	10.932	1305.57
37.5	796	565	11	10.933	10.929	10.931	1306.13
37.5	797	372	28	10.927	10.924	10.935	1305.26
37.5	798	407	44	10.930	10.928	10.930	1305.53
37.5	799	404	13	10.927	10.927	10.933	1305.39
37.5	800	413	15	10.932	10.925	10.931	1305.51
37.5	801	407	34	10.930	10.923	10.935	1305.39
37.5	802	473	30	10.933	10.928	10.929	1305.84
37.5	803	474	23	10.936	10.931	10.922	1305.64
37.5	804	440	34	10.931	10.925	10.933	1305.66
37.5	805	433	0	10.929	10.929	10.929	1305.36
37.5	806	404	39	10.933	10.929	10.927	1305.68
37.5	807	407	17	10.931	10.924	10.932	1305.32
37.5	808	475	49	10.935	10.929	10.925	1305.65
37.5	809	409	0	10.927	10.927	10.934	1305.55
37.5	810	478	11	10.932	10.929	10.930	1305.83
37.5	811	509	3	10.934	10.929	10.928	1305.81
37.5	812	508	21	10.934	10.931	10.928	1306.05
37.5	813	471	0	10.930	10.928	10.934	1305.97
37.5	814	471	21	10.937	10.928	10.921	1305.26
37.5	815	336	42	10.928	10.923	10.934	1305.20
37.5	816	368	27	10.928	10.923	10.935	1305.28
37.5	817	406	47	10.935	10.928	10.923	1305.23
37.5	818	408	8	10.932	10.928	10.928	1305.53
37.5	819	544	21	10.935	10.931	10.926	1306.00
37.5	820	508	21	10.934	10.931	10.928	1305.97
37.5	821	478	11	10.933	10.928	10.930	1305.90
37.5	822	475	49	10.935	10.929	10.924	1305.64
37.5	823	512	10	10.933	10.930	10.928	1305.95
37.5	824	483	9	10.932	10.928	10.930	1305.79
37.5	825	477	43	10.935	10.933	10.921	1305.70
37.5	826	408	0	10.931	10.931	10.928	1305.79
37.5	827	407	17	10.931	10.924	10.932	1305.34

Continued on next page

fraction [%]	pattern [#]	E_{rel} [meV]	E_g [meV]	a [Å]	b [Å]	c [Å]	volume [Å^3]
37.5	828	405	43	10.929	10.925	10.935	1305.52
37.5	829	474	23	10.936	10.931	10.922	1305.60
37.5	830	407	31	10.933	10.926	10.929	1305.52
37.5	831	404	13	10.927	10.927	10.933	1305.40
37.5	832	407	7	10.933	10.928	10.930	1305.96
37.5	833	407	48	10.935	10.928	10.920	1304.98
37.5	834	367	27	10.928	10.924	10.934	1305.31
37.5	835	412	13	10.932	10.927	10.931	1305.80
37.5	836	407	45	10.931	10.929	10.929	1305.64
37.5	837	371	28	10.927	10.924	10.935	1305.25
37.5	838	335	38	10.932	10.928	10.927	1305.38
37.5	839	565	11	10.933	10.929	10.930	1306.10
37.5	840	543	24	10.937	10.934	10.921	1305.90
37.5	841	503	1	10.929	10.928	10.931	1305.48
37.5	842	509	3	10.934	10.929	10.928	1305.78
37.5	843	471	20	10.937	10.927	10.921	1305.10
37.5	844	513	5	10.933	10.927	10.929	1305.70
37.5	845	471	19	10.935	10.927	10.924	1305.35
37.5	846	473	30	10.933	10.928	10.929	1305.82
37.5	847	433	0	10.929	10.928	10.931	1305.42
37.5	848	568	41	10.933	10.929	10.933	1306.38
37.5	849	509	29	10.935	10.928	10.930	1306.11
37.5	850	471	0	10.934	10.930	10.928	1305.95
37.5	851	478	0	10.930	10.933	10.930	1306.15
37.5	852	439	30	10.936	10.928	10.927	1305.80
50.0	103	710	47	10.939	10.939	10.923	1307.17
50.0	104	638	43	10.934	10.940	10.922	1306.46
50.0	105	600	33	10.931	10.937	10.931	1306.88
50.0	106	619	38	10.934	10.937	10.924	1306.40
50.0	107	615	42	10.938	10.935	10.922	1306.42
50.0	108	568	23	10.930	10.940	10.923	1306.17
50.0	109	547	37	10.933	10.935	10.926	1306.09
50.0	110	548	30	10.932	10.939	10.921	1306.09
50.0	111	558	9	10.932	10.937	10.924	1305.99
50.0	112	546	26	10.934	10.937	10.922	1306.12
50.0	113	567	64	10.934	10.934	10.926	1306.30
50.0	114	527	53	10.932	10.934	10.927	1306.06
50.0	115	534	46	10.934	10.935	10.923	1305.98
50.0	116	494	35	10.937	10.929	10.924	1305.75
50.0	117	545	37	10.937	10.931	10.926	1306.20
50.0	118	497	51	10.931	10.938	10.921	1305.73
50.0	119	460	32	10.930	10.936	10.925	1305.87
50.0	120	474	46	10.930	10.932	10.927	1305.74
50.0	121	476	40	10.935	10.933	10.932	1306.90

Continued on next page

fraction [%]	pattern [#]	E_{rel} [meV]	E_g [meV]	a [Å]	b [Å]	c [Å]	volume [Å^3]
50.0	122	426	0	10.930	10.930	10.932	1305.94
50.0	270	614	39	10.932	10.934	10.933	1306.86
50.0	271	617	33	10.935	10.939	10.923	1306.55
50.0	272	544	3	10.929	10.933	10.930	1306.00
50.0	273	692	18	10.932	10.935	10.932	1306.83
50.0	274	724	12	10.933	10.933	10.934	1306.96
50.0	275	544	48	10.927	10.930	10.936	1306.15
50.0	276	544	42	10.933	10.936	10.924	1306.05
50.0	277	654	38	10.935	10.935	10.933	1307.20
50.0	278	691	16	10.930	10.936	10.932	1306.77
50.0	279	546	37	10.930	10.937	10.926	1306.18
50.0	280	658	49	10.932	10.932	10.935	1306.79
50.0	281	692	19	10.932	10.935	10.932	1306.85
50.0	282	622	6	10.932	10.934	10.930	1306.46
50.0	283	654	10	10.934	10.933	10.932	1306.81
50.0	284	798	0	10.933	10.936	10.936	1307.59
50.0	285	430	24	10.931	10.936	10.920	1305.35
50.0	286	392	38	10.932	10.932	10.924	1305.45
50.0	287	546	43	10.933	10.935	10.925	1306.06
50.0	288	545	19	10.933	10.933	10.925	1305.86
50.0	289	391	32	10.927	10.933	10.930	1305.71
50.0	290	547	26	10.926	10.935	10.933	1306.16
50.0	291	542	28	10.931	10.936	10.925	1305.99
50.0	292	475	8	10.928	10.932	10.929	1305.63
50.0	293	471	9	10.930	10.924	10.933	1305.39
50.0	294	655	11	10.932	10.933	10.932	1306.56
50.0	295	357	39	10.928	10.937	10.919	1305.03
50.0	296	473	43	10.929	10.932	10.933	1306.19
50.0	297	474	10	10.925	10.935	10.930	1305.70
50.0	298	475	46	10.931	10.933	10.926	1305.70
50.0	299	474	31	10.934	10.933	10.919	1305.27
50.0	300	622	15	10.929	10.936	10.931	1306.48
50.0	301	476	26	10.928	10.937	10.926	1305.82
50.0	302	473	26	10.930	10.935	10.923	1305.53
50.0	303	622	5	10.932	10.935	10.930	1306.50
50.0	304	585	3	10.933	10.933	10.931	1306.54
50.0	305	466	19	10.929	10.929	10.933	1305.87
50.0	306	427	40	10.932	10.936	10.918	1305.30
50.0	307	544	8	10.931	10.934	10.928	1306.14
50.0	308	617	28	10.936	10.936	10.922	1306.18
50.0	309	430	50	10.931	10.935	10.922	1305.52
50.0	310	550	13	10.930	10.932	10.931	1306.15
50.0	311	619	39	10.936	10.938	10.922	1306.39
50.0	312	474	4	10.926	10.937	10.925	1305.59

Continued on next page

fraction [%]	pattern [#]	E_{rel} [meV]	E_g [meV]	a [Å]	b [Å]	c [Å]	volume [Å^3]
50.0	313	542	19	10.931	10.930	10.931	1305.98
50.0	314	690	14	10.935	10.935	10.931	1307.15
50.0	315	394	24	10.929	10.929	10.929	1305.52
50.0	316	475	0	10.935	10.928	10.931	1306.18
50.0	317	548	48	10.928	10.929	10.937	1306.23
50.0	318	473	12	10.932	10.932	10.929	1306.02
50.0	319	545	23	10.934	10.930	10.931	1306.38
50.0	320	658	49	10.932	10.931	10.935	1306.74
50.0	321	478	15	10.928	10.936	10.929	1306.11
50.0	322	547	39	10.933	10.934	10.931	1306.62
50.0	323	661	44	10.934	10.934	10.932	1307.03
50.0	324	622	15	10.930	10.935	10.931	1306.48
50.0	325	274	19	10.930	10.932	10.919	1304.65
50.0	326	396	29	10.928	10.928	10.932	1305.55
50.0	327	432	31	10.929	10.934	10.924	1305.50
50.0	328	358	45	10.932	10.933	10.918	1304.87
50.0	329	392	32	10.932	10.926	10.929	1305.50
50.0	330	547	38	10.935	10.934	10.925	1306.17
50.0	331	361	44	10.930	10.938	10.918	1305.32
50.0	332	393	37	10.931	10.931	10.924	1305.25
50.0	333	549	44	10.934	10.937	10.921	1305.90
50.0	334	473	11	10.930	10.931	10.928	1305.58
50.0	335	324	2	10.930	10.930	10.928	1305.48
50.0	336	361	39	10.932	10.935	10.917	1304.95
50.0	337	479	49	10.928	10.928	10.935	1305.89
50.0	338	476	27	10.935	10.932	10.923	1305.83
50.0	339	478	40	10.929	10.932	10.930	1305.93
50.0	374	618	39	10.939	10.937	10.922	1306.65
50.0	375	547	41	10.935	10.933	10.925	1306.20
50.0	376	548	48	10.929	10.928	10.937	1306.22
50.0	377	662	46	10.932	10.932	10.935	1306.80
50.0	378	692	18	10.935	10.932	10.932	1306.86
50.0	379	542	18	10.930	10.930	10.931	1305.99
50.0	380	616	28	10.938	10.937	10.923	1306.63
50.0	381	691	16	10.937	10.931	10.932	1306.84
50.0	382	723	13	10.933	10.934	10.936	1307.28
50.0	383	546	26	10.935	10.937	10.922	1306.19
50.0	384	622	15	10.936	10.930	10.931	1306.50
50.0	385	655	11	10.932	10.933	10.932	1306.55
50.0	386	658	49	10.931	10.933	10.935	1306.77
50.0	387	691	16	10.936	10.930	10.932	1306.83
50.0	388	798	0	10.935	10.933	10.935	1307.34
50.0	389	392	36	10.931	10.931	10.927	1305.54
50.0	390	432	32	10.935	10.929	10.924	1305.54

Continued on next page

fraction [%]	pattern [#]	E_{rel} [meV]	E_g [meV]	a [Å]	b [Å]	c [Å]	volume [Å^3]
50.0	391	548	43	10.936	10.933	10.924	1306.16
50.0	392	542	28	10.936	10.931	10.925	1306.05
50.0	393	361	38	10.934	10.931	10.918	1304.95
50.0	394	478	42	10.935	10.932	10.924	1305.79
50.0	395	472	23	10.931	10.926	10.935	1306.02
50.0	396	479	49	10.928	10.927	10.935	1305.87
50.0	397	474	11	10.934	10.924	10.931	1305.62
50.0	398	623	7	10.934	10.931	10.931	1306.52
50.0	399	392	35	10.932	10.935	10.920	1305.42
50.0	400	473	12	10.932	10.930	10.926	1305.52
50.0	401	471	9	10.925	10.930	10.932	1305.43
50.0	402	547	37	10.933	10.935	10.925	1306.20
50.0	403	545	19	10.934	10.933	10.925	1305.89
50.0	404	655	11	10.933	10.932	10.932	1306.54
50.0	405	476	26	10.929	10.933	10.927	1305.65
50.0	406	474	31	10.933	10.934	10.920	1305.35
50.0	407	585	4	10.933	10.933	10.931	1306.54
50.0	408	622	15	10.936	10.929	10.931	1306.47
50.0	409	431	50	10.935	10.931	10.922	1305.47
50.0	410	467	20	10.928	10.928	10.933	1305.73
50.0	411	549	10	10.938	10.929	10.928	1306.38
50.0	412	617	32	10.939	10.935	10.923	1306.64
50.0	413	394	22	10.929	10.929	10.929	1305.41
50.0	414	477	15	10.937	10.931	10.931	1306.71
50.0	415	545	36	10.937	10.929	10.931	1306.56
50.0	416	475	0	10.927	10.934	10.931	1305.97
50.0	417	544	47	10.931	10.928	10.935	1306.13
50.0	418	658	49	10.932	10.931	10.935	1306.75
50.0	419	426	40	10.934	10.931	10.923	1305.57
50.0	420	474	4	10.938	10.926	10.925	1305.57
50.0	421	544	4	10.933	10.929	10.930	1305.99
50.0	422	544	8	10.934	10.932	10.929	1306.20
50.0	423	616	42	10.938	10.935	10.922	1306.22
50.0	424	691	18	10.935	10.932	10.932	1306.87
50.0	425	473	11	10.932	10.933	10.929	1306.19
50.0	426	544	43	10.937	10.935	10.921	1306.17
50.0	427	623	7	10.934	10.931	10.931	1306.57
50.0	428	654	37	10.935	10.935	10.932	1307.23
50.0	429	273	21	10.934	10.931	10.918	1304.91
50.0	430	361	44	10.938	10.930	10.918	1305.32
50.0	431	392	33	10.934	10.929	10.925	1305.50
50.0	432	396	28	10.930	10.930	10.931	1305.74
50.0	433	430	24	10.936	10.931	10.919	1305.26
50.0	434	547	26	10.936	10.927	10.932	1306.34

Continued on next page

fraction [%]	pattern [#]	E_{rel} [meV]	E_g [meV]	a [Å]	b [Å]	c [Å]	volume [Å^3]
50.0	435	325	3	10.928	10.928	10.928	1305.11
50.0	436	357	36	10.935	10.927	10.923	1305.19
50.0	437	476	28	10.938	10.930	10.922	1305.80
50.0	438	474	45	10.929	10.927	10.935	1305.90
50.0	439	358	44	10.933	10.931	10.921	1305.17
50.0	440	392	35	10.928	10.929	10.931	1305.42
50.0	441	475	8	10.932	10.928	10.930	1305.72
50.0	442	545	43	10.935	10.933	10.926	1306.31
50.0	443	475	47	10.935	10.933	10.923	1305.79
50.0	444	638	43	10.940	10.934	10.922	1306.59
50.0	445	569	45	10.937	10.937	10.922	1306.51
50.0	446	535	39	10.934	10.933	10.924	1305.91
50.0	447	547	39	10.933	10.934	10.929	1306.54
50.0	448	616	33	10.939	10.935	10.923	1306.65
50.0	449	528	44	10.936	10.936	10.921	1306.17
50.0	450	568	51	10.935	10.935	10.920	1305.85
50.0	451	544	41	10.936	10.933	10.925	1306.15
50.0	452	616	27	10.936	10.934	10.927	1306.55
50.0	453	497	51	10.932	10.938	10.921	1305.78
50.0	454	475	28	10.935	10.938	10.922	1306.50
50.0	455	545	43	10.933	10.935	10.926	1306.28
50.0	456	476	26	10.929	10.937	10.927	1306.04
50.0	457	548	43	10.936	10.933	10.924	1306.22
50.0	458	558	7	10.937	10.934	10.922	1306.14
50.0	459	546	43	10.934	10.936	10.924	1306.14
50.0	460	549	42	10.936	10.933	10.924	1306.11
50.0	461	566	0	10.934	10.933	10.928	1306.28
50.0	462	600	36	10.937	10.932	10.926	1306.32
50.0	463	475	28	10.935	10.938	10.922	1306.40
50.0	464	496	51	10.933	10.939	10.922	1306.30
50.0	465	528	41	10.933	10.934	10.926	1306.12
50.0	466	460	37	10.929	10.935	10.926	1305.77
50.0	467	494	29	10.939	10.930	10.921	1305.66
50.0	468	476	27	10.929	10.937	10.926	1305.98
50.0	469	494	30	10.929	10.939	10.920	1305.56
50.0	470	535	39	10.934	10.934	10.924	1305.98
50.0	471	426	29	10.927	10.939	10.922	1305.43
50.0	472	460	38	10.930	10.935	10.925	1305.67
50.0	473	616	32	10.940	10.935	10.924	1306.75
50.0	474	616	27	10.936	10.933	10.927	1306.48
50.0	475	707	26	10.941	10.931	10.927	1306.79
50.0	476	548	41	10.933	10.935	10.924	1306.02
50.0	477	639	43	10.939	10.933	10.921	1306.17
50.0	478	600	35	10.936	10.927	10.933	1306.38

Continued on next page

fraction [%]	pattern [#]	E_{rel} [meV]	E_g [meV]	a [Å]	b [Å]	c [Å]	volume [Å^3]
50.0	479	544	41	10.936	10.933	10.925	1306.22
50.0	480	566	0	10.934	10.933	10.928	1306.29
50.0	481	557	7	10.937	10.934	10.923	1306.22
50.0	482	601	35	10.937	10.933	10.926	1306.47
50.0	483	535	38	10.933	10.934	10.924	1305.89
50.0	484	494	21	10.930	10.930	10.935	1306.41
50.0	485	548	48	10.928	10.929	10.937	1306.21
50.0	486	544	4	10.933	10.929	10.930	1306.02
50.0	487	496	29	10.932	10.932	10.928	1305.87
50.0	488	528	42	10.934	10.934	10.924	1306.02
50.0	489	544	49	10.930	10.927	10.936	1306.16
50.0	490	541	19	10.931	10.931	10.931	1306.09
50.0	491	460	30	10.927	10.934	10.931	1306.03
50.0	492	479	49	10.928	10.927	10.935	1305.85
50.0	493	475	8	10.928	10.932	10.930	1305.76
50.0	494	474	42	10.929	10.934	10.929	1306.00
50.0	495	472	11	10.931	10.930	10.930	1305.83
50.0	496	521	1	10.929	10.928	10.936	1306.09
50.0	497	544	20	10.934	10.935	10.922	1305.84
50.0	498	542	26	10.934	10.927	10.933	1306.20
50.0	499	600	36	10.938	10.932	10.926	1306.39
50.0	500	561	49	10.934	10.929	10.922	1305.23
50.0	501	474	31	10.933	10.934	10.919	1305.25
50.0	502	534	47	10.935	10.935	10.921	1305.84
50.0	503	490	59	10.932	10.933	10.923	1305.51
50.0	504	494	32	10.928	10.927	10.935	1305.76
50.0	505	455	0	10.932	10.923	10.931	1305.25
50.0	506	472	27	10.930	10.935	10.924	1305.61
50.0	507	494	30	10.931	10.929	10.933	1306.11
50.0	508	456	5	10.924	10.931	10.932	1305.51
50.0	509	527	55	10.935	10.933	10.922	1305.85
50.0	510	491	59	10.933	10.933	10.922	1305.53
50.0	511	458	33	10.928	10.932	10.938	1306.63
50.0	512	421	43	10.923	10.928	10.935	1305.27
50.0	513	549	13	10.932	10.930	10.931	1306.21
50.0	514	544	8	10.931	10.933	10.929	1306.01
50.0	515	567	27	10.926	10.937	10.935	1306.72
50.0	516	479	16	10.931	10.932	10.928	1305.83
50.0	517	504	9	10.930	10.930	10.931	1305.89
50.0	518	459	0	10.928	10.935	10.930	1306.05
50.0	519	473	11	10.931	10.932	10.929	1306.00
50.0	520	461	0	10.933	10.925	10.932	1305.69
50.0	521	490	0	10.932	10.932	10.935	1306.84
50.0	522	427	30	10.930	10.925	10.933	1305.57

Continued on next page

fraction [%]	pattern [#]	E_{rel} [meV]	E_g [meV]	a [Å]	b [Å]	c [Å]	volume [Å^3]
50.0	523	521	8	10.937	10.932	10.924	1306.04
50.0	580	558	8	10.937	10.932	10.925	1306.14
50.0	581	558	7	10.932	10.936	10.924	1306.02
50.0	582	522	1	10.928	10.929	10.934	1305.95
50.0	583	798	1	10.933	10.935	10.935	1307.27
50.0	584	798	0	10.936	10.933	10.935	1307.46
50.0	585	1068	0	10.941	10.941	10.937	1309.14
50.0	586	273	19	10.929	10.932	10.920	1304.77
50.0	587	273	19	10.932	10.929	10.921	1304.80
50.0	588	558	7	10.936	10.932	10.924	1306.02
50.0	589	521	9	10.937	10.933	10.920	1305.83
50.0	590	558	9	10.934	10.938	10.924	1306.38
50.0	591	521	9	10.932	10.937	10.922	1305.84
50.0	592	522	1	10.928	10.927	10.935	1305.73
50.0	593	485	3	10.933	10.922	10.934	1305.62
50.0	594	485	2	10.922	10.933	10.935	1305.72
50.0	595	18	48	10.926	10.926	10.922	1303.98
50.0	641	567	64	10.934	10.934	10.926	1306.16
50.0	642	638	43	10.934	10.940	10.922	1306.43
50.0	643	534	47	10.935	10.935	10.921	1305.86
50.0	644	546	37	10.931	10.937	10.925	1306.19
50.0	645	619	38	10.936	10.934	10.925	1306.47
50.0	646	528	54	10.932	10.934	10.925	1305.87
50.0	647	497	51	10.938	10.931	10.921	1305.73
50.0	648	474	48	10.936	10.934	10.921	1305.89
50.0	649	547	37	10.935	10.933	10.926	1306.23
50.0	650	546	26	10.934	10.937	10.922	1306.09
50.0	651	615	40	10.933	10.935	10.929	1306.54
50.0	652	478	42	10.933	10.936	10.922	1305.84
50.0	653	547	26	10.936	10.927	10.932	1306.30
50.0	654	558	8	10.937	10.932	10.924	1306.12
50.0	655	568	23	10.930	10.940	10.923	1306.20
50.0	656	601	34	10.932	10.937	10.926	1306.33
50.0	657	461	32	10.930	10.936	10.922	1305.58
50.0	658	495	35	10.939	10.929	10.922	1305.77
50.0	659	427	0	10.928	10.928	10.934	1305.75
50.0	660	710	47	10.939	10.939	10.923	1306.96
50.0	661	527	54	10.933	10.934	10.925	1306.06
50.0	662	600	36	10.931	10.937	10.928	1306.51
50.0	663	495	29	10.929	10.932	10.928	1305.66
50.0	664	543	45	10.930	10.936	10.929	1306.37
50.0	665	542	19	10.930	10.930	10.931	1305.96
50.0	666	494	32	10.928	10.929	10.935	1305.91
50.0	667	460	37	10.935	10.929	10.927	1305.84

Continued on next page

fraction [%]	pattern [#]	E_{rel} [meV]	E_g [meV]	a [Å]	b [Å]	c [Å]	volume [Å^3]
50.0	668	474	46	10.929	10.927	10.935	1305.87
50.0	669	472	11	10.931	10.932	10.932	1306.30
50.0	670	534	46	10.934	10.934	10.924	1305.89
50.0	671	549	48	10.929	10.928	10.936	1306.17
50.0	672	543	4	10.930	10.933	10.930	1306.06
50.0	673	479	49	10.927	10.928	10.935	1305.87
50.0	674	475	8	10.932	10.928	10.929	1305.63
50.0	675	522	1	10.927	10.928	10.935	1305.74
50.0	676	542	28	10.931	10.936	10.925	1305.99
50.0	677	472	24	10.933	10.928	10.930	1305.91
50.0	678	528	42	10.934	10.934	10.924	1306.02
50.0	679	490	59	10.933	10.934	10.923	1305.73
50.0	680	544	16	10.928	10.931	10.935	1306.15
50.0	681	601	35	10.933	10.937	10.925	1306.40
50.0	682	559	50	10.932	10.937	10.924	1306.02
50.0	683	495	31	10.930	10.930	10.934	1306.17
50.0	684	455	5	10.931	10.924	10.932	1305.39
50.0	685	473	28	10.931	10.929	10.930	1305.70
50.0	686	495	20	10.930	10.930	10.932	1305.93
50.0	687	455	0	10.922	10.933	10.931	1305.31
50.0	688	462	35	10.937	10.932	10.918	1305.35
50.0	689	421	49	10.936	10.929	10.920	1305.14
50.0	690	535	38	10.934	10.933	10.925	1306.01
50.0	691	490	59	10.933	10.932	10.922	1305.46
50.0	692	544	8	10.933	10.931	10.929	1306.16
50.0	693	473	12	10.930	10.932	10.929	1305.85
50.0	694	490	1	10.930	10.930	10.932	1306.06
50.0	695	550	13	10.930	10.933	10.931	1306.19
50.0	696	567	27	10.938	10.927	10.935	1306.85
50.0	697	461	0	10.924	10.932	10.934	1305.81
50.0	698	477	15	10.936	10.930	10.930	1306.38
50.0	699	460	0	10.932	10.925	10.933	1305.82
50.0	700	427	31	10.923	10.931	10.934	1305.65
50.0	701	504	10	10.929	10.929	10.935	1306.09
50.0	702	521	8	10.931	10.937	10.923	1305.78
50.0	759	494	35	10.938	10.929	10.922	1305.72
50.0	760	493	25	10.935	10.927	10.930	1306.11
50.0	761	460	0	10.931	10.925	10.934	1305.76
50.0	762	476	0	10.932	10.925	10.934	1305.83
50.0	763	474	4	10.937	10.925	10.927	1305.60
50.0	764	456	6	10.931	10.923	10.934	1305.54
50.0	765	475	12	10.934	10.924	10.931	1305.60
50.0	766	470	9	10.931	10.925	10.932	1305.47
50.0	767	485	2	10.934	10.922	10.935	1305.89

Continued on next page

fraction [%]	pattern [#]	E_{rel} [meV]	E_g [meV]	a [Å]	b [Å]	c [Å]	volume [Å^3]
50.0	768	470	9	10.931	10.925	10.932	1305.47
50.0	769	474	11	10.934	10.924	10.932	1305.74
50.0	770	494	29	10.939	10.930	10.921	1305.80
50.0	771	454	0	10.933	10.923	10.932	1305.55
50.0	772	494	32	10.934	10.926	10.933	1306.07
50.0	773	456	4	10.930	10.925	10.931	1305.32
50.0	774	461	0	10.933	10.925	10.931	1305.64
50.0	775	424	3	10.935	10.921	10.930	1305.22
50.0	776	455	0	10.932	10.924	10.931	1305.38
50.0	777	417	30	10.922	10.922	10.939	1304.86
50.0	778	474	3	10.937	10.925	10.926	1305.52
50.0	779	475	0	10.932	10.926	10.934	1305.93
50.0	780	461	0	10.933	10.925	10.932	1305.81
50.0	781	460	0	10.933	10.926	10.932	1305.75
50.0	782	427	0	10.927	10.927	10.934	1305.53
50.0	783	424	1	10.935	10.921	10.929	1305.11
50.0	784	485	2	10.933	10.922	10.935	1305.69
62.5	100	409	37	10.930	10.930	10.930	1305.75
62.5	101	476	38	10.934	10.931	10.926	1305.90
62.5	102	437	37	10.935	10.929	10.931	1306.31
62.5	146	638	26	10.932	10.936	10.932	1306.85
62.5	147	636	29	10.932	10.935	10.932	1306.87
62.5	148	798	10	10.938	10.931	10.936	1307.58
62.5	149	831	0	10.934	10.934	10.933	1307.07
62.5	150	405	34	10.931	10.933	10.924	1305.54
62.5	151	406	44	10.934	10.935	10.918	1305.36
62.5	152	371	25	10.929	10.929	10.929	1305.39
62.5	153	569	27	10.930	10.931	10.934	1306.36
62.5	154	565	10	10.934	10.930	10.930	1306.19
62.5	155	367	25	10.925	10.931	10.931	1305.42
62.5	156	568	25	10.930	10.929	10.935	1306.17
62.5	157	565	10	10.929	10.933	10.931	1306.14
62.5	158	763	0	10.932	10.932	10.935	1306.85
62.5	159	442	28	10.934	10.933	10.920	1305.38
62.5	160	442	27	10.933	10.933	10.923	1305.68
62.5	161	405	43	10.924	10.929	10.935	1305.50
62.5	162	568	41	10.929	10.933	10.933	1306.35
62.5	163	636	30	10.931	10.931	10.935	1306.62
62.5	164	405	43	10.928	10.924	10.935	1305.44
62.5	165	568	40	10.934	10.929	10.932	1306.31
62.5	166	638	27	10.932	10.932	10.935	1306.70
62.5	167	798	10	10.931	10.938	10.934	1307.35
62.5	168	207	12	10.929	10.929	10.921	1304.40
62.5	169	205	15	10.933	10.932	10.921	1305.33

Continued on next page

fraction [%]	pattern [#]	E_{rel} [meV]	E_g [meV]	a [Å]	b [Å]	c [Å]	volume [Å^3]
62.5	170	372	32	10.934	10.933	10.920	1305.41
62.5	171	406	44	10.934	10.933	10.918	1305.24
62.5	172	372	30	10.931	10.931	10.926	1305.53
62.5	173	406	35	10.934	10.932	10.919	1305.22
62.5	174	335	38	10.928	10.933	10.926	1305.34
62.5	175	368	27	10.929	10.923	10.934	1305.26
62.5	176	567	24	10.931	10.931	10.934	1306.41
62.5	177	336	37	10.933	10.930	10.923	1305.28
62.5	178	371	28	10.925	10.927	10.934	1305.31
62.5	179	568	25	10.936	10.933	10.933	1307.11
62.5	180	581	45	10.936	10.936	10.922	1306.14
62.5	181	543	35	10.937	10.935	10.921	1306.09
62.5	182	543	32	10.935	10.936	10.923	1306.10
62.5	183	510	54	10.935	10.934	10.919	1305.53
62.5	184	573	7	10.936	10.933	10.925	1306.28
62.5	185	644	14	10.937	10.935	10.923	1306.35
62.5	186	480	45	10.933	10.933	10.925	1305.81
62.5	187	479	33	10.932	10.937	10.921	1305.75
62.5	188	408	47	10.932	10.930	10.922	1305.12
62.5	189	510	41	10.931	10.937	10.921	1305.57
62.5	190	543	24	10.937	10.933	10.921	1305.89
62.5	191	407	8	10.928	10.933	10.930	1305.99
62.5	192	408	47	10.931	10.930	10.929	1305.81
62.5	193	476	38	10.932	10.934	10.925	1305.89
62.5	194	510	10	10.933	10.932	10.931	1306.45
62.5	195	407	42	10.930	10.934	10.924	1305.52
62.5	196	476	8	10.932	10.934	10.924	1305.75
62.5	197	508	21	10.931	10.934	10.928	1305.99
62.5	198	439	37	10.928	10.934	10.927	1305.62
62.5	199	473	33	10.935	10.931	10.923	1305.67
62.5	200	575	9	10.935	10.934	10.922	1305.95
62.5	201	549	31	10.937	10.933	10.921	1305.85
62.5	202	551	25	10.934	10.934	10.926	1306.30
62.5	203	477	41	10.932	10.933	10.925	1305.76
62.5	204	543	21	10.932	10.935	10.925	1305.99
62.5	205	650	35	10.938	10.933	10.922	1306.15
62.5	206	477	11	10.932	10.929	10.930	1305.94
62.5	207	478	27	10.936	10.930	10.926	1305.89
62.5	208	508	3	10.935	10.928	10.929	1305.90
62.5	209	616	8	10.936	10.932	10.928	1306.48
62.5	210	479	50	10.934	10.933	10.925	1305.84
62.5	211	513	5	10.933	10.928	10.930	1305.79
62.5	212	616	32	10.938	10.933	10.926	1306.61
62.5	213	474	23	10.931	10.936	10.922	1305.63

Continued on next page

fraction [%]	pattern [#]	E_{rel} [meV]	E_g [meV]	a [Å]	b [Å]	c [Å]	volume [Å^3]
62.5	214	579	44	10.936	10.931	10.927	1306.29
62.5	215	645	4	10.935	10.935	10.925	1306.32
62.5	216	450	20	10.933	10.933	10.922	1305.51
62.5	217	411	49	10.935	10.933	10.918	1305.30
62.5	218	480	47	10.934	10.934	10.922	1305.73
62.5	219	552	28	10.936	10.932	10.925	1306.12
62.5	220	411	43	10.931	10.934	10.922	1305.47
62.5	221	483	27	10.930	10.935	10.925	1305.78
62.5	222	551	38	10.936	10.936	10.920	1306.00
62.5	223	406	47	10.927	10.934	10.925	1305.35
62.5	224	475	49	10.935	10.929	10.924	1305.59
62.5	225	579	49	10.936	10.937	10.922	1306.30
62.5	226	377	31	10.932	10.932	10.923	1305.43
62.5	227	413	15	10.933	10.925	10.931	1305.66
62.5	228	482	9	10.928	10.933	10.930	1305.89
62.5	229	410	41	10.934	10.934	10.919	1305.47
62.5	230	480	40	10.935	10.930	10.927	1306.06
62.5	231	550	30	10.937	10.934	10.921	1306.11
62.5	232	411	33	10.929	10.936	10.919	1305.08
62.5	233	478	49	10.935	10.935	10.923	1306.17
62.5	234	550	22	10.933	10.935	10.925	1306.12
62.5	235	509	52	10.933	10.935	10.920	1305.47
62.5	236	543	13	10.927	10.933	10.932	1305.94
62.5	237	507	33	10.931	10.932	10.932	1306.27
62.5	238	511	32	10.926	10.930	10.936	1305.98
62.5	239	473	3	10.928	10.931	10.930	1305.58
62.5	240	573	13	10.931	10.935	10.930	1306.44
62.5	241	571	3	10.929	10.935	10.929	1306.08
62.5	242	475	33	10.931	10.934	10.926	1305.80
62.5	243	476	37	10.929	10.936	10.925	1305.76
62.5	244	403	10	10.929	10.929	10.929	1305.41
62.5	245	544	13	10.927	10.930	10.932	1305.73
62.5	246	503	3	10.928	10.928	10.932	1305.53
62.5	247	407	33	10.925	10.932	10.932	1305.63
62.5	248	405	42	10.931	10.932	10.923	1305.28
62.5	249	507	27	10.927	10.930	10.935	1305.97
62.5	250	471	20	10.927	10.936	10.921	1305.08
62.5	251	406	36	10.929	10.937	10.920	1305.23
62.5	252	511	28	10.927	10.931	10.935	1306.00
62.5	253	470	18	10.924	10.936	10.930	1305.74
62.5	254	473	16	10.927	10.931	10.932	1305.83
62.5	255	434	0	10.928	10.928	10.930	1305.21
62.5	256	477	16	10.930	10.935	10.926	1305.81
62.5	257	483	11	10.929	10.934	10.928	1305.80

Continued on next page

fraction [%]	pattern [#]	E_{rel} [meV]	E_g [meV]	a [Å]	b [Å]	c [Å]	volume [Å^3]
62.5	258	407	16	10.925	10.933	10.930	1305.54
62.5	259	510	30	10.925	10.933	10.934	1305.94
62.5	260	409	0	10.927	10.927	10.934	1305.53
62.5	261	406	14	10.929	10.934	10.924	1305.48
62.5	262	471	0	10.931	10.928	10.933	1305.99
62.5	263	411	15	10.929	10.934	10.925	1305.47
62.5	264	478	0	10.928	10.931	10.933	1305.97
62.5	265	439	33	10.926	10.932	10.934	1305.97
62.5	266	411	11	10.927	10.931	10.930	1305.54
62.5	267	372	24	10.933	10.935	10.919	1305.38
62.5	268	376	24	10.929	10.936	10.917	1304.85
62.5	269	340	0	10.927	10.931	10.926	1305.00
62.5	340	511	28	10.930	10.927	10.935	1305.99
62.5	341	543	13	10.932	10.928	10.933	1306.07
62.5	342	473	16	10.931	10.926	10.932	1305.71
62.5	343	507	27	10.930	10.926	10.935	1305.97
62.5	344	574	14	10.932	10.928	10.933	1306.08
62.5	345	570	3	10.935	10.930	10.928	1306.08
62.5	346	478	38	10.937	10.929	10.920	1305.28
62.5	347	407	36	10.936	10.928	10.919	1305.02
62.5	348	407	32	10.932	10.925	10.931	1305.48
62.5	349	511	31	10.930	10.926	10.935	1305.97
62.5	350	471	19	10.936	10.926	10.924	1305.25
62.5	351	404	12	10.927	10.927	10.931	1305.24
62.5	352	476	34	10.934	10.931	10.924	1305.57
62.5	353	542	11	10.931	10.929	10.932	1305.97
62.5	354	503	3	10.928	10.928	10.932	1305.46
62.5	355	405	42	10.931	10.930	10.924	1305.13
62.5	356	473	3	10.931	10.928	10.931	1305.69
62.5	357	434	0	10.927	10.928	10.930	1305.21
62.5	358	508	36	10.931	10.927	10.935	1306.01
62.5	359	471	19	10.935	10.928	10.925	1305.38
62.5	360	482	11	10.934	10.929	10.928	1305.83
62.5	361	411	15	10.933	10.929	10.925	1305.36
62.5	362	408	0	10.931	10.931	10.930	1305.97
62.5	363	477	0	10.931	10.929	10.939	1306.78
62.5	364	407	17	10.931	10.923	10.932	1305.31
62.5	365	476	16	10.934	10.930	10.927	1305.96
62.5	366	510	31	10.932	10.926	10.934	1305.98
62.5	367	406	14	10.934	10.930	10.922	1305.29
62.5	368	440	34	10.932	10.925	10.933	1305.71
62.5	369	471	0	10.928	10.931	10.934	1306.00
62.5	370	376	24	10.937	10.930	10.918	1305.06
62.5	371	411	12	10.931	10.927	10.931	1305.51

Continued on next page

fraction [%]	pattern [#]	E_{rel} [meV]	E_g [meV]	a [Å]	b [Å]	c [Å]	volume [Å^3]
62.5	372	340	0	10.932	10.927	10.927	1305.16
62.5	373	372	25	10.935	10.932	10.919	1305.41
62.5	47	650	35	10.934	10.939	10.921	1306.16
62.5	48	617	31	10.933	10.937	10.926	1306.55
62.5	49	617	8	10.934	10.935	10.926	1306.36
62.5	50	579	45	10.932	10.937	10.927	1306.34
62.5	51	643	14	10.936	10.937	10.923	1306.45
62.5	52	645	4	10.935	10.936	10.927	1306.61
62.5	53	551	27	10.936	10.937	10.923	1306.31
62.5	54	548	31	10.934	10.938	10.922	1306.16
62.5	55	478	41	10.933	10.932	10.924	1305.60
62.5	56	580	43	10.935	10.935	10.925	1306.34
62.5	57	543	21	10.935	10.932	10.925	1305.96
62.5	58	478	11	10.928	10.932	10.930	1305.80
62.5	59	479	50	10.933	10.933	10.925	1305.86
62.5	60	543	32	10.936	10.935	10.923	1306.24
62.5	61	512	4	10.931	10.932	10.931	1306.25
62.5	62	478	29	10.932	10.937	10.921	1305.72
62.5	63	543	35	10.936	10.938	10.921	1306.29
62.5	64	508	3	10.929	10.934	10.928	1305.84
62.5	65	509	50	10.930	10.930	10.933	1306.10
62.5	66	473	21	10.932	10.929	10.930	1305.88
62.5	67	573	7	10.933	10.936	10.925	1306.20
62.5	68	550	38	10.936	10.936	10.921	1306.19
62.5	69	552	30	10.935	10.937	10.921	1306.09
62.5	70	475	49	10.929	10.935	10.926	1305.77
62.5	71	543	24	10.933	10.937	10.921	1305.97
62.5	72	579	49	10.937	10.936	10.922	1306.36
62.5	73	483	10	10.933	10.928	10.930	1305.74
62.5	74	478	49	10.935	10.934	10.922	1306.00
62.5	75	508	21	10.934	10.931	10.928	1306.03
62.5	76	551	23	10.935	10.934	10.921	1305.86
62.5	77	481	41	10.931	10.935	10.926	1305.99
62.5	78	511	10	10.933	10.931	10.928	1305.96
62.5	79	551	31	10.934	10.937	10.921	1306.02
62.5	80	473	33	10.932	10.935	10.921	1305.61
62.5	81	509	52	10.935	10.934	10.920	1305.61
62.5	82	574	8	10.933	10.936	10.925	1306.18
62.5	83	450	20	10.933	10.933	10.922	1305.52
62.5	84	412	45	10.934	10.933	10.919	1305.32
62.5	85	479	32	10.937	10.932	10.921	1305.81
62.5	86	483	28	10.935	10.932	10.922	1305.63
62.5	87	411	50	10.933	10.934	10.918	1305.13
62.5	88	480	43	10.930	10.931	10.932	1306.07

Continued on next page

fraction [%]	pattern [#]	E_{rel} [meV]	E_g [meV]	a [Å]	b [Å]	c [Å]	volume [Å^3]
62.5	89	479	46	10.933	10.934	10.925	1305.87
62.5	90	408	48	10.931	10.933	10.922	1305.34
62.5	91	406	46	10.935	10.928	10.925	1305.42
62.5	92	509	41	10.937	10.931	10.924	1305.88
62.5	93	377	33	10.933	10.934	10.918	1305.20
62.5	94	407	7	10.934	10.927	10.929	1305.70
62.5	95	412	12	10.931	10.932	10.930	1306.11
62.5	96	407	43	10.935	10.930	10.921	1305.17
62.5	97	411	33	10.935	10.930	10.920	1305.16
62.5	98	476	8	10.934	10.931	10.924	1305.73
62.5	99	408	47	10.930	10.931	10.929	1305.81
75.0	10	438	32	10.931	10.935	10.919	1305.19
75.0	11	554	6	10.932	10.937	10.923	1305.96
75.0	123	553	7	10.936	10.932	10.925	1306.19
75.0	124	369	29	10.934	10.933	10.920	1305.29
75.0	12	517	6	10.931	10.937	10.924	1305.96
75.0	125	367	32	10.929	10.934	10.923	1305.31
75.0	126	483	1	10.933	10.928	10.928	1305.67
75.0	127	518	6	10.936	10.931	10.922	1305.68
75.0	128	440	33	10.935	10.935	10.920	1305.72
75.0	129	438	33	10.936	10.933	10.919	1305.54
75.0	130	624	0	10.933	10.933	10.930	1306.50
75.0	131	290	27	10.931	10.931	10.920	1304.83
75.0	132	291	24	10.931	10.931	10.923	1305.11
75.0	13	291	22	10.929	10.930	10.926	1305.22
75.0	133	254	22	10.930	10.930	10.922	1304.86
75.0	134	515	0	10.930	10.929	10.934	1306.02
75.0	135	364	13	10.928	10.926	10.931	1305.18
75.0	136	364	13	10.926	10.928	10.932	1305.22
75.0	137	515	1	10.934	10.933	10.927	1306.15
75.0	138	477	12	10.933	10.933	10.922	1305.61
75.0	139	366	49	10.925	10.928	10.934	1305.42
75.0	140	365	45	10.932	10.931	10.927	1305.78
75.0	141	483	0	10.928	10.928	10.933	1305.74
75.0	142	251	29	10.927	10.927	10.930	1304.97
75.0	14	290	28	10.931	10.932	10.919	1304.79
75.0	143	251	30	10.927	10.927	10.932	1305.13
75.0	144	217	46	10.927	10.928	10.924	1304.38
75.0	145	216	45	10.929	10.929	10.924	1304.75
75.0	15	254	24	10.933	10.932	10.918	1304.88
75.0	16	369	29	10.933	10.934	10.920	1305.28
75.0	17	367	32	10.934	10.930	10.922	1305.32
75.0	18	483	0	10.929	10.933	10.927	1305.68
75.0	19	444	32	10.935	10.933	10.919	1305.31

Continued on next page

fraction [%]	pattern [#]	E_{rel} [meV]	E_g [meV]	a [Å]	b [Å]	c [Å]	volume [Å^3]
75.0	20	426	37	10.935	10.932	10.922	1305.60
75.0	21	391	27	10.928	10.929	10.930	1305.37
75.0	22	387	11	10.929	10.927	10.931	1305.30
75.0	23	354	45	10.935	10.931	10.919	1305.11
75.0	24	370	40	10.929	10.930	10.929	1305.56
75.0	25	373	22	10.929	10.927	10.932	1305.45
75.0	26	459	29	10.933	10.932	10.923	1305.50
75.0	27	425	37	10.936	10.929	10.922	1305.44
75.0	28	426	39	10.935	10.933	10.918	1305.27
75.0	29	387	38	10.932	10.931	10.923	1305.26
75.0	30	370	30	10.931	10.929	10.926	1305.33
75.0	31	446	32	10.935	10.931	10.918	1305.10
75.0	32	445	32	10.937	10.932	10.920	1305.60
75.0	33	442	30	10.932	10.933	10.928	1306.08
75.0	34	371	33	10.934	10.931	10.918	1304.84
75.0	35	387	38	10.932	10.931	10.923	1305.26
75.0	36	425	39	10.936	10.930	10.919	1305.16
75.0	37	373	22	10.929	10.927	10.932	1305.46
75.0	38	372	31	10.932	10.927	10.929	1305.55
75.0	39	353	43	10.935	10.928	10.923	1305.29
75.0	40	394	18	10.926	10.928	10.933	1305.40
75.0	41	372	43	10.933	10.932	10.919	1305.09
75.0	42	354	45	10.935	10.931	10.919	1305.12
75.0	43	390	25	10.930	10.931	10.931	1305.90
75.0	44	317	39	10.930	10.930	10.924	1305.00
75.0	45	353	45	10.936	10.930	10.919	1305.20
75.0	46	372	32	10.932	10.927	10.929	1305.50
75.0	8	623	0	10.937	10.933	10.930	1306.85
75.0	9	440	33	10.933	10.934	10.920	1305.43
87.5	2	263	2	10.930	10.931	10.924	1305.09
87.5	3	298	34	10.932	10.932	10.917	1304.53
87.5	4	196	8	10.931	10.930	10.921	1304.77
87.5	5	196	7	10.928	10.929	10.924	1304.73
87.5	6	226	25	10.930	10.930	10.918	1304.41
87.5	7	262	2	10.931	10.930	10.924	1305.20
100.0	1	0	66	10.929	10.929	10.923	1304.63

Table A.3: Statistical analysis of the Bader charges for each disorder fraction at the PBE-level.

	0 %				12.5 %			
atom	Cu	Sn	Zn	S	Cu	Sn	Zn	S
min	0.475	1.382	0.849	-0.796	0.474	1.362	0.839	-0.830
1st quart	0.475	1.382	0.849	-0.796	0.475	1.372	0.847	-0.801
median	0.477	1.382	0.849	-0.796	0.478	1.378	0.851	-0.796
mean	0.477	1.382	0.849	-0.796	0.479	1.376	0.849	-0.796
3rd quart	0.478	1.382	0.849	-0.796	0.482	1.381	0.853	-0.791
max	0.478	1.382	0.849	-0.796	0.486	1.382	0.854	-0.758
	25.0 %				37.5 %			
atom	Cu	Sn	Zn	S	Cu	Sn	Zn	S
min	0.470	1.355	0.840	-0.841	0.471	1.353	0.842	-0.843
1st quart	0.476	1.369	0.848	-0.805	0.477	1.368	0.850	-0.811
median	0.479	1.373	0.851	-0.797	0.480	1.372	0.852	-0.797
mean	0.480	1.374	0.851	-0.796	0.481	1.372	0.852	-0.797
3rd quart	0.483	1.377	0.854	-0.788	0.484	1.376	0.854	-0.784
max	0.495	1.390	0.864	-0.747	0.498	1.394	0.864	-0.742
	50.0 %				62.5 %			
atom	Cu	Sn	Zn	S	Cu	Sn	Zn	S
min	0.470	1.353	0.843	-0.850	0.471	1.353	0.842	-0.845
1st quart	0.478	1.367	0.850	-0.813	0.477	1.368	0.850	-0.810
median	0.481	1.371	0.852	-0.797	0.480	1.372	0.852	-0.797
mean	0.481	1.372	0.852	-0.797	0.481	1.372	0.852	-0.797
3rd quart	0.484	1.376	0.854	-0.783	0.484	1.376	0.854	-0.786
max	0.497	1.393	0.863	-0.741	0.498	1.395	0.865	-0.742
	75.0 %				87.5 %			
atom	Cu	Sn	Zn	S	Cu	Sn	Zn	S
min	0.470	1.355	0.840	-0.840	0.474	1.362	0.839	-0.831
1st quart	0.476	1.370	0.848	-0.805	0.476	1.372	0.847	-0.801
median	0.479	1.374	0.851	-0.797	0.478	1.378	0.851	-0.796
mean	0.480	1.374	0.851	-0.797	0.479	1.376	0.850	-0.796
3rd quart	0.483	1.378	0.854	-0.787	0.481	1.381	0.853	-0.791
max	0.495	1.390	0.864	-0.748	0.487	1.382	0.854	-0.758
	100.0 %							
atom	Cu	Sn	Zn	S				
min	0.476	1.381	0.849	-0.796				
1st quart	0.476	1.381	0.849	-0.796				
median	0.477	1.381	0.849	-0.796				
mean	0.477	1.381	0.849	-0.796				
3rd quart	0.478	1.381	0.849	-0.796				
max	0.478	1.381	0.849	-0.796				

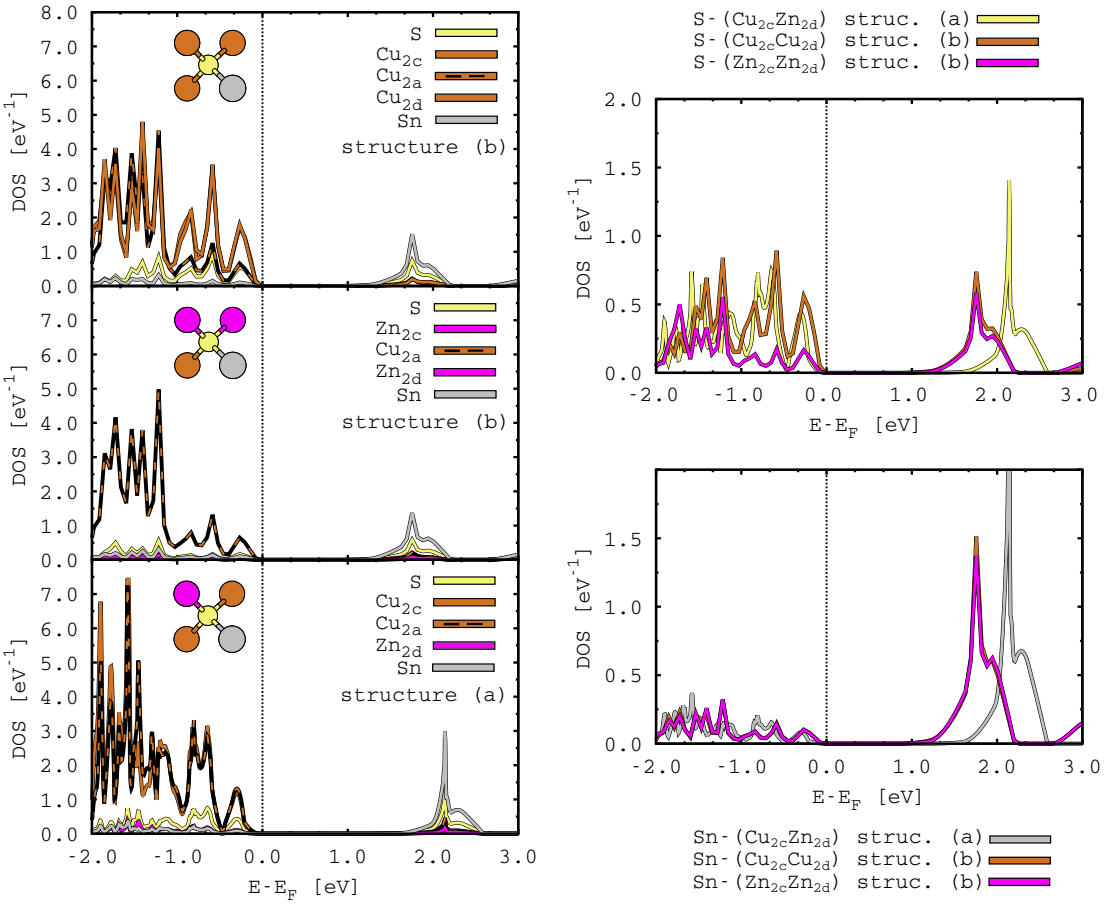

Figure A.4: HSE06 DOS on top of the PBE-optimized structure for structure (b) and the reference structure (a) with their occurring binding motifs. The Fermi energy of the different structures are aligned for comparison. Zn is shown in pink, Cu in brown, Sn in gray and S in yellow.

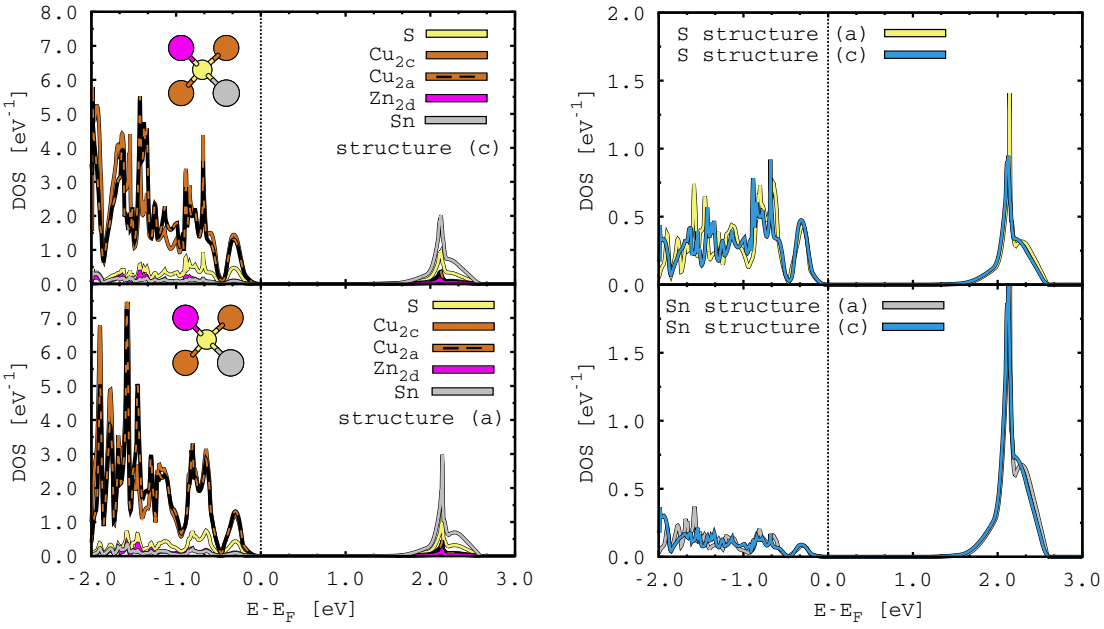

Figure A.5: HSE06 DOS on top of the PBE-optimized structure for structure (c) and the reference structure (a) with their occurring binding motifs. The Fermi energy of the different structures are aligned for comparison. Zn is shown in pink, Cu in brown, Sn in gray and S in yellow.

Appendix B

Nanostructuring by Cu_2ZnSnS_4 Surfaces

Table B.1: Surface energies of unrelaxed and relaxed CZTS surfaces obtained by eq. 4.2 and the extrapolation scheme after eq. 4.4 in J/m^2 at the PBE-level.

(001)			(100)			(110)		
term.	urlx	rlx	term.	urlx	rlx	term.	urlx	rlx
t1†	1.661	0.877	t1†	2.288	1.897	t1a†	2.004	1.753
t2†	2.471	2.057	t2*	0.481	-0.162	t1b†	0.670	0.165
t3†	0.395	0.299	t3†	1.878	1.335	t2a†	0.977	0.656
t4†	1.217	0.810	t4†	0.901	0.390	t2b†	0.430	0.248
t1+t4	2.832	1.656	t5†	1.310	0.948	t3a†	1.379	0.488
t2+t3	2.823	2.338	t1+t2	2.769	1.735	t3b†	1.508	0.908
			t3+t4	2.766	1.700	t1a+t1b	2.652	1.889
			t5+t5	2.612	1.804	t2a+t2b	1.416	0.870
						t3a+t3b	2.818	1.382
(101)			(111)			(112)		
term.	urlx	rlx	term.	urlx	rlx	term.	urlx	rlx
t1a+t1b	1.912	1.150	t1a+t1b	2.482	1.107	t1a+t1b	4.854	2.339
t2a+t2b	1.965	1.106	t2a+t2b	1.915	1.047	t2a+t2b	4.047	1.742
t3a+t3b	1.842	1.114	t3a+t3b	1.428	0.839	t3a+t3b	3.154	1.422
t4a+t4b	2.191	1.527	t4a+t4b	2.458	1.461	t4a+t4b	2.282	1.265
t5a+t5b	2.090	1.504	t5a+t5b	2.073	1.163	t5a+t5b	1.361	0.768
t6a+t6b	2.193	1.386	t6a+t6b	1.442	0.856			
t7a+t7b	2.316	1.396						
t8a+t8b	1.608	0.770						

† extrapolation scheme after eq. 4.4

tx+ty conventional scheme after eq. 4.2

* t1+t2-t1†

Table B.2: Relaxation energies in J/m^2 for all calculated surfaces at the PBE-level. The relaxation energies are obtained by double-sided slab relaxations (tx+ty) and single-sided relaxations (*) after eq. 4.2.

(001)		(100)		(110)	
term.	E_{relax}	term.	E_{relax}	term.	E_{relax}
t1*	0.766	t1*	0.436	t1a*	0.256
t2*	0.399	t2*	0.685	t1b*	0.507
t3*	0.085	t1+t2	1.034	t1a+t1b	0.762
t4*	0.399	t3*	0.554	t2a*	0.352
t1+t4	1.176	t4*	0.510	t2b*	0.194
t2+t3	0.485	t3+t4	1.066	t2a+t2b	0.546
		t5*	0.404	t3a*	0.887
		t5+t5	0.808	t3b*	0.550
				t3a+t3b	1.436
(101)		(111)		(112)	
term.	E_{relax}	term.	E_{relax}	term.	E_{relax}
t1a*	0.266	t1a*	0.782	t1a*	1.228
t1b*	0.494	t1b*	0.416	t1b*	0.901
t1a+t1b	0.762	t1a+t1b	1.376	t1a+t1b	2.515
t2a*	0.557	t2a*	0.585	t2a*	1.500
t2b*	0.303	t2b*	0.279	t2b*	0.801
t2a+t2b	0.859	t2a+t2b	0.868	t2a+t2b	2.305
t3a*	0.057	t3a*	0.471	t3a*	1.170
t3b*	0.667	t3b*	0.113	t3b*	0.556
t3a+t3b	0.729	t3a+t3b	0.589	t3a+t3b	1.732
t4a*	0.312	t4a*	0.595	t4a*	0.642
t4b*	0.351	t4b*	0.402	t4b*	0.286
t4a+t4b	0.664	t4a+t4b	0.998	t4a+t4b	1.016
t5a*	0.302	t5a*	0.563	t5a*	0.558
t5b*	0.283	t5b*	0.348	t5b*	0.036
t5a+t5b	0.586	t5a+t5b	0.910	t5a+t5b	0.594
t6a*	0.663	t6a*	0.409		
t6b*	0.144	t6b*	0.183		
t6a+t6b	0.807	t6a+t6b	0.586		
t7a*	0.309				
t7b*	0.611				
t7a+t7b	0.919				
t8a*	0.596				
t8b*	0.243				
t8a+t8b	0.838				

* single-sided relaxation after eq. 4.2

tx+ty double-sided relaxation after eq. 4.2

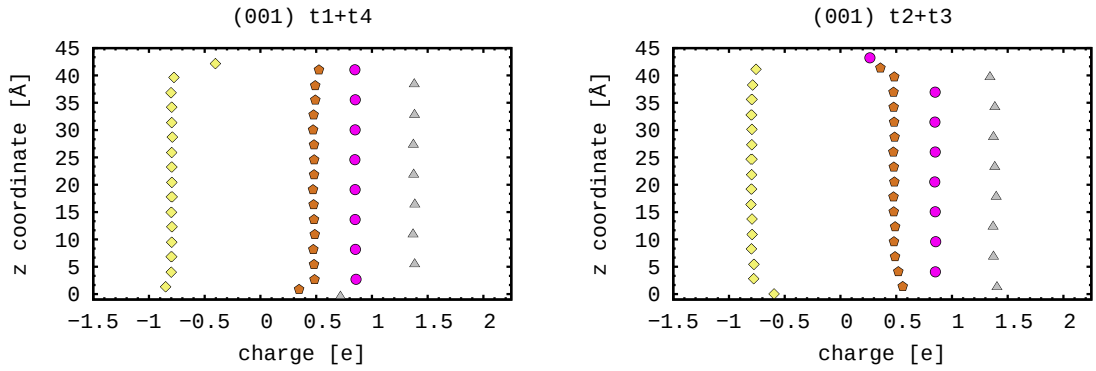

Figure B.1: Bader charges for every relaxed slab of the (001) surface. Zn is shown in pink, Cu in brown, Sn in gray and S in yellow.

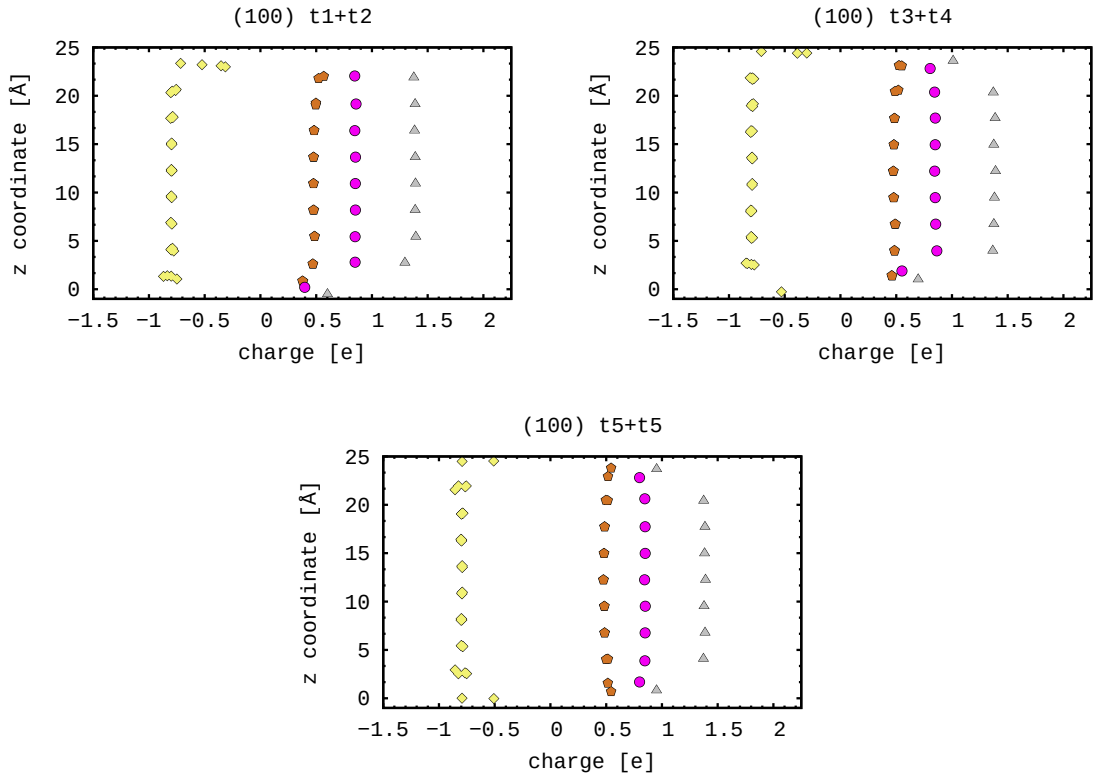

Figure B.2: Bader charges for every relaxed slab of the (100) surface. Zn is shown in pink, Cu in brown, Sn in gray and S in yellow.

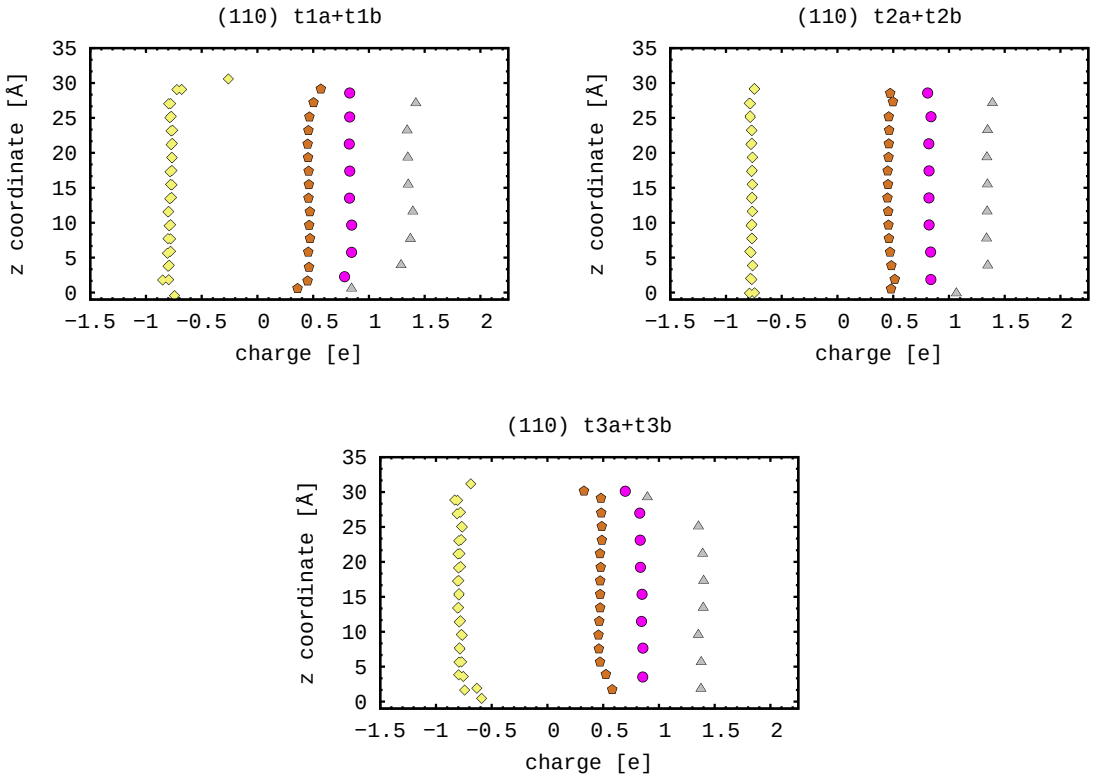

Figure B.3: Bader charges for every relaxed slab of the (110) surface. Zn is shown in pink, Cu in brown, Sn in gray and S in yellow.

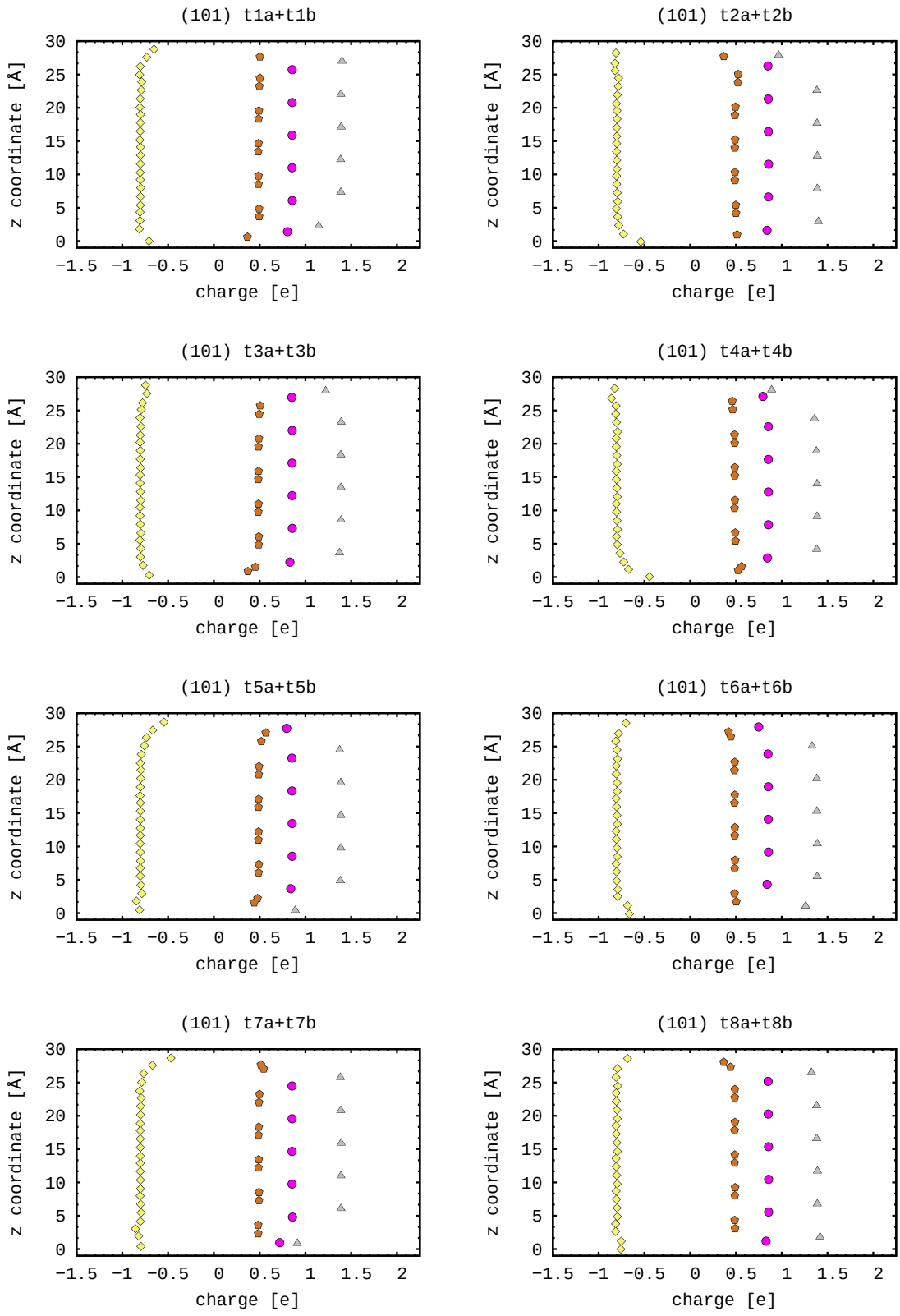

Figure B.4: Bader charges for every relaxed slab of the (101) surface. Zn is shown in pink, Cu in brown, Sn in gray and S in yellow.

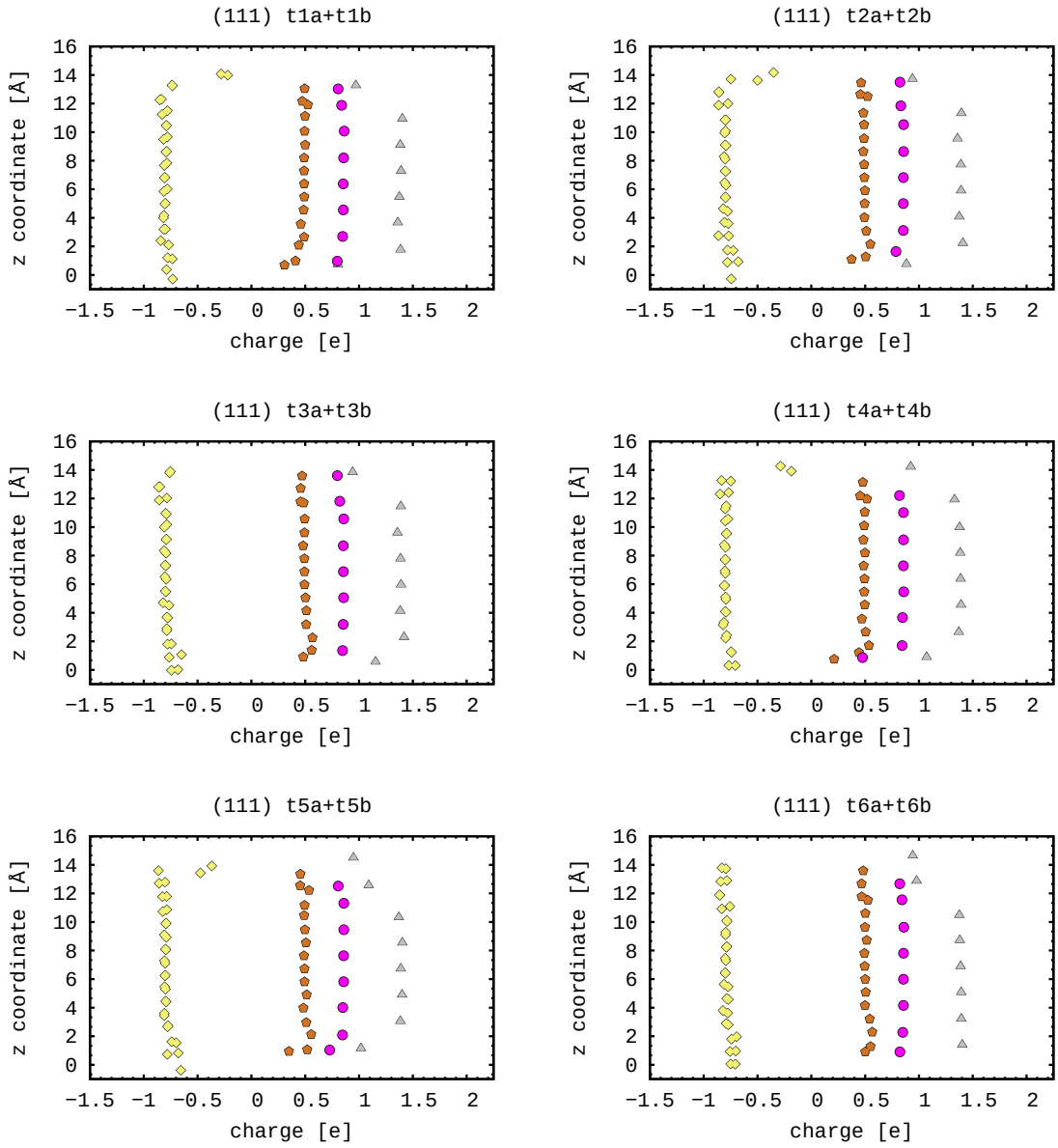

Figure B.5: Bader charges for all relaxed slabs of the (111) surface. Zn is shown in pink, Cu in brown, Sn in gray and S in yellow.

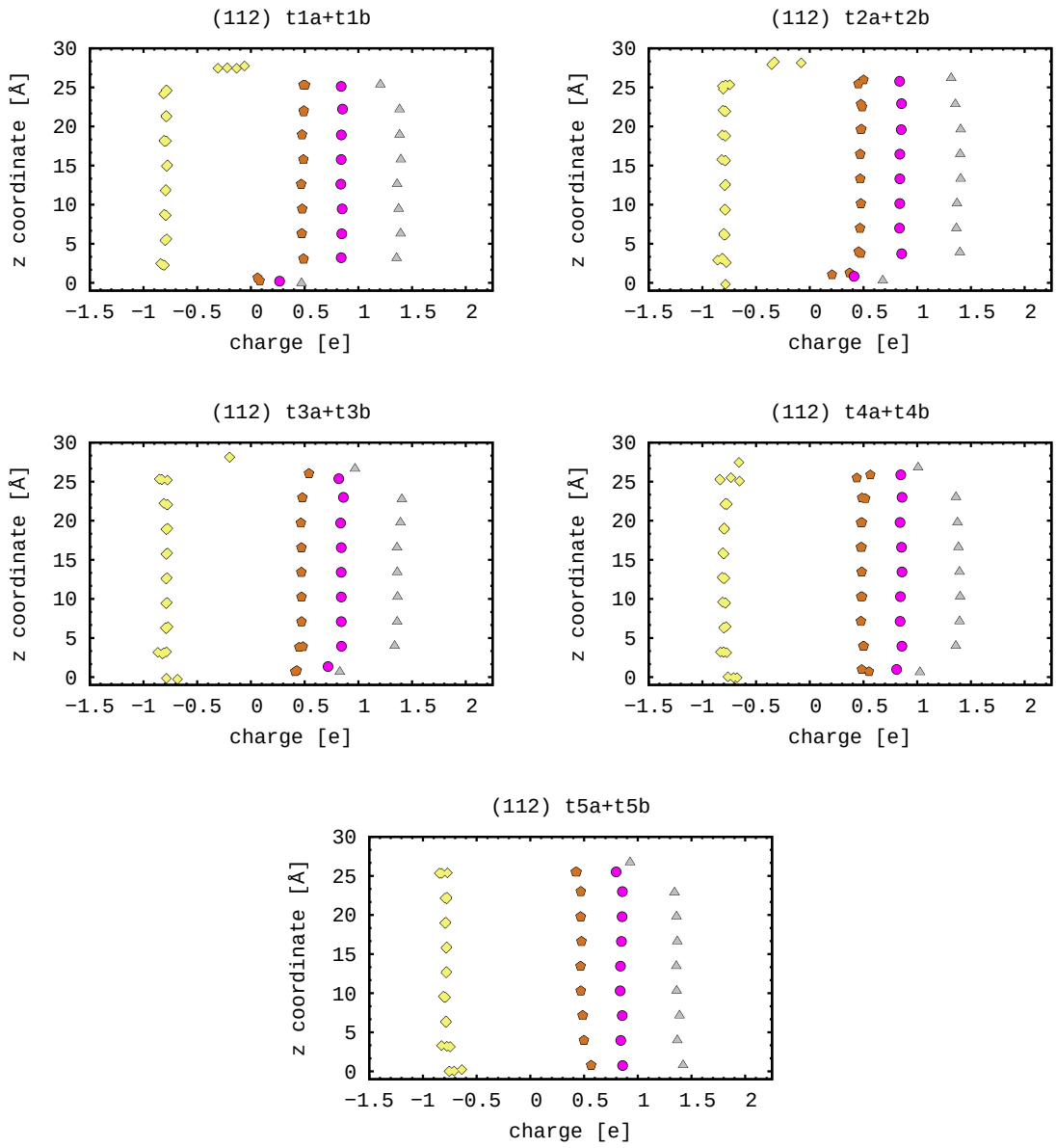

Figure B.6: Bader charges for all relaxed slabs of the (112) surface. Zn is shown in pink, Cu in brown, Sn in gray and S in yellow.

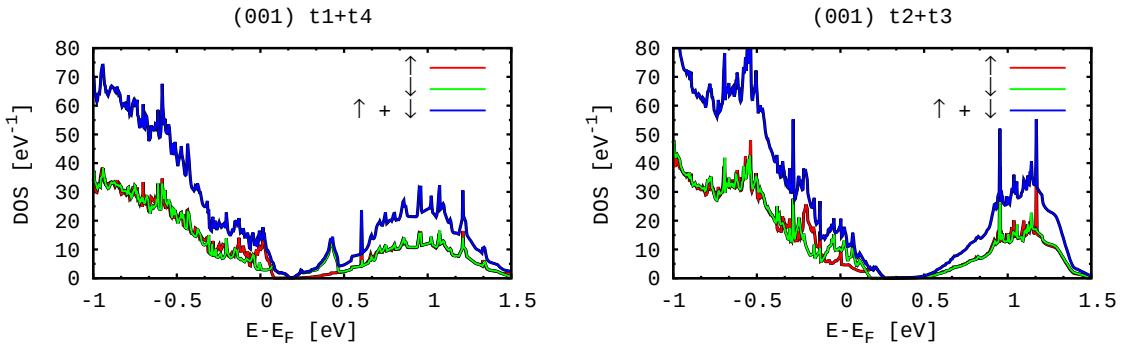

Figure B.7: Surface DOS of all relaxed stoichiometric (001) slabs at the PBE-level. The different spin components are denoted by ↑ and ↓.

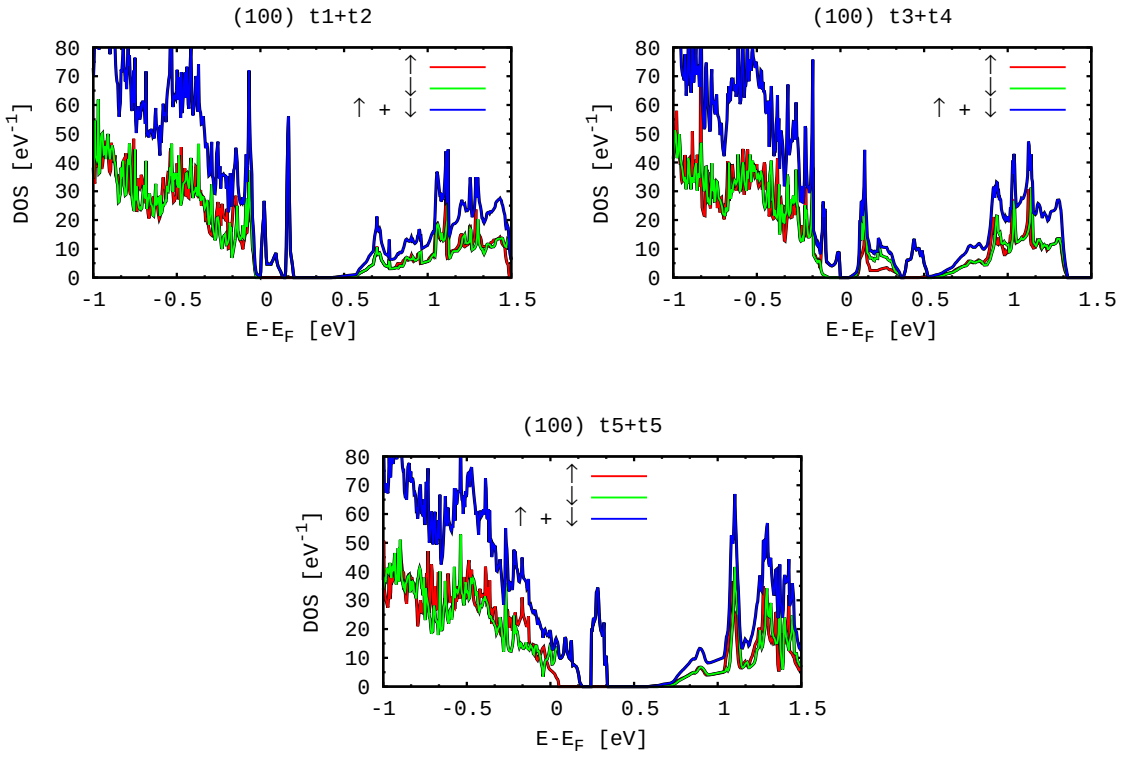

Figure B.8: Surface DOS of all relaxed stoichiometric (100) slabs at the PBE-level. The different spin components are denoted by ↑ and ↓.

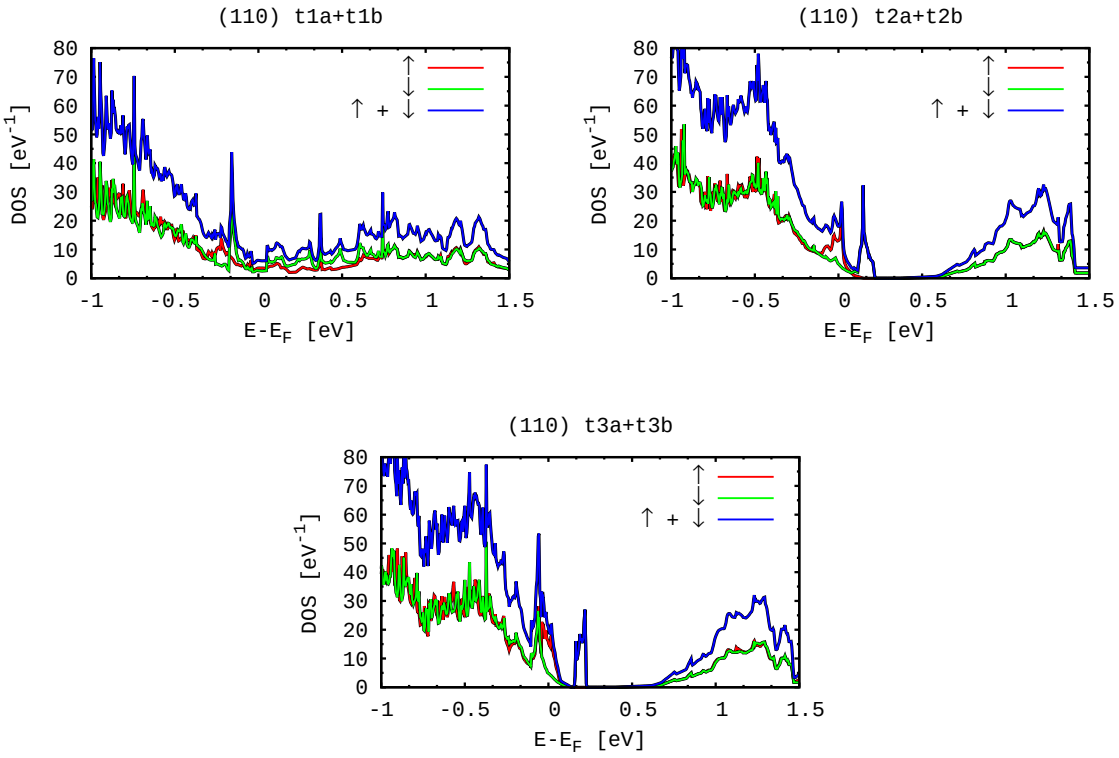

Figure B.9: Surface DOS of all relaxed stoichiometric (110) slabs at the PBE-level. The different spin components are denoted by ↑ and ↓.

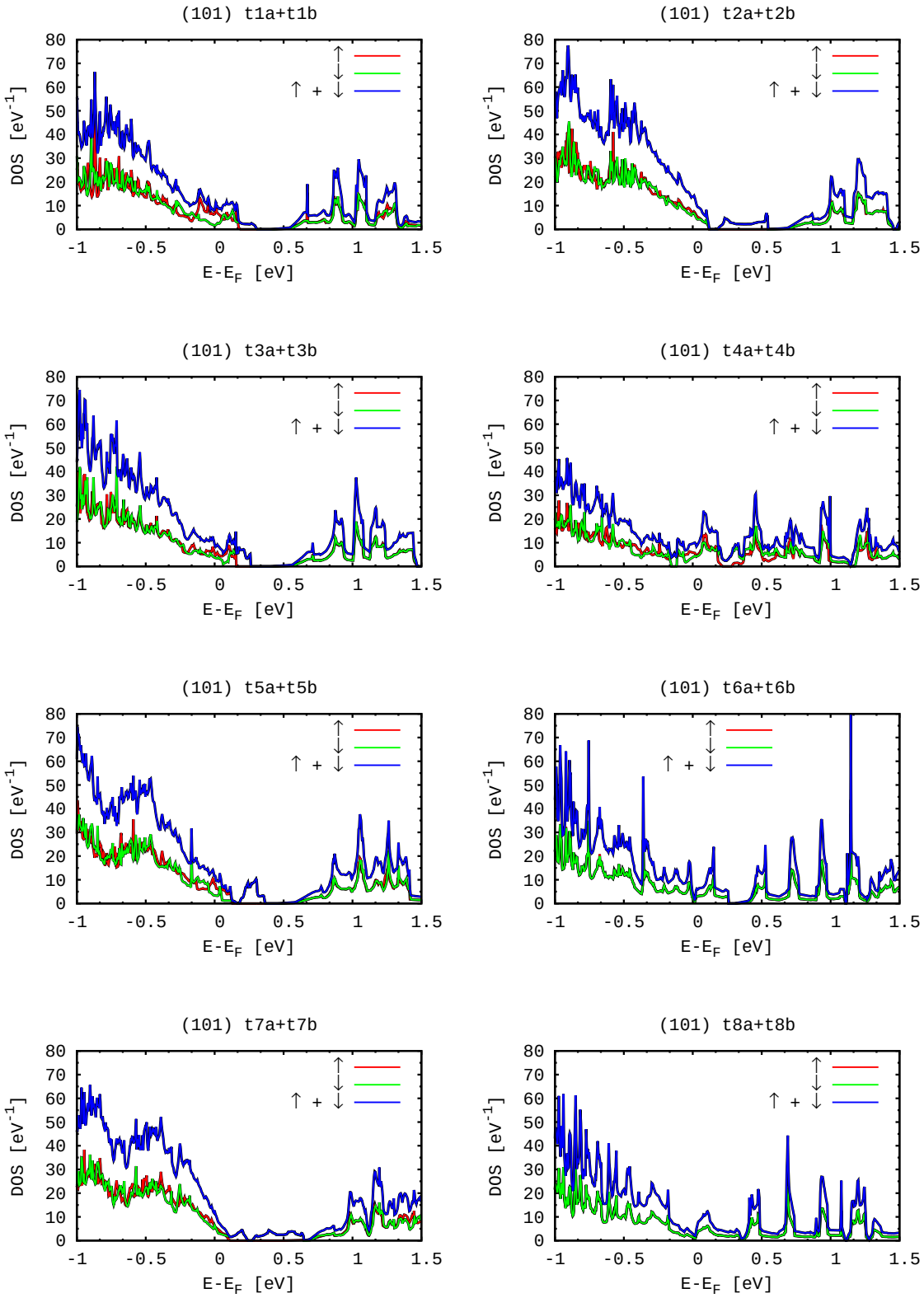

Figure B.10: Surface DOS of the relaxed (101) slabs at the PBE-level. The different spin components are denoted by ↑ and ↓.

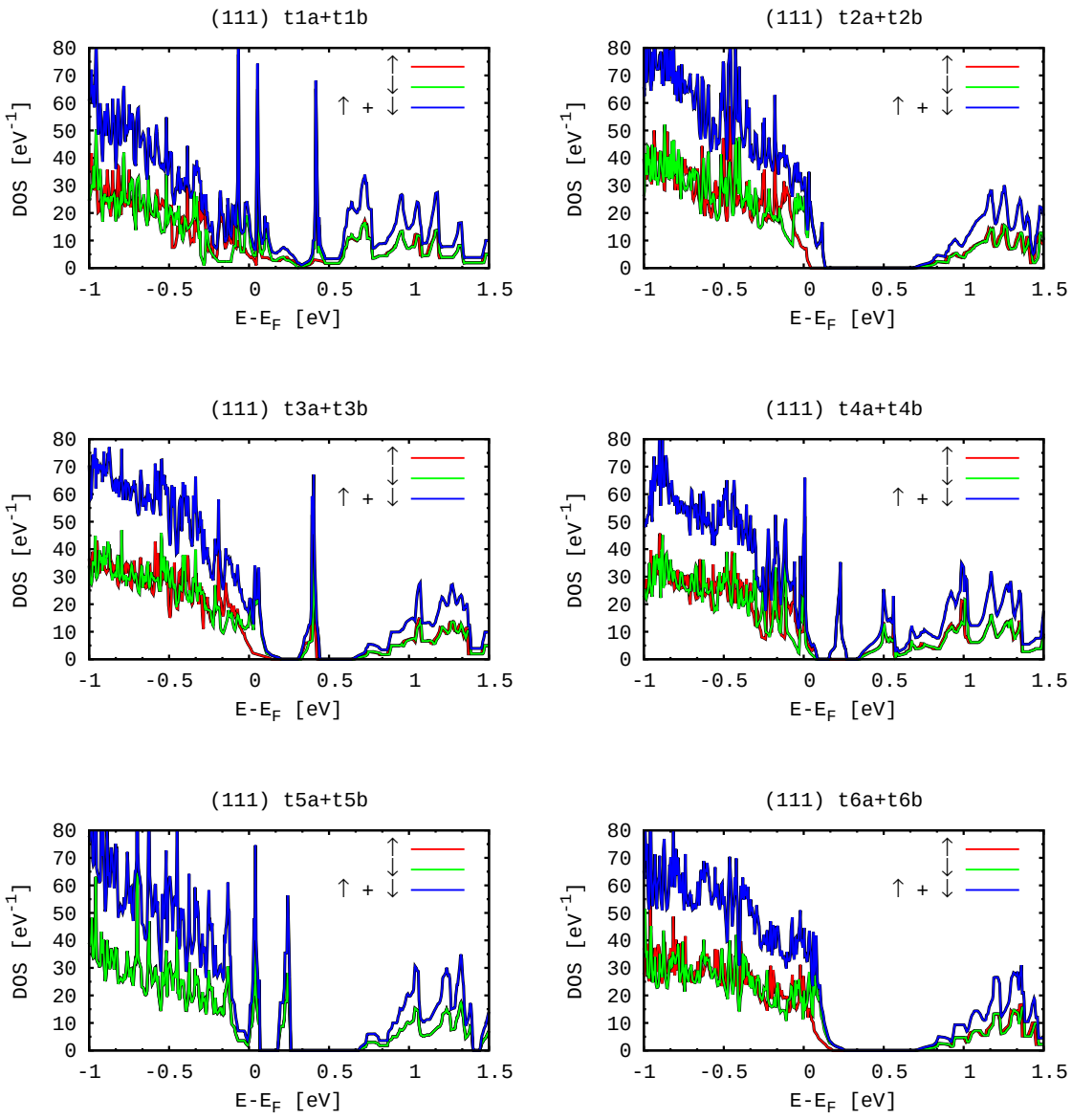

Figure B.11: Surface DOS of all relaxed stoichiometric (111) slabs at the PBE-level. The different spin components are denoted by ↑ and ↓.

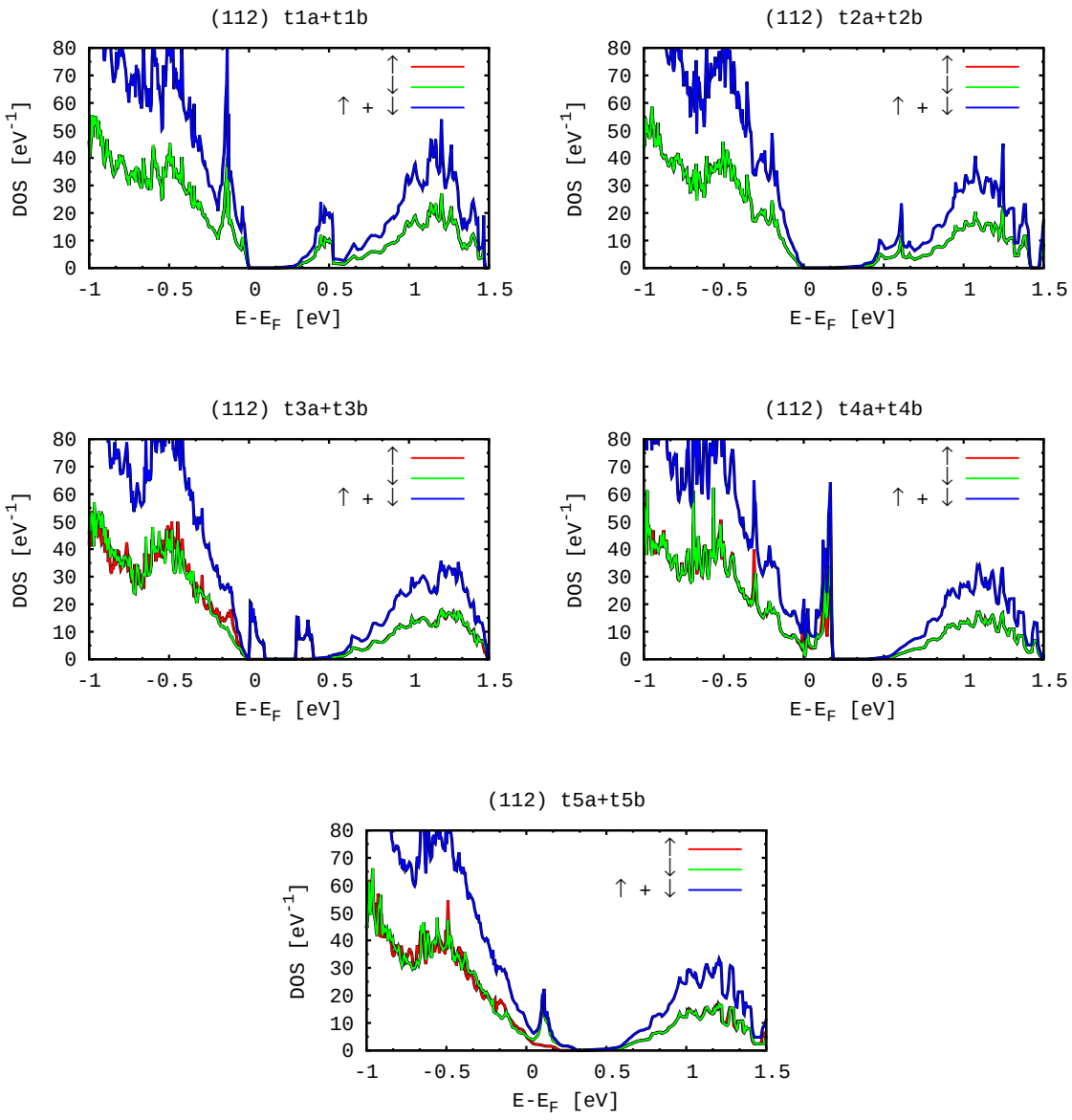

Figure B.12: Surface DOS of all relaxed stoichiometric (112) slabs at the PBE-level. The different spin components are denoted by ↑ and ↓.

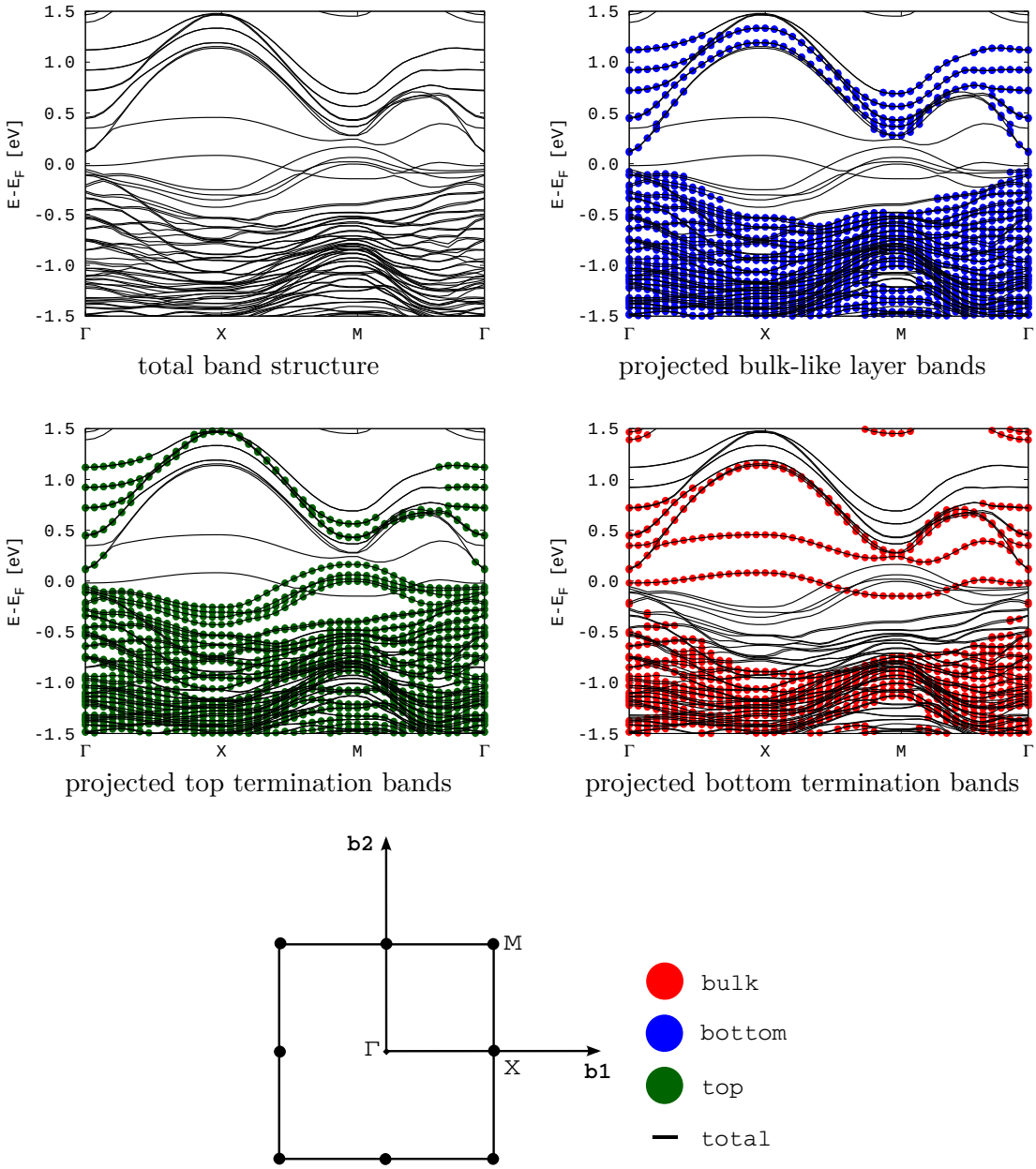

Figure B.13: PBE surface band structure for the most stable stoichiometric slab of the (001) surface. The different band structures show the projection of the band structure onto different parts of the slab. The *bulk-like layer bands* are a band structure projection on the middle layer in the slab. The *top termination bands* and *bottom termination bands* are the projections of the band structure on the terminating layers of the slab. The projections are indicated by a dotted line.

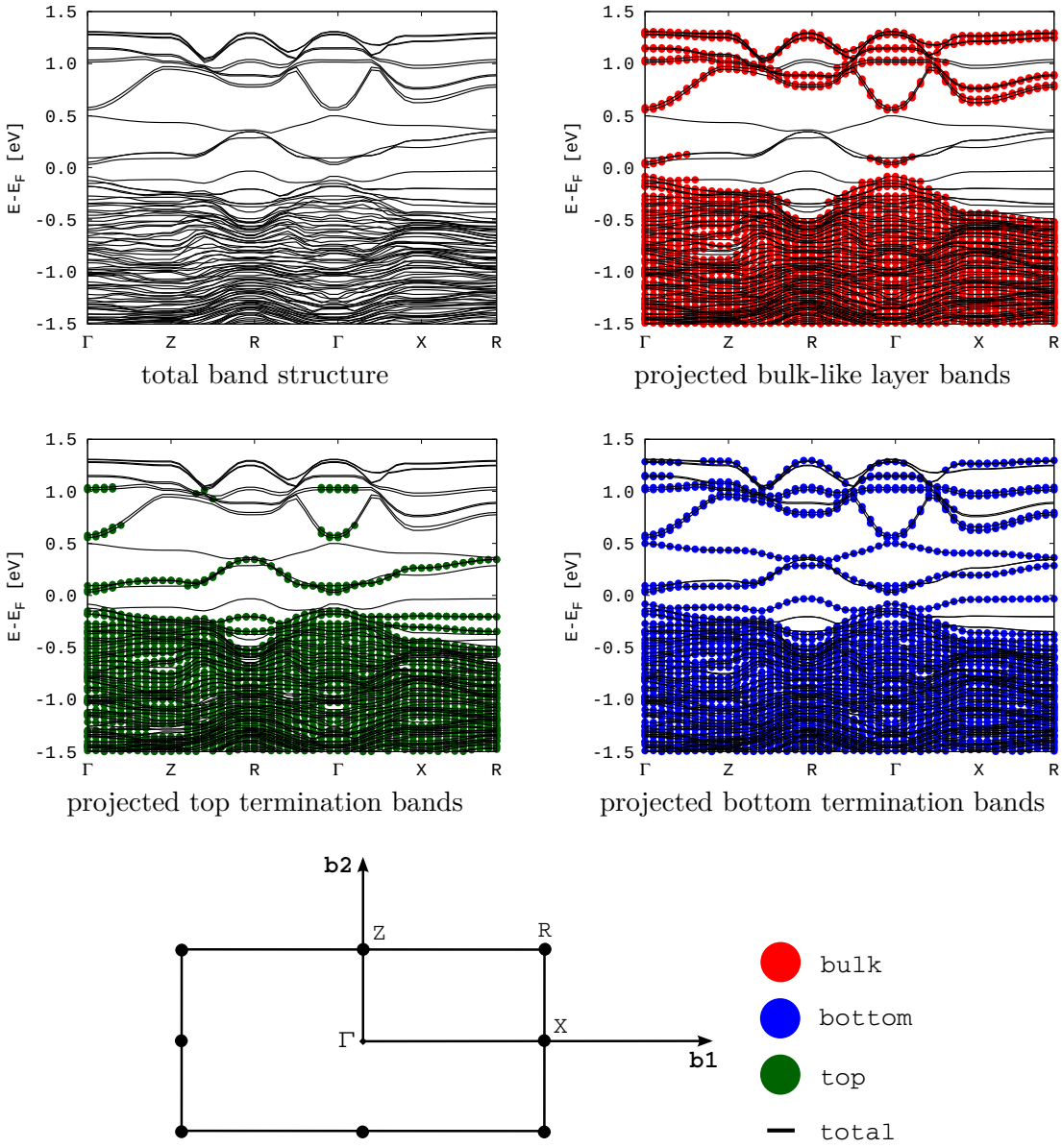

Figure B.14: PBE surface band structure for the most stable stoichiometric slab of the (100) surface. The different band structures show the projection of the band structure onto different parts of the slab. The *bulk-like layer bands* are a band structure projection on the middle layer in the slab. The *top termination bands* and *bottom termination bands* are the projections of the band structure on the terminating layers of the slab. The projections are indicated by a dotted line.

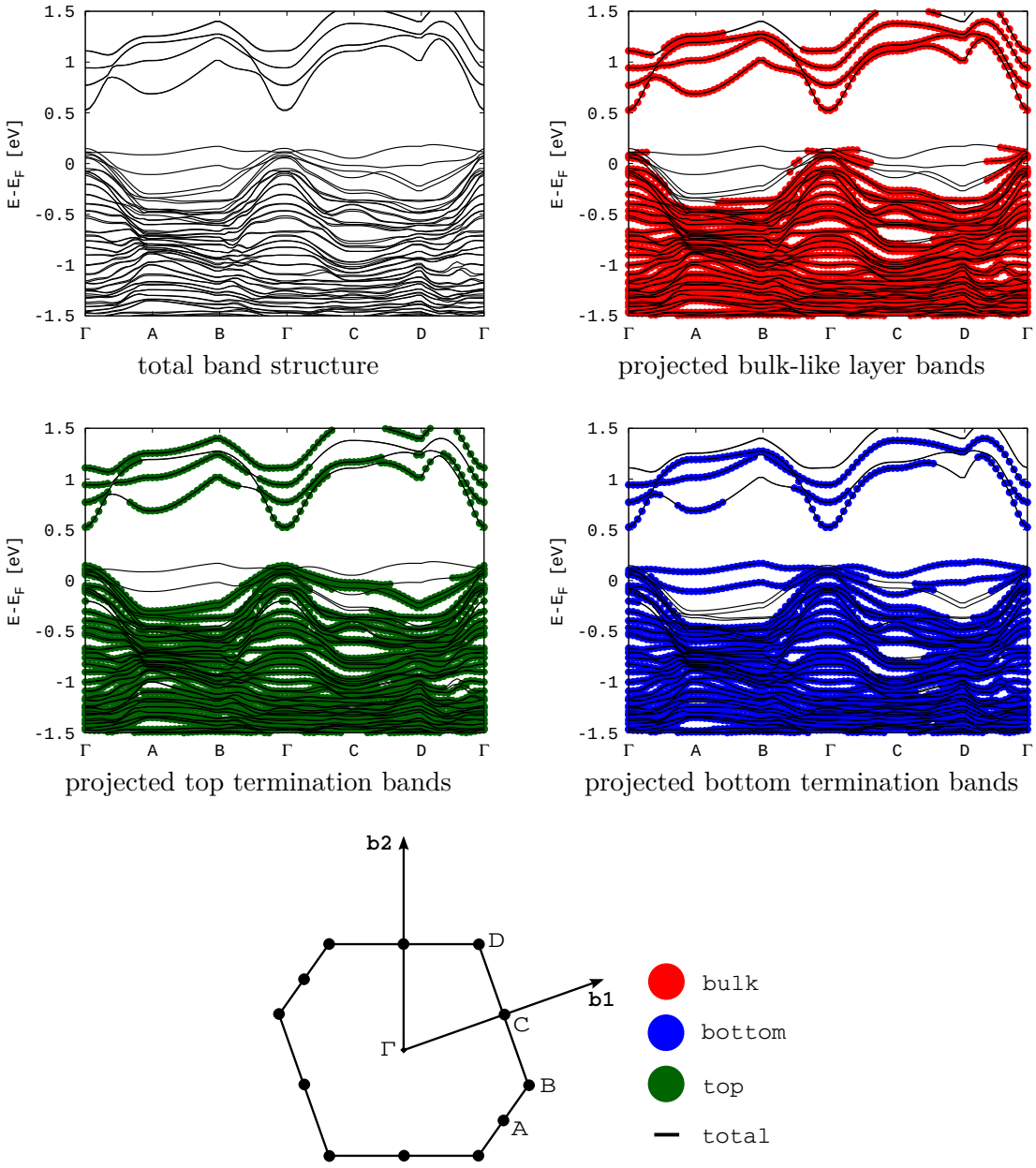

Figure B.15: PBE surface band structure for the most stable stoichiometric slab of the (110) surface. The different band structures show the projection of the band structure onto different parts of the slab. The *bulk-like layer bands* are a band structure projection on the middle layer in the slab. The *top termination bands* and *bottom termination bands* are the projections of the band structure on the terminating layers of the slab. The projections are indicated by a dotted line.

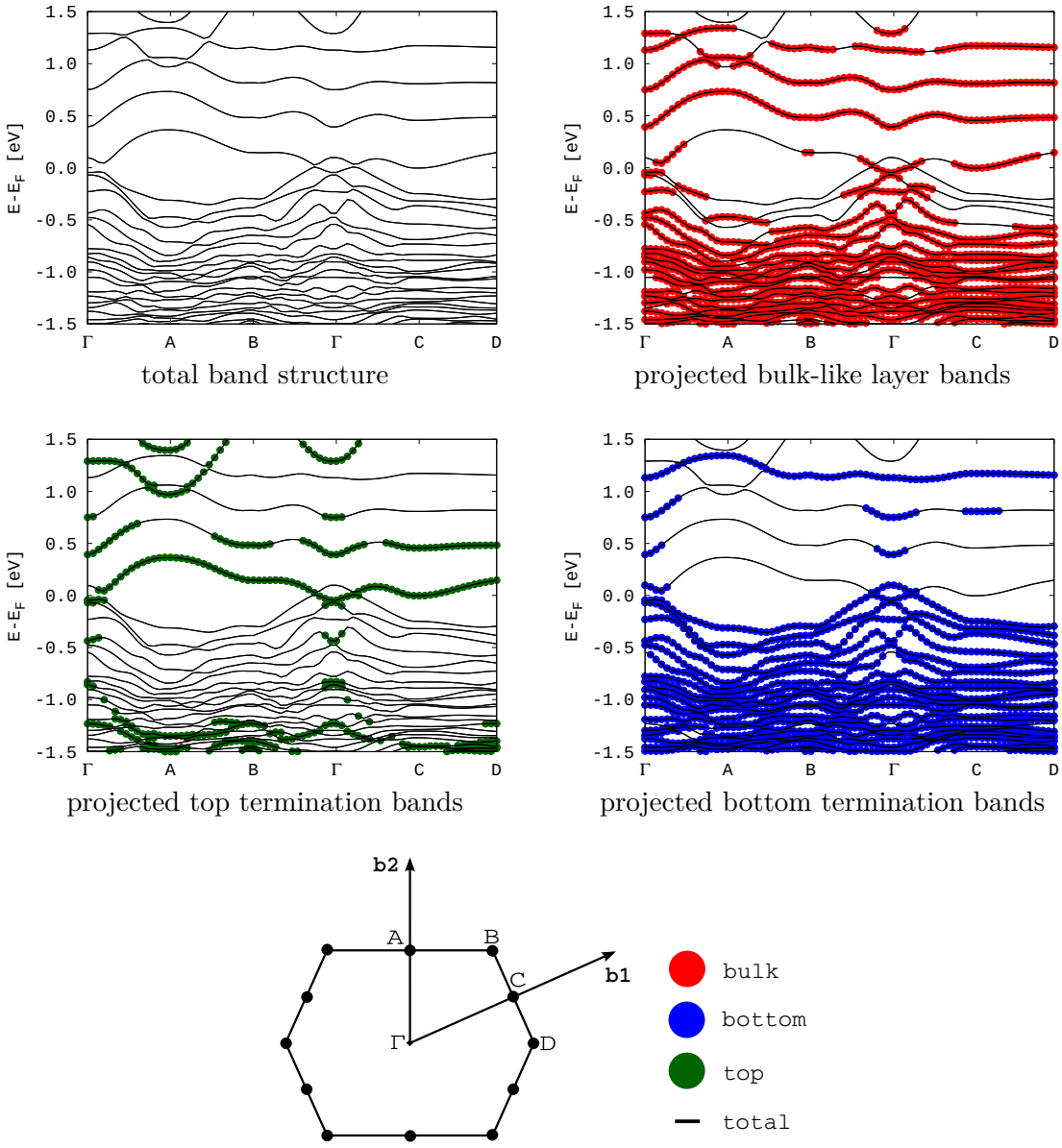

Figure B.16: PBE surface band structure for the most stable stoichiometric slab of the (101) surface. The different band structures show the projection of the band structure onto different parts of the slab. The *bulk-like layer bands* are a band structure projection on the middle layer in the slab. The *top termination bands* and *bottom termination bands* are the projections of the band structure on the terminating layers of the slab. The projections are indicated by a dotted line.

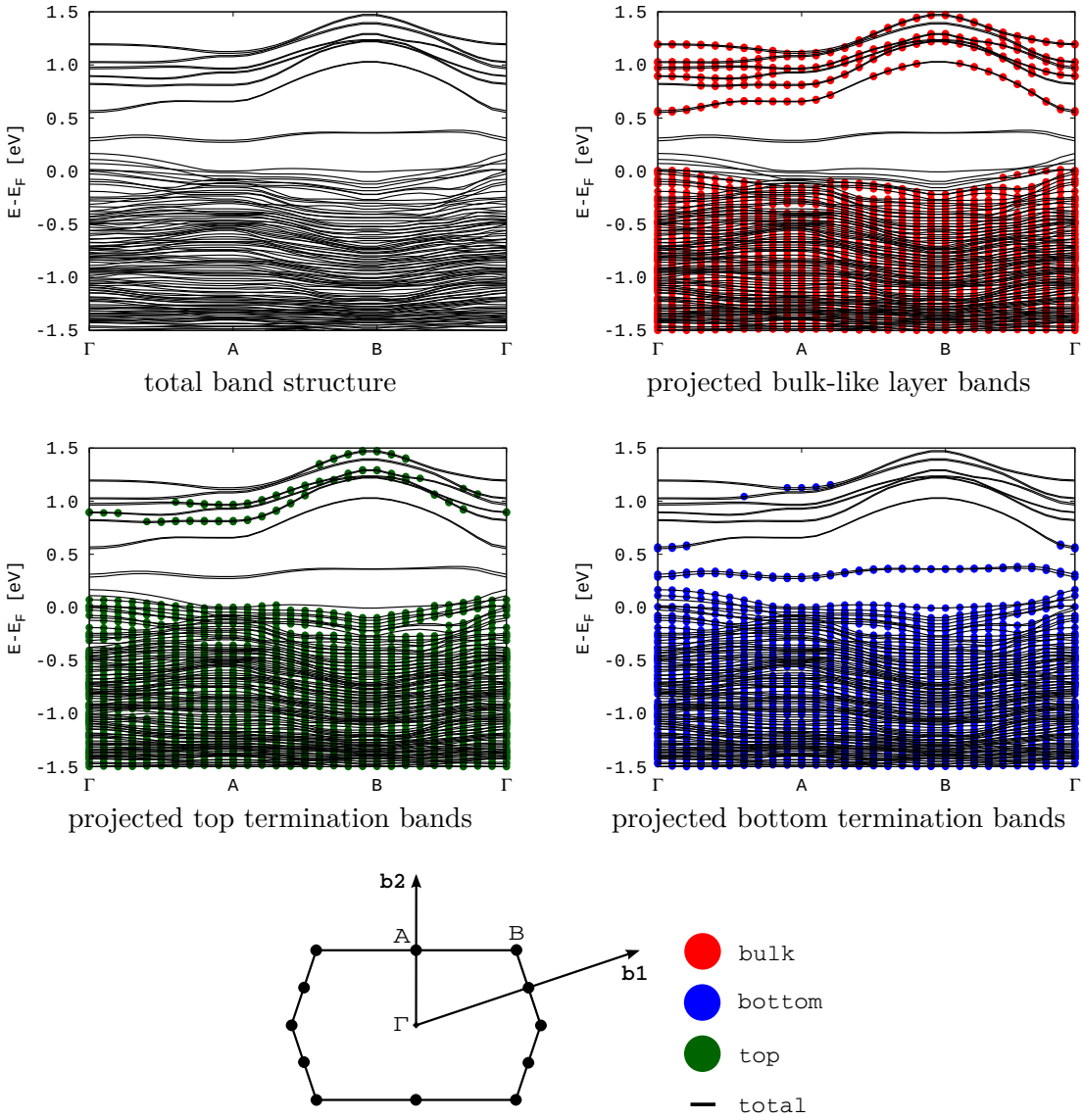

Figure B.17: PBE surface band structure for the most stable stoichiometric slab of the (111) surface. The different band structures show the projection of the band structure onto different parts of the slab. The *bulk-like layer bands* are a band structure projection on the middle layer in the slab. The *top termination bands* and *bottom termination bands* are the projections of the band structure on the terminating layers of the slab. The projections are indicated by a dotted line.

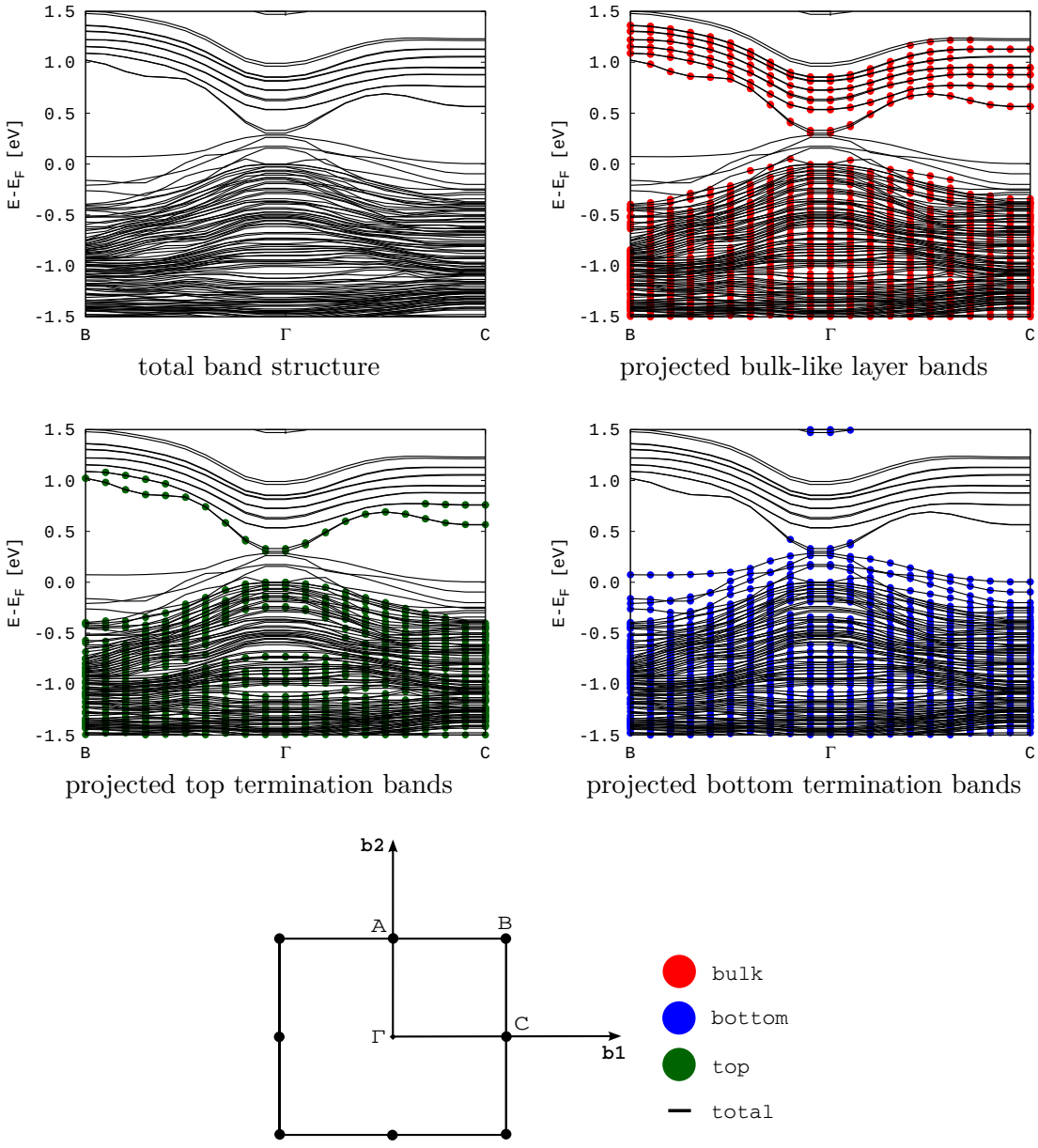

Figure B.18: PBE surface band structure for the most stable stoichiometric slab of the (112) surface. The different band structures show the projection of the band structure onto different parts of the slab. The *bulk-like layer bands* are a band structure projection on the middle layer in the slab. The *top termination bands* and *bottom termination bands* are the projections of the band structure on the terminating layers of the slab. The projections are indicated by a dotted line.